

APPLIED
COMPUTATIONAL
ELECTROMAGNETICS
SOCIETY
JOURNAL

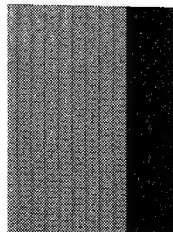
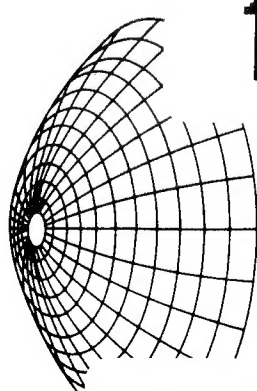
SPECIAL ISSUE
ON
ADVANCES IN
THE APPLICATION OF
THE
METHOD OF MOMENTS
TO
ELECTROMAGNETIC RADIATION
AND
SCATTERING PROBLEMS

GUEST EDITORS
A.W. GLISSON
AND
A.A. KISHK

19951122 018

1995
Vol. 10 No. 3

ISSN 1054-4887



DISTRIBUTION STATEMENT A
Approved for public release;
Distribution Unlimited

U.S. GOVERNMENT PRINTING OFFICE: 1995 500-760-001

19951122 018

GENERAL PURPOSE AND SCOPE. The Applied Computational Electromagnetics Society Journal hereinafter known as the **ACES Journal** is devoted to the exchange of information in computational electromagnetics, to the advancement of the state-of-the-art, and to the promotion of related technical activities. A primary objective of the information exchange is the elimination of the need to "re-invent the wheel" to solve a previously-solved computational problem in electrical engineering, physics, or related fields of study. The technical activities promoted by this publication include code validation, performance analysis, and input/output standardization; code or technique optimization and error minimization; innovations in solution technique or in data input/output; identification of new applications for electromagnetics modeling codes and techniques; integration of computational electromagnetics techniques with new computer architectures; and correlation of computational parameters with physical mechanisms.

SUBMISSIONS CONTENT. The **ACES Journal** welcomes original, previously unpublished papers, relating to **applied computational electromagnetics**.

Typical papers will represent the computational electromagnetics aspects of research in electrical engineering, physics, or related disciplines. However, papers which represent research in **applied computational electromagnetics** itself are equally acceptable.

For additional details, see "Information for Authors" on the back cover.

SUBSCRIPTIONS. All members of the Applied Computational Electromagnetics Society (**ACES**) who have paid their subscription fees are entitled to receive the **ACES Journal** with a minimum of two issues per calendar year. See page 157 for subscription/membership form.

Back issues, when available, are \$15.00 each. Subscriptions to **ACES**, orders for back issues of the **ACES Journal** and changes of addresses should be sent to:

Dr. Richard Adler
ACES Executive Officer
ECE Department, Code ECAB
Naval Postgraduate School
833 Dyer Road, Room 437
Monterey, CA 93943-5121 USA

Allow four week's advance notice for change of address. Claims for missing issues will not be honored because of insufficient notice or address change or loss in mail unless the secretary is notified within 60 days for USA and Canadian subscribers or 90 days for subscribers in other countries, from the last day of the month of publication. For information regarding reprints of individual papers or other materials, see "Information for Authors".

LIABILITY. Neither ACES or the **ACES Journal** editors are responsible for any consequence of misinformation or claims, express or implied, in any published material in an **ACES Journal** issue. This also applies to advertising, for which only camera-ready copies are accepted. Authors are responsible for information contained in their papers. If any material submitted for publication includes material which has already been published elsewhere, it is the author's responsibility to obtain written permission to reproduce such material.

| | |
|----------------------|---------------------------|
| Accesion For | |
| NTIS | CRA&I |
| DTIC | TAB |
| Unannounced | |
| Justification _____ | |
| By _____ | |
| Distribution / _____ | |
| Availability Codes | |
| Dist | Avail and / or Special |
| A-1 | |

APPLIED

COMPUTATIONAL

ELECTROMAGNETICS

SOCIETY

Journal

November 1995

Vol. 10 No. 3

ISSN 1054-4887



The ACES Journal is abstracted in INSPEC, in Engineering Index, and in DTIC.

The second, third, fourth, and fifth illustrations on the front cover have been obtained from Lawrence Livermore National laboratory.

The first illustration on the front cover has been obtained from FLUX2D software, CEDRAT S.S. France, MAGSOFT Corporation, New York.

DTIC QUALITY INSPECTED 1

**THE APPLIED COMPUTATIONAL ELECTROMAGNETICS
SOCIETY JOURNAL**

SPECIAL ISSUE

on

**ADVANCES IN THE APPLICATION OF THE METHOD OF MOMENTS
TO ELECTROMAGNETIC RADIATION AND SCATTERING PROBLEMS**

SPECIAL GUEST EDITORS

A.W. Glisson

A.A. Kishk

Department of Electrical Engineering

University of Mississippi

University, MS 38677

REVIEWERS

N.G. Alexopoulos
University of California
Los Angeles, CA USA

E. Arvas
Syracuse University
Syracuse, NY USA

Gerald Burke
Lawrence Livermore Lab
Livermore, CA USA

M.F. Catedra
Universidad de Cantabria
Santander, SPAIN

W.C. Chew
University of Illinois
Urbana, IL USA

C.G. Christodoulou
University of Central Florida
Orlando, FL USA

R.E. Collin
Case Western Reserve University
Cleveland, OH USA

L.M. Correia
Universidade Tecnica de Lisboa
Lisbon, PORTUGAL

D. De Zutter
Universiteit Gent
Ghent, BELGIUM

K.R. Demarest
University of Kansas
Lawrence, KS USA

M. Drissi
LCST/INSA
Rennes, FRANCE

D.G. Dudley
University of Arizona
Tucson, AZ USA

G.V. Eleftheriades
Ecole Polytechnique
Lausanne, SWITZERLAND

R.K. Gordon
University of Mississippi
University, MS USA

R.D. Graglia
Politecnico di Torino
Torino, ITALY

D.L. Jaggard
University of PA
Philadelphia, PA USA

R. Jost
SRI International
Herndon, VA USA

S.J. Kubina
Concordia University
Montreal, Quebec, CANADA

F.M. Landstorfer
Universitat Stuttgart
Stuttgart, GERMANY

Y. Leviatan
Israel Institute of Technology
Haifa, ISRAEL

C. Lu
University of Illinois
Urbana, IL USA

REVIEWERS (Continued)

| | | |
|---|--|--|
| K. Mahadevan SG Microwaves, Inc. Kitchener, On, CANADA | S.M. Rao Auburn University Auburn, AL USA | M.J. Tsai University of California Los Angeles, CA USA |
| J.R. Mautz Syracuse University Syracuse, NY USA | S.R. Rengarajan California State University Northridge, CA USA | J.L. Volakis University of Michigan Ann Arbor, MI USA |
| K.A. Michalski Texas A&M University College Station, TX USA | T.K. Sarkar Syracuse University Syracuse, NY USA | K.W. Whites University of Kentucky Lexington, KY USA |
| T. Nakata Okayama University Okayama, JAPAN | J. Schmitz Rome Laboratory Hanscom AFB, MA USA | D.L. Wilkes Syracuse Research Corp. Syracuse, NY USA |
| E.H. Newman Ohio State University Columbus, OH USA | A. Sebak University of Manitoba Winnipeg, Manitoba, CANADA | D.R. Wilton University of Houston Houston, TX USA |
| R. Ott SWL, Inc. Albuquerque, NM USA | L. Shafai University of Manitoba Winnipeg, Manitoba, CANADA | E. Yip Boeing Company Seattle, WA USA |
| R.A. Pearlman McDonnell Douglas Corporation St. Louis, MO USA | A. Sihvola Helsinki University of Technology Espoo, FINLAND | R.W. Ziolkowski University of Arizona Tucson, AZ USA |
| G. Pelosi University of Florence Florence, ITALY | | |

THE APPLIED COMPUTATIONAL ELECTROMAGNETICS SOCIETY JOURNAL

EDITORS

EDITOR-IN-CHIEF/ACES

W. Perry Wheless, Jr.
University of Alabama, EE Dept.
PO Box 870286
Tuscaloosa, AL 35487-0286 USA

ASSOC. EDITOR-IN-CHIEF/JOURNAL

Adalbert Konrad
University of Toronto
Toronto, Ont. CANADA

Brian A. Austin
University of Liverpool
Liverpool, UK

Fulvio Bessi
Ingegneria dei Sistemi S.p.A.
Pisa, ITALY

Robert Bevensee
Box 812
Alamo, CA USA

John R. Bowler
University of Surrey
Surrey, UK

Robert T. Brown
Lockheed Aeronautical Sys. Co.
Valencia, CA, USA

Chalmers M. Butler
Clemson University
Clemson, SC, USA

Edgar Coffey
Advanced Electromagnetics
Albuquerque, NM, USA

Tony Fleming
Telecom Australia
Clayton, Victoria, AUSTRALIA

EDITOR-IN-CHIEF/JOURNAL

Duncan C. Baker
EE Dept. University of Pretoria
0002 Pretoria, SOUTH AFRICA

EDITOR-IN-CHIEF, EMERITUS

Robert M. Bevensee
Box 812
Alamo, CA 94507-0516 USA

Christian Hafner
Swiss Federal Inst. of Technology
Zurich, SWITZERLAND

Roger Harrington
Syracuse University
Syracuse, NY, U.S.A.

Donald F. Herrick
ERIM
Ann Arbor, MI, USA

Kueichien C. Hill
Wright Laboratory
Wright-Patterson AFB, OH, USA

Todd H. Hubing
University of Missouri-Rolla
Rolla, MO, USA

Nathan Ida
The University of Akron
Akron, OH, USA

Magdy F. Iskander
University of Utah
Salt Lake City, UT, USA

Kiyohiko Itoh
Hokkaido University
Sappora, JAPAN

MANAGING EDITOR

Richard W. Adler
ECE Department Code ECAB
833 Dyer Rd. Room 437
Naval Postgraduate School
Monterey, CA 93943-5121, USA

EDITOR-IN-CHIEF, EMERITUS

David E. Stein
USAF Scientific Advisory Board
Pentagon
Washington, DC 20330 USA

Peter Krylstedt
National Defence Research Est.
Sundybyberg, SWEDEN

Stanley Kubina
Concordia University
Montreal, Quebec, CANADA

Karl J. Langenberg
Universitat Kassel
Kassel, GERMANY

Ronald Marhefka
Ohio State University
Columbus, OH, USA

Gerald Meunier
INPG/ENSIEG
St. Martin-d'Heres Cedex,
FRANCE

Edmund K. Miller
Ohio University
Athens, OH, USA

Kenzo Miya
University of Tokyo
Tokyo, JAPAN

Osama A. Mohammed
Florida International Univ.
Miami, FL, USA

EDITORS (Continued)

Pat Foster
Microwave & Antenna Systems
Gt. Malvern, Worc. UK

Gregory R. Haack
DSTO
AUSTRALIA

Gerrit Mur
Technische Universiteit Delft
Delft, NETHERLANDS

Takayoshi Nakata
Okayama University
Okayama, JAPAN

Andrew F. Peterson
Georgia Institute of Technology
Atlanta, GA, U.S.A.

Harold A. Sabbagh
Sabbagh Associates
Bloomington, IN, U.S.A.

Randy J. Jost
SRI International
Arlington, VA, USA

Linda P.B. Katehi
University of Michigan
Ann Arbor, MI, USA

Chris Smith
Kaman Sciences Corp.
Colorado Springs, CO, U.S.A.

David E. Stein
USAF Scientific Advisory Board
Pentagon
Washington, DC 20330, USA

C.W. "Bill" Trowbridge
Vector Fields Limited
Oxford, UK

Jean-Claude Verite
Electricite de France
Clamart, Cedex, FRANCE

Giorgio Molinari
University of Genova
Genova, ITALY

Frederic A. Molinet
Societe Mothesim
Le Plessis-Robinson, FRANCE

Frank Walker
Boeing Defence & Space Group
Seattle, WA U.S.A.

Keith W. Whites
University of Kentucky
Lexington, KY, U.S.A.

John W. Williams
SAIC
Germantown, MD 20874

Manfred Wurm
FB Technik
Kiel, GERMANY

THE APPLIED COMPUTATIONAL ELECTROMAGNETICS

SPECIAL ISSUE OF THE JOURNAL

on

ADVANCES IN THE APPLICATION OF THE METHOD OF MOMENTS TO ELECTROMAGNETIC RADIATION AND SCATTERING PROBLEMS

TABLE OF CONTENTS

| | |
|---|---------------|
| Vol. 10 No. 3 | November 1995 |
| "Editorial" by A.W. Glisson and A.A. Kishk | 7 |
| "Model-Based Parameter Estimation in Electromagnetics: III-- Applications to EM Integral Equations" (Invited) by E.K. Miller | 9 |
| "An Examination of the Effect of Mechanical Deformation on the Input Impedance of HF LPDA's Using MBPE" by J.T. de Beer and D.C. Baker | 30 |
| "Current Based Hybrid Moment Method Analysis of Electromagnetic Radiation and Scattering Problems" by U. Jakobus and F.M. Landstorfer | 38 |
| "Hybrid Method of Moments Solution for a Perturbed Dielectric Circular Cylinder" by W.D. Wood, Jr..... | 47 |
| "A Low-Frequency Formulation of the Method of Moments via Surface Charges" by N. Esposito, A. Musolino, and M. Raugi | 53 |
| "A Study of a Recent, Moment-Method Algorithm that is Accurate to Very Low Frequencies" by M. Burton and S. Kashyap | 58 |
| "A Study of Two Numerical Solution Procedures for the Electric Field Integral Equation at Low Frequency" by W.L. Wu, A.W. Glisson, and D. Kajfez | 69 |
| "Electromagnetic Scattering from Two Dimensional Anisotropic Impedance Objects under Oblique Plane Wave Incidence" by A.A. Kishk and P.S. Kildal | 81 |
| "Electromagnetic Scattering by an Arbitrarily Shaped Surface with an Anisotropic Impedance Boundary Condition" by A.W. Glisson, M. Orman, F. Falco, and D. Koppel..... | 93 |
| "Parametric Mapping of Vector Basis Functions for Surface Integral Equation Formulations" by A.F. Peterson and K.R. Aberegg..... | 107 |
| "A Technique for Avoiding the EFIE 'Interior Resonance' Problem Applied to an MM Solution of Electromagnetic Radiation from Bodies of Revolution" by P. Steyn and D.B. Davidson | 116 |
| "Computation of Multipole Moments for Short Thin Wire Chiral Structures" by I.P. Theron, D.B. Davidson and J.H. Cloete | 129 |
| "Application of the UMOM for the Computation of the Scattering by Dielectrics Coated with Weakly Nonlinear Layers" by S. Caorsi, A. Massa, and M. Pastorino | 139 |
| "EM Simulation of Packaged MMIC and Microstrip Antennas Using Microwave Explorer" by A. Sadigh, K. Kottapalli, and P. Petre | 146 |
| Institutional Membership | 153 |
| Copyright Form | 155 |
| ACES Membership Form | 157 |
| Advertising Rates | 158 |
| Copy Information | 158 |

© 1995, The Applied Computational Electromagnetics Society

EDITORIAL

The application of the method of moments (MOM) for the solution of electromagnetic radiation and scattering problems represents a fairly mature area of research. The method of moments is widely applied to the solution of practical electromagnetics problems. There are still advances to be made in the area, however, both in the direct application of the method and manner in which it is used. For example, when MOM is used to obtain frequency scan data, the computationally intensive nature of the method is compounded by the necessity of solving the problem at multiple frequencies. In the invited first paper of this special issue, Ed Miller provides a good review of the work that has been done in the area of application of model-based parameter estimation (MBPE) to integral equation methods, which may be used to reduce the number of different frequencies required for which the problem must be solved. He also provides some speculations about the types of other things that may be done using MBPE and how these relate to MOM solutions. Two other closely related papers by Ed on MBPE will appear in the ACES Newsletter.

There are a total of 14 papers in the special issue. The second paper of the issue continues the MBPE theme and illustrates its application to a mechanical deformation study of an antenna. The next two papers present hybrid techniques employing MOM which seek to extend the range of usefulness of the method to higher frequencies. Although it might come as a surprise to some, the very low-frequency range also presents problems, and three papers address the improvement of the solution accuracy of the method of moments for low-frequency problems. Scattering by bodies having anisotropic impedance boundary conditions is then considered in two papers. Several of the papers in the special issue involve the use of triangular patch models and one of these addresses the problem of improving the model by using a parametric mapping of the vector basis functions on curved patches. One paper considers an alternative procedure for avoiding the interior resonance problem associated with the use of the electric field integral equation. Two other papers address problems involving complex boundary conditions including thin wire chiral structures and weakly nonlinear coatings on dielectric cylinders. The final paper of the issue illustrates the application of MOM to simulation of complex multilayer configurations for MMIC and microstrip antennas.

BIOGRAPHY OF DR. ALLEN W. GLISSON

Allen W. Glisson was born in Meridian, Mississippi, on June 26, 1951. He received the B.S., M.S., and Ph.D. degrees in electrical engineering from the University of Mississippi, in 1973, 1975, and 1978, respectively.

From 1973 to 1978 he served as a Research Assistant in the Electrical Engineering Department of the University of Mississippi. In 1978, he joined the faculty of the University of Mississippi, where he is currently Professor of Electrical Engineering. Dr. Glisson was selected as the Outstanding Engineering Faculty Member at the University of Mississippi in 1986. He received a Ralph R. Teetor Educational Award in 1989. His current research interests include the development and application of numerical techniques for treating electromagnetic radiation and scattering problems, and modeling of dielectric resonators and dielectric resonator antennas. Dr. Glisson has been very involved in the areas of numerical modeling of arbitrarily shaped bodies and bodies of revolution with surface integral equation formulations. He has also served as a consultant to several different industrial organizations in the area of numerical modeling in electromagnetics.

Dr. Glisson is a member of the Sigma Xi Research Society and the Honor Societies Tau Beta Pi, Phi Kappa Phi, and Eta Kappa Nu. He is a Senior Member of the IEEE and is a member of four professional societies within the IEEE, a member of Commission B of the International Union of Radio Science, and a member of the Applied Computational Electromagnetics Society. He was a U.S. delegate to the 22nd, 23rd, and 24th General Assemblies of URSI. Dr. Glisson has received a best paper award from the SUMMA Foundation and twice received a citation for excellence in refereeing from the American Geophysical Union. Since 1984, he has served as the Associate Editor for Book Reviews and Abstracts for the **IEEE Antennas and Propagation Society Magazine**. Dr. Glisson has also recently served as an Associate Editor for **Radio Science** and as the secretary of Commission B of the U.S. National Committee of URSI.

BIOGRAPHY OF DR. AHMED A. KISHK

Ahmed A. Kishk received the B.S. degree in Electrical Engineering from Cairo University, Cairo, Egypt, in 1977, and in Applied Mathematics from Ain-Shams University, Cairo, Egypt, in 1980. In 1981 he joined the Department of Electrical Engineering, University of Manitoba, Winnipeec, Canada, where he obtained his M.Eng. and Ph.D. degrees in 1983 and 1986 respectively.

From 1977 to 1981, he was a research assistant and an instructor at the Faculty of Engineering, Cairo University. From 1981 to 1985, he was a research assistant at the Department of Electrical Engineering, University of Manitoba. From December 1985 to August 1986, he was a research associate fellow at the same department. In 1986, he joined the Department of Electrical Engineering, University of Mississippi, as an Assistant Professor. In summer of 1989, he was a Visiting Research Scientist at the Royal Military College of Canada, Kingston, Ontario. He was on sabbatical leave at Chalmers University of Technology during 1994-1995 academic year. He is now a Professor at the University of Mississippi since 1995. He was an Associate Editor of *Antennas & Propagation Magazine* from 1990 to 1993. He is now an Editor of *Antennas & Propagation Magazine*.

His research interests include the areas of electromagnetic, numerical solutions of applied electromagnetic problems and antenna design, especially antenna feeds for satellite earth stations, microstrip antennas, land mobile satellite antennas, and dielectric resonator antennas. He has published over 165 technical papers, presentations, technical reports and patents. He is a co-author of the **Microwave Horns and Feeds** book with Professors A.D. Olver, P.J.B. Clarricoats, and L. Shafai. Also, he is a co-author of chapter two in the **Handbook of Microstrip Antennas**, edited by J.R. James and P.S. Hall and published by Peter Peregrinus Limited, United Kingdom, 1989. Dr. Kishk received the 1994 best paper award for a paper published in the Applied Computational Electromagnetics Society Journal. One of his students received the Doctor of Philosophy Achievement Award in Engineering for his work on Dielectric Resonator Antennas from the University of Mississippi. Dr. Kishk is a senior member of IEEE (Antennas and Propagation Society and Microwave Theory and Techniques), member of Sigma Xi Society, member of the U.S. National Committee of International Union of Radio Science (URSI) Commission B, member of the Applied Computational Electromagnetics Society, and member of the Electromagnetic Academy.

MODEL-BASED PARAMETER ESTIMATION IN ELECTROMAGNETICS:

III--Applications to EM Integral Equations

E. K. Miller
3225 Calle Celestial, Santa Fe, NM 87501

0. ABSTRACT

Problem solving in electromagnetics, whether by analysis, measurement or computation, involves not only activities specific to these particular categories, but also some concepts that are common to all. Fields and sources are sampled as a function of time, frequency, space, angle, etc. and boundary conditions are satisfied through mathematical imposition or experimental conditions. The source samples, usually the unknowns in a problem, are found numerically or analytically by requiring them to satisfy both the appropriate form of Maxwell's Equations as relationships between them, together with the applicable boundary conditions. Alternatively, source samples may be measured under prescribed experimental conditions. These sampled relationships can be interpreted from the viewpoint of signal and information processing, and are mathematically similar to various kinds of filtering operations. It is this similarity that is discussed here in the context of model-based parameter estimation, where the dependence of electromagnetic fields and sources that produce them are both regarded as generalized signals.

MBPE substitutes the requirement of obtaining all samples of desired quantities (physical observables such as impedance, gain, RCS, etc. or numerical observables such as impedance-matrix coefficients, geometrical-diffraction coefficients, etc.) from first-principles models (FPMs) or from measured data (MD) by instead using a reduced-order, physically-based approximation, a fitting model (FM), to interpolate between, or extrapolate from, FPM or MD samples. When used for electromagnetic observables, MBPE can reduce the number of samples that are required to represent responses of interest, thus increasing the efficiency of obtaining them. When used in connection with the FPM itself, MBPE can decrease the computational cost of its implementation. Some specific possibilities for improving FPM efficiency are surveyed, specifically in terms of using FMs to simplify frequency and spatial variations associated with FPMs. Examples of MBPE applications are included here as well as speculative possibilities for their further development in improving FPM performance.

1.0 BACKGROUND AND MOTIVATION

The computational basis for solving most problems in physics and engineering, including computational electromagnetics (CEM) derives from first-principles mathematical descriptions, or first-principles models (FPMs), of the applicable physics. The computer models which derive from a FPM are developed using numerical analysis, a process that, as has been observed by Oppenheim and Schafer (1975), can be logically interpreted as generalized signal, or information, processing. Consider, for example, solving the LaPlace equation using finite differences, where $\nabla^2 V = 0 \approx (f_{i+1} + f_{i-1} - 2f_i)/h^2$ is equivalent to $f_i = (f_{i+1} + f_{i-1})/2$, showing that the potential at point i is the average of its neighboring values, with similar results obtained in two and three dimensions. Thus, the LaPlacian operator has the property of acting as a spatial, low-pass filter. More elaborate differential equations and numerical treatments produce different "computational molecules" or filters but ultimately lead to expressing a sample of an unknown from the applicable differential equation evaluated in terms of weighted sums of the unknowns in its neighborhood. In this sense, their computational molecules are equivalent to generalized spatial filters. Similar observations apply when solving integral equations numerically, but where the weighted sums that yield a sample of a specific unknown involve all other unknown samples.

Since numerical analysis does exhibit properties in common with signal processing, and also considering that one of the most productive uses of EM fields is the transmission of information, it seems reasonable to inquire about whether there may be possible benefits of examining CEM from a signal-, or information-processing, perspective. As discussed in part I of this article [Miller (1995)], referred to hereafter as RI, EM observables, however obtained, are well-approximated, or exactly described, by series of complex exponentials or complex poles. When the independent variables in the exponential and pole series are the time-frequency transform pair, their sums yield transient waveforms and frequency spectra, while other independent variables (see Table I of RI) are associated with different kinds of observables. For convenience,

the terms waveform domain (WD) and spectral domain (SD), respectively, will be used as generic descriptions whatever are the actual observables given by the exponential and pole series.

Continuing the theme begun in RI, we denote the exponential and pole series as “fitting models” (FMs) whose unknown coefficients are obtained numerically by their being “fitted” to samples of a FPM that they are intended to approximate and replace and which we denote as “generating models” (GMs). This procedure is known as model-based parameter estimation (MBPE). Although MBPE is discussed here specifically with respect to some representative EM applications and particular FMs, it should be appreciated that it is a very general procedure that is applicable to essentially any process, physical or otherwise, for which a reduced-order, parametric model can be deduced. Also, it must be noted that MBPE is not “curve fitting” in the sense that term is normally used, which also can involve finding the parameters of some function which is fit to the available data. The essential difference between MBPE and curve fitting is that the former uses a FM based on the problem physics, while the latter need not do so, which is why MBPE might be characterized as “smart” curve fitting. When curve fitting includes the goal of finding the correct FM for the process that generated the given data, this approach can also be described as “system identification.” It’s worth emphasizing that MBPE is not limited to physical processes but forms the basis for variously named analytical procedures {e.g., Kummer’s method, Richardson extrapolation and Romberg quadrature [Ralston (1965)]} whose purpose is to speed the numerical convergence of mathematical representations involving integrals and infinite sums and wherein the integrand function or the sequence of partial sums can be regarded as a generalized “signal.” In discussing a non-linear procedure he developed for a similar purpose, Shanks (1955) referred to such phenomena as “physical” and “mathematical” transients. In essence, any process that produces a sequence or set of samples is a candidate for MBPE.

In the first part of this article, RI [Miller (1995)], the mathematical background of MBPE is presented for WD and SD signals, showing that the associated FMs can be quantified using function sampling, derivative sampling, or a combination thereof. The second part, RII [Miller (1996)] demonstrates use of MBPE for developing approximate, reduced-order representations of a variety of EM observables in the WD and SD, an example of which is included in this special issue [de Beer and Baker (1995)]. In this article we discuss application of MBPE to improving the computational efficiency of a FPM.

2.0 MBPE APPLICATION TO A FREQUENCY-DOMAIN INTEGRAL-EQUATION, FIRST-PRINCIPLE MODEL

Almost all EM boundary-value problems involve finding the fields over some surface or throughout some volume due to sources distributed over that same surface or volume. When using an integral-equation formulation, these source-field relationships are given by a Green’s function or some equivalent field propagator, whereas a differential-equation model employs the Maxwell curl equations as the propagator. The spatial behavior of the fields might be viewed for some purposes as a generalized signal, as can angle, time and frequency dependencies of such fields as well. Such a perspective can suggest alternate ways of representing the fields in signal-processing terms for numerical purposes to simplify whatever computations that must be done, a viewpoint that is explored here.

For moment-method models based on a frequency-domain integral equation (FDIE) (other FPMs can be analyzed in a similar context), the number of arithmetic operations or operation count (OC), required for solution at a single frequency f_i , OC_i , will depend on the number of unknowns, X_{Si} , used in the model approximately as

$$OC_i \sim A_X X_{Si}^2 + B_X X_{Si}^3 \quad (1a)$$

or, in terms of frequency, f , as

$$OC_i \sim A_f f_i^4 + B_f f_i^6 \quad (1b)$$

for a three-dimensional object requiring two-dimensional sampling (i.e., sampling over its surface). When a solution is desired over some frequency interval, as is usually the case, then the total operation count, OC_T , can be estimated as

$$OC_T \sim \sum A_f f_i^4 + B_f f_i^6, i = 1, \dots, F \quad (2)$$

where there are a total of F solution frequencies.

The “A” terms here account for filling the “system” matrix [known as the impedance or \underline{Z} matrix when an electric-field integral equation (EFIE) is used], and the “B” terms account for solving the system matrix in factored or inverted form as a “solution” matrix (known as the admittance or \underline{Y} matrix when using an EFIE). Use of iterative solution techniques changes the above B terms to $B'_X X_{Si}^2$ and $B'_f f_i^4$ but where B'_f can be much larger than B_f . Various, so-called “fast” techniques are being developed with the goal of

reducing the highest-order terms in Eq. (1a) to of order $X_{Si} \log(X_{Si})$. Clearly, any means of reducing F would also be helpful in decreasing the total computational cost, a point that is considered in detail in Sections 4 and 5. First, let's consider how the impact on OC_i of the individual terms in Eq. (1) can be mitigated.

It can be observed that as the frequency increases from zero for a given problem, OC_i at first grows in proportion to FX_i^2 or Ff_i^4 , but it eventually becomes proportional to FX_i^3 or Ff_i^6 when the higher-order term begins to dominate, assuming a constant spatial sampling density per λ^2 . By reducing both the number of impedance matrices that need to be computed from the defining formulation when impedance-matrix computation dominates OC_i , and the number of admittance matrices that need to be solved from the impedance matrix when solution time dominates OC_i , it should be possible to significantly reduce the OC_T required to cover a specified bandwidth. This might be done by modeling the frequency behavior of the impedance matrix for smaller problems, and the frequency behavior of the admittance matrix for larger problems, in both cases with the goal of reducing the number of FPM evaluations needed, i.e. to reduce F in Eq. (2), and to thus minimize OC_T . It should be noted that the “crossover” point in X_{Si} between fill-time and solution-time domination of OC_i , can vary from as few as 200 unknowns to as many as 10,000 unknowns. Thus, the \underline{Z} and \underline{Y} matrices, or their interaction coefficients, both become candidates for MBPE, albeit using different kinds of FMs as is considered below.

In addition to modeling the frequency behavior of \underline{Z} and \underline{Y} , it is also worth considering whether the spatial behaviors of either of these matrices can be modeled. From a signal-processing perspective, the spatial variation of the field over an object due to a given localized source (e.g., a subdomain basis function) on that object might be regarded as a generalized signal. If this field “signal” can be predicted or estimated using a FM that is computationally simpler than using the defining equations normally employed for calculating the exact interaction coefficients, the magnitude of the A_f term in Eq. (2) could be commensurately reduced. Alternatively, if a first-principles evaluation of only a subset of the X_s^2 interaction coefficients needs to be done, say CX_s where $C \ll X_s$, and the rest can be estimated from the rigorously computed coefficients, then the effect would be to change the $A_x X_s^2$ term to

of order $CA_x X_s$, if the cost of obtaining the estimated values is much less than that of the rigorously computed coefficients.

A specific example of reducing the A_f term in Eq. (2) is to compute none of the X_s^2 interaction coefficients in \underline{Z} from first principles, but instead to estimate them using some appropriate FM based on a small set of precomputed, first-principles field samples. This approach, summarized in Section 4 below, was used by Burke and Miller (1984) for reducing the cost of evaluating the Sommerfeld integrals that arises when modeling objects near an interface where the FMs are analytical approximations to these integrals. Their approach is an extension of earlier work described by Miller et al. (1977) where linear interpolation of sampled Sommerfeld integrals for the matrix coefficients was used as a curve-fitting procedure rather than MBPE. Other problems having special Green’s functions are also candidates for this procedure, another example of which is provided by modeling sources between infinite parallel planes [Demarest et al. (1989)]. In these instances, the reduction in OC_i is reflected in a decrease in the A_f coefficient in Eq. (1).

Another way of reducing the effect of the A_f term is to exploit the fact that, as the source and observation points become more widely separated, the complexity of their interaction fields is reduced. This is easy to see by considering that the fields in the vicinity of a linear source distribution of a few wavelengths in extent are to be pointwise sampled along a line parallel to, and a distance ϵ away from, the source. In order to develop an accurate-enough representation, it would necessary to sample the field at some minimum density per wavelength. Now consider the situation as the sampling line is moved further and further away from the source. The field variation along that line will become less complex as the near-field components decrease with increasing distance and finally only the $1/t$ field remains. Furthermore, with increasing observation distance, the spatial variation of the field along a line of fixed length further decreases in complexity because the angle subtended by this line at the source monotonically decreases. In other words, at a great enough, finite distance away from the source, the field variation becomes a function of subtended angle rather than of linear distance over some fixed observation range.

Thus, the effective rank of the interaction between sources of given size decreases as their separation distance increases, reducing the complexity of that interaction, and, consequently, the amount of computation needed to determine it to some specified

accuracy. This idea is exploited in techniques such as the fast multipole method [Coifman, et al. (1993)], impedance-matrix localization [Canning (1990)], recursive models [Chew (1993)], etc., where rank reduction is explicitly employed, or where more distant interaction coefficients are approximated by simpler expressions [Vecchi et al. (1993)]. Such approaches effectively employ exact interaction coefficients when the source and observations points are close and controlled approximations as their separation distance increases. This results in an A_f coefficient that becomes smaller as source-observation distance increases, or a reduced matrix-fill time. In addition, because the interaction complexity decreases with increasing distance for fixed source and observations spans, the complexity, or effective number of interaction coefficients also decreases, reducing the OC_i of multiplying the impedance matrix by a source vector from of order $(X_i)^2$ to of order X_i . The OC_i associated with solving a matrix having X_i unknowns by iteration thus trends towards order X_i or $X_i \log X_i$ from being of order $(X_i)^2$.

Whether spatial variations in the solution or admittance matrix might be exploited in a similar fashion is not so clear. Certainly, a valid solution to the original problem must exhibit spatial dependencies consistent with the geometry and excitation involved and be consistent with Maxwell's equations. Graphical examination of the \underline{Y} matrix for simple objects like a straight wire [Miller et al. (1981) and below] reveals that it exhibits a standing-wave character, not a surprising result in that the currents on such structures are well-known to have such behavior. In other words, the "traveling-wave" nature of the Green's function in the formulation domain, reflected in terms like $\exp(ikR)/R$, is converted to a standing-wave response in the solution domain, where amplitude maxima occur at resonances associated with the object poles. Thus, an appropriate FM for the admittance matrix should apparently be expected to be of wave-domain type as well. These kinds of ideas are now explored from the perspective of MBPE in the following section.

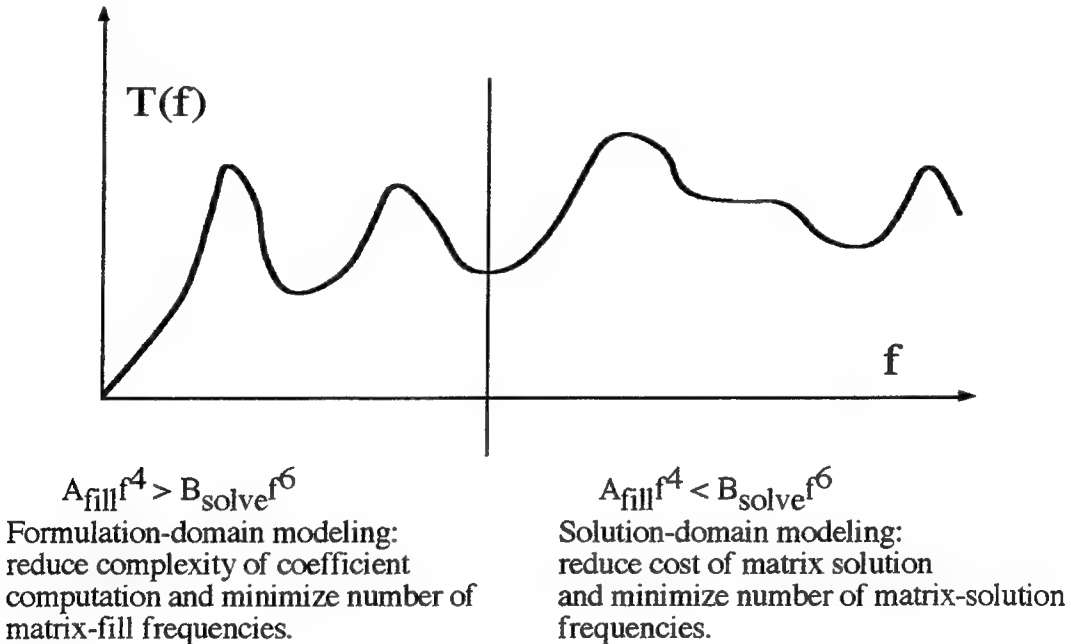


Figure 1. Illustration showing where matrix-fill and matrix-solution operation counts dominate for a frequency-domain integral equation solved using L-U decomposition and assuming that a fixed sampling density per wavelength is used as frequency is increased. At lower frequencies a computational benefit can be realized by finding ways to compute interaction coefficients more efficiently or to reduce the number of rigorously computed \underline{Z} matrices. At higher frequencies, a computational benefit results from reducing the number of solutions, or \underline{Y} matrices.

3.0 THE TWO APPLICATION DOMAINS IN INTEGRAL-EQUATION MODELING

We have discussed MBPE in CEM from the perspective of whether the quantities of interest exhibit wavelike or polelike behavior, referring to their

respective occurrences by the designations waveform domain and spectral domain, respectively, determined by the mathematical description that applies to a given quantity. There is another domain pair that is also useful for problem categorization, one describing the

domain wherein a boundary-value problem is defined, and the other describing the domain wherein a solution to that problem is presented. We refer to the former as the "formulation" domain, in which a formal mathematical statement originating from Maxwell's Equations is developed for a problem, and to the latter as the "solution" domain, in which that original formulation has been mathematically solved. In the formulation domain we begin with known exciting fields to which to-be-found induced sources are required by Maxwell's Equations to satisfy the appropriate boundary conditions. Finding these induced sources requires inverting the original source-field relationship. For all but the simplest problems the inversion requires numerical computation.

A potential approach to alleviating the computational requirements that arise in either the formulation domain or solution domain is to exploit the underlying physical and mathematical behavior of EM fields, as is embodied in first-principles analysis of wave-equation problems, through a simplifying, reduced-order, signal-processing formalism. Of course, knowledge of the problem physics is required to begin with as any solution process, analytical or numerical, can not be initiated without having the applicable physics captured in appropriate mathematical form, something that in terms of Maxwell's Equations might be characterized as a microscopic description. But the physical behavior of greater practical interest is usually macroscopic in nature, as it is not generally the fine details of the current distribution on an antenna or the near fields around a scatterer, but the antenna input impedance and gain, or scattering cross section, that are needed for system design. The macroscopic description is naturally a reduced-order one and provides the context for MBPE.

As previously observed, MBPE involves fitting physically motivated analytical approximations (the model) to accurately computed or measured EM observables from which unknown coefficients (the model parameters) are numerically obtained. These fitting models can then be used in subsequent applications to more efficiently characterize time, frequency, angle and space responses as well as to provide more insightful access to the underlying physics. In the solution domain, MBPE can be applied directly to the spatial and frequency dependencies of the computed observables themselves, such as currents and fields as discussed in RII, or instead to the solution matrix from which these quantities are obtained, as is discussed here.

Alternatively, we might also employ MBPE in the formulation domain, where it is the behavior of the first-principles analytical representation that is being approximated by reduced-order FMs. In that case, the

frequency and space dependence to be represented would be that of the defining source-field relationships as contained in the system matrix. In contrast to working in the solution domain, where resonance effects dominate the EM behavior, growing phase change and geometric attenuation of the fields of increasingly distant sources dominate the behavior when working in the formulation domain. While the most appropriate FM will depend on the particular quantity being modeled, exponential- and pole-series models are widely applicable. For example, the frequency and spatial variations of a FDIE are suitable for exponential, or WD, FMs in the formulation domain, whereas in the solution domain pole-series FMs are suitable for frequency and angle variations and exponential-series FMs for their spatial variation. Formulation-domain approaches are described by Newman (1988) and Benthien and Schenck (1991), and solution-domain approaches are presented in Burke et al. (1988, 1989). Other kinds of FMs can be found useful, e.g. based on the geometrical theory of diffraction, for other analytical formulations and solutions. Some of these possibilities are discussed in the following sections. Each of these two FMs and problem domains are considered in the following.

4.0 FORMULATION-DOMAIN MODELING

4.1 Waveform-Based MBPE in the Formulation Domain

The question to be considered here is how waveform-based MBPE might be used for improving the numerical solution of a FDIE. First observe that the coefficients that appear in the impedance matrix for an FDIE model can be expressed in the generic form

$$Z_{m,n}(\omega) = \int_{\Delta_n} S_n(\omega) K_{R,m,n}(\omega) K_{\Delta,m,n}(\omega) d\Delta_n \quad (3)$$

where m and n denote the observation and source patches, respectively; S_n is the source on patch Δ_n ; $K_{R,m,n}$ is the patch-to-patch (or P-P) part of the IE kernel; and $K_{\Delta,m,n}$ is the in-patch (or I-P) part of the kernel, where we have assumed a subdomain numerical model is being used. These terms refer, respectively, to that part of the kernel function whose frequency and spatial dependence is driven by an exponential phase change due to the P-P distance as contrasted with those variations due to variable positions within the source (and, possibly, observation) patches. Because increasing the P-P distance and increasing the frequency both increase the phase of $K_{R,m,n}$, changes in one or the other of these variables have similar effects on interaction phase, an effect that is exploited in using scale models in making

experimental measurements. Considering frequency variations specifically, except for the patches that are close to each other (with respect to the wavelength), the P-P term would normally represent a faster frequency variation while the I-P would always represent a slower frequency dependence because patches need to be small relative to a wavelength while the interpatch distance can be arbitrarily large. The $X_S x X_S$ set of interaction coefficients defined by Eq. (3) provides all the information needed to represent an object's EM characteristics, to the degree permitted by a numerical model based on it, but the source-field, integral-equation relationship represented by $\underline{Z} \cdot \underline{I} = \underline{V}$ must be inverted to $\underline{I} = \underline{Y} \cdot \underline{V}$ to obtain the desired solution.

The P-P, or fast, term always has the form, for IE-based models,

$$K_{R,m,n}(\omega) = e^{jkr_{m,n}/r_{m,n}} \quad (4)$$

where $r_{m,n}$, the separation between the origins of the source- and observation-patch local coordinates, is assumed to be a far-field distance and k is the wavenumber, a form that emphasizes the traveling-wave nature of the impedance-matrix coefficients. Integration over the source patch (and, possibly, the observation patch if using other than delta-function field sampling; though here we explicitly consider only source integration) involves changes in the fast term of order $\exp(jk\Delta r_{mn})$, where $k\Delta r_{mn} \ll 1$ is the distance variation caused by scanning over patch n . The interaction coefficient $Z_{m,n}$ can, thus, be rewritten as

$$Z_{m,n}(\omega) = e^{jkR_{m,n}} \int_{\Delta_n} S_n(\omega) K'_{\Delta,m,n}(\omega) d\Delta_n \quad (5)$$

with $R_{m,n} + \Delta r_{mn} = r_{m,n}$ and $K'_{\Delta,m,n}$ a modified slow-variation kernel. This form of interaction coefficient suggests that we can estimate $Z_{m,n}(\omega_2)$ at a new frequency ω_2 from an accurately computed value at frequency ω_1 as

$$Z_{m,n}(\omega_2) \approx Z_{m,n}(\omega_1) e^{j(\omega_2 - \omega_1)(R_{m,n}/c)} M_{m,n}(\omega_2 - \omega_1) \quad (6)$$

where $M_{m,n}(\omega_2 - \omega_1)$ is an interpolation model that accounts for the slowly varying part of the kernel function whose specific form would depend not only on object geometry but on whatever frequency dependence might have been incorporated into the basis

and testing functions that are used. Exploiting a capability for modeling the spatial variation and its decreasing complexity with increasing distance is more involved, but is essentially embodied in "fast" methods which seek to reduce the OC of filling \underline{Z} and performing $\underline{Z} \cdot \underline{I}$ multiplies from of order X_S^2 to of order $X_S \log(X_S)$ [e.g., see Canning (1990), Chew (1993), Coifman et al. (1993)]. The specific problem of modeling the frequency variations in \underline{Z} is considered next.

4.1.1 Modeling Frequency Variations-- Antenna Applications.

The model $M_{m,n}$ might be represented in various ways including using low-order polynomials (the model) whose coefficients (the parameters) are computed from samples of $Z_{m,n}$ at selected frequencies [Newman (1988), Bentien and Schenck (1991)]. When sinusoidal bases functions specifically are used, it may also be advantageous to develop a recursive form for $M_{m,n}$. By accurately computing the impedance matrix at widely spaced frequencies and using estimated values at intervening frequencies, the goal is to obtain acceptably accurate results across a wide bandwidth without the cost of computing the impedance matrix at all sampling frequencies desired. As an example application, the analytical behavior of the impedance-matrix coefficients has been approximated for small variations in frequency about the computation point ω_1 by [Newman (1988)]

$$M_{m,n}(\omega - \omega_1)|_{\text{imag}} = A_i + B_i \ln(\omega - \omega_1) + C_i(\omega - \omega_1) \quad (7)$$

$$M_{m,n}(\omega - \omega_1)|_{\text{real}} = A_r + B_r(\omega - \omega_1) + C_r(\omega - \omega_1)^2 \quad (8)$$

A result obtained by Newman is presented in Fig. 2 where the input impedance of a center-fed dipole antenna is plotted as a function of frequency over its first two resonance frequencies. Two different curves are shown, one for a GM sample interval of 300 MHz and the other of 600 MHz.

Virga and Rahmat-Samii (1995) used \underline{Z} -matrix frequency modeling for more complex communications antennas, one result for which is shown in Fig. 3. There the input impedance of a 4-turn helical antenna on an infinite ground plane is plotted versus frequency as obtained by direct evaluation and from two interpolation methods. The interpolated results are obtained using a simple quadratic FM and a second FM that incorporates the singularity of interaction coefficients for segments closer than one-half

wavelength and otherwise uses Eqs. (6) to (8). The authors report an approximately 30-to-1 computer savings results from modeling the $\underline{\underline{Z}}$ matrix as compared with direct evaluation at a total of 301 frequency samples.

4.1.2 Modeling Frequency Variations:

Elastodynamic Scattering.

Benthien and Schenck (1991) have used an approach similar to the above for modeling elastodynamic problems whose frequency responses, it should be noted, can be much more complex in structure than typical EM spectra. One interesting aspect of their work is that they are able to span a bandwidth that includes several resonances with only two FPM system-matrix computations at its

endpoints while using MBPE for frequencies between them, in contrast to modeling the solution (admittance) matrix where the equivalent of two samples per resonance are required [RII]. The resonance structure is manifested only when the solution has been developed, or the source-field description has been inverted. This difference stems from the fact, so long as phase changes are handled accurately enough across a given frequency interval over which the phasor between the most widely spaced points on the object being modeled rotates through several (say n) times 2π , then n to $2n$ resonances can be predicted by using only 2 FPM samples. Examples of Benthien and Schenck's results are included in Figs. 4 and 5.

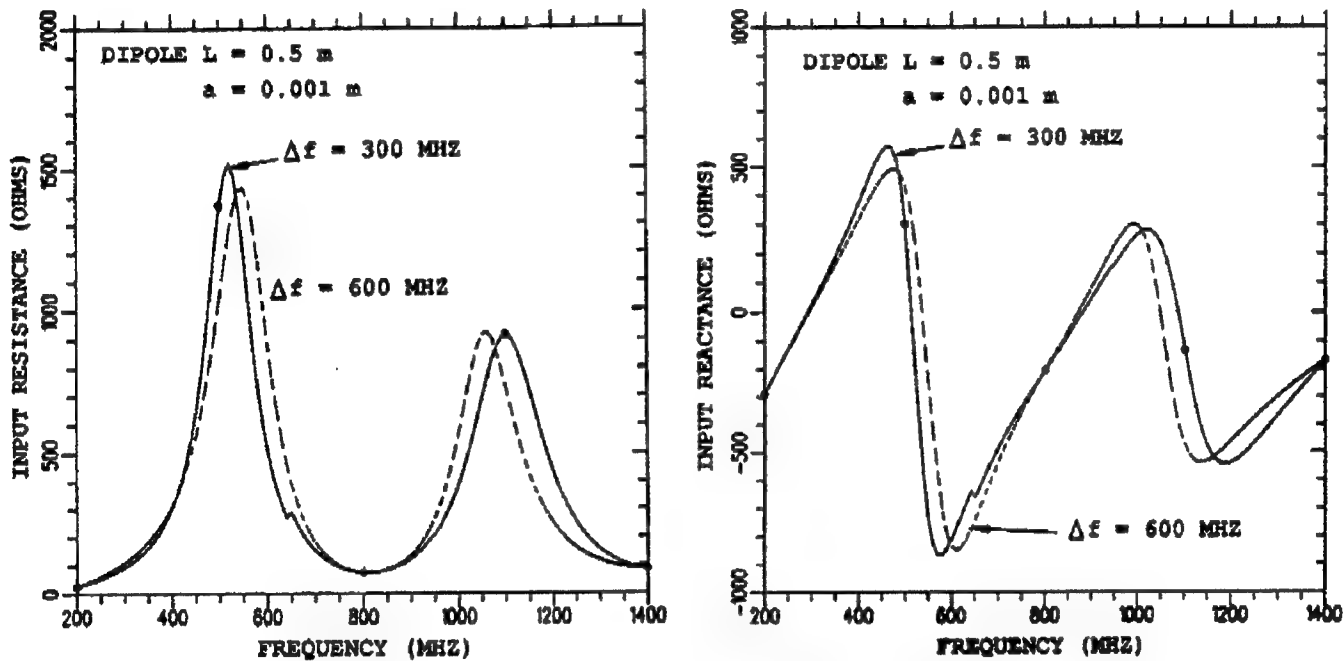


Figure 2. Results from using MBPE and two different FMs to represent the interaction coefficients of the $\underline{\underline{Z}}$ matrix of a center-fed, half-wave dipole antenna [Newman (1988)]. The FMs employ the approach of Eqs. (31) to (33) and are based on GM samples spaced 300 MHz apart (the solid line) and 600 MHz apart (the dashed line). The discontinuity in the impedance curves occurs at the point where a FM replaces a GM sample at one end of its span with a new one at the other as successive GM samples are employed.

4.1.3. Modeling Spatial Variations:

The Sommerfeld Problem.

A computationally demanding problem is that of determining the Sommerfeld fields that result from the interaction of elementary sources with a half space and which become part of the Green's function in an IE model for antennas near ground, microstrip structures, etc. One of the first approaches to this problem to incorporate numerically the rigor of the Sommerfeld integrals while avoiding their computational complexity used a two-dimensional mesh of pre-computed Sommerfeld integrals [Miller et al. (1977)]. This permitted evaluating the impedance-matrix coefficients for wire objects located on one side of an interface

from simple bivariate interpolation, since the fields are then functions of only two variables, their lateral separation ρ and the sum of the vertical coordinates, z' and z , of the source and observations points relative to the interface, respectively. This essentially curve-fitting approach, used in NEC-2, reduced the matrix fill time to being little more than what is needed for a perfectly conducting ground where image theory is analytically rigorous. An example of the field variation on the same side of the interface as a fixed source located near an interface is shown as a function of observation position in Fig. 6. Clearly, the field is quite well-behaved and can be accurately approximated using linear interpolation.

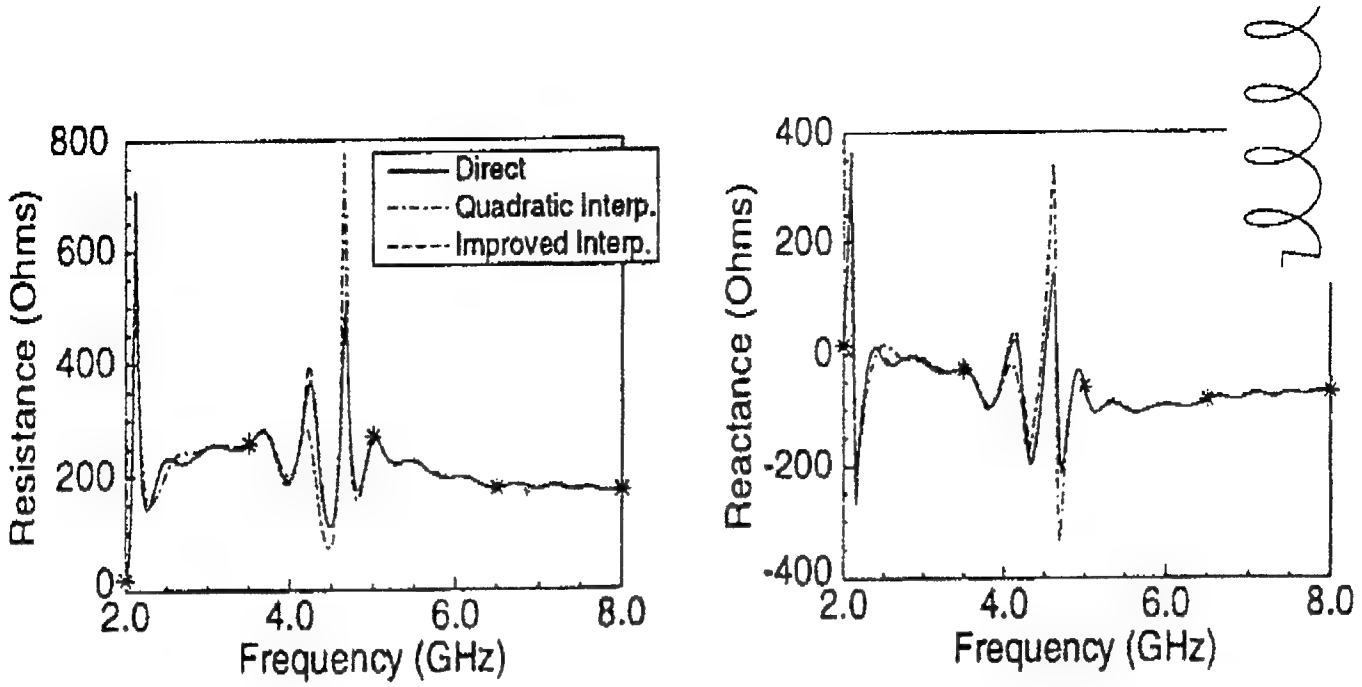


Figure 3. Results from using MBPE and two different FMs of the interaction coefficients of the $\underline{\underline{Z}}$ matrix for a helical antenna. Values obtained from straight-line interpolation of 301 GM samples (solid line) are compared with a quadratic FM (dot-dash line) and a FM defined by Eqs. (6) to (8) (dashed line) [Virga and Rahmat-Samii (1995)]. The GM samples used for the FM results are indicated by the starred points.

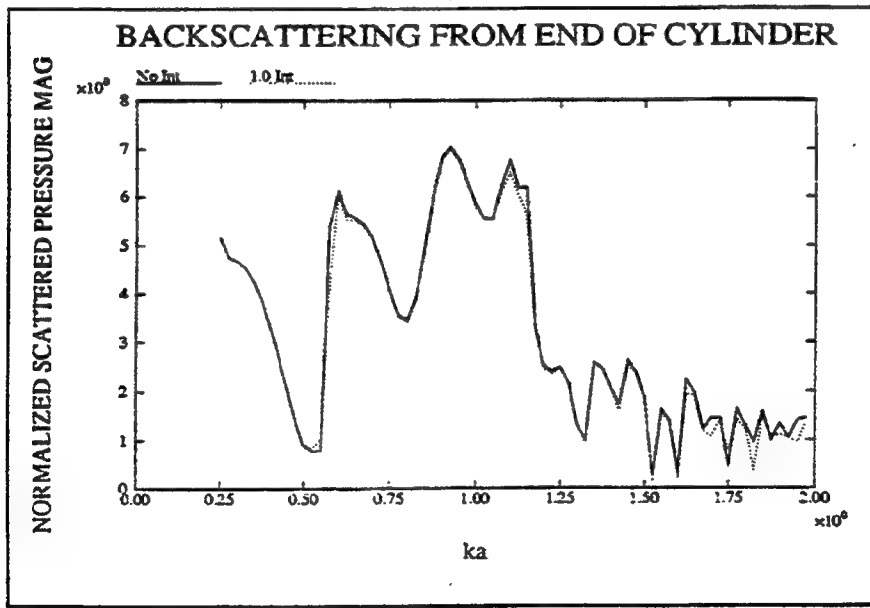


Figure 4. Results for acoustic backscattering from the end of a circular cylinder as a function of frequency obtained from the basic model without interpolation (solid line) and using MBPE on samples spaced 1.0 unit apart in ka (dotted line) [Benthien and Schenck (1991)]. A linear interpolation model is used for, $M_{m,n}(\omega_2 - \omega_1)$ in Eq. (6) to obtain the estimated interaction coefficients. The $\underline{\underline{Z}}$ -matrix FM samples themselves are spaced too far apart to adequately resolve the fine structure of the response. A second series of pole-based FMs might be used to rectify this problem, as additional FM samples developed in the solution domain would require much less computation than using the formulation-domain FMs each of which involve solution of a large matrix.

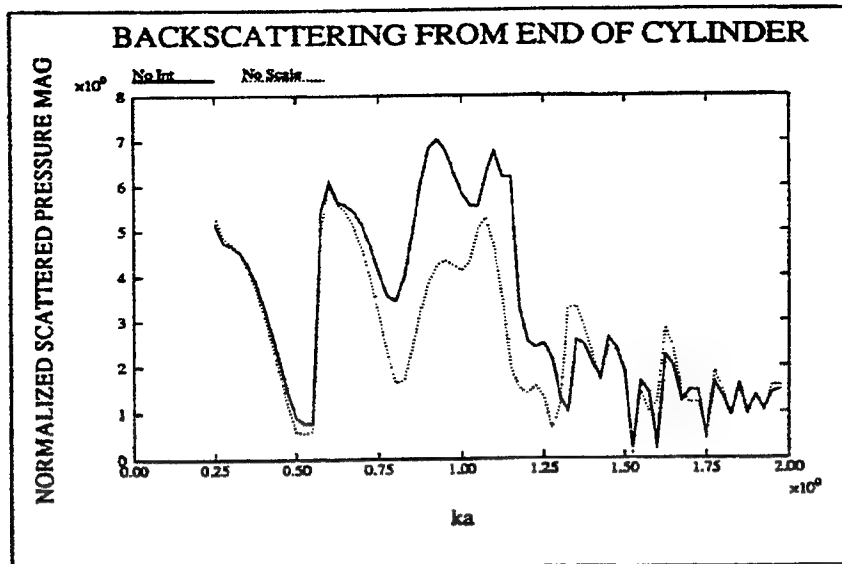


Figure 5. Results for acoustic backscattering from the end of a circular cylinder as a function of frequency obtained from the basic model without interpolation (solid line) and using MBPE on samples spaced 0.4 units apart in ka (dotted line) [Benthien and Schenck (1991)]. The Z-matrix interaction coefficients are estimated between their rigorously computed samples using a linear-interpolation model in Eq. (6), but absorbing the "scaling" factor, $\exp[j(\omega_2 - \omega_1)R_{m,n}/c]$, in $M_{m,n}(\omega_2 - \omega_1)$. Comparison of Figs. 5 and 6 emphasizes the importance of including the dominant functional variations of the quantity being estimated in the MBPE process.

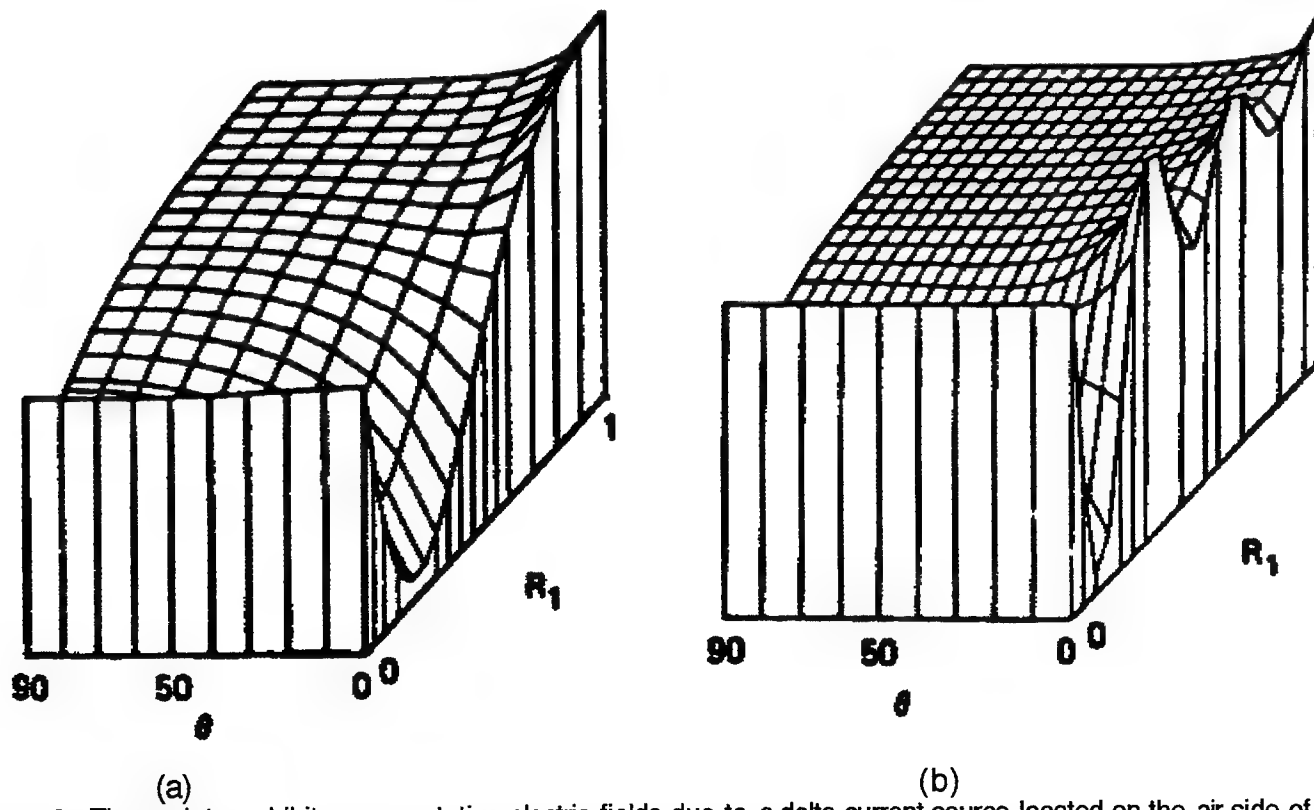


Figure 6. These plots exhibit representative electric fields due to a delta-current source located on the air side of an air-earth interface as a function of radial distance R_1 and elevation angle θ for a lossy, (a), and a lossless, (b), lower medium, respectively. The field is seen to be spatially less variable than the mathematical complexity of the Sommerfeld integral which gives it might imply. An interference between the different-wavelength above-surface and below-surface fields can be observed along the interface (where $\theta = 0$).

Later, in extending NEC-2 to model objects interacting across an interface, a problem where three-dimensional interpolation would have been required since the fields are then functions of lateral separation and the distance from the interface of both the source and observation point, an unattractive prospect, MBPE was then employed. The analytical "models" in this case are extracted from various asymptotic and other approximations that are applicable to the parameter range of interest so that Sommerfeld integrals of the form

$$V_{\pm}^T = 2 \int_0^{\infty} \frac{e^{-\gamma_{-+}|z'|-|\gamma_{\pm}|z}}{k_-^2 \gamma_+ + k_+^2 \gamma_-} J_0(\lambda \rho) \lambda d\lambda, \quad (9)$$

are replaced by expressions like

$$\tilde{T}_p^V \approx \frac{-i\omega\mu_0 K}{4\pi} \left[\frac{k_+^2}{k_+^2 + k_-^2} \left(\frac{1 - \sin\theta}{\cos\theta} \right) - S \cos\theta \right] R^{-1},$$

where

$$\theta = \tan^{-1} \frac{|z - z'|}{\rho}, \quad S = \frac{z'}{R}, \quad \text{and} \quad K = \frac{k_-^2 - k_+^2}{k_-^2 + k_+^2} \quad (10)$$

with the details described by Burke and Miller (1984). Finally, the fields needed for the integral-equation model are then approximated by

$$E(r, z, z') \approx \sum A_n f_n(\rho, z, z'); \quad n = 1, \dots, N \quad (11)$$

where the $f_n(\rho, z, z')$ functions comprise the model and A_n are the model parameters. This MBPE approach for the interface problem provides an essentially rigorous numerical model for objects interacting across an infinite, planar interface at a cost of increasing the matrix fill time by only 5-10 times over what modeling the same object(s) in free space would require. An example of one electric-field component transmitted to a lower medium from an above-surface source is shown in Fig. 7.

An alternate approach for the half-space problem based on a series of complex images developed using Prony's Method is described by Shubair and Chow (1993). For a vertically oriented antenna, a series of three to five image antennas are found to be adequate for the one-sided problem (antenna on one side of the interface). A similar approach for a horizontal antenna is reported by Fang et al. (1988).

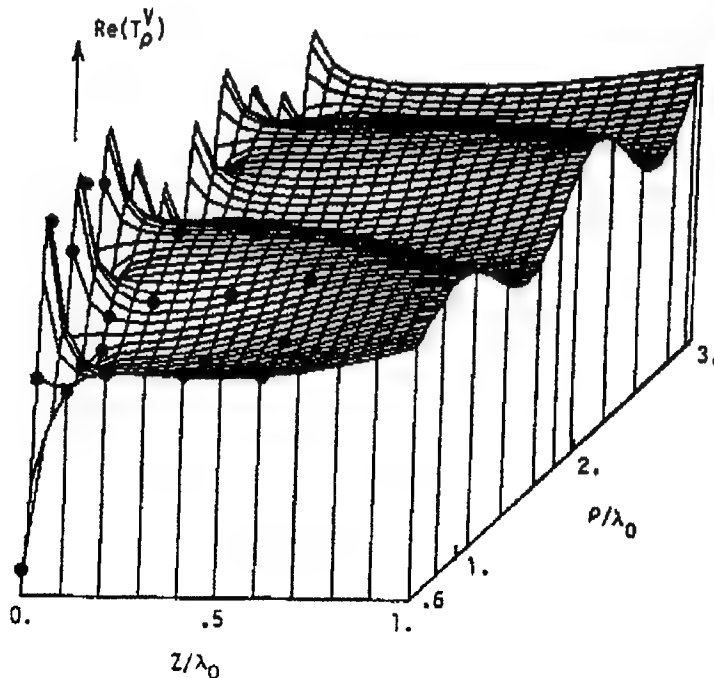


Figure 7. The MBPE FM results for the T_p^V field as a function of radial and vertical location beneath an interface for a source located above it [Burke and Miller (1984)]. Also shown by the dots are the Sommerfeld-integral values used as GMs for the FM approximation. Although not clearly shown because they overlap, the exact and MBPE results are both plotted in this figure.

4.1.4 Modeling Spatial Variations:

Waveguide Fields. Other opportunities for Green's-function applications of MBPE arise from separation-of-variables solutions for exterior problems involving cylinders, spheroids, etc. where infinite series of special functions occur and for interior problems where the Green's function can then involve an infinite series of images. An example of the latter application is reported by Demarest et al. (1989) for a wire antenna located in the region between infinite, parallel, perfectly conducting planes for which some results are shown in Fig. 8. The microscopic source-field description contained in the infinite-series Green's function for this problem is replaced by low-order FMs of the spatial field behavior that provide a much more efficient, yet acceptably accurate, numerical representation of these fields. These FMs substantially increase the efficiency of computing the interaction coefficients in an FDIE model by a factor of about 20 for the example shown. We note that the Green's function for this particular problem has the characteristics of both the WD and SD FMs, since the contribution of each image is pole-like, having a $1/(x - x_n)$ amplitude multiplied by a wave-like phase factor $\exp(-ik(x - x_n))$. The signal fields of this kind of Green's function might be described as having a hybrid character, with the goal of the FM being to replace both with a simpler analytical description.

4.1.5. Modeling Spatial Variations: Moment-Method Impedance Matrices.

The preceding examples deal with modeling the frequency variation of the coefficients of a FDIE system matrix as a means of reducing the number of needed FPM-matrix evaluations when spanning many resonances across some frequency band to reduce the overall operation count. Alternatively, we might examine the feasibility of reducing the number of FDIE-matrix coefficients that need FPM evaluation at a given frequency as way to reduce the OC at a given frequency. This kind of approach is described by Vecchi et al. (1994) and demonstrated by application to a microstrip line with a coupled dipole, an example of which is presented in Fig. 9. According to Vecchi et al., there is no appreciable difference between results obtained using the FM and the exact results.

Spatial variations of impedance and admittance matrices can be better appreciated by presenting them as surface plots, an example of which is included in Fig. 10a for a straight wire where the numbering of the subdomains used for this model is sequential from 1 to N. The axes represent the matrix rows and columns and the normalized height of the surface at row = m, column =

n above the row-column plane represents the magnitude of a given interaction coefficient, $|Z_{m,n}|$. The plotting routine passes a smooth surface through the set of $|Z_{m,n}|$ values, and so may introduce a "fractional" interpolation between the discrete set of row-column indices. It's well-known, of course, that the impedance matrix for a straight wire or a strip is of Toeplitz form and so this particular matrix could be fully displayed by a single row or column. The matrix for the same wire bent to form a polygonal approximation of a circular loop would look very similar on this same linear scale except that there would be large components near the corners opposite the main diagonal, assuming the wire segments are numbered in order as well. Were a spatial FM to be used for these impedance matrices, the phase variation would also be needed, or as an alternative the real and imaginary parts might be used instead. The use of magnitude and phase for modeling Z seems the more appropriate since they are "smoother" [Brown and Prata (1994)].

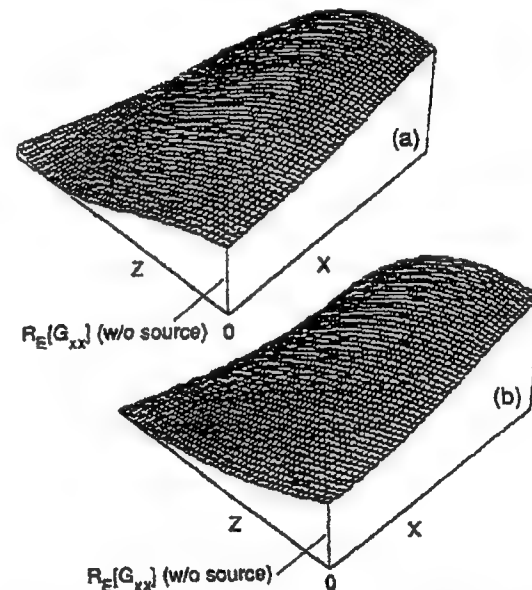


Figure 8. Results for the G_{xx} component of the dyadic Green's function (x -directed source perpendicular to waveguide walls, and x -directed field) as obtained from direct evaluation of the defining equation, (a), and as evaluated using a FM consisting of two multiplied 3rd-order polynomials in x and z , (b) [Demarest et al. (1989)]. The current on a dipole antenna located midway between the waveguide walls obtained from using (b) are within 5% of those resulting from (a).

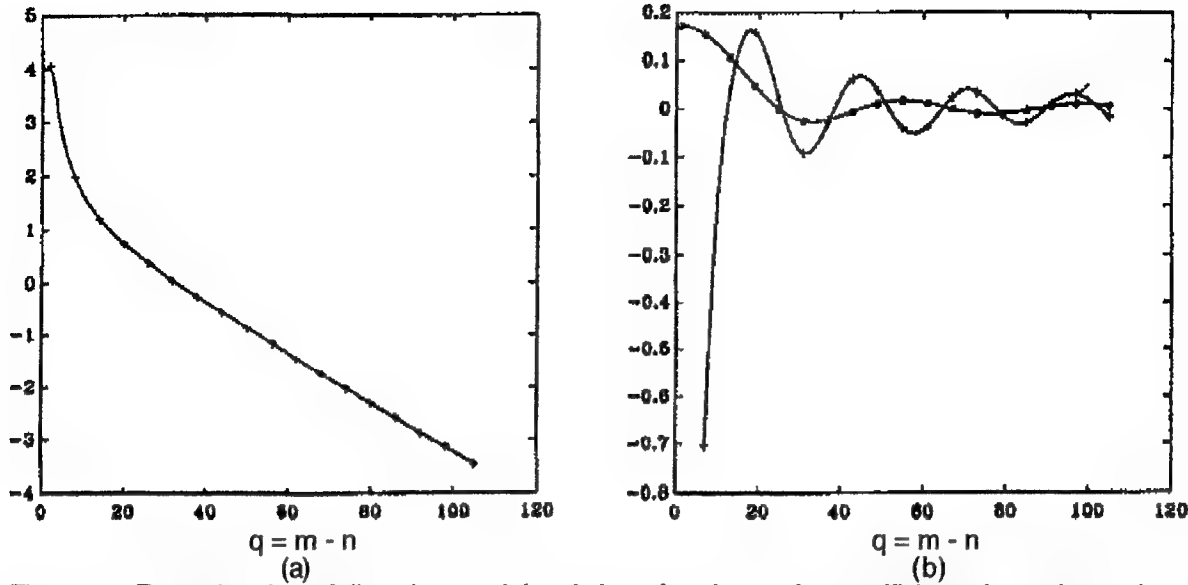


Figure 9. Example of modeling the spatial variation of an interaction coefficients for an integral-equation system matrix of a microstrip line with a coupled dipole using a Galerkin subdomain [Vecchi et al. (1994)]. Result in (a) is \log_{10} of the static, singular part of the self-impedance matrix for the line as a function of the difference between the source and observation subdomain indices. The '+'s show the points where the interactions are sampled for the FM, the solid line is the exact result and the dashed line is the FM result. The FM in this case is a polynomial applied to $Z_S[\log(q)]$. The results in (b) are obtained for the frequency-dependent part of the interaction coefficient, where the solid line is the exact result, the dashed line is FM approximation, again using a polynomial, and the o's and +'s indicate the real and imaginary samples used for evaluating the FMs.

An example for a more interesting structure, an 8-turn helical spiral having a total wire length of 16 wavelengths, is shown in Fig. 10b, also using a linear magnitude scale. A “splitting” of the coefficients along the main diagonal may be observed, due to the changing orientation of the neighboring wire segments as they spiral around the helix. This effect can be seen to continue as a ripple in the coefficients further away from the main diagonal.

More information is conveyed by plotting the log of the matrix coefficients, for which two examples are included in Fig. 11. The first, in (a), is for a wire two-free-space wavelengths in length, located parallel to, and 10^{-4} free-space wavelengths beneath, the interface between an upper free space and a lower half space having a relative dielectric constant of 10. There the interference between the waves propagating above and below the interface is seen in a somewhat different way than demonstrated in Fig. 6 for the Sommerfeld field alone. Aside from the fact that this matrix is also of Toeplitz form, and therefore more simply filled and solved than an arbitrary matrix, the regular variation of the coefficients in a given row or column indicates the feasibility of using a suitable spatial FM for reducing matrix-fill complexity.

When the same two-wavelength wire is rotated 90

degrees to penetrate the earth-air interface normally at its midpoint, the impedance matrix shown in Fig. 11b is obtained. The matrix is now block-Toeplitz but is otherwise nearly as simple spatially as is the case for the same object located in free space.

A much more complicated structure because it has a surface, rather than a linear, geometry is a wire mesh for which an impedance matrix is presented in Fig. 12. This plot dramatizes the problem encountered when attempting to visually display source-field relationships over a two-dimensional surface (or a three-dimensional volume) in terms of a two-dimensional matrix of interaction coefficients. The interactions are dependent on the four spatial coordinates that define observation- and source-patch locations Δ_m and Δ_n , respectively, as well on other details of the numerical model, and when projected onto the two-dimensional surface of the impedance matrix their associated spatial relationships are disordered. The field “signal” is no longer simply discerned by observing the behavior of a row or column from \underline{Z} but instead requires following a path through the matrix determined by the numbers assigned to the individual unknowns. This does not mean that the spatial variation of the fields can no longer be modeled, but that matrix indices can no longer serve as the FM variables.

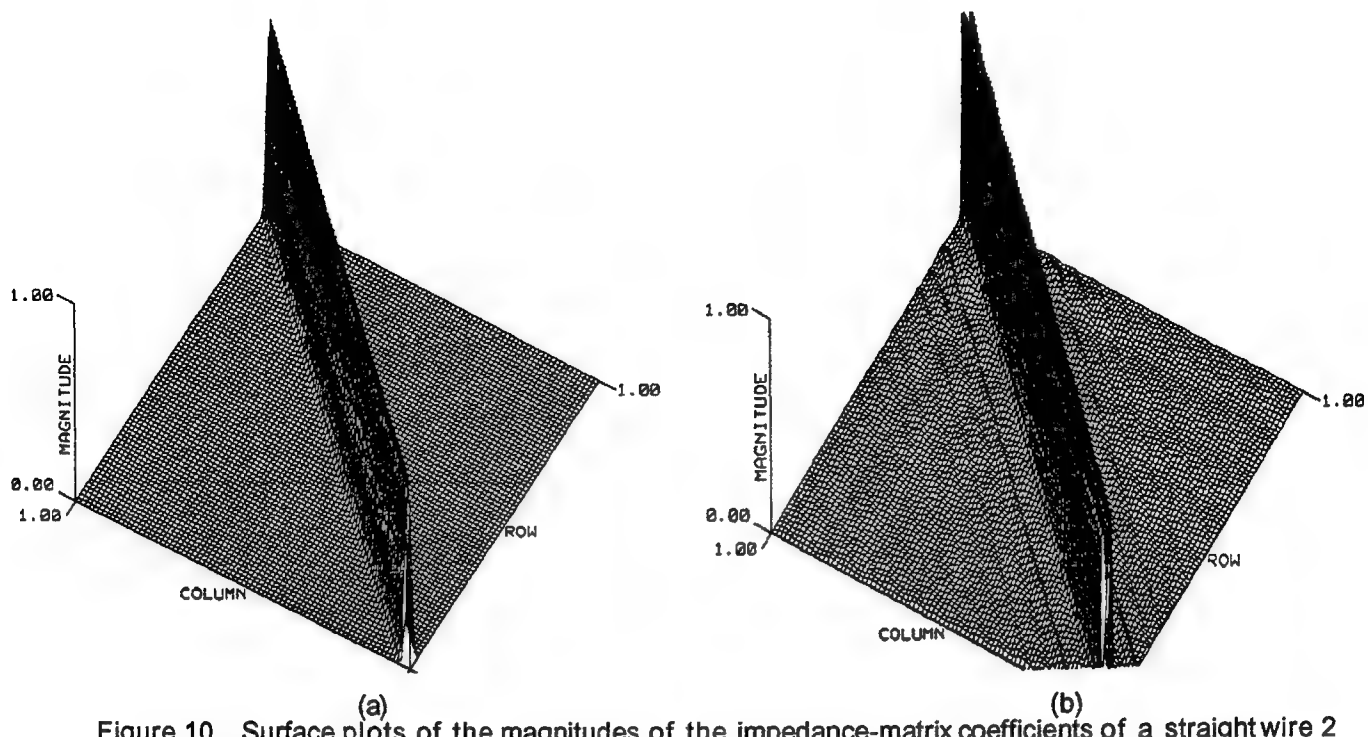


Figure 10. Surface plots of the magnitudes of the impedance-matrix coefficients of a straight wire 2 wavelengths long, (a), and an 8-turn helical spiral 16 wavelengths long, (b).

4.2 Using Spectral MBPE in the Formulation Domain

A spectral FM would not be expected to be applicable to an integral equation based on a space-based Green's function, but could be appropriate for a transformed or modal Green's function where the variable is spatial wavenumber rather than distance. That possibility is not considered further in this discussion.

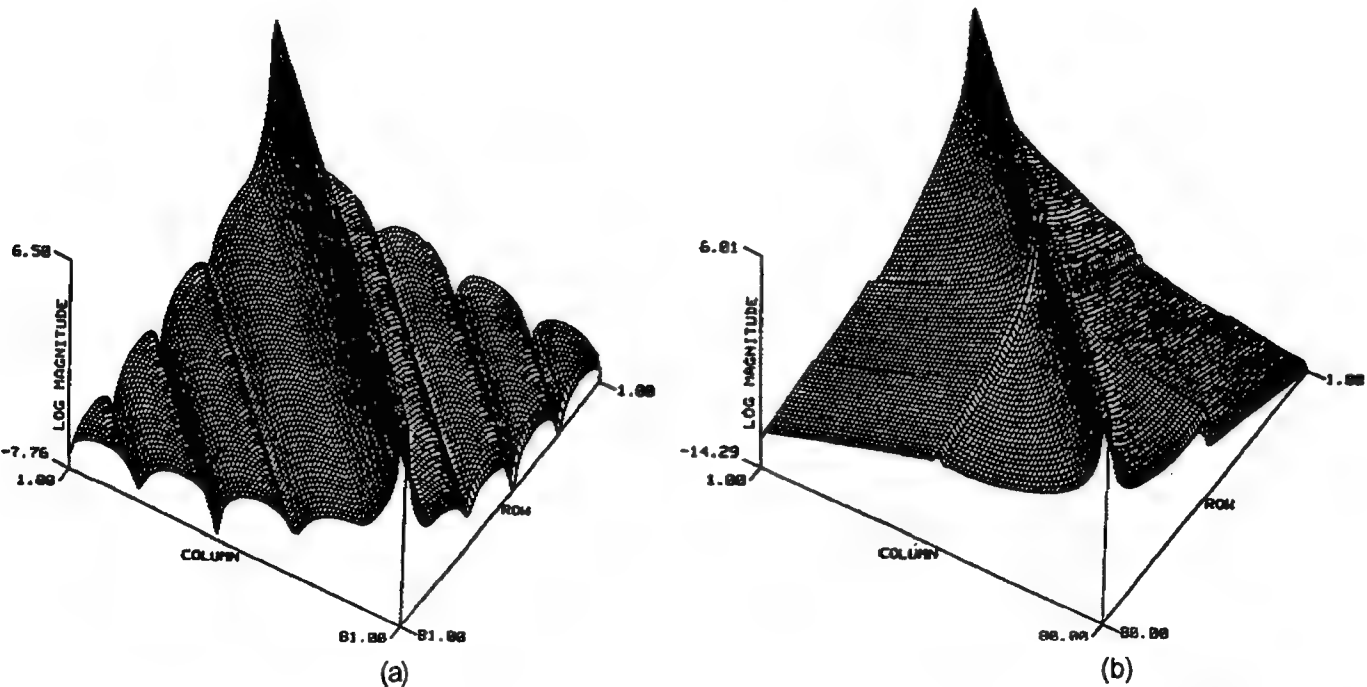


Figure 11. Surface plots of the magnitudes of the impedance-matrix coefficients of a straight wire 2 wavelengths long in free space when parallel to, and 10^{-4} wavelengths beneath, an air-ground ($\epsilon_r = 10$) interface, (a), and the same wire oriented normally to the interface with half its length in each half space, (b).

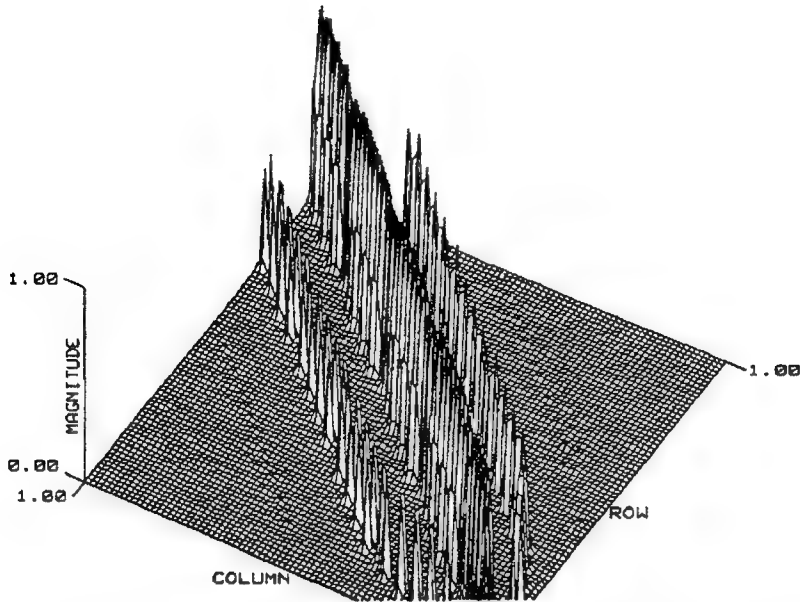


Figure 12. Surface plots of the magnitudes of the impedance-matrix coefficients of a 5-wire \times 5-wire mesh of wires whose total length is two wavelengths. The irregular appearance of this matrix results from the fact although the unknowns can be numbered in a sequential fashion, their separation is no longer linearly dependent on their respective indices.

5.0 SOLUTION-DOMAIN MBPE

5.1 Using Waveform MBPE in the Solution Domain

At least two kinds of CEM quantities in the solution domain possess wavelike nature, the source solutions themselves and the far-field angular dependence.

5.1.1 Modeling Spatial Variations.

While the spatial forms of the formulation-domain problem description provided by the impedance matrices are relatively uncomplicated, due to the basic simplicity of the Green's function source-field description, their solution-domain counterparts in the form of admittances matrices are not since the coefficients of the latter must encompass all possible source distributions that can occur on a given structure. Thus, whereas the impedance-matrix coefficients decline essentially monotonically with increasing distance, the admittance-matrix coefficients will in general not do this because, unless loss is a predominant effect, traveling-wave currents must be included among the distributions that can arise, becoming standing waves when impedance or other discontinuities occur on the structure being modeled. Never-the-less, the "signal" represented by the spatial variation of the induced sources, which is generally the current for conducting objects, is basically comprised of exponential waves and is therefore a potential candidate for MBPE using a WD FM. The potential significance of this possibility is that were a model for the spatial current response to be available, the number of parameters needed to quantify this current could be

substantially less than the X_s coefficients otherwise used when developing an iterative solution, or the X_s^2 when the system matrix is factored. By combining iteration with MBPE of the spatial current, it may be feasible to obtain an acceptably accurate solution via iteration that requires $\sim KX_s$ operations per iteration

step rather than the X_s^2 normally involved, where K is the number of spatial current samples actually computed from the impedance matrix, an OC comparable to some of the "fast" methods mentioned above.

In order to explore the possibility of modeling the spatial variation of the admittance-matrix coefficients, a number of admittance-matrix, or $|Y_{i,j}|$, plots for some simple wire objects are plotted below.¹ The admittance

¹ Note that since the current on a structure represented by \underline{Y} is given by $\underline{I} = \underline{Y} \cdot \underline{V}$, the current that results from exciting it as an antenna at a single point, or segment $i = e$, is $I_e = Y_{i,e} V_e$. Consequently, the current for this excitation is proportional to column "e" of the admittance matrix, and so as the excitation is scanned from $e = 1$ to $e = X_s$, the current that results can be discerned from observing the spatial behavior of column 1 to X_s of $|Y_{i,j}|$. We can thus refer to the plots of the admittance matrix as simply displaying its coefficients, or alternatively, a current distribution on the structure for which the matrix has been derived.

matrices for a two-wavelength straight wire and two-wavelength circular loop are shown in Fig. 13. It's clear in Fig. 13b for the loop that the spatial current is invariant in shape with respect to where the loop is excited, but simply rotates around the loop as the excitation point changes. It's not as clear, but suggestive from Fig. 13a for the straight wire, that the shape of its current distribution is also largely insensitive to where the wire is excited, but that the magnitude of that current varies periodically with a changing excitation point. For these simple objects, it appears that not only might the current

spatial dependence be described by a low-order, WD FM, but that, for the case of the straight wire, the dependence on excitation point can also be modeled.

Admittance-matrix plots for an 8-turn helix of total wire length 4 and 16 wavelengths, respectively, are shown in Fig. 14. The dramatic difference between the two results is due to the fact that in the former case, the helix is below cutoff because the circumference of the helical turns is less than a wavelength whereas the latter, being above the cutoff frequency, results in an attenuated traveling wave. Again, an exponential-series FM for the current appears to be a good approximation for either case.

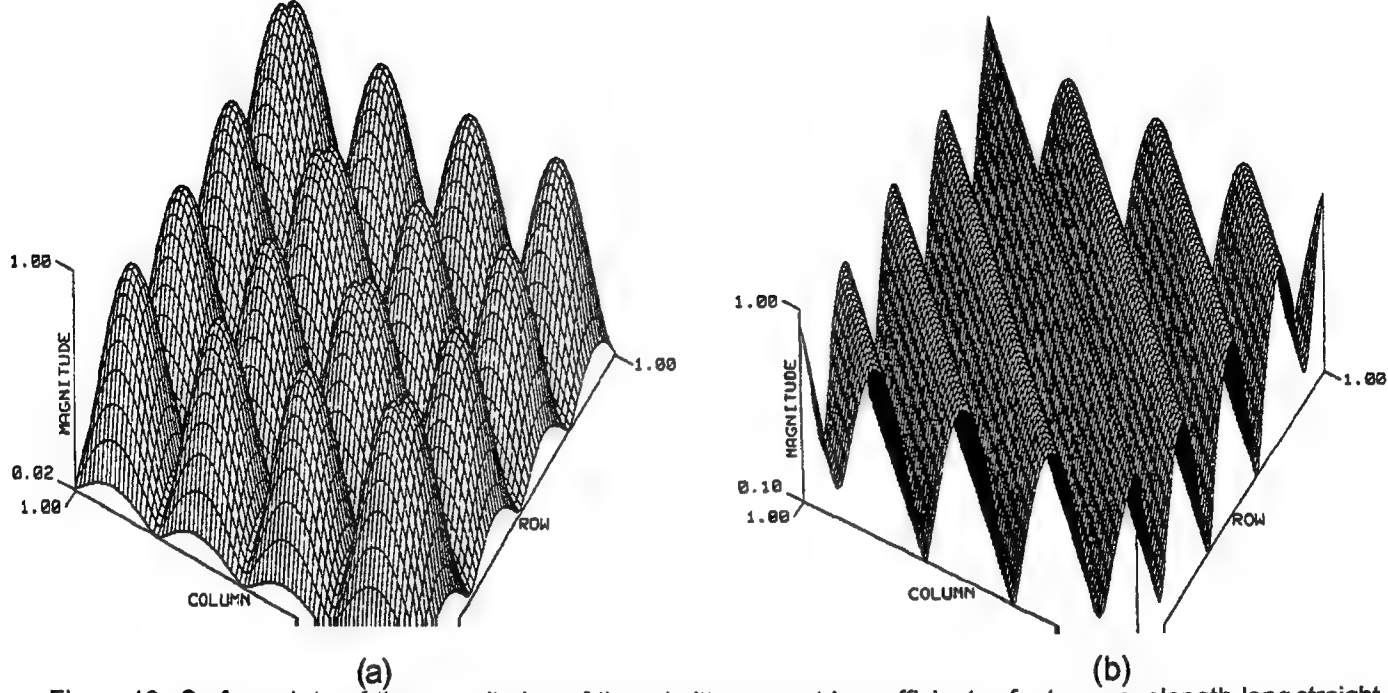


Figure 13. Surface plots of the magnitudes of the admittance-matrix coefficients of a two-wavelength-long straight wire, (a), and a circular loop, (b). Although the impedance-matrix magnitudes exhibit no explicit wavelength dependence (refer to the impedance matrix for the straight wire in Fig. 9a), the effects of standing waves are clearly evident in the admittance matrices. Also, whereas the field "signal" in the formulation domain, as represented by the impedance-matrix coefficients, falls off with distance, the corresponding current "signal" in the solution domain, does not necessarily do so, instead exhibiting the propagating-wave nature expected on such structures.

The plots in Fig. 15 show the magnitudes of the admittance matrix coefficients for a wire two-free-space-wavelengths long that is parallel to, and 10^{-4} wavelengths above and 10^{-4} wavelengths beneath, the interface between free space and a dielectric half space of $\epsilon_r = 10$. The transition between a spatial current distribution having a dominant wavelength characteristic of free space and that of the dielectric is seen to occur over a very small vertical movement of the wire.

The results of Fig. 16 are for the same horizontal wire as Fig. 15a but with a half-space relative permittivity of $\epsilon_r = 10 - j10$, (a), and for the two-wavelength wire

oriented perpendicular to the interface with its midpoint at the interface, (b). The effect of the half-space loss on the horizontal-wire current distribution of part (a) is seen to cause an increased attenuation, which, in terms of a exponential-series FM indicates that the effective wavenumber has developed a larger real part. In Fig. 16b, the vertical wire can be seen to carry two distinctly different current waves on each half having a wavelength appropriate to the medium in which that wire half is located. For the cases of Figs. 15 and 16, an exponential-series FM for the current would again seem to be a good approximation.

The final result of this sequence, Fig. 17, is the admittance matrix of the wire mesh whose impedance

matrix is shown in Fig. 12. Not unexpectedly, there is no discernible pattern in this plot for the reasons previously stated. Both the graphical presentation of such matrices for two-dimensional surfaces and the

associated FMs needed for their spatial modeling would need to take into account their higher-order dimensionality, as compared with the one-dimensional nature of wires.

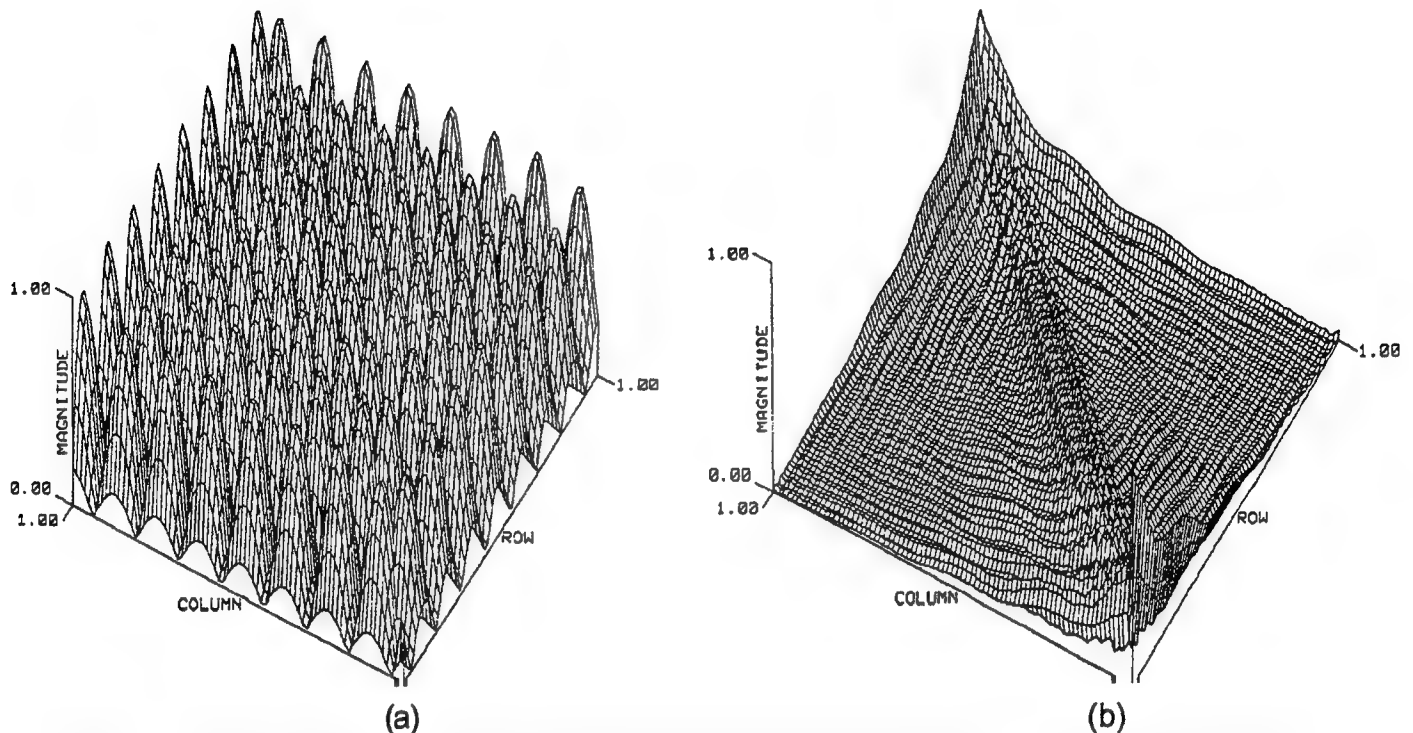


Figure 14. Surface plots of the magnitudes of the admittance-matrix coefficients for an 8-turn helix of total wire length 4 wavelengths, (a), and 16 wavelengths, (b). In (a), the structure is below cutoff since the helix circumference, C , is less than λ , whereas for (b), $C \sim 2\lambda$, so that the dominant current behavior changes from a standing wave to a damped traveling wave.

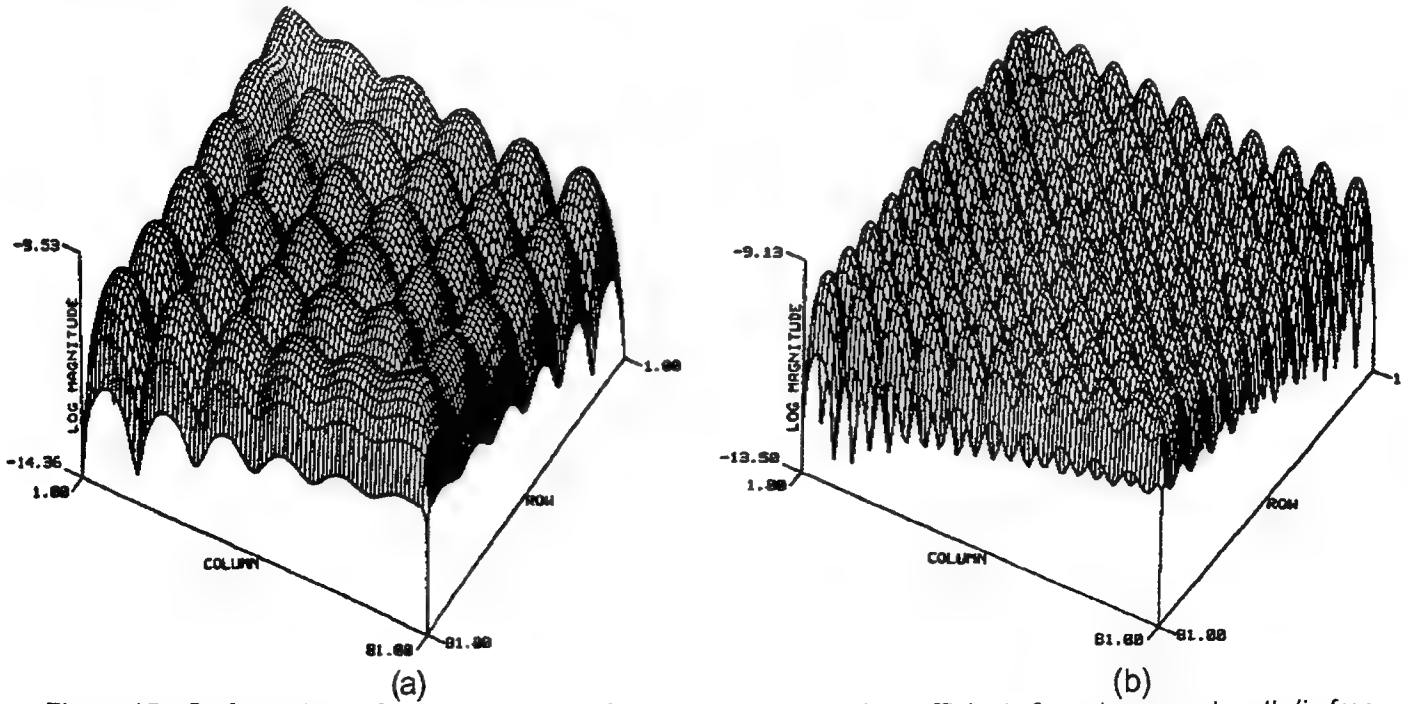


Figure 15. Surface plots of the magnitudes of the admittance-matrix coefficients for a two-wavelength (in free-space) wire parallel to a dielectric half-space of $\epsilon_r = 10$ when 10^{-4} wavelengths above the interface, (a), and 10^{-4} beneath the interface, (b). The damped, standing-wave nature of the current is again evident, with a change from the free-space value to the half-space value taking place over a vertical distance of $\sim 10^{-4}$ wavelengths, or less.

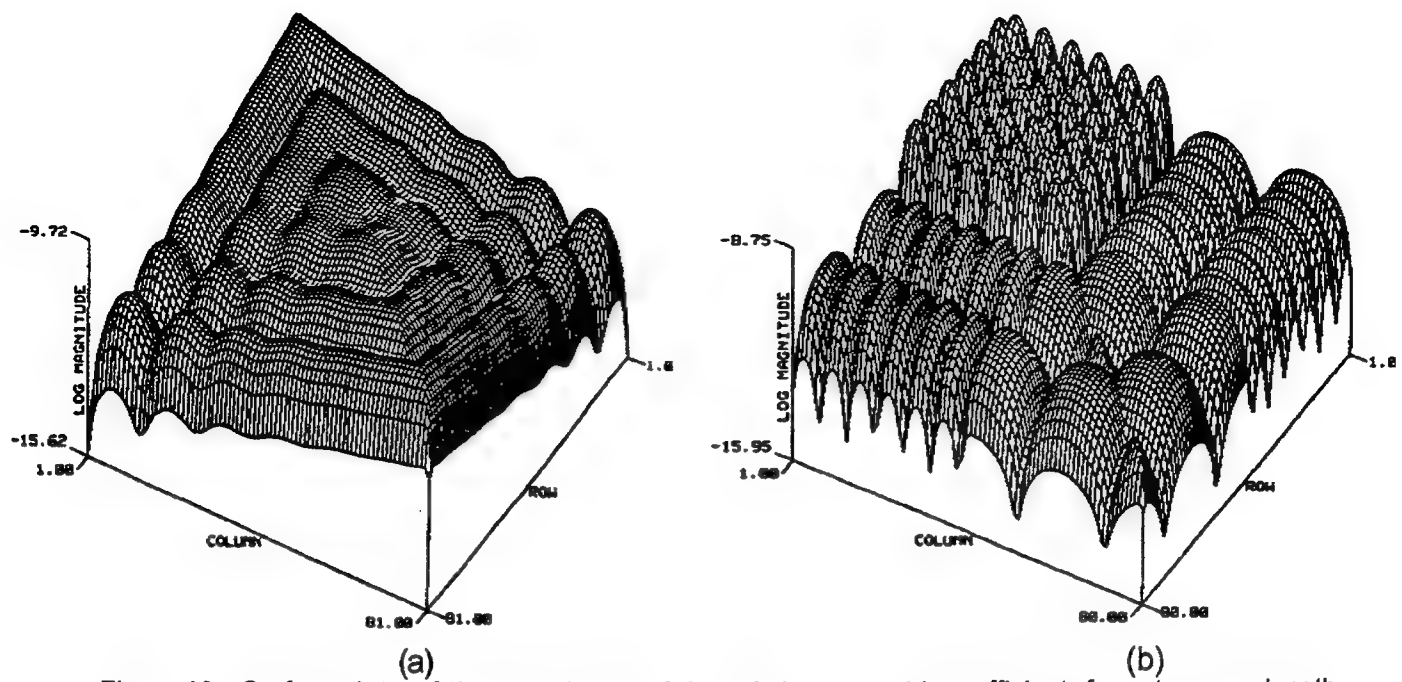


Figure 16. Surface plots of the magnitudes of the admittance-matrix coefficients for a two-wavelength wire in free space when parallel to and 10^{-4} free-space wavelengths above a half space with $\epsilon_r = 10 - j10$, (a), and for the same wire when perpendicular to a dielectric half space of $\epsilon_r = 10$ with its center at the interface, (b). The influence of the lossy lower half space is evident in the increased current attenuation exhibited in (a) as compared with 15a. The change in dominant current wavelength in the vertical wire is clearly demonstrated in (b) on each half of the wire. Again, an appropriate Fitting Model for such currents is an exponential series, or waveform-domain, form.

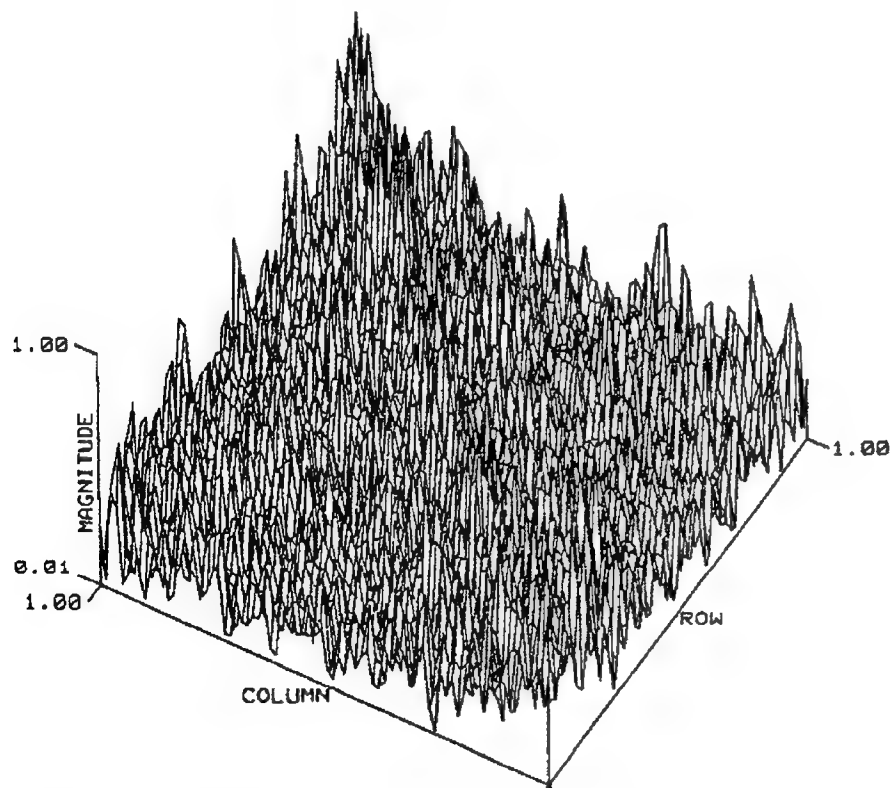


Figure 17. Surface plot of the magnitudes of the admittance-matrix coefficients for a 5-wire \times 5-wire mesh of wires whose total length is two wavelengths. The irregular appearance of this matrix results from the fact although the unknowns can be numbered in a sequential fashion, their separation is no longer linearly dependent on the respective indices used to construct the system and solution matrices.

5.1.2 Modeling Angle Variations of the Far Field.

The far-field approximation universally used to obtain the distant field of a known source distribution depends only on the angular coordinates of the far-field observation point relative to the coordinate-system origin and the source location projected onto the line-of-sight from that origin. For a simple linear array of discrete sources, the far electric field \mathbf{E} can be expressed in the general form

$$\mathbf{E}(\theta) \approx \sum S_n \exp[ikd_n \cos(\theta)]; n = 1, \dots, N \quad (12)$$

where S_n and d_n are, respectively, the amplitude and location along the array of source n of which there are a total of N . The radiation pattern is normally developed by sampling the far fields finely enough in angle such that a straight-line interpolation between the field samples can be employed to develop an approximation continuous in observation angle. Clearly, Eq. (12) has the form of an exponential series and is a candidate for a WD FM. Two- and three-dimensional source distributions have a more complicated far-field expression, but otherwise retain the basic structure of Eq. (12), being functions of two observation angles, elevation and azimuth in a spherical coordinate system.

For extended source distributions, where N exceeds 50 or so, it is not computationally practical to employ a single FM for the entire pattern since ill-conditioned data matrices are encountered. Furthermore, a pattern that is a function of two angles can not be directly modeled using the basic Prony model described in RI. Instead, observation windows of limited angular extent can be used so that low-order FMs can accurately approximate the pattern over that window. The pattern can then be developed by employing enough FMs so that a continuous range of observation angles is encompassed over the angle variations that are desired. This approach has been described by Roberts and McNamara (1994) and is summarized in RI.

5.2 Using Spectral MBPE in the Solution Domain

In RI, the use of FMs to represent the frequency dependence of EM observables was discussed and demonstrated using various examples. Here we consider the more fundamental problem of modeling the frequency dependence of the admittance matrix itself using both function sampling and derivative sampling.

5.2.1 Modeling the Admittance Matrix.

As previously discussed, the impedance or system matrix arising from an FDIE model contains all the interaction information needed to describe the EM

properties of an object being modeled. In a numerical model, this information is represented by the fields produced at observation patches in response to unit-amplitude source patches, both sets of which span the entire object. The relative amplitudes and phase-changes associated with the X_s^2 source-field patch pairs convey object size implicitly in these interactions. The inverse of these relationships in the form of the admittance matrix is needed to establish the absolute source amplitudes that satisfy the required boundary conditions. The solution, or admittance, matrix explicitly includes aspects of object size and shape the effects of which are exhibited as periodic body resonances as a function of frequency. Thus, the model appropriate for MBPE representation of the admittance matrix must be capable of handling frequency-dependent resonances.

Since the observables that the solution matrix provides are well-approximated by pole series, or more generally rational functions, as demonstrated in RI, it follows that the solution matrix itself might also be modeled using rational functions. This conclusion follows by noting that for a single-port antenna its input admittance is defined as the ratio of the feedpoint current to the exciting voltage. For a wire antenna excited at segment j then, having already shown that the admittance can be modeled by a rational function, the $Y_{j,j}$ coefficient of the solution matrix must also have this model. Similarly, the currents on the other wire segments for that excitation, given by $Y_{i,j}$ where $i = 1, \dots, i-1, i+1, \dots, X_s$ if there are a total X_s segments, can also be modeled using a rational function. These observations extend to exciting other segments of the wire one at a time, indicating that each coefficient in the solution matrix can be represented by a rational-function FM. Furthermore, since each of these coefficients shares the same resonance structure and thus the same denominator polynomial, the solution matrix can be modeled by a denominator polynomial multiplying a matrix of numerator polynomials, as exhibited by

$$Y(s) = \frac{1}{D(s)} \begin{bmatrix} X & \cdots & X & n_{1a}(s) & \cdots & n_{1b}(s) & \cdots \\ X & \cdots & X & n_{2a}(s) & \cdots & n_{2b}(s) & \cdots \\ X & \cdots & X & n_{3a}(s) & \cdots & n_{3b}(s) & \cdots \\ \vdots & \vdots & \vdots & \vdots & \vdots & \vdots & \vdots \\ X & \cdots & X & n_{X_s a}(s) & \cdots & n_{X_s b}(s) & \cdots \end{bmatrix} \quad (13)$$

where $n_{i,j}(s)$ is the numerator polynomial for coefficient i,j , $D(s)$ is the common denominator and a and b are the indices of those excitation ports whose current response have been modeled. This form permits direct representation of the wire current for an arbitrary right-hand-side excitation so long as its frequency lies within the valid bandwidth of the solution matrix or of the rational function FMs that comprise its coefficients.

5.2.2 Sampling Admittance-Matrices

Derivatives. The FM approaches discussed here for estimating frequency responses require sampled values of the impedance or admittance matrices from which the MBPE parameters can be computed and from which the FM is thus quantified. The sampling can be done either as a function of frequency; as a function of derivative, with respect to frequency at a given frequency; or a combination thereof Miller and Burke (1991). Also, since an EM frequency response has complex-conjugate behavior around zero frequency, this knowledge can be employed to provide virtual samples that further improve the MBPE performance, i.e., negative-frequency samples can be employed at essentially no further FPM cost.

For practical reasons of numerical conditioning and accuracy, however, it is advisable not to cover too-wide a frequency interval with a single model. The approach that now seems most attractive is to employ a series of frequency windows that slide over the frequency interval to be modeled. These windows can be of lower order to avoid the conditioning problems that can otherwise. Using sliding, and overlapping, windows also can yield some estimate of the numerical accuracy of the modeled transfer function by comparing the results of two, or more, windows in their region of overlap where they share common samples, some examples for which are included in RI. Here, we outline specifically the additional computational benefits that arise from derivative sampling.

On writing the moment-method equations that arise from an integral-equation formulation in matrix form,

the impedance equation

$$\sum_{i=1}^{X_s} Z_{i,j}(\omega) I_j(\omega) = V_i(\omega) \quad (14)$$

is obtained where these various quantities are evaluated at the frequency ω . A solution for the current can then be formally written as an admittance equation

$$I_i(\omega) = \sum_{j=1}^{X_s} Y_{i,j}(\omega) V_j(\omega) \quad (15)$$

where $Y_{i,j}$ is the inverse of $Z_{i,j}$. We should note however that the approach developed here for the frequency derivatives could be implemented using LU factorization, iteration, or any other solution method.

Upon differentiating the impedance equation with respect to frequency there is obtained

$$\sum_{j=1}^{X_s} [Z_{i,j}(\omega) I'_j(\omega) + Z'_{i,j}(\omega) I_j(\omega)] = V'_i(\omega) \quad (16)$$

where the prime denotes a frequency derivative. A solution of the differentiated impedance equation for the differentiated current can then be written

$$I'_i(\omega) = \sum_{j=1}^{X_s} Y_{i,j}(\omega) \left(V'_j(\omega) - \sum_{k=1}^{X_s} Z'_{j,k}(\omega) I_k(\omega) \right) \quad (17)$$

where we observe that while the differentiated impedance matrix appears as part of a modified right-hand-side of the differentiated admittance equation, I' is given in terms of an undifferentiated admittance matrix. Computing the differentiated current thus requires an additional number of computations beyond those needed for solution of the undifferentiated current proportional to X_s^2 rather than the X_s^3 that would apply to obtain another frequency sample (assuming that LU decomposition is used rather than iteration).

Continuing this process, the n 'th frequency derivative of the current is given by

$$I_i^{(n)}(\omega) = \sum_{j=1}^{X_s} Y_{ij}(\omega) \left[V_j^{(n)}(\omega) - \sum_{m=1}^n C_{nm} \left(\sum_{k=1}^{X_s} Z_{jk}^{(m)}(\omega) I_k^{(n-m)}(\omega) \right) \right] \quad (18)$$

where again $C_{n,k}$ is the binomial coefficient and the superscript in parenthesis indicates differentiation with respect to frequency of the order indicated.

It is especially important to observe that information about the n 'th frequency derivative of the current continues to require an operation count proportional to X_s^2 . Expressed in another way, each additional frequency derivative of the solution vector for the current can be computed in a number of operations proportional to $A(n, N_{rhs})/X_s$ where A is a function which depends on the order of the derivative and the number of right-hand-sides for which the solution is sought. If the frequency derivatives provide information comparable to that available from the frequency samples themselves, it can be appreciated that there could be a substantial computational advantage to using the solution derivatives in estimating the transfer functions. The problem of implementing the above approach in the NEC code is discussed by Miller and Burke (1991).

6.0 CONCLUDING COMMENTS

The applicability of low-order fitting models (FMs) in computational electromagnetics both to reduce the sampling density of computed observables and to decrease the computational cost of obtaining these observables has been the focus of this and a companion article [RII, Miller (1995)]. Both of these possibilities rest on the fact that much EM modeling is redundant, in that source and field variations as a function of time, frequency, angle and space can be accurately described by physically derived FMs that permit equivalent information to be determined from fewer computations.

A conclusion to be reached from this observation is that first-principles models (FPMs) need not be employed in the manner they most often now are to obtain desired information. Rather, supplementary information is available from our knowledge of EM mathematics and physics, allowing us to employ reduced-order models to represent observables obtained from a FPM or to reduce the complexity of the FPMs themselves. This substitution offers the possibilities of greatly decreasing the number of evaluations required of FPMs and the cost of their evaluation, with a consequent reduction in the overall computer cost required to obtain the information desired.

In the context of using an FDIE solved using the moment method, modeling the frequency variation of the impedance matrix saves an operation count (OC) proportional to X_s^2 for each frequency sample that can be eliminated. Similarly, modeling the frequency variation of the admittance matrix produces an OC savings proportional to X_s^3 for each sample eliminated. Modeling the spatial variation of the impedance matrix can reduce the OC of a solution towards $X_s \log(X_s)$, which forms the basis for the newer, "fast" techniques. Modeling the spatial variation of the admittance matrix might offer similar kinds of savings, but has not yet been tested. For problems solved using a FPM and requiring hours of computer time for each new frequency sample, the savings in computer resources resulting from matrix modeling can be substantial. The models discussed, especially for the admittance matrix, not only provide a more useful representation of the physical behavior continuous in the independent variable, but are valuable for other purposes such as obtaining transient responses.

7.0 ACKNOWLEDGEMENT

The author gratefully acknowledges the contributions of G. J. Burke and J. K. Breakall in providing the matrix plots used in this article.

8.0 REFERENCES

Benthien, G. W. and H. A. Schenck (1991), "Structural-Acoustic Coupling," in *Boundary Element Methods in Acoustics*, ed. R. D. Ciskowski and C. A. Brebbia, Computational Mechanics Publications.

Brown, K. W. and A. Prata (1994), "Efficient Analysis of Large Cylindrical Reflector Antennas Using a Nonlinear Solution of the Electric Field Integral Equation," IEEE Antennas and Propagation Society International Symposium, Seattle, WA, pp. 42-45.

- Burke, G. J. and E. K. Miller (1984), "Modeling Antennas Near to and Penetrating a Lossy Interface", *IEEE Transactions on Antennas and Propagation*, AP-32, pp. 1040-1049.
- Burke, G. J. and E. K. Miller (1988), "Use of Frequency-Derivative Information to Reconstruct an Electromagnetic Transfer Function," *Proceedings of the Fourth Annual ACES Review*, Naval Postgraduate School, Monterey, CA, March.
- Burke, G. J., E. K. Miller, S. Chakrabarti, and K. Demarest (1989), Using Model-Based Parameter Estimation to Increase the Efficiency of Computing Electromagnetic Transfer Functions," *IEEE Trans. Magnetics*, Vol. 25, No. 4, pp. 2807-2809, July.
- Canning, F. X. (1990), "Transformations That Produce a Sparse Moment Matrix", *J. Electromagnetic Waves and Applications*, 4, pp. 983-993.
- Chew, W. C. (1993), "Fast Algorithms for Wave Scattering Developed at the University of Illinois' Electromagnetics Laboratory," *IEEE Antennas and Propagation Magazine*, 35, no. 4, pp. 22-32.
- Coifman, R., V. Rokhlin and S. Wandzura (1993), "The Fast Multipole Method for the Wave Equation: A Pedestrian Prescription," *IEEE Antennas and Propagation Magazine*, 34, no. 3, pp. 7-12.
- de Beer, J. T. and D. C. Baker (1995), "An Examination of the Effect of Mechanical Deformation on the Input Impedance of HF LPDA's Using MBPE", *Applied Computational Electromagnetics Society Journal*, this issue.
- Demarest, K. R., E. K. Miller, K. Kalbasi, and L-K Wu (1989), "A Computationally Efficient Method of Evaluating Green's Functions for 1-, 2-, and 3D Enclosures", *IEEE Transactions on Magnetics*, 25(4), pp. 2878-2880.
- Fang, D. G., J. J. Yang, and G. L. Delisle, (1988), "Discrete Image Theory for Horizontal Electric Dipoles in a Multilayered Medium," *IEE Proceedings*, 135, pp. 297-303.
- Miller, E. K. (1995), "Model-Based Parameter Estimation in Electromagnetics: I--Background and Theoretical Development," *Applied Computational Electromagnetics Society Newsletter*, submitted for publication.
- Miller, E. K. (1996), "Model-Based Parameter Estimation in Electromagnetics: II--Applications to EM Observables," *Applied Computational Electromagnetics Society Newsletter*, submitted for publication.
- Miller, E. K., J. N. Brittingham, and J. T. Okada (1977), "Bivariate- Interpolation Approach for Efficiently and Accurately Modeling Antennas Near a Half Space", *Electronics Letters*, 13, pp. 690-691.
- Miller, E. K., F. J. Deadrick, G. J. Burke and J. A. Landt (1981), "Computer-Graphics Applications in Electromagnetic Computer Modeling, *Electromagnetics*, 1, pp. 135-153.
- Miller, E. K. and G. J. Burke (1991), "Using Model-Based Parameter Estimation to Increase the Physical Interpretability and Numerical Efficiency of Computational Electromagnetics," *Computer Physics Communications*, 68, pp. 43-75.
- Newman, E. H. (1988), "Generation of Wide band Data From the Method of Moments by Interpolating the Impedance Matrix," *IEEE Trans. Antennas Propagat.*, Vol. 36, No. 12, pp. 1820-1824.
- Oppenheim, A. W. and R. W. Schafer (1975), *Digital Signal Processing*, Prentice-Hall, Inc., Englewood Cliffs, NJ.
- Ralston, A. (1965), *A First Course in Numerical Analysis*, McGraw-Hill Book Co.
- Roberts, A. R. and D. A. McNamara (1994), "Interpolating Radiation Patterns Using Prony's Method," in *Proceedings of Symposium on Antennas and Propagation and Microwave Theory and Techniques*, University of Stellenbosch, Stellenbosch, South Africa, October, pp. 151-154.
- Shanks, Daniel (1955), "Non-Linear Transformations of Divergent and Slowly Convergent Sequences," *Journal of Mathematics and Physics*, the Technology Press, Massachusetts Institute of Technology, Cambridge, MA, pp. 1-42.
- Shubair, R. M. and Y. L. Chow (1993), "A Simple and Accurate Complex Image Interpretation of Vertical Antennas Present in Contiguous Dielectric Half-Spaces," *IEEE Transactions on Antennas and Propagation*, AP-41, pp. 806-812.
- Vecchi, G., P. Pirinoli, L. Matekovits and M. Orefice (1993), "Singular Value Decomposition in Resonant Printed Antenna Analysis," in *Proceedings of Joint 3rd International Conference of Electromagnetics in Aerospace Applications*, pp. 343-346.
- Virga, K. and Y. Rahmat-Samii (1995), "Wide-Band Evaluation of Communications Antennas Using [Z] Matrix Interpolation with the Method of Moments," in *IEEE Antennas and Propagation Society International Symposium*, Newport Beach, CA, pp. 1262-1265.

An examination of the effect of mechanical deformation on the input impedance of HF LPDA's using MBPE

J. Tobias de Beer and Duncan C. Baker

Department of Electrical and Electronic Engineering,
University of Pretoria, 0002 Pretoria, South Africa.
e-mail: duncan.baker@ee.up.ac.za

Abstract

This article examines the application of Model Based Parameter Estimation (MBPE) to the evaluation of the input impedance of HF Log Periodic Dipole Arrays (LPDA) during mechanical deformation. A study of cases of lengthening, shortening and displacing one element as well as the effect of mechanical sagging of the array is made. It is found that MBPE is a useful tool for minimizing computations and/or measurements in the study of mechanical deformation.

1 Introduction:

The MBPE [1] technique is used to predict deviations in the input-impedance of a 4 to 30 MHz Log Periodic Dipole Array (LPDA). All the analyses were made using NEC-2 [2]. The work reported in this article is based in part on work done for the M.Eng. degree by one of the authors [3]. The MBPE technique works well if sufficient samples are used as input. Four (4) frequency samples per element¹ were found to be more than adequate for a good estimate of the impedance characteristics of the antenna. Over-sampling (that is for the MBPE model) occurred at very high sampling rates - in the order of 60 samples per element. The use of MBPE allows the forecasting of problem areas in the evaluation of the input impedance. By means of a more complete analysis, an evaluation of the accuracy of these predictions can be made. MBPE may be used to give an early warning of possible instabilities in the input impedance of an LPDA. Although the input impedance of the LPDA does not show instabilities within the operating frequency band, these may occur outside the band. During deformation of the LPDA, changes in the input impedance are to be expected, perhaps radical changes and singularities. MBPE can be used to provide early warning of such problems. (Early in the sense that it is

not necessary to compute a very fine grid of frequency samples - which is computationally expensive). The development of MBPE described and used here is based on the work of Burke, Miller et al [1].

2 The Basics of MBPE

MBPE uses a control system type pole-null structure to represent the input impedance of an antenna (or other system) as a Laplacian transfer function. The LPDA actually consists of an array of dipoles, each easily represented by a pole-null combination. Because of this the characteristics of LPDA's, and many other antennas, could possibly be examined using this technique.

2.1 Mathematical model

In general, Equation 1 is used to represent a pole-null system. (In this case the input impedance of the LPDA.)

$$F(s) = F(j\omega) = G \frac{(s + z_1)(s + z_2)\dots}{(s + p_1)(s + p_2)\dots} \quad (1)$$

In Equation 1 z_n represents nulls, p_n represents poles and G represents the gain, and s is the complex frequency usually represented only by $j\omega$. The poles and nulls, p_n and z_n , will be detected in the form $\sigma + j\omega$, where σ is the damping constant and $j\omega$ the complex angular frequency.

Unlike control system applications, estimation of the placement of the poles and nulls is not done by the structure or the properties of subsystems. The model will instead be applied in a curve fitting environment.

Equation 1 can conveniently be converted to:

$$F(s) = \frac{n_0 + n_1 s + n_2 s^2 + n_3 s^3 \dots}{1 + p_1 s + p_2 s^2 + p_3 s^3 \dots} \quad (2)$$

Since the values of s ($s = j\omega$) and $F(s)$ (from input data) are known, Equation 2 can conveniently be solved. For multiple inputs for s and $F(s)$ a matrix equation

¹An element is a single dipole, The LPDA consists of a number of dipoles spaced and scaled periodically

is obtained. This is used for solving Equation 2, with mathematical routines such as Gauss-Jordan elimination (see for example [4]). The result returns the values of n_n and p_n . The actual placement of the poles and nulls is not important as a first objective, but they can easily be found from the values of n_n and p_n . The main objective is to reconstruct the frequency response of the system (of the input impedance in this case). Equation 2 is used to do just this. MBPE will be able to fill in the missing parts in the data, according to the pole null structure detected.

2.2 MBPE and the Data

Since MBPE tends to become unstable if too many data points are used, this study is limited to the use of four poles and four nulls per sliding window. The effect of using too many data points is well illustrated in Figure 1. In this case 40 poles and 39 nulls were used. These errors do not necessarily indicate a failure of the model but are rather due to limitations in numerical accuracy during the Gauss-Jordan elimination process (see for example [4]). An exact solution of Equation 2 would result in zero errors at the supplied data points. This is clearly not the case as seen in Figure 1.

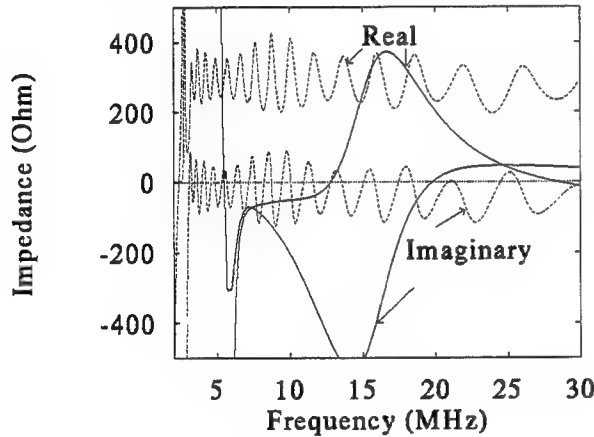


Figure 1: Illustration of the effect of using too many samples simultaneously. MBPE was applied on 80 points of data with 40 poles and 39 nulls (solid lines). For reference 640 frequency points (from NEC2) were used, with straight line interpolation (SLI), of the same structure (dotted lines).

Due to the wide frequency range of the LPDA, the application of MBPE will be on data-windows (with width = $1 + \text{poles} + \text{nulls}$). This means MBPE is applied to frequency points 1 to 9, and then to frequency points 2 to 10 etc. All the outcomes are plotted on the same graph, since for a good solution these graphs are supposed to lie on the same curve. This can also be used

to determine how stable the solution is. If the different graphs (over the same data area) differ too much from each other, further investigation should be made on that area. Instabilities are caused either by some singularity in that area or under-sampling or some kind of failure in the model. Using more data points to solve the problem will give a more stable solution, and better illumination of any singularities. It is also useful to investigate the placement of the poles and nulls as illustrated in Section 3.2.

The main objective is to have more than one pole-null pair per element. This amounts to more than 2 samples per element depending on the window size used. This corresponds with the Nyquist sampling criteria. At a total of 50 samples across the band ($2 - 30\text{ MHz}$), an error, in the real part of the impedance, of 4.9% was detected. This might be accurate for many applications, but for the investigation of deformations on the LPDA this accuracy is not high enough. Furthermore the poles and nulls detected, should move around under deformation. For these reasons a sample rate of about four (4) samples per element is used for the investigation of deformations. It is also important to use the correct method of frequency incrementing. Since the lengths of the elements in the LPDA are spaced periodically in frequency, we must also space our samples in a similar way. Throughout this article, logarithmic sampling is used.

3 The ‘Ideal’ LPDA and MBPE

The term ‘ideal’, as used here, means undeformed. In later sections, the applications of MBPE to deformed LPDA’s, whether mechanical sagging, displacement or length changes of elements, are discussed. The ideal LPDA is described in Section 3.1. Application of MBPE to the input impedance of this LPDA is described in Section 3.2. Sections 4, 5 and 6, examine the effects of mechanical deformations on this LPDA.

3.1 Construction of the LPDA

A 20 element LPDA with a 30° apex (α), element reduction factor (τ) of 0.87 and a rear element total length of 42.13m was used for this study. The whole structure is located at a height of 20m above ground. The ground parameters used are: a relative dielectric constant (ϵ_r) of 15 and a conductivity (σ) of 0.005S/m . The center fed transmission line has an impedance of 450Ω . The transmission line is terminated in a short 21.065m beyond the rear element. This construction is represented in Figure 2. In Section 6 the same structure is used, with nonconducting catenaries to support the structure as used in practice. This antenna is similar to that used in [3] and [5].

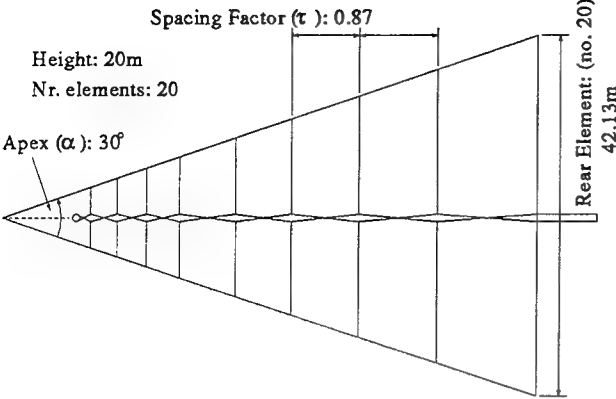


Figure 2: The construction parameters of the LPDA used for this study. (Transmission line shown crossed to illustrate alternating connections of elements. The shorted stub length is 21.065m)

3.2 Input Impedance of the Ideal LPDA

Due to the log periodic structure of the LPDA, logarithmic repetitions are expected for the input impedance. Since frequencies corresponding to the resonant lengths of the elements are spaced logarithmically in the frequency band, samples are spaced in the same way. NEC-2 was used to determine the input impedance of the LPDA.

The result of application of MBPE to 20 frequency data points is shown in Figure 3. Also shown for reference are the results of a 640 frequency point solution with straight line interpolation. A sliding sample ‘window’² with only 4 poles and 4 nulls were used for this solution. Multiple overlapping solid curves in Figure 3 arise from this sliding window. Although the MBPE data is stable, it is very clear that not enough samples were used in this case. This sample rate violates the Nyquist sample criteria. A sample rate of 50 samples (above Nyquist) across the band gave stable results, but not accurate enough to use with the study of deformations. At 60 samples (across 2 – 30 MHz) the stability of MBPE solutions was much improved. However, with medium to heavy deformations, errors occurred due to movement of poles and nulls. The authors therefore decided to use a sample rate of 80 samples across the band as a standard for the investigation of deformations.

Applying MBPE to the same LPDA with 80 frequency samples, a clear picture of the actual response of the LPDA is obtained. Figure 4 gives a more complete picture of the behavior of the LPDA. The data from the MBPE and a 640 frequency sample point Straight Line Interpolation (SLI) are plotted on the same graph in Figures 4 and 5. This gives an indication of the potential of the MBPE technique.

²see Section 2.2 Paragraph 2

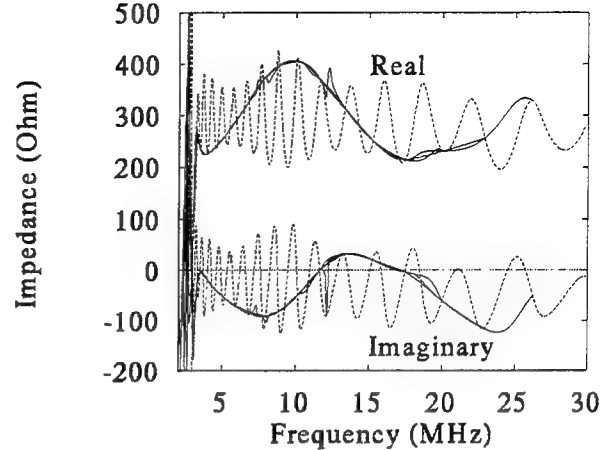


Figure 3: The input impedance of the LPDA with MBPE (with 4 nulls and 4 poles) applied to 20 sample points in frequency (solid lines). Reference curve for 640 frequency sample points shown as dotted lines (SLI). See text.

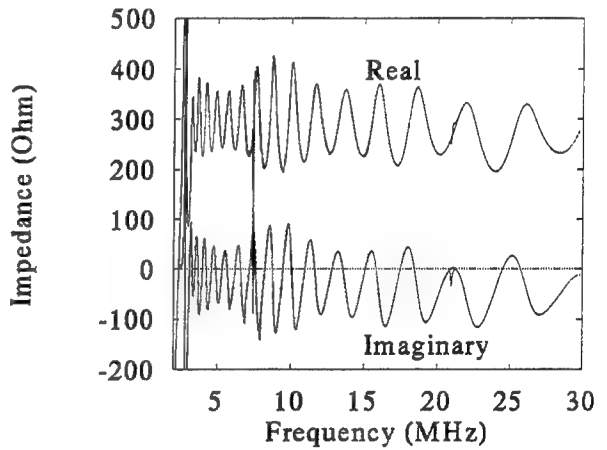


Figure 4: The input impedance of the LPDA with MBPE (with 4 nulls and 4 poles) applied to 80 sample points in frequency (solid lines). Reference curve for 640 frequency sample points shown as dotted lines (SLI). See text.

From Figure 4 and 5 it is clear that a singularity occurred at about 2.8 MHz. This is due to the short used at the end of the LPDA’s transmission line to increase bandwidth. Since the antenna is designed to work from 4 to 30 MHz it is clear that this 2.8 MHz point is not in the design area. Still, this irregularity shows the effectiveness of MBPE for detecting such anomalies.

Figure 4 can be used as reference for investigating how the input impedance of the LPDA changes with deviations. The 640 point solution for the ideal LPDA is used as a reference for further sections investigating the effect of deformation of the LPDA from the ideal.

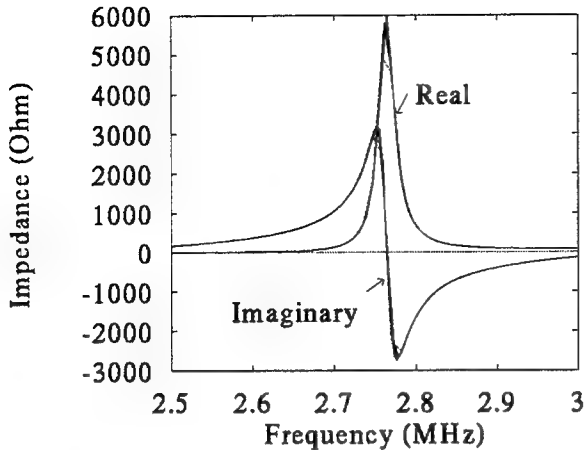


Figure 5: The input impedance of the LPDA with MBPE (with 4 nulls and 4 poles) applied to 80 sample points in frequency (solid lines). The response of 640 sample points illustrate possible margins (dotted lines, SLI).

Another instability was also detected at about $7MHz$. Further examination of the 640 point solution, shows a small inflection in the input impedance for this frequency, as is shown more clearly in the expanded frequency scale in Figures 8 and 9, later. For this case it is essential to look at the poles and nulls detected at that area. The poles and nulls detected in the frequency band 7.015 to $9.202MHz$ are shown in Figure 6. It is clear that a pole-null pair was detected at a point in the s-plane, corresponding to $7MHz$. This explains the occurrence of the instability at $7MHz$. Further investigation showed that this instability was caused by the short at the end of the transmission line.

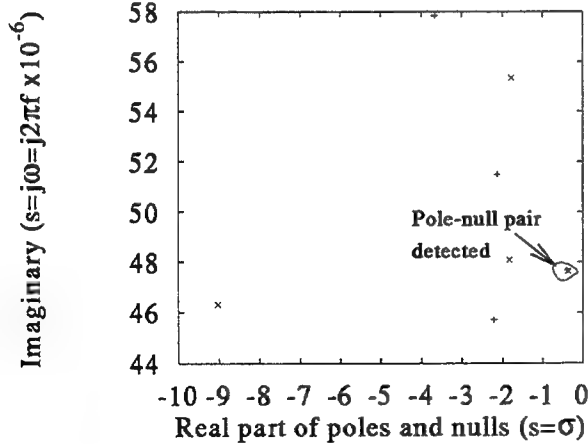


Figure 6: The pole null pair detected, by MBPE, at about $8MHz$. This figure represents the frequency band 7.015 to $9.202MHz$. The poles are shown by crosses and the nulls with pluses.

For the evaluation of the effect of physical deformation of the LPDA, one would prefer to have some kind of curve fit to another dimension. An ideal case would be to fit a curve to the poles and nulls with a polynomial fit. This would result in the position of the poles and nulls being represented by a polynomial as shown in Equation 3, where z is the pole or null, z_0 and k_n are constants and d is a value connected to the deformation:

$$z = z_0(k_0 + dk_1 + d^2k_2 \dots d^n k_n) \quad (3)$$

Each element (dipole) in the LPDA can essentially be represented by a pole and a null. These poles and nulls are spaced to have poles approximately where the real part of the impedance is a maximum, and nulls where it is a minimum. These are the fundamental poles and nulls for the impedance. To complete the curve-fit - since MBPE is an exact solution - some extra poles and nulls are detected. The presence of these extra poles and nulls moves the fundamental poles and nulls. These extra poles and nulls sometimes occur in pairs on the resonant part of the s-plane. For different extremes of a deformation the extra poles and nulls are detected at completely different places. If a curve fit on the extra poles and nulls is made, the intermediate extra poles and nulls may cause very unstable solutions. Since the fundamental poles and nulls are moved by the detection of extra poles and nulls, this further complicates the application of a polynomial curve-fit. In Figure 7 the poles and nulls from the 12 to $20MHz$ band are shown. The difference between the poles and nulls detected on the same data-set by merely using different windows of data is illustrated.

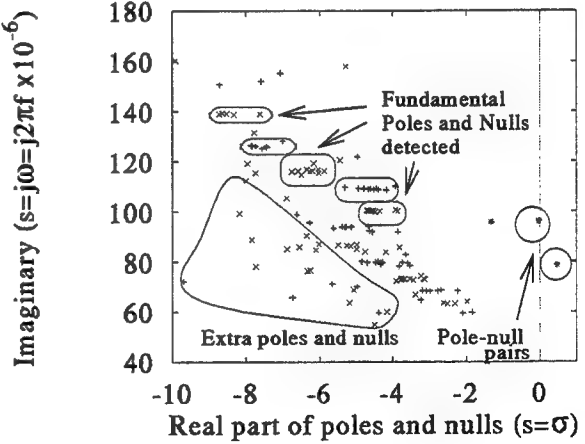


Figure 7: The poles and nulls detected across the 12 to $20MHz$ band of the LPDA. Groupings of poles and nulls can be found, but they are not uniquely defined. Poles and nulls (usually in pairs) were also detected in the resonant ($\sigma > 0$) region.

Due to the quality of the results obtained from MBPE

an attempt was made to implement a curve fit on the poles and nulls detected during application of MBPE to a two dimensional impedance plot, with both frequency and deformation dependence. These results were however difficult to interpret, and essentially meaningless.

Due to the difficulty of implementing a two dimensional fit, the rest of this paper is limited to the use of MBPE at discrete deviations for single parameters.

4 The effects of changing the element length

For this and the following sections, physical deviations from the structure of an ideal LPDA, as used in [5], are considered. Data can not be compared directly to that in [5], since only 20 linearly spaced sample points were used in [5]. With the help of MBPE the validity of assumptions made in [5] is evaluated, since MBPE gives a better indication of the actual response than the few data points used in [5]. The first case study will be on the deviation in the length of one of the elements of the LPDA. The effects on the radiation pattern of the LPDA were found to be minimal [5, 3].

4.1 Increasing the 10MHz element length

In this case the length of element no. 13, with an isolated free space resonance of around 10MHz is increased by 6.5% of its original length. (This is much more than allowed in Smith [6]). At first there does not seem to be much difference between the impedance of this deformation and that of the ideal LPDA.

With the application of MBPE, more definite deviations in the input impedance of the LPDA can be detected, as can be seen in Figure 8. This is still not as radical as assumed by Smith [6], but not as insensitive as expected in [5]. The effect of this deviation is clearly illustrated in Figure 8.

To verify the results from MBPE, the MBPE model used in Figure 8 was compared with a 640 data point solution. From this comparison it was clear that the MBPE is a very good approximation and therefore can be used as a basis for further comparisons to the ideal LPDA.

4.2 Decreasing the length of the 10MHz element

Decreasing the length of an element produces results similar to those in Section 4.1. The deviations shown in Figure 8, are expected to be reversed. In Figure 9 the

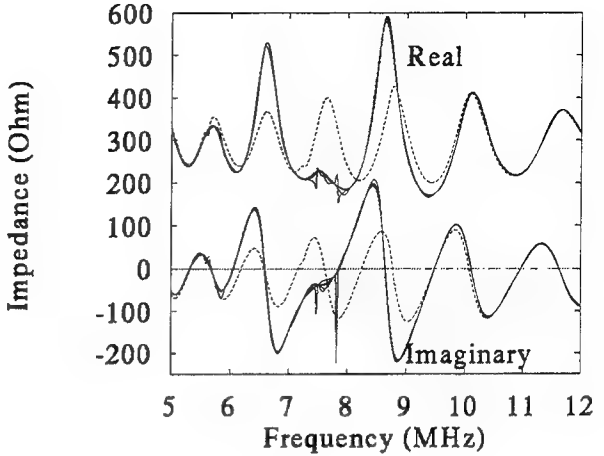


Figure 8: The comparison of the input impedance of the ideal LPDA (dotted lines, SLI) and the input impedance of a LPDA with the length of the element around 10MHz increased by 6.5% of its original length (solid line, MBPE).

results from applying MBPE for this case, are compared to the ideal LPDA. The effects in Figure 8 can be explained with three fundamental poles at about 8MHz. (The centre pole would be associated with the deformed element.) The center pole moved away, ($\sigma \ll 0$) and the two neighboring poles moved closer to the $j\omega = 0$ axis.³ (Please also refer to Figures 6 and 7 for the use of $j\omega$ and σ .) In Figure 9 this effect has inverted: the center pole moved closer to the $j\omega = 0$ axis, and its neighboring poles moved away. The instabilities at about 7.6MHz are caused by the short at the end of the transmission line.

From the above it is clear that the effects of these deviations show up at lower frequency values than expected due to the actual operation of the LPDA. An LPDA typically has an active region of a few localized elements at any in-band frequency. This active region is displaced towards elements shorter than those which would normally correspond to resonance in isolation at a given in-band frequency. This may explain why the deviations occur at lower frequencies than expected, since at that stage the deformed element will be in use.

5 Displacing the 10MHz element

In this section the 13'th element, corresponding to resonance at 10MHz, is moved along the transmission line by 10% of its spacing from the previous element. The results (with MBPE applied) of moving the element towards the region of the LPDA with longer elements, are shown in Figure 10, and those from moving the element

³ $j\omega$: Angular frequency. σ : Damping coefficient.

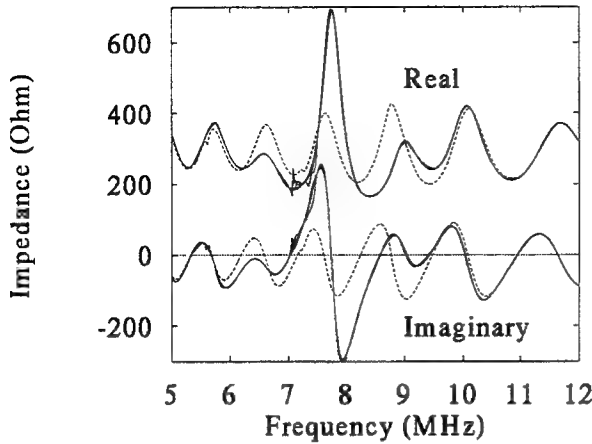


Figure 9: The comparison of the input impedance of the ideal LPDA (dotted line, SLI) and the input impedance of a LPDA with the length of the element around 10MHz decreased by 6.5% of its ideal length (solid line, MBPE).

towards the shorter elements in Figure 11. From these two figures it is clear that this change does not have much effect on the input impedance of the LPDA.

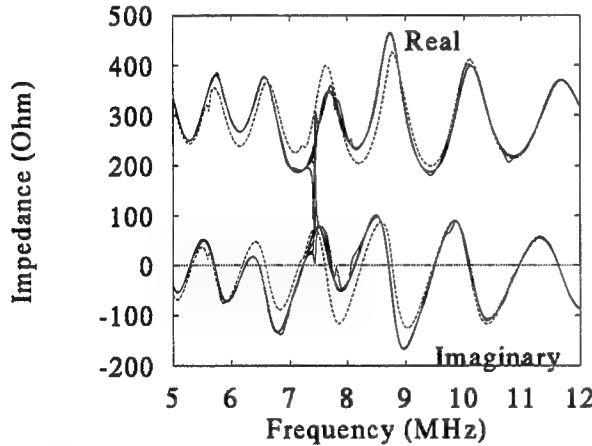


Figure 10: The comparison of the input impedance of an ideal LPDA (dotted lines, SLI) and a LPDA where the element corresponding to 10MHz is moved 10% of its spacing towards the wide-end of the LPDA (solid lines, MBPE).

In Figure 10 an instability or ‘glitch’ occurred at about 21 MHz . These glitches also occurred in the impedances examined in Figures 8 and 9, and in some other implementations, these glitches occurred at the edge of the data window used. The MBPE technique has no *a priori* knowledge of the impedance values outside the data-window and therefore sometimes place poles and nulls close to the window in irregular places. This causes the

ends of the reconstructed window to be more unstable. MBPE can be used to reconstruct the impedance of an antenna outside the sample window, but it was found that such expectations outside the data-window were not very accurate for the LPDA. It was also found that the reconstruction in the center of the window is more reliable than on the edges. This effect can be eliminated by only using the inner eg. 60% of the reconstructed window.

From Figures 10 and 11 the effects of misplacement could also be explained using movement of poles and nulls.

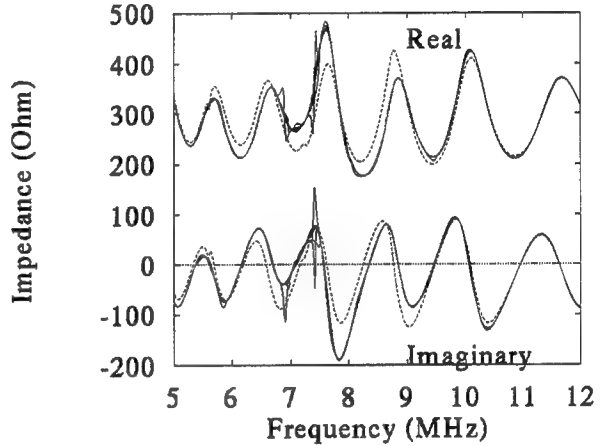


Figure 11: The comparison of the input impedance of an ideal LPDA (dotted lines, SLI) and a LPDA where the element corresponding to 10MHz is moved 10% of its spacing towards the small-end of the LPDA (solid lines, MBPE).

6 Mechanical sagging of the LPDA

In this section the use of MBPE to investigate the effects of mechanical sagging, is examined. The same deformations as used in [5] are used here. Once again the results of these sagged cases are compared to those of the ideal LPDA.

The program TOWEROPT, used for structural analysis and optimizations, (See [5]) was used to evaluate the sagging of a practical LPDA at discrete points. These points were used to construct a NEC input file. The effects of sagging was evaluated with the aid of NEC-2. Practical load parameters were used for the structure, namely: 117gm/m for the conductors and 275gm/m for the parafil ropes. A tensile strength of 20kN was used for the ‘parafil’⁴ rope. All possible information available was

⁴‘Parafil’ is a trade name for a class of pre-strained terylene rope encased in a UV absorbing sheath (see [7])

used for the construction of the TOWEROPT input file. (This include for example the weight of the fiberglass joints used to join the parafil rope with the conductors etc.) This was done to get the best practical evaluation possible. Only one adjustable parameter, prestrain, was available. By adjusting the prestrain, on certain cables, different cases of sagging could be evaluated.

The moderately sagged and extremely sagged cases as described in [5] were compared to the ideal LPDA. Comparisons as in Figure 12 for the extremely sagged case and Figure 13 for the moderately sagged case were obtained.

Figure 12 displays the effect of extreme sagging on the LPDA. This case represents an antenna laid out on the ground, with no prestrains in the cables/ropes, which is then hoisted to a height of 20m. In this case the final strain in the cables was only 8% of its rated strength. The maximum physical sag of 4.33m occurred at element sixteen - corresponding to 18% of the total element length. The maximum percentage sag was at element four with 28% sagging. This case is represented by a zero prestrain value in the stay-wires and supports.

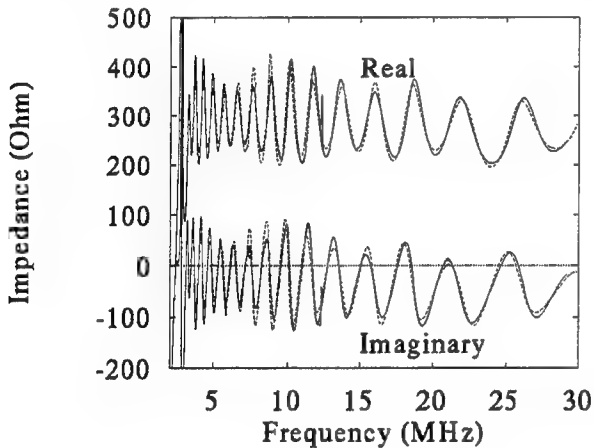


Figure 12: Comparison between predicted impedances for the Extremely sagged LPDA (solid lines, MBPE) and the ideal LPDA (dotted lines, SLI).

Figure 13 displays the input impedance of the moderately sagged case. The same type of approach as above, except, some of the cables were prestrained⁵, corresponding to ropes 2% shorter than the actual distance between their connecting points, and then stretched to reach these points. The structure was then 'hoisted' to a height of 20m as described above. This gave a maximum tension of 40% of the breaking strength of the catenary material used. This case is represented by a 2% prestrain in the parafil stay-wires and supports.

⁵The prestrained cables were: the transmission line tension rope, the rear element pull-up ropes and the stay-wires on the sides of the antenna

It is clear that the effects of mechanical sagging on the input impedance are very limited. The limitations set in Smith [6] are clearly very conservative. The effects on the radiation pattern may be of more concern as suggested in [5], although these effects were also limited.

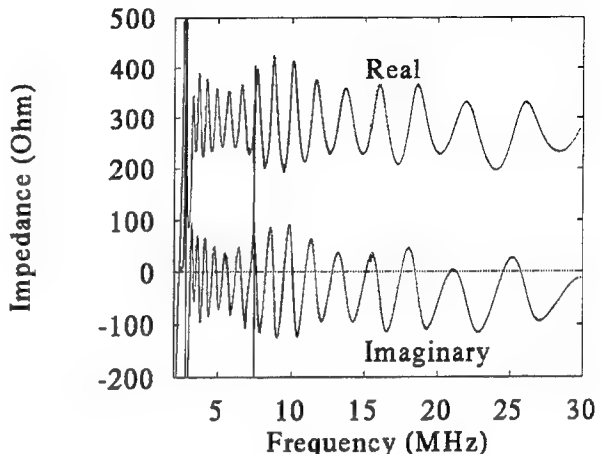


Figure 13: Comparison between predicted impedances for the Moderately sagged LPDA (solid lines, MBPE) and the ideal LPDA (dotted lines, SLI).

7 Conclusion

MBPE is a useful tool for investigating singularities in LPDA's (and antennas in general). It has proved to be very helpful in the study of deformation of an LPDA. Since the study of mechanical deformation needs a whole new set of data for each 'mechanical movement'⁶, it is computationally intensive. By reducing the amount of computations for a given mechanical movement one can - for the same amount of computation time - get a much better view of how the antenna reacts. MBPE also gives a clear indication of problem areas in the frequency band used. Sometimes a deviation of an element shows its effect in a different place in the frequency band from that expected as discussed in Section 4.

Acknowledgement

The authors gratefully acknowledge the suggestion by E.K. Miller to use the MBPE method [1] for the investigation, as well as useful discussions held with him concerning the method.

⁶Mechanical Movement: This includes any type of mechanical deformation of concern - whether sagging, wind loading or even improper construction

References

- [1] Burke G.J., E.K. Miller, S. Chakrabarti and K.R. Demarest; "Using Model-Based Parameter Estimation to Increase the Efficiency of Computing Electromagnetic Transfer Functions", *IEEE Transactions on Magnetics*, 25(4), pp. 2807-2809.
- [2] Burke, G.J. and A.J. Poggio; "Numerical Electromagnetics Code (NEC) - Method of Moments", Technical Document TD116, Naval Ocean Systems Center, San Diego, California, 1981.
- [3] De Beer J.T.; **Influence of Mechanical Deformation of an HF Log-Periodic Dipole Array Antenna on its Performance Characteristics** - M.Eng. Thesis, University of Pretoria, To be submitted during 1995.
- [4] Press, H.P., B.P. Flannery, S.A. Teukolsky and W.. Vetterling; "Numerical Recipes : The Art of Scientific Computation", Cambridge University Press, Melbourne Australia, 1986.
- [5] Baker D.C., J.T. de Beer and N. Stander; "The Effects of Exceeding Mechanical Design Constraints on the Performance of HF Log-Periodic Dipole Arrays", *10th Annual Review of Progress in Applied Computational Electromagnetics*, Vol. I., pp. 516-523, March 1994.
- [6] Smith, C.E.; "Log Periodic Antenna Design Handbook", First Edition, Smith Electronics Inc., Cleveland, Ohio, 44141, 1966.
- [7] Baker, D.C.; "A Limited Comparison of Predicted and Measured Results for an HF Ground-Arrayed Log Periodic Dipole Array, *ACES Journal*, Vol. 5, No. 1, pp. 25-38, 1990.

Current-Based Hybrid Moment Method Analysis of Electromagnetic Radiation and Scattering Problems

Ulrich Jakobus and Friedrich M. Landstorfer

Institut für Hochfrequenztechnik, Universität Stuttgart,
Pfaffenwaldring 47, 70550 Stuttgart, Germany

ABSTRACT. A current-based hybrid method combining the method of moments (MM) with asymptotic current expansions for the higher frequency range is presented for the analysis of arbitrarily shaped, three-dimensional, perfectly conducting electromagnetic radiation and scattering problems. Some examples demonstrate the drastic saving in memory requirement and CPU-time when applying the hybrid method as compared to the conventional MM. Even though the proposed method is a frequency domain formulation, some time domain results based on a Fourier transform are presented as they show an accurate description of diffracted and creeping waves.

1 Introduction

The MM [1] is a widely employed method to deal with perfectly conducting, lossy, or dielectric scattering problems either in the frequency or time domain. Here we will concentrate on three-dimensional, perfectly conducting bodies.

Rao et al. [2] proposed a current basis function \tilde{f}_n defined over triangular patches to deal with this type of problem in the frequency domain. The electric surface current density \tilde{J} is expressed as a linear superposition of basis functions

$$\tilde{J} = \sum_{n=1}^N \alpha_n \cdot \tilde{f}_n \quad (1)$$

with unknown coefficients α_n . The electric field integral equation leads to a system of linear equations to determine these N unknown coefficients. Therefore, the memory requirement to store the elements of the matrix is of order N^2 , and the CPU time to solve the system of linear equations is of order $N^{2..3}$, depending on the applied algorithm, e.g. Gauß elimination or conjugate gradient method.

The required number of triangular patches depends on the size of the scattering body with respect to the wavelength. In our experience, a value of about $N \approx 70 \dots 100$ basis functions for modelling a surface with an area of a square wavelength λ^2 seems to be appropriate. This

means that for a two-dimensional surface of fixed area the necessary number N of basis functions grows proportional to f^2 , the square of the frequency. The result is a memory requirement proportional to f^4 , and the CPU-time grows as $f^{4\dots 6}$.

These dependencies obviously show that the conventional MM is restricted to the lower frequency range. The hybrid method proposed in the next section can overcome this difficulty.

2 Hybrid method

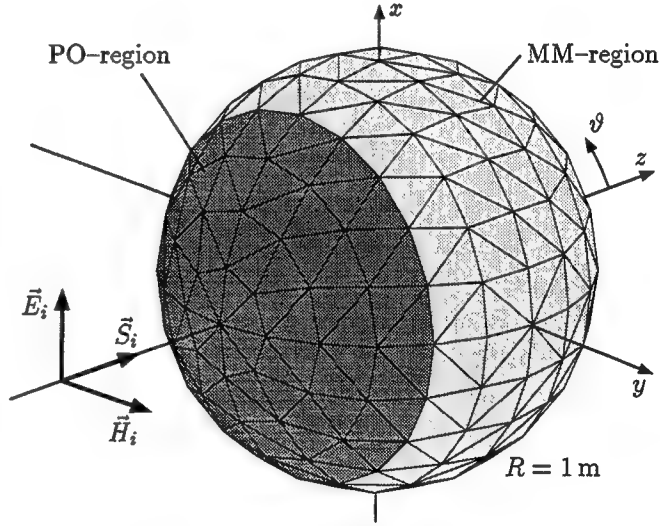


Fig. 1: Plane electromagnetic wave incident on a perfectly conducting sphere with radius $R = 1$ m.

Consider the example depicted in Fig. 1 where a plane electromagnetic wave is incident on a perfectly conducting sphere with radius $R = 1$ m. The surface of the sphere has been subdivided into triangular patches, where basis functions \tilde{f}_n according to Ref. [2] are applied in eqn. (1) to represent the current density \tilde{J} on the surface of the sphere.

Ray-based hybrid methods combining the MM with the geometrical theory of diffraction [3, 4, 5] are not very

suitable to deal with this class of problems involving one large scattering body. Their scope of application is, for instance, radiation problems with an antenna located in front of a large scatterer. Here, however, current-based hybrid methods [6, 7, 8, 9, 10] seem to be more advantageous. As depicted in Fig. 1, we can subdivide the surface into a MM- (light shading) and a PO-region (dark shading), where the physical optics approximation is applied.

In general, the MM-region may consist of wires and surfaces while the PO approximation can be applied only to surfaces. We subdivide metallic wires into electrically short segments and employ triangular basis functions to represent the electric current I^{MM} . On the surfaces in both regions we use an expansion according to eqn. (1) for the surface current density:

$$\vec{J}^{MM} = \sum_{n=1}^{N^{MM}} \alpha_n \cdot \vec{f}_n \quad (2)$$

$$\vec{J}^{PO} = \sum_{n=N^{MM}+1}^{N^{MM}+N^{PO}} \alpha_n \cdot \vec{f}_n. \quad (3)$$

Every basis function \vec{f}_n extends over two adjacent triangular patches [2]. Basis functions located at the boundary between the MM- and the PO-region, i.e. one of the two patches lies in the PO-region and the other in the MM-region, are assigned to the MM-region. This allows a continuous current modeling across the boundary.

Only the N^{MM} unknown coefficients α_n in eqn. (2) are determined by solving a system of linear equations which results from the electric field integral equation and a Galerkin testing procedure. The remaining N^{PO} coefficients α_n in eqn. (3) are based on the physical optics approximation

$$\begin{aligned} \vec{J}^{PO}(\vec{r}) &= 2\delta_i \cdot \hat{n} \times \vec{H}_i(\vec{r}) \\ &+ \sum_{n=1}^{N^{MM}} 2\alpha_n \delta_n \cdot \hat{n} \times \vec{\mathcal{H}} \left\{ \vec{f}_n \right\}. \end{aligned} \quad (4)$$

The first contribution in eqn. (4) represents the conventional PO current density caused by the incident magnetic field strength \vec{H}_i of the excitation. The vector \hat{n} denotes a unit vector normal to the surface at the observation point \vec{r} . A coefficient δ_i accounts for shadowing effects. If \vec{r} lies in the shadowed region, δ_i must be set to zero. Otherwise δ_i equals ± 1 , the sign depending on the direction of incidence with respect to the orientation of \hat{n} .

The second contribution in eqn. (4) accounts for the coupling between the MM- and the PO-region. A summation takes place over basis functions \vec{f}_n in the MM-region

with respective coefficients α_n . The operator $\vec{\mathcal{H}}$ acting on \vec{f}_n yields the magnetic field strength caused by the basis function \vec{f}_n and can be expressed as

$$\vec{\mathcal{H}} \left\{ \vec{f}_n \right\} = -\frac{1}{4\pi} \iint_{A'} \vec{f}_n(\vec{r}') \times \vec{\nabla} G(\vec{r}, \vec{r}') dA' \quad (5)$$

with the free space Green's function

$$G(\vec{r}, \vec{r}') = \frac{e^{-j\beta|\vec{r}-\vec{r}'|}}{|\vec{r}-\vec{r}'|} \quad (6)$$

and the wave number $\beta = \frac{2\pi}{\lambda}$. The vector product $2\hat{n} \times$ in eqn. (4) leads to the PO-current density. Again, coefficients δ_n must be considered to account for shadowing effects.

The coefficients α_n in eqn. (3) can be obtained directly from eqn. (4), thus circumventing the process of solving a system of linear equations.

All further details of the hybrid method can be found in Ref. [11]. In that paper we also developed correction terms \vec{J}^{FW} (fringe wave) based on the exact solution for the half-plane scattering problem to account for effects of edges of polygonal plates. Further correction terms to consider the edges of perfectly conducting wedges are presented in Ref. [12]. The following examples show that these high frequency current approximations implemented in a hybrid method together with the MM represent a powerful tool for the analysis of a wide variety of electromagnetic radiation and scattering problems.

3 Examples

The first example has already been depicted in Fig. 1. The perfectly conducting sphere of radius $R = 1$ m is subdivided into 368 triangular patches resulting in 552 basis functions \vec{f}_n associated with the interior edges between the triangular patches. A plane electromagnetic wave polarized in x -direction and propagating in positive z -direction is incident on the sphere.

We have chosen this particular example because the results can be compared to the exact solution available in the literature (e.g. Ref. [13]). First we have calculated the monostatic radar cross section (RCS) σ of the sphere in the frequency domain using the MM or the PO approximation, respectively, on the entire surface of the sphere, i.e. contrary to Fig. 1 no subdivision into a MM- and a PO-region has been made.

The result is depicted in Fig. 2. It shows an excellent agreement between the exact solution (dash-dotted line)

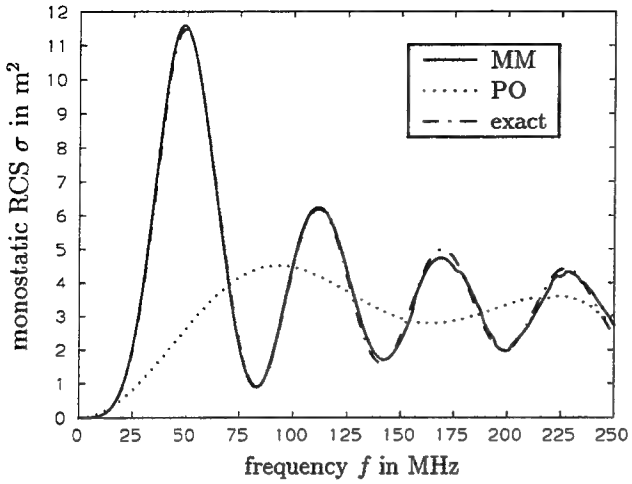


Fig. 2: Monostatic radar cross section σ of the sphere as a function of the frequency f .

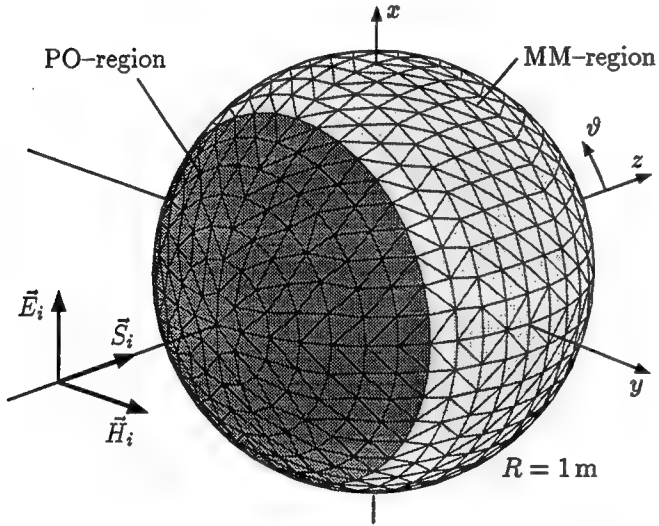


Fig. 3: Adaptive subdivision of the surface of the sphere into triangular patches (1272 triangles here, 368 patches in Fig. 1).

and the MM solution (solid line). The PO solution (dotted line) fails, mainly because of the small size of the sphere. At $f = 150$ MHz the diameter of the sphere just equals one wavelength λ .

It should be noted that the implemented computer code allows an adaptive segmentation based on the actual value of the wavelength. When dealing with low frequencies the sphere is subdivided into 368 patches as shown in Fig. 1. With increasing frequency the program automatically chooses a larger number of patches, e.g. at 500 MHz 1272 triangles are used as depicted in Fig. 3. This varying number of patches causes the small jumps

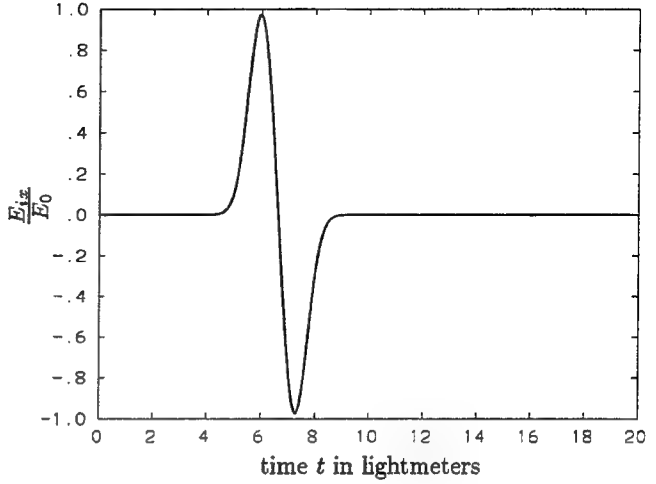


Fig. 4: Pulse incident on the sphere according to eqn. (7) at the origin $\vec{r} = 0$ with $a = 1.5 \frac{1}{\text{m}}$, $t_1 = 6 \text{ lm}$, and $t_2 = 7.25 \text{ lm}$.

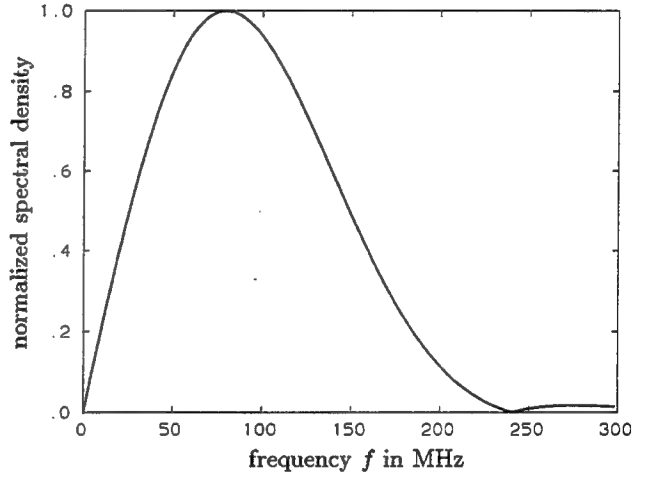


Fig. 5: Normalized spectral density for the pulse according to eqn. (7) with $a = 1.5 \frac{1}{\text{m}}$, $t_1 = 6 \text{ lm}$, and $t_2 = 7.25 \text{ lm}$ as depicted in Fig. 4.

that can be observed in the MM-solution in Fig. 2 e.g. at about 225 MHz.

Now we will investigate the time domain response when a pulse described by

$$\vec{E}_i(\vec{r}, t) = \vec{E}_0 \cdot \left(e^{-a^2 [c(t-t_1)-\vec{r}\cdot\hat{\beta}]^2} - e^{-a^2 [c(t-t_2)-\vec{r}\cdot\hat{\beta}]^2} \right) \quad (7)$$

with $a = 1.5 \frac{1}{\text{m}}$, $t_1 = 20 \text{ ns}$, $t_2 = 24.18 \text{ ns}$, $\vec{E}_0 = E_0 \hat{x}$, and $\hat{\beta} = \hat{z}$ is incident on the sphere. c denotes the velocity of light in free space. It is useful to specify the time t in units of lightmeters (lm) with $1 \text{ lm} = \frac{1 \text{ m}}{c} \approx 3.34 \text{ ns}$. Thus we have $t_1 = 6 \text{ lm}$ and $t_2 = 7.25 \text{ lm}$.

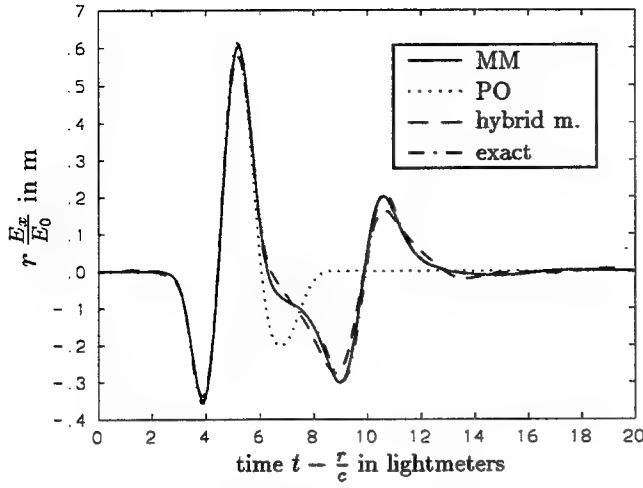


Fig. 6: Backscattered pulse in the farfield as a function of time for the pulse according to Fig. 4 incident on the perfectly conducting sphere.

Fig. 4 shows the shape of the incident pulse as a function of time. The corresponding normalized spectral density is depicted in Fig. 5. We have chosen two successive Gauß pulses with a time delay of $t_2 - t_1 = 1.25$ lm so that the spectral intensity is maximum at about 79 MHz.

The backscattered pulse in the farfield region can be calculated by means of Fourier transforming the complex frequency response, as depicted in Fig. 2, multiplied with the complex spectral intensity of the excitation. The result is shown in Fig. 6, where r denotes the distance of the observation point in the farfield. The time t is shifted by $\frac{r}{c}$ so that $t - \frac{r}{c} = 0$ describes the propagation of a pulse starting at $t = 0$ at the origin of the coordinate system or at the center of the sphere, respectively. Looking at Fig. 3, we can see that the maximum of the incident wave at $t = 6$ lm in Fig. 4 is reflected at the point $x = y = 0$ and $z = -R = -1$ m at the time $t = 5$ lm. This reflected wave can be observed in the farfield at the time $t - \frac{r}{c} = 4$ lm, which is in accordance with the calculated response in Fig. 6.

The solid line in Fig. 6 represents a solution based on an application of the MM on the whole surface of the sphere, i.e. no asymptotic current expansion is involved. This curve is in excellent agreement with the exact result (dash-dotted line). The dotted line is the result of the PO approximation on the whole surface of the sphere. This solution differs distinctly from the exact result for times $t - \frac{r}{c} > 6$ lm. The additional negative peak of the exact solution at $t - \frac{r}{c} \approx 9$ lm can be interpreted as a creeping wave with a time delay of $\frac{\pi R}{c} \approx 3.14$ lm arriving at $t - \frac{r}{c} \approx (6 + 3.14)$ lm in the farfield region. This creeping wave term is absent in the PO solution.

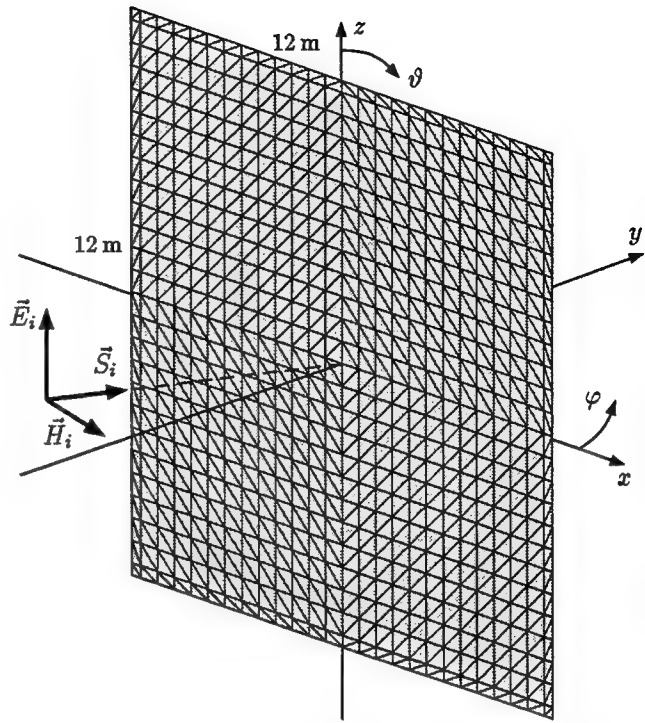


Fig. 7: Plane electromagnetic wave incident on a perfectly conducting square plate with side length 12 m.

Now we will demonstrate the application of the hybrid method. For frequencies lower than 75 MHz (compare to Fig. 5) we employ the conventional MM for the whole surface of the sphere. This is not a disadvantage, as we make use of an adaptive segmentation scheme and for these low frequencies only a moderate number of unknowns is required. The hybrid method is used for frequencies above 75 MHz. The range $0^\circ \leq \vartheta \leq 120^\circ$ in Fig. 3 represents the MM-region while PO is applied on the remaining part of the surface (dark shading). The resulting backscattered pulse is depicted in Fig. 6 by the dashed line. Good agreement with the exact solution can be observed also for times $t - \frac{r}{c} > 6$ lm when PO fails.

A second example is shown in Fig. 7. A plane electromagnetic wave according to eqn. (7) with $a = 1 \frac{1}{m}$, $t_1 = 6$ lm, and $t_2 = 8$ lm is incident on a perfectly conducting square plate with side length 12 m. First the case of perpendicular incidence with $\vartheta_i = 90^\circ$ and $\varphi_i = 270^\circ$ will be considered, i.e. the wave is propagating in positive y -direction with $\vec{E}_0 = E_0 \hat{z}$ and $\vec{H}_0 = H_0 \hat{x}$ in eqn. (7).

The backscattered pulse in the farfield region is depicted in Fig. 8. The solid line corresponds to the solution based on the MM applied to the entire structure. The dotted curve is the result of the PO approximation $J_z^{PO} = 2 H_{ix}$. We can modify this PO current density by a heuristic superposition of correction terms \vec{J}^{FW} asso-

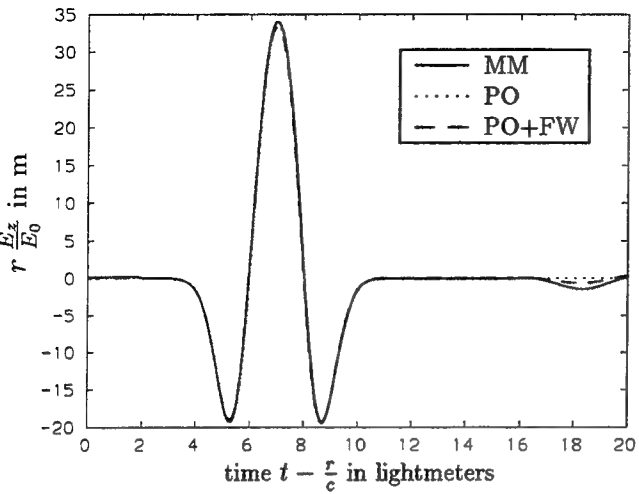


Fig. 8: Backscattered pulse in the farfield as a function of time for the perfectly conducting plate with perpendicular incidence.

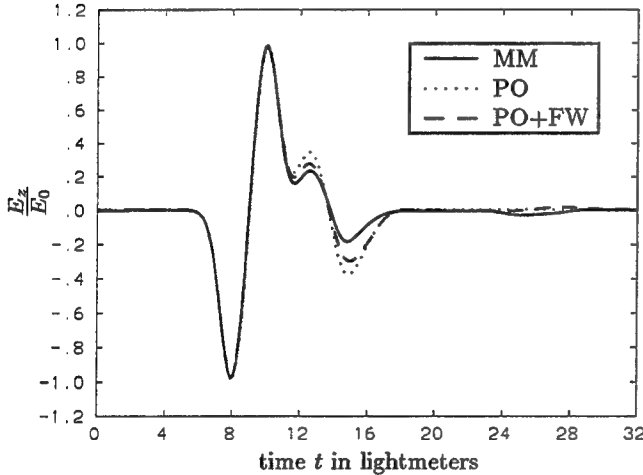


Fig. 9: Scattered pulse in the nearfield at an observation point $x = z = 0$ and $y = -2$ m as a function of time for the perfectly conducting plate with perpendicular incidence.

ciated with the four edges of the plate [11]. This leads to the dashed line in Fig. 8. If we try to interpret the results with diffraction theory, we find one reflected and four edge diffracted rays that overlap because of the same time delay for an observation point on the negative y -axis in the far field. The double diffracted rays have an additional time delay of 12 lm and can be observed in Fig. 8 at $t - \frac{r}{c} \approx 18$ lm.

We can separate the reflected pulse and the four edge diffracted pulses by choosing an observation point in the nearfield. Fig. 9 shows the scattered field at an observation point $x = z = 0$ and $y = -2$ m. The maximum of

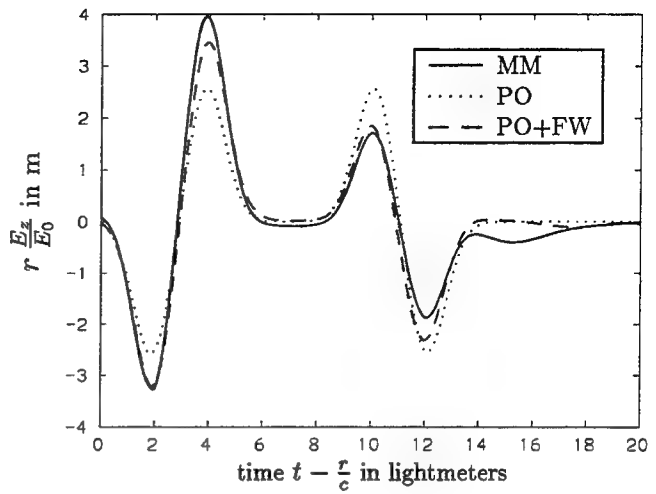


Fig. 10: Backscattered pulse in the farfield as a function of time for the perfectly conducting plate with direction of incidence $\vartheta_i = 90^\circ$ and $\varphi_i = 250^\circ$.

the incident pulse, which is reflected at $t = t_1 = 6$ lm, arrives at the observation point at $t = 8$ lm. The first maximum of the four edge diffracted pulses can be observed at $t = (6 + \sqrt{6^2 + 2^2})$ lm ≈ 12.32 lm, whereas the double diffracted pulses arrive at $t \approx 24.32$ lm.

The two figures 8 and 9 show that the agreement between the MM solution acting as reference and the PO solution is very accurate concerning the reflected pulse. However, this is not true for other than perpendicular incidence.

Fig. 10 shows the monostatic backscattered pulse in the farfield for the direction of incidence $\vartheta_i = 90^\circ$ and $\varphi_i = 250^\circ$. If we try to interpret this figure with diffraction theory, we find that for the first maximum of the incident pulse at $t = 6$ lm a diffraction process at the point $x = -6$ m and $y = z = 0$ takes place. The farfield response can be observed at $t - \frac{r}{c} = (6 - 2 \cdot 6 \sin 20^\circ)$ lm ≈ 1.9 lm. This time agrees well with Fig. 10, but we can observe that the amplitude of the pulse based on the PO solution (dotted line) differs from the MM solution (solid line). Only through the superposition of correction terms (dashed line) can the amplitude be improved. This applies equally to the second pulse caused by a diffraction process at the point $x = 6$ m and $y = z = 0$, which can be observed in Fig. 10 at $t - \frac{r}{c} = (6 + 2 \cdot 6 \sin 20^\circ)$ lm ≈ 10.1 lm.

A further example is shown in Fig. 11. A backfire Yagi-Uda antenna consisting of three shape optimized elements [14, 15] is located in front of a perfectly conducting square plate with a side length of 3λ . As opposed to the previous examples, we will restrict our investigations to one single frequency.

The radiation patterns in the E- and H-plane of the

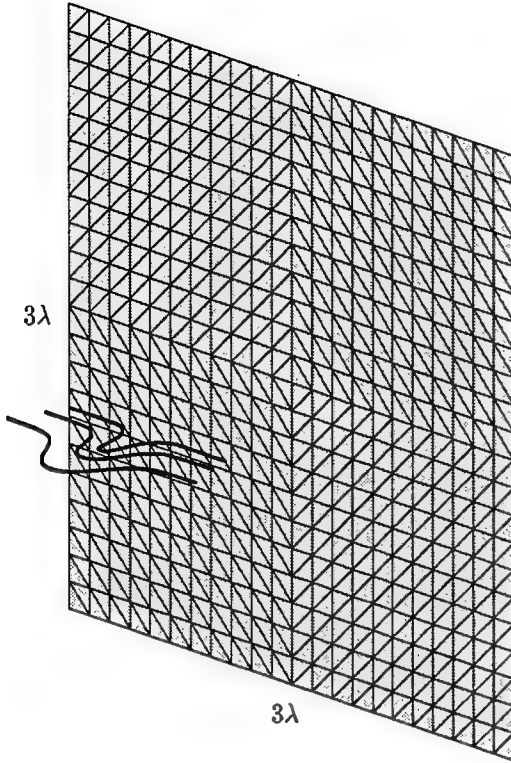


Fig. 11: Backfire Yagi-Uda antenna of three shaped optimized elements in front of a reflector of size $3\lambda \times 3\lambda$.

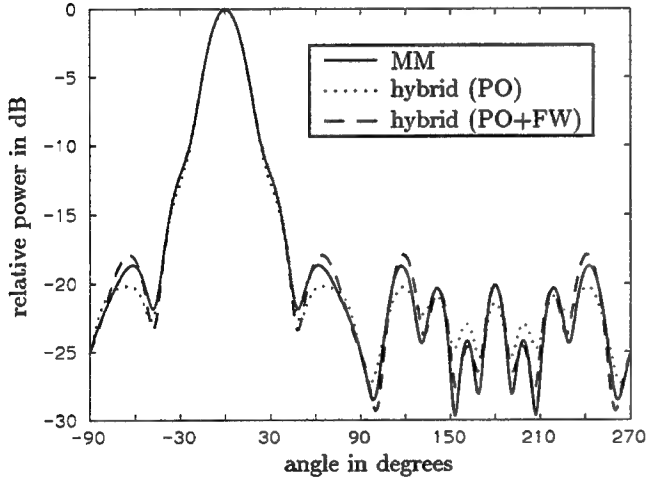


Fig. 12: E-plane radiation pattern of the shape optimized Yagi-Uda antenna in front of a reflector.

Yagi-Uda antenna are depicted in Fig. 12 and 13, respectively. The solid line results from a calculation based on the conventional MM. Applying the hybrid method proposed in Section 2, we assign the wire antenna to the MM-region and the surface of the reflector to the PO-region. This yields a radiation pattern shown by

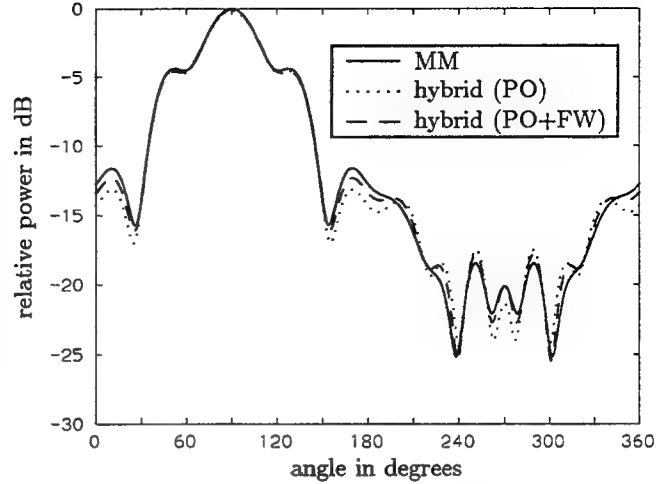


Fig. 13: H-plane radiation pattern of the shape optimized Yagi-Uda antenna in front of a reflector.

Table 1: Input impedance, gain, memory requirement and CPU-time for the backfire Yagi-Uda array in front of a reflector.

| | MM | hybrid method PO | hybrid method PO+FW |
|---|-------|---------------------|------------------------|
| input impedance in Ω | | | |
| real part | 15.6 | 15.4 | 15.5 |
| imaginary part | -56.9 | -56.8 | -56.9 |
| gain in dB | 12.67 | 12.47 | 12.62 |
| no. of basis functions | | | |
| MM-region | 1494 | 86 | 86 |
| PO-region | - | 1408 | 1408 |
| number of unknowns (exploiting symmetry) | 397 | 45 | 45 |
| memory for matrix in kByte | 2463 | 32 | 32 |
| CPU-time in sec (HP 9000/710) | 380 | 163 | 325 |

the dotted lines in Figs. 12 and 13. Superimposing additional correction terms \vec{J}^{FW} to the PO current density on the surface of the plate leads to the results depicted by dashed lines.

Values of the input impedance and the gain of the antenna as obtained by the three methods are tabulated in Table 1.

In the introduction we claimed that the application of the hybrid method leads to a drastic reduction in memory requirement and CPU time as compared to the conventional MM. This is confirmed in Table 1. 86 triangular

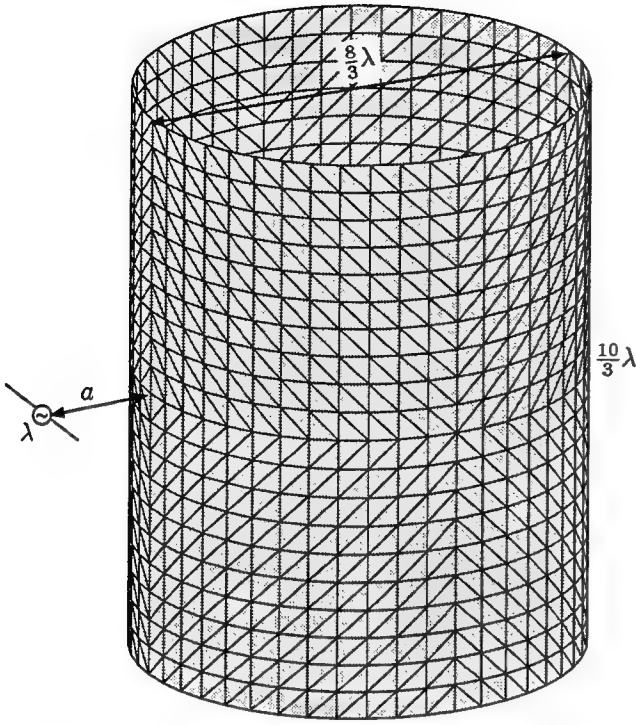


Fig. 14: λ -dipole antenna in front of a circular cylinder of finite length with variable distance a .

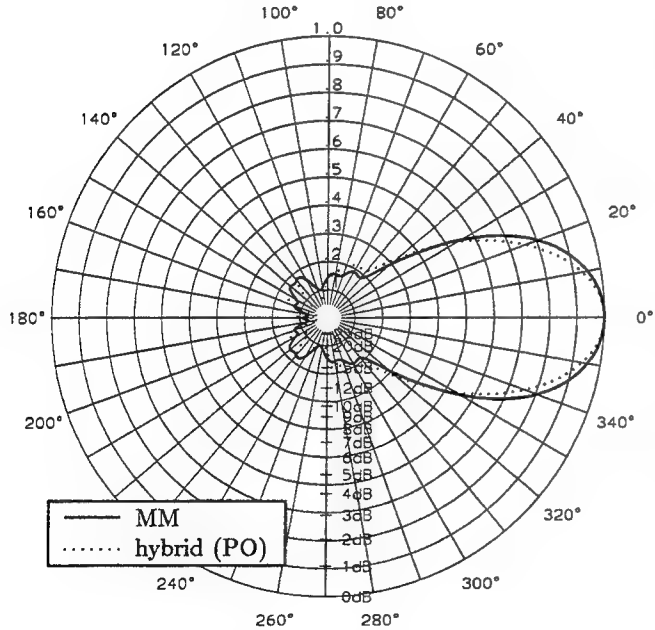


Fig. 15: E-plane radiation pattern of the λ -dipole antenna in front of a circular cylinder ($a = 0.7 \lambda$).

basis functions defined along the wire segments are required to model the wire antenna. On the surface of

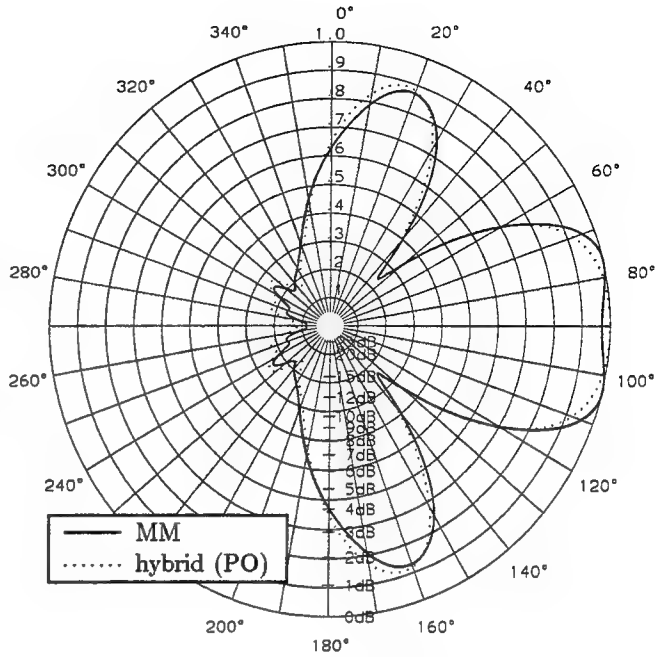


Fig. 16: H-plane radiation pattern of the λ -dipole antenna in front of a circular cylinder ($a = 0.7 \lambda$).

the reflector 1408 basis functions f_n are used leading to a total number of 1494 basis functions for the conventional MM. Exploiting symmetry of the structure, the total number of unknown coefficients which have to be calculated from the solution of a system of linear equations can be reduced to 397. When applying the hybrid method, this number equals 45. Consequently, we have a reduction in memory requirement for the matrix of the system of linear equations by a factor of about 77.

Finally, one last example shown in Fig. 14 shall be investigated. A λ -dipole antenna is located in front of a circular cylinder of finite length with variable distance a . The cylinder has a diameter of $\frac{8}{3}\lambda$ and a height of $\frac{10}{3}\lambda$.

When applying the hybrid method, the dipole antenna represents the MM-region and the PO-region consists of the surface of the cylinder. Note that we have used conventional PO on the cylindrical surface. Similar to accounting for effects of edges of polygonal plates by correction terms \vec{J}^{FW} , we are presently investigating the improvement of the PO-current for curved surfaces by correction terms derived from the Fock theory [16]. Results will be reported in an upcoming paper.

The four figures 15–18 show the E-plane and H-plane radiation pattern, respectively, for the two distances $a = 0.7 \lambda$ and $a = 0.9 \lambda$, respectively. The solid line is based on a calculation with the conventional MM whereas the dotted curve shows the result of the hybrid method. Good agreement can be observed.

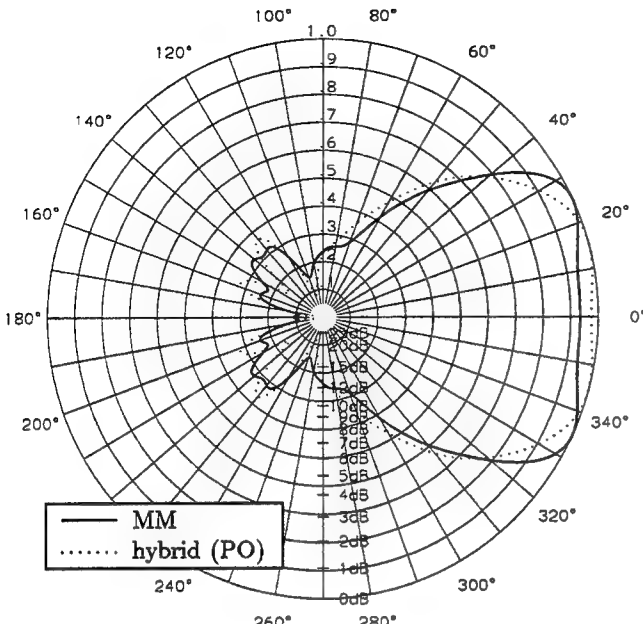


Fig. 17: E-plane radiation pattern of the λ -dipole antenna in front of a circular cylinder ($a = 0.9 \lambda$).

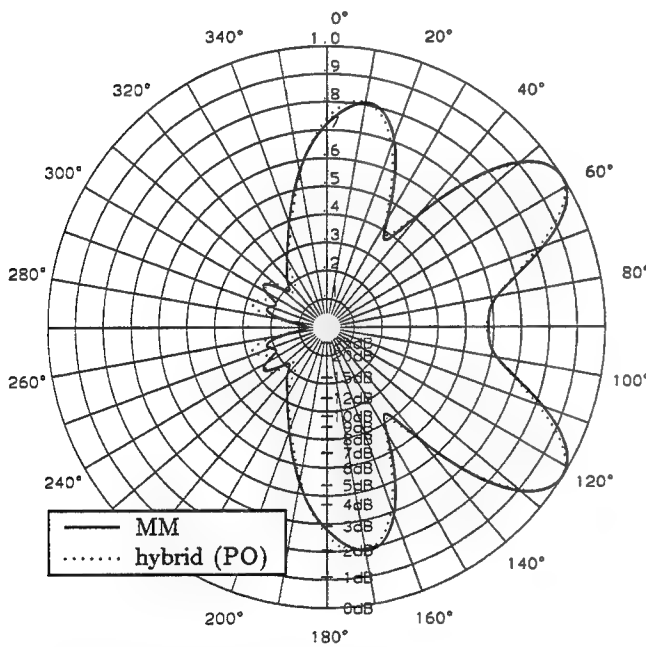


Fig. 18: H-plane radiation pattern of the λ -dipole antenna in front of a circular cylinder ($a = 0.9 \lambda$).

Table 2 summarizes memory requirement and CPU-time for this example.

Table 2: Memory requirement and CPU-time for the λ -dipole antenna in front of a circular cylinder.

| | MM | hybrid m. |
|---|------|-----------|
| number of basis functions | | |
| MM-region | 2852 | 20 |
| PO-region | — | 2832 |
| number of unknowns (exploiting symmetry) | 726 | 11 |
| memory for matrix in kByte | 8236 | 2 |
| CPU-time in sec (HP 9000/735) | 258 | 54 |

4 Conclusions

A hybrid method has been presented combining the MM with asymptotic current expansions for the higher frequency range. In the simplest case the conventional PO approximation is employed. For polygonal scattering bodies we have improved the asymptotic PO current density by heuristic correction terms to take the effects of edges into account. Currently we are also investigating the application of Fock currents for curved surfaces.

Some examples have demonstrated the accuracy of the hybrid method as compared to the conventional MM even though a drastic reduction in memory requirement and CPU-time can be achieved. Some computational results have been transformed from the frequency domain into the time domain allowing a physical interpretation with diffraction theory considering reflected, creeping and diffracted waves.

References

- [1] R. F. Harrington, *Field Computation by Moment Methods*. Macmillan Company, New York, 1968.
- [2] S. M. Rao, D. R. Wilton, and A. W. Glisson, "Electromagnetic scattering by surfaces of arbitrary shape," *IEEE Transactions on Antennas and Propagation*, vol. 30, pp. 409–418, May 1982.
- [3] W. D. Burnside, C. L. Yu, and R. J. Marhefka, "A technique to combine the geometrical theory of diffraction and the moment method," *IEEE Transactions on Antennas and Propagation*, vol. 23, pp. 551–558, July 1975.

- [4] G. A. Thiele and T. H. Newhouse, "A hybrid technique for combining moment methods with the geometrical theory of diffraction," *IEEE Transactions on Antennas and Propagation*, vol. 23, pp. 62–69, Jan. 1975.
- [5] J. N. Sahalos and G. A. Thiele, "On the application of the GTD-MM technique and its limitations," *IEEE Transactions on Antennas and Propagation*, vol. 29, pp. 780–786, Sept. 1981.
- [6] L. N. Medgyesi-Mitschang and D.-S. Y. Wang, "Review of hybrid methods on antenna theory," *Annales des Télécommunications*, vol. 44, no. 9-10, pp. 445–455, 1989.
- [7] L. N. Medgyesi-Mitschang and D.-S. Wang, "Hybrid methods in computational electromagnetics: a review," *Computer Physics Communications*, vol. 68, pp. 76–94, 1991.
- [8] C. S. Kim and Y. Rahmat-Samii, "Low profile antenna study using the physical optics hybrid method (POHM)," in *IEEE International Symposium on Antennas and Propagation, London, Ontario*, pp. 1350–1353, June 1991.
- [9] U. Jakobus, J. Christ, and F. M. Landstorfer, "PO-MoM analysis of cavity-backed antennas," in *ICAP '93, IEE 8th International Conference on Antennas and Propagation, Edinburgh, Conf. Publication Number 370*, pp. 111–114, Apr. 1993.
- [10] L. N. Medgyesi-Mitschang and J. M. Putnam, "Hybrid formulation for arbitrary 3-D bodies," in *10th Annual Review of Progress in Applied Computational Electromagnetics, ACES Conference, Monterey*, vol. II, pp. 267–274, Mar. 1994.
- [11] U. Jakobus and F. M. Landstorfer, "Improved PO-MM hybrid formulation for scattering from three-dimensional perfectly conducting bodies of arbitrary shape," *IEEE Transactions on Antennas and Propagation*, vol. 43, pp. 162–169, Feb. 1995.
- [12] U. Jakobus and F. M. Landstorfer, "Correction of the PO current density close to perfectly conducting wedges by the UTD," *Electronics Letters*, vol. 30, pp. 2111–2112, Dec. 1994.
- [13] R. F. Harrington, *Time Harmonic Electromagnetic Fields*. McGraw Hill, New York, 1961.
- [14] F. M. Landstorfer, "A new type of directional antenna," in *IEEE Symposium on Antennas and Propagation, Mass., USA*, pp. 169–172, Oct. 1976.
- [15] F. M. Landstorfer and R. R. Sacher, *Optimisation of Wire Antennas*. Research Studies Press, John Wiley & Sons, New York, 1985.
- [16] V. A. Fock, *Electromagnetic Diffraction and Propagation Problems, International Series of Monographs on Electromagnetic Waves*, vol. 1. Pergamon Press, Oxford, 1965.

Hybrid Method of Moments Solution for a Perturbed Dielectric Circular Cylinder

William D. Wood, Jr.

Department of Electrical and Computer Engineering
Air Force Institute of Technology
Wright-Patterson Air Force Base, Ohio, 45433

1 Abstract

A hybrid technique is developed, using the integral equation/moment method solution approach with non-free space Green's functions, for a class of scattering problems involving nearly-circular 2-D dielectric cylinders under TM_z illumination. The technique is applicable to other nearly-canonical 2-D penetrable scatterers, and may be extended to certain 3-D geometries. Applications to several 2-D geometries are demonstrated, with scattering predictions compared to those from a standard moment method code.

2 Introduction

The method of moments (MM) is one of the most powerful techniques for solving electromagnetic radiation and scattering problems in the frequency domain. Most implementations of the MM begin with invoking the surface or volume equivalence theorems, in which all material in the problem is replaced with free-space along with equivalent scattering currents. This results in an integral equation in which the unknown currents are integrated against the free-space Green's function.

The power of such a formulation lies in its generality; the same free-space Green's function can be used for any geometry. However, in some cases, this generality comes at the expense of computational efficiency, since the unknown currents must span the volume or boundary of the scatterer. On the other hand, if the geometry under consideration is "close" to a canonical geometry for which the Green's function is known, then computational savings can be reaped if the integral equation is set up to exploit the Green's function. (For an excellent overview of this hybrid technique, see Newman [4].) An example of such a geometry is a nearly-circular, nearly-homogeneous ("perturbed") two-dimensional (2-D)

dielectric cylinder.

In this paper, a hybrid Green's function/method of moments (GF/MM) solution will be presented for the plane-wave scattering from a perturbed dielectric cylinder in the TM_z polarization. First, the geometry of the perturbed dielectric circular cylinder will be defined. Second, the Green's function for the circular, homogeneous 2-D dielectric cylinder will be developed. Third, the integral equation for the scattering from the perturbed dielectric cylinder will be developed. Fourth, a volumetric pulse/point-matching MM solution will be presented. Fifth, numerical results will be presented for several representative perturbation geometries.

3 Geometry

Consider a dielectric circular cylinder with radius a and constant dielectric constant ϵ_c that is perturbed by an arbitrary protrusion and/or inclusion, as shown in Figure 1. We will denote the cross-section of the protrusion as Ω_p , and the cross-section of the inclusion as Ω_i . The protrusion material has relative permittivity ϵ_p , while the inclusion material has relative permittivity ϵ_i .

In the most general case, Ω_p represents any region outside the original circular cylinder, and Ω_i represents any region inside it. These perturbed regions can even be inhomogeneous (that is, ϵ_p and ϵ_i can vary within Ω_p and Ω_i , respectively), although ϵ_c must be a constant.

4 Green's Function

The Green's function for a circular, homogeneous dielectric cylinder is well known [7]. Ruck [6] uses it to give a formula, in terms of an infinite series, for the scattering width of a dielectric cylinder.

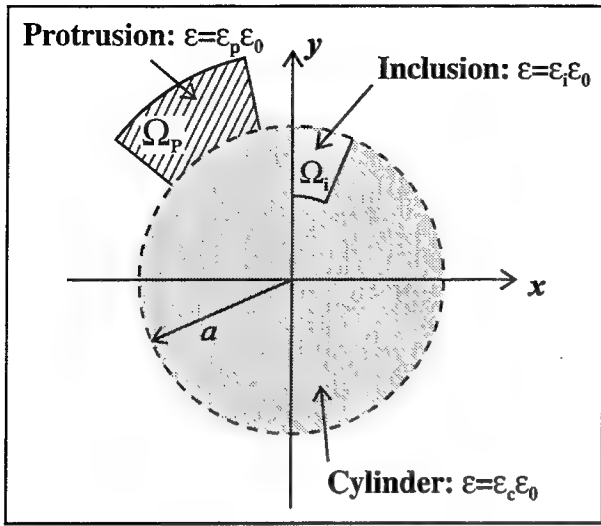


Figure 1: Perturbed Circular Cylinder Geometry

In general, for the TM_z polarization, the 2-D Green's function $G(\bar{\rho}, \bar{\rho}')$ is proportional to the \hat{z} -directed electric field at observation point $\bar{\rho}$ due to a \hat{z} -directed monochromatic electric line source of unit strength at source point $\bar{\rho}'$. It obeys the inhomogeneous Helmholtz equation

$$(\nabla_t^2 + k^2) G(\bar{\rho}, \bar{\rho}') = -\delta(\bar{\rho} - \bar{\rho}') \quad (1)$$

where $\nabla_t^2 = \partial^2/\partial x^2 + \partial^2/\partial y^2$ and k is the propagation constant of the medium containing the observation point. The propagation constant outside the cylinder is $k_0 = \sqrt{\epsilon_0 \mu_0}$, while the propagation constant inside the cylinder is $k_1 = \sqrt{\epsilon_c} k_0$, where ϵ_0 and μ_0 are the permittivity and permeability of free space, respectively. The time convention $e^{j\omega t}$ is assumed and suppressed. Finding the Green's function for an arbitrary geometry is generally non-trivial. However, if the geometry consists of a homogeneous, linear, isotropic dielectric circular cylinder centered at the origin and having radius a and relative dielectric constant ϵ_c , then the Green's function is reasonably straightforward to find by choosing it to obey the same boundary conditions as the electric field. Specifically, we choose $G(\bar{\rho}, \bar{\rho}')$ to satisfy periodic boundary conditions in ϕ and continuity boundary conditions at $\rho = a$:

$$G(\bar{\rho}, \bar{\rho}')|_{\phi=0} = G(\bar{\rho}, \bar{\rho}')|_{\phi=2\pi} \quad (2)$$

$$\frac{\partial G(\bar{\rho}, \bar{\rho}')}{\partial \phi}|_{\phi=0} = \frac{\partial G(\bar{\rho}, \bar{\rho}')}{\partial \phi}|_{\phi=2\pi} \quad (3)$$

$$\lim_{\delta \rightarrow 0} G(\bar{\rho}, \bar{\rho}')|_{\rho=a-\delta} = \lim_{\delta \rightarrow 0} G(\bar{\rho}, \bar{\rho}')|_{\rho=a+\delta} \quad (4)$$

$$\lim_{\delta \rightarrow 0} \frac{\partial G(\bar{\rho}, \bar{\rho}')}{\partial \rho} \Big|_{\rho=a-\delta} = \lim_{\delta \rightarrow 0} \frac{\partial G(\bar{\rho}, \bar{\rho}')}{\partial \rho} \Big|_{\rho=a+\delta} \quad (5)$$

In addition, we expect the Green's function to obey the radiation condition as $\rho \rightarrow \infty$, and to remain bounded as $\rho \rightarrow 0$. The structure of the Green's function $G(\bar{\rho}, \bar{\rho}')$ allows us to identify two components such that

$$G(\bar{\rho}, \bar{\rho}') = G_0(\bar{\rho}, \bar{\rho}') + G_s(\bar{\rho}, \bar{\rho}') \quad (6)$$

The first component, $G_0(\bar{\rho}, \bar{\rho}')$, has the same form as the 2-D free-space Green's function and the second component, $G_s(\bar{\rho}, \bar{\rho}')$, is an infinite series of eigenfunctions. The expression for $G(\bar{\rho}, \bar{\rho}')$ takes on different forms depending on whether the source and observation points lie inside or outside the cylinder.

4.1 Case 1: $\rho, \rho' < a$

When both the source and observation points lie inside the dielectric circular cylinder (i.e., $\rho, \rho' < a$), the components of the Green's function are given by

$$G_0(\bar{\rho}, \bar{\rho}') = -\frac{j}{4} H_0^{(2)}(k_1 |\bar{\rho} - \bar{\rho}'|) \quad (7)$$

$$G_s(\bar{\rho}, \bar{\rho}') = \sum_{l=0}^{\infty} S_l^{(1)}(\rho, \rho') \cos [l(\phi - \phi')] \quad (8)$$

where

$$S_l^{(1)}(\rho, \rho') = \frac{j}{4} \frac{\epsilon_l B_l}{A_l} J_l(k_1 \rho) J_l(k_1 \rho') \quad (9)$$

$$A_l = J_l(k_1 a) H_{l+1}^{(2)}(k_0 a) - (k_1/k_0) J_{l+1}(k_1 a) H_l^{(2)}(k_0 a) \quad (10)$$

$$B_l = H_l^{(2)}(k_1 a) H_{l+1}^{(2)}(k_0 a) - (k_1/k_0) H_{l+1}^{(2)}(k_1 a) H_l^{(2)}(k_0 a) \quad (11)$$

$J_l(z)$ is the Bessel function of the first kind of order l and $H_l^{(2)}(z)$ is the Hankel function of the second kind of order l . The neumann number ϵ_l is defined as one when $l = 0$ and zero when $l \neq 0$.

4.2 Case 2: $\rho, \rho' > a$

When both the source and observation points lie outside the dielectric circular cylinder (i.e., $\rho, \rho' > a$), the components of the Green's function are given by

$$G_0(\bar{\rho}, \bar{\rho}') = -\frac{j}{4} H_0^{(2)}(k_0 |\bar{\rho} - \bar{\rho}'|) \quad (12)$$

$$G_s(\bar{\rho}, \bar{\rho}') = \sum_{l=0}^{\infty} S_l^{(2)}(\rho, \rho') \cos [l(\phi - \phi')] \quad (13)$$

where

$$S_l^{(2)}(\rho, \rho') = \frac{j}{4} \frac{\epsilon_l C_l}{A_l} H_l^{(2)}(k_0 \rho) H_l^{(2)}(k_0 \rho') \quad (14)$$

$$C_l = J_l(k_1 a) J_{l+1}(k_0 a) - (k_1/k_0) J_{l+1}(k_1 a) J_l(k_0 a) \quad (15)$$

and the other quantities are as previously defined.

4.3 Case 3: $\rho < a < \rho'$ or $\rho' < a < \rho$

When the source and observation points lie in different regions (i.e., one inside and the other outside the dielectric cylinder), the components of the Green's function are given by

$$G_0(\bar{\rho}, \bar{\rho}') = 0 \quad (16)$$

$$G_s(\bar{\rho}, \bar{\rho}') = \sum_{l=0}^{\infty} S_l^{(3)}(\rho, \rho') \cos[l(\phi - \phi')] \quad (17)$$

where

$$S_l^{(3)}(\rho, \rho') = \frac{1}{2\pi} \frac{\epsilon_l}{A_l} J_l(k_1 \rho_{<}) H_l^{(2)}(k_0 \rho_{>}) \quad (18)$$

$$\rho_{<} = \min(\rho, \rho') \quad (19)$$

$$\rho_{>} = \max(\rho, \rho') \quad (20)$$

and the other quantities are as previously defined.

Equations 6, 7, 8, 12, 13, 16, and 17 specify the Green's function for an arbitrary pair of source and observation point locations in the presence of a homogeneous dielectric circular cylinder. The Green's function can now be used to formulate an integral equation for the case of the perturbed cylinder.

5 Integral Equation

Let us denote the total \hat{z} -directed electric field as the sum of generalized incident field E_z^{gi} and scattered field E_z^s components,

$$E_z(\bar{\rho}) = E_z^{gi}(\bar{\rho}) + E_z^s(\bar{\rho}) \quad (21)$$

where the generalized incident field is that field which would exist in the presence of the unperturbed cylinder. Invoking the volume equivalence principle [1], we may replace the perturbed geometry with the unperturbed cylinder along with an equivalent \hat{z} -directed electric current density $J_z(\bar{\rho})$. $J_z(\bar{\rho})$ is related to the total electric field by

$$J_z(\bar{\rho}) = j\omega\epsilon_0 [\epsilon(\bar{\rho}) - \tilde{\epsilon}(\bar{\rho})] E_z(\bar{\rho}) \quad (22)$$

where $\epsilon(\bar{\rho})$ is the relative permittivity of the perturbed geometry and $\tilde{\epsilon}(\bar{\rho})$ is the relative permittivity of the unperturbed geometry. Note that J_z is nonzero only within the region $\Omega_p \cup \Omega_i$. The equivalent currents radiate the scattered field via the radiation integral

$$E_z^s(\bar{\rho}) = L(J_z) = -j\omega\mu_0 \iint_{\Omega_p \cup \Omega_i} J_z(\bar{\rho}') G(\bar{\rho}, \bar{\rho}') d\bar{\rho}' \quad (23)$$

where $G(\bar{\rho}, \bar{\rho}')$ is the Green's function of Equation (6).

Combining Equations (21), (22), and (23), we may write the integral equation

$$E_z^{gi}(\bar{\rho}) = \frac{J_z(\bar{\rho})}{j\omega\epsilon_0 [\epsilon(\bar{\rho}) - \tilde{\epsilon}(\bar{\rho})]} - L(J_z) \quad (24)$$

6 Moment Method Solution

Let us approximate the unknown current density $J_z(\bar{\rho})$ using a pulse basis expansion,

$$J_z(\bar{\rho}) \approx \sum_{n=1}^N c_n P_n(\bar{\rho}) \quad (25)$$

where

$$P_n(\bar{\rho}) = \begin{cases} 1, & \bar{\rho} \in \Omega_n \\ 0, & \bar{\rho} \notin \Omega_n \end{cases} \quad (26)$$

and the non-overlapping set $\{\Omega_n\}_{n=1}^N$ spans $\Omega_p \cup \Omega_i$. We will further assume that $\epsilon(\bar{\rho})$ is constant over each Ω_n . Since $J_z(\bar{\rho})$ is assumed constant over each Ω_n , these regions should be chosen to be reasonably small and squarish [5]. A good rule of thumb is that no linear dimension of Ω_n should exceed $\lambda/15$.

If we plug our expansion for $J_z(\bar{\rho})$ into the integral equation (24) and enforce it at the center of each pulse, we generate an N -by- N linear system of equations,

$$E_z^{gi}(\bar{\rho}_m) \approx \sum_{n=1}^N c_n \left[\frac{P_n(\bar{\rho}_m)}{j\omega\epsilon_0 \Delta\epsilon_m} - L_m(P_n) \right] \quad (27)$$

valid for $m = 1 \dots N$ where

$$\Delta\epsilon_m = \epsilon(\bar{\rho}_m) - \tilde{\epsilon}(\bar{\rho}_m) \quad (28)$$

$$L_m(P_n) = L(P_n)|_{\bar{\rho}=\bar{\rho}_m} \quad (29)$$

Due to the sifting property of the pulse bases, the first term in brackets of Equation (27) is only active when $m = n$; that is, $P_n(\bar{\rho}_m) = \delta_{mn}$ where δ_{mn} is

the Kronecker delta. Equation (27) can be expressed in matrix form as

$$\begin{bmatrix} E_z^{gi}(\bar{\rho}_1) \\ \vdots \\ E_z^{gi}(\bar{\rho}_N) \end{bmatrix} \approx \begin{bmatrix} Z_{11} & \cdots & Z_{1N} \\ \vdots & \ddots & \vdots \\ Z_{N1} & \cdots & Z_{NN} \end{bmatrix} \begin{bmatrix} c_1 \\ \vdots \\ c_N \end{bmatrix} \quad (30)$$

where

$$Z_{mn} = \frac{\delta_{mn}}{j\omega\epsilon_0\Delta\epsilon_m} - L_m(P_n) \quad (31)$$

for $m, n = 1 \dots N$.

6.1 The Generalized Incident Field

Let the generalized incident field $E_z^{gi}(\bar{\rho})$ be caused by an electric line source of unit strength at $\bar{\rho}^i$. Thus,

$$E_z^{gi}(\bar{\rho}) = -jk_0\eta_0 G(\bar{\rho}, \bar{\rho}^i) \quad (32)$$

where $\eta_0 = \sqrt{\mu_0/\epsilon_0}$ is the impedance of free space. As $\rho^i \rightarrow \infty$, $E_z^{gi}(\bar{\rho})$ becomes indistinguishable from the excitation of a uniform plane-wave incident from the ϕ^i direction. Using the large-argument asymptotic form of the Hankel function [3] in the Green's functions of sections 4.2 and 4.3, we find, for $\rho < a$,

$$\begin{aligned} E_z^{gi}(\bar{\rho}) \approx & \frac{\eta_0}{2\pi} \sqrt{\frac{2k_0}{j\pi\rho^i}} e^{-jk_0\rho^i} \times \\ & \sum_{l=0}^{\infty} \frac{\epsilon_l}{A_l} j^l J_l(k_0\rho) \cos[l(\phi - \phi^i)] \end{aligned} \quad (33)$$

and for $\rho > a$,

$$\begin{aligned} E_z^{gi}(\bar{\rho}) \approx & \frac{-j\eta_0}{4} \sqrt{\frac{2k_0}{j\pi\rho^i}} e^{-jk_0\rho^i} \left\{ e^{jk_0\rho \cos(\phi - \phi^i)} - \right. \\ & \left. - \sum_{l=0}^{\infty} \frac{\epsilon_l C_l}{A_l} j^l H_l^{(2)}(k_0\rho) \cos[l(\phi - \phi^i)] \right\} \end{aligned} \quad (34)$$

6.2 The Scattered Field

Once the generalized incident field at the match points have been calculated and the elements of the $[Z]$ matrix have been found, then Equation (30) can be solved for the coefficients c_n . The scattered field at observation point $\bar{\rho}^o$ is then the sum of the fields radiated by the currents J_z and the field scattered by the unperturbed dielectric circular cylinder. Letting $\rho^o \rightarrow \infty$, we find

$$\begin{aligned} E_z^s(\bar{\rho}^o) \approx & -jk_0\eta_0 \left\{ G_s(\bar{\rho}^o, \bar{\rho}^i) + \right. \\ & \left. + \sum_{n=1}^N c_n \int_{\Omega_n} G(\bar{\rho}^o, \bar{\rho}') d\bar{\rho}' \right\} \end{aligned} \quad (35)$$

Notice that we have purposely omitted the direct radiation from the source to the observation point. If we further assume that the far-field radiation of the scattering currents can be approximated by the far-field radiation of appropriately weighted line sources located at the match points, then we can write

$$\begin{aligned} E_z^s(\bar{\rho}^o) \approx & -jk_0\eta_0 \left\{ G_s(\bar{\rho}^o, \bar{\rho}^i) + \right. \\ & \left. + \sum_{n=1}^N c_n (\text{Area}_n) G(\bar{\rho}^o, \bar{\rho}_n) \right\} \end{aligned} \quad (36)$$

where (Area_n) is the area of the n -th pulse basis function. The echo width of the perturbed cylinder is defined to be [2]

$$L_e = \lim_{\rho \rightarrow \infty} 2\pi\rho \left| \frac{E_z^s(\bar{\rho})}{E_z^i(\bar{0})} \right|^2 \quad (37)$$

where $E_z^i(\bar{0})$ is the incident field at the origin produced by the line source at $\bar{\rho}^i$ radiating in free space. If we let the source and observer recede to infinity at the same rate ($\rho^i = \rho^o = \rho \rightarrow \infty$), then we can combine Equations (36) and (37) to write

$$\begin{aligned} L_e(\phi^i, \phi^o) \approx & \lim_{\rho \rightarrow \infty} 2\pi\rho \left| \frac{G_s(\bar{\rho}, \bar{\rho}^i)}{E_z^i(\bar{0})} + \right. \\ & \left. + \frac{\sum_{n=1}^N c_n (\text{Area}_n) G(\bar{\rho}, \bar{\rho}_n)}{E_z^i(\bar{0})} \right|^2 \end{aligned} \quad (38)$$

Equation (38) represents the bistatic echo width of a perturbed dielectric circular cylinder. If $\phi^i = \phi^o$, then Equation (38) gives the monostatic echo width.

7 Results

The hybrid GF/MM technique was tested against a standard surface integral equation MM (SIE MM) program for bistatic echo width predictions. The SIE MM program expands electric and magnetic surface currents along the perimeter of the homogeneous dielectric scatterer, using pulse basis functions and Galerkin testing. Each program was written in FORTRAN and executed on a Sun SPARCStation 2. Three perturbation geometries were chosen, each based on a dielectric circular cylinder having radius $a/\lambda_0 = 0.5$ and relative permittivity $\epsilon_c = 2.0$. The bistatic echo width for the unperturbed geometry is shown in Figure 2, in units of dB relative to one free-space wavelength.

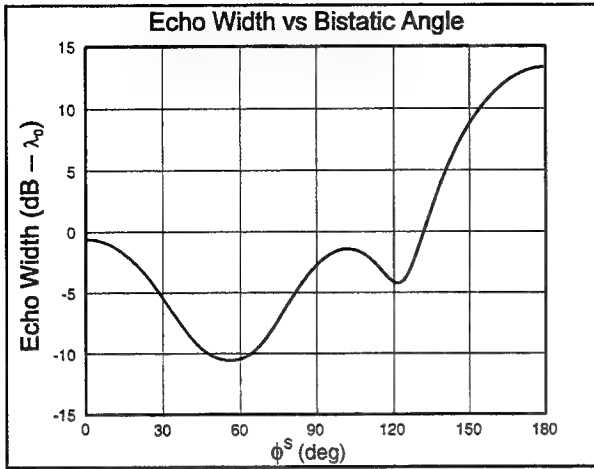


Figure 2: Bistatic Echo Width for Unperturbed Geometry: $a/\lambda_0 = 0.5$, $\epsilon_c = 2.0$

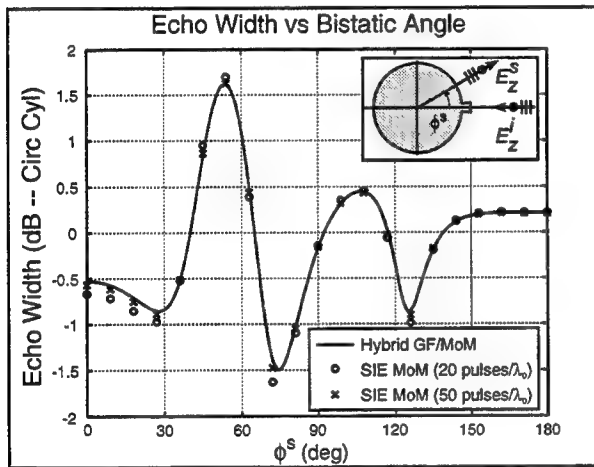


Figure 3: Bistatic Echo Width for Geometry #1: $a/\lambda_0 = 0.5$, $\epsilon_c = 2.0$, $\Omega_p = \{\bar{\rho} : 0.5 < \rho/\lambda_0 < 0.6$, $-5^\circ < \phi < 5^\circ\}$.

The first perturbed geometry consists of a single protrusion on the right side of the dielectric circular cylinder, as shown in the inset of Figure 3. The protrusion extends from $\rho/\lambda_0 = 0.5$ to 0.6, and from $\phi = -5^\circ$ to 5° . The protrusion material has relative permittivity $\epsilon_p = 2.0$, so that the perturbed dielectric cylinder is homogeneous. Figure 3 shows the bistatic echo width for $\phi^i = 0^\circ$ and ϕ^s from 0° to 180° . The bistatic echo width is plotted in units of dB relative to the bistatic echo width of the corresponding unperturbed dielectric circular cylinder (Figure 2). The results show that the SIE

Table 1: Computer Usage Summary

| Geometry | Hybrid GF/MM | | SIE MM | | |
|----------|--------------|------------|------------------------|-----|------------|
| | N | Time (sec) | Pulses per λ_0 | N | Time (sec) |
| 1 | 4 | 0.6 | 20 | 138 | 4.8 |
| | | | 50 | 340 | 47.9 |
| 2 | 8 | 1.9 | 20 | 148 | 5.5 |
| | | | 50 | 364 | 58.1 |
| 3 | 3 | 0.4 | 20 | 154 | 6.3 |
| | | | 50 | 376 | 63.7 |

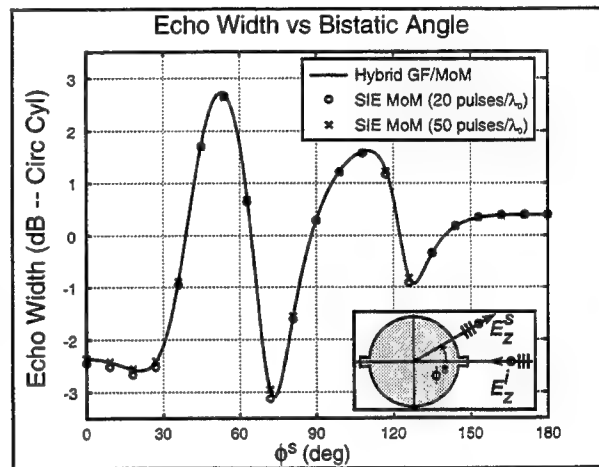


Figure 4: Bistatic Echo Width for Geometry #2: $a\lambda_0 = 0.5$, $\epsilon_c = 2.0$, $\Omega_p = \{\bar{\rho} : 0.5 < \rho/\lambda_0 < 0.6$, $-5^\circ < \phi < 5^\circ, 175^\circ < \phi < 185^\circ\}$.

MM formulation requires 50 pulses per wavelength to achieve the accuracy of the hybrid GF/MM formulation with only 4 total unknowns. Table 1 shows that the hybrid GF/MM program executes nearly 80 times faster than the SIE MM program for this geometry.

The second perturbed geometry is similar to the first geometry, except that a second, identically-shaped protrusion is added to the left side of the circular cylinder. Figure 4 shows excellent agreement between the hybrid GF/MM and SIE MM formulations. As with the first geometry, the GF/MM program with 8 total unknowns gives nearly identical echo width predictions as the SIE MM program with over 300 unknowns. Table 1 shows that the hybrid GF/MM program executes nearly 30 times faster than the SIE MM program for this geometry.

The third perturbed geometry consists of a sin-

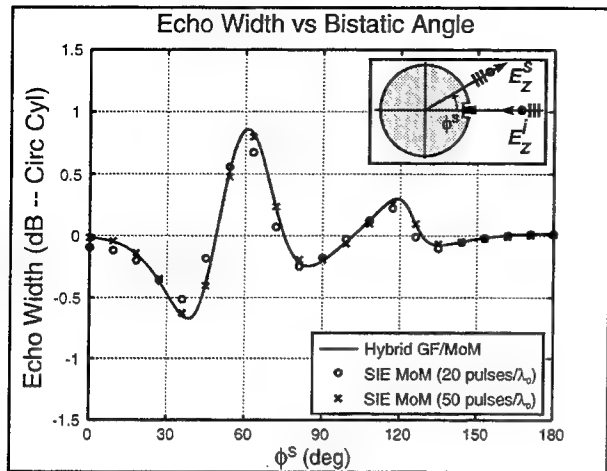


Figure 5: Bistatic Echo Width for Geometry #3: $a/\lambda_0 = 0.5$, $\epsilon_c = 2.0$, $\Omega_p = \{\bar{\rho} : 0.5 < \rho/\lambda_0 < 0.567, -3.3^\circ < \phi < 3.3^\circ\}$, $\Omega_i = \{\bar{\rho} : 0.433 < \rho/\lambda_0 < 0.5, 3.3^\circ < |\phi| < 10^\circ\}$.

ngle protrusion sandwiched between two identical inclusions. The protrusion occupies the region $0.5 < \rho/\lambda_0 < 0.567$ and $-3.3^\circ < \phi < 3.3^\circ$, and is filled with a dielectric having relative permittivity $\epsilon_p = \epsilon_c = 2.0$. The top and bottom inclusions occupy the regions $0.433 < \rho/\lambda_0 < 0.5$ and $3.3^\circ < |\phi| < 10^\circ$. Both inclusions are unfilled; that is, $\epsilon_i = 1$. As shown in Figure 5, the hybrid GF/MM formulation with 3 unknowns gives nearly identical echo width predictions as the SIE MM formulation with over 350 unknowns. The time savings reaped by the hybrid GF/MM formulation relative to the SIE MM formulation exceeds 100.

8 Conclusions

This paper has presented a technique (the hybrid GF/MM) to increase the efficiency of the method of moments when calculating the scattering properties of geometries that are sufficiently “close” to a canonical geometry. The technique was developed in detail for the case of a homogeneous dielectric cylinder, although the technique may be applied to any penetrable geometry for which the Green’s function can be found. Excellent agreement was shown between the hybrid GF/MM and standard MM formulations, and considerable savings in computer requirements were reported.

9 Acknowledgments

The author expresses his appreciation to Maj J. Paul Skinner for his expert guidance and insight in the development of the hybrid GF/MM technique.

References

- [1] Balanis, Constantine A. *Advanced Engineering Electromagnetics*. John Wiley, New York, 1989.
- [2] Harrington, Roger F. *Time-Harmonic Electromagnetic Fields*. McGraw-Hill, New York, 1961.
- [3] M. Abramowitz and I. Stegun, editor. *Handbook of Mathematical Functions*. Number 55 in Applied Mathematics Series. U.S. Government Printing Office, Washington, D.C., 1972.
- [4] Newman, E.H. An Overview of the Hybrid MM/Green’s Function Method in Electromagnetics. *Proceedings of the IEEE*, 76(3):270–282, March 1988.
- [5] Richmond, Jack H. Wave Scattering by a Dielectric Cylinder of Arbitrary Cross-Section Shape. *IEEE Transactions on Antennas and Propagation*, AP-13:334–342, May 1965.
- [6] Ruck, G.T. et al. *Radar Cross Section Handbook*, volume 2. Plenum, 1970.
- [7] Stratton, Julius A. *Electromagnetic Theory*. McGraw-Hill, New York, 1941.

A Low-Frequency Formulation of the Method of Moments via Surface Charges

Nunzio Esposito, Antonino Musolino, Marco Raugi

Dipartimento di Sistemi Elettrici e Automazione, Università di Pisa, Via Diotisalvi 2, 56126 Pisa.

Abstract-In this paper a formulation of the method of moments for the analysis of low frequency problems is presented.

In the considered frequency range, the integral solution of Maxwell equations in terms of magnetic vector potential and electric scalar potential respectively function of currents and charges is obtained imposing the Coulomb gauge.

By combining Gauss law and current continuity at the boundaries among regions with different conductivity a first set of equations is obtained. Writing Ohm's law inside the conductive regions another integral equation set that allows the determination of the conduction current and surface charges unknowns is obtained. The method of moments is then applied to this system of equations.

The use of pulse functions as subsectional bases allows a quick matrix set up especially when regular volume shapes are selected. Calculated results are compared with results obtained with other methods relating to benchmark problems.

I. INTRODUCTION

Time and frequency domain formulations of the method of moments [1], have been widely used for the analysis of the electromagnetic scattering by arbitrary shaped perfectly conducting bodies excited by electromagnetic pulses and incident waves [2], [3].

The proposed techniques, using different patches for the body modeling, have been proved to be simple and useful procedures to solve those problems handling open and closed curved structures of finite extent [4], [5].

In this paper, we investigate the extension of the method in the low frequency range. In this case, some basic features of the theoretical basis of the high frequency formulations of the method cannot be assumed:

- Considering finite conductivity, we cannot use the equation set usually given by enforcing the tangential component of the electric field equal to zero at the surface of the conductive bodies.
- Considering Coulomb gauge together with the hypothesis of $\text{div } \mathbf{J} = 0$ in the conductive volume we cannot use the direct relation between vector and scalar potentials, usually given by the Lorentz gauge.

Therefore, in order to obtain a system of volume integral equations in the conduction current unknowns, we have to take into account different equations in the considered frequency range. A first set of equation in terms of scalar and vector potential is obtained considering, in presence of finite conductivity, Ohm's law and the electric field definition inside the conductive volumes. The scalar potential is given by the surface free charge distribution at

the boundaries among media with different conductivity. Then, an equation set relating surface charges and volume currents has to be obtained. The relation among charges and currents is determined considering Gauss law and current density continuity at these boundaries. Time and frequency formulations can be adopted depending on the transient or steady state analysis to be performed. Of course, as in the high frequency range, the numerical efficiency of the presented procedure in terms of computational costs and accuracy of the results is influenced by the original domain approximation and by the shape function that can be adopted.

II. FORMULATION

We consider a massive conductor Ω with boundary Γ taking into account the presence of an external lumped parameter circuit as shown in fig. 1.

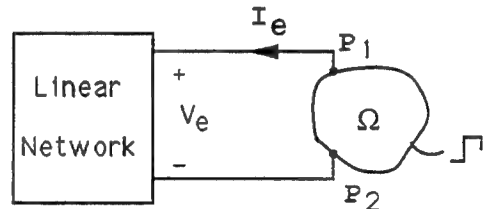


Fig. 1 Considered system

Combining the definition of the electric field $E(r,t)$ and Ohm's law we have:

$$E = -\frac{\partial A}{\partial t} - \nabla \Phi = \frac{J}{\sigma} \quad (1)$$

we consider the magnetic vector potential A expression:

$$A(r,t) = \frac{\mu_0}{4\pi} \iiint_{\Omega} \frac{J(r',t)}{|r-r'|} d\Omega \quad (2)$$

The scalar potential Φ is given by:

$$\Phi(r,t) = \frac{1}{4\pi\epsilon_0} \iint_{\Gamma} \frac{\rho_{\Gamma}(r',t)}{|r-r'|} d\Gamma \quad (3)$$

where $\rho_{\Gamma}(r',t)$ is the surface free charge distribution at the boundary Γ . Substituting (2) and (3) in (1) we have:

$$\begin{aligned} J(r,t) = & -\frac{\mu_0}{4\pi} \iiint_{\Omega} \frac{\partial J(r',t')}{\partial t} \frac{1}{|r-r'|} d\Omega + \\ & -\frac{1}{4\pi\epsilon_0} \nabla \iint_{\Gamma} \frac{\rho_{\Gamma}(r',t)}{|r-r'|} d\Gamma \end{aligned} \quad (4)$$

Equation (4) has to be evaluated for the three components x, y, z in space. In order to determine an expression that relates surface charges and conduction current we combine Gauss law, current density continuity and Ohm's law at the surface Γ :

$$\begin{aligned} \operatorname{div}_{\Sigma} E &= E_n^+ - E_n^- = \frac{\rho_{\Gamma}}{\epsilon_0}; \\ \operatorname{div}_{\Sigma} J &= -J_n^- = -\frac{\partial \rho_{\Gamma}}{\partial r}; \quad J_n^- = \sigma E_n^-; \end{aligned} \quad (5)$$

where the subscript n denotes the normal component, the superscripts + and - denote the outside and inside limit values with respect to the surface Γ and $\operatorname{div}_{\Sigma}$ is the surface divergence. Combining these equations we obtain:

$$\begin{aligned} \frac{1}{\sigma} \frac{\partial \rho_{\Gamma}}{\partial r} + \frac{\rho_{\Gamma}}{\epsilon_0} &= E_n^+ = -\frac{\mu_0}{4\pi} \iiint_{\Omega} \frac{\partial J(r', t')}{\partial r} \frac{1}{|r^+ - r'|} d\Omega - \\ &- \frac{1}{4\pi\epsilon_0} \nabla \iint_{\Gamma} \frac{\rho_{\Gamma}(r', t)}{|r^+ - r'|} d\Gamma \end{aligned} \quad (6)$$

The current $J(r, t)$ and the surface charges $\rho_{\Gamma}(r, t)$ can be approximated as:

$$J(r, t) = \sum_{n=1}^N I_n(t) f_n(r) \quad (7)$$

$$\rho(r, t) = \sum_{n=1}^M \rho_n(t) g_n(r) \quad (8)$$

where $f_n(r)$ and $g_n(r)$ are the n -th component of the selected vector basis function representing the spatial variation of the two quantities, $I_n(t)$ and $\rho_n(t)$ are their time-varying unknown coefficients. Then, we obtain:

$$\begin{aligned} \frac{\sum_{n=1}^N I_n(t) f_n(r)}{\sigma} &= -\frac{\mu_0}{4\pi} \sum_{n=1}^N \frac{\partial I_n(t)}{\partial r} \iiint_{\Omega} \frac{f_n(r')}{|r - r'|} d\Omega - \\ &- \sum_{n=1}^M \frac{\rho_n(t)}{4\pi\epsilon_0} \iint_{\Gamma} g_n(r') \nabla \frac{1}{|r - r'|} d\Gamma \end{aligned} \quad (9)$$

$$\begin{aligned} \sum_{n=1}^M g_n(r^+) \left[\frac{\partial \rho_n(t)}{\sigma \partial r} + \frac{\rho_n(t)}{\epsilon_0} \right] &= \\ &= -\frac{\mu_0}{4\pi} \sum_{n=1}^N \frac{\partial I_n(t)}{\partial r} \iiint_{\Omega} \frac{f_n(r')}{|r^+ - r'|} d\Omega + \\ &- \frac{1}{4\pi\epsilon_0} \sum_{n=1}^M \rho_n(t) \iint_{\Gamma} g_n(r') \nabla \frac{1}{|r^+ - r'|} d\Gamma \end{aligned} \quad (10)$$

The presence of the external lumped parameter circuit is taken into account considering that at points P_1 and P_2 we have:

$$I_e - \iint_S J_n^- dS = - \iint_S \frac{\partial \rho_{\Gamma}}{\partial t} dS; \quad (11)$$

where S is the area of the surface elements at P_1 and P_2 . Writing the nodal or mesh equations of the linear lumped parameters network we have:

$$I_e(t) = G(t) + YV_e(t) \quad (12a)$$

$$\begin{aligned} V_e(t) &= \Phi(P_1, t) - \Phi(P_2, t) = \\ &= \frac{1}{4\pi\epsilon_0} \iint_{\Gamma} \frac{\rho_{\Gamma}(r', t)}{|P_1 - r'|} - \frac{\rho_{\Gamma}(r', t)}{|P_2 - r'|} d\Gamma \end{aligned} \quad (12b)$$

where $G(t)$ is due to the independent generators and Y is an integral-differential operator due to the impedances of the network.

Imposing (9) at N points in the conductive body Ω , (12a) (12b) and (10) at $M-2$ points on the surface Γ we obtain a system of equations in the $N+M$ unknown coefficients $I_n(t)$ and $\rho_n(t)$ to which the testing procedure (point matching, Galerkin etc.) is applied.

Approximating the time differentiation with finite difference equations (9) (10) (12a) and (12b) directly represent the time domain formulation of the proposed procedure. The frequency domain formulation can be easily derived replacing the time differentiation with the $j\omega$ operator and assuming the $e^{j\omega t}$ dependence of the unknown quantities, obtaining the algebraic complex system:

$$\begin{aligned} \sum_{n=1}^N I_n \left[\frac{f_n(r)}{\sigma} + \frac{j\omega\mu_0}{4\pi} \iiint_{\Omega} \frac{f_n(r')}{|r - r'|} d\Omega \right] &= \\ &- \sum_{n=1}^M \frac{\rho_n}{4\pi\epsilon_0} \iint_{\Gamma} g_n(r') \nabla \frac{1}{|r - r'|} d\Gamma \end{aligned} \quad (13)$$

$$\begin{aligned} \sum_{n=1}^M \rho_n \left[g_n(r^+) \left(\frac{j\omega}{\sigma} + \frac{1}{\epsilon_0} \right) + \frac{1}{4\pi\epsilon_0} \iint_{\Gamma} g_n(r') \nabla \frac{1}{|r^+ - r'|} d\Gamma \right] &= \\ &- \frac{j\omega\mu_0}{4\pi} \sum_{n=1}^N I_n \iiint_{\Omega} \frac{f_n(r')}{|r^+ - r'|} d\Omega \end{aligned} \quad (14)$$

III. BASIS FUNCTIONS

We define the following coefficients:

$$\begin{aligned} \iiint_{\Omega} \frac{f_n(r')}{|r - r'|} d\Omega &= \alpha_n(r); \quad g_n(r^+) = g_n; \\ \iint_{\Gamma} g_n(r') \nabla \frac{1}{|r - r'|} d\Gamma &= - \iint_{\Gamma} \frac{g_n(r')}{|r - r'|^2} d\Gamma = \beta_n(r); \end{aligned} \quad (15)$$

Then, considering for example subsectional bases [1] for N elementary volumes in the domain Ω and M elementary surfaces on the boundary Γ and writing (9) and (10) in the k -th elementary volume and surface (referring for example to the frequency domain formulation) we obtain:

Finite Elements methods.

$$I_k \frac{f_k(r_k)}{\sigma} + \frac{j\omega\mu_0}{4\pi} \sum_{n=1}^N I_n \alpha_n(r_k) = - \sum_{n=1}^M \frac{\rho_n}{4\pi\epsilon_0} \beta_n(r_k) \quad (16)$$

$$\begin{aligned} \rho_k g_k \left(\frac{j\omega}{\sigma} + \frac{1}{\epsilon_0} \right) + \frac{1}{4\pi\epsilon_0} \sum_{n=1}^M \rho_n \beta_n(r^+) = \\ = - \frac{j\omega\mu_0}{4\pi} \sum_{n=1}^N I_n \alpha_n(r^+) \end{aligned} \quad (17)$$

$$I_e = G + Y(\omega)V_e \quad (18a)$$

$$V_e = \Phi(P_1) - \Phi(P_2) = \frac{1}{4\pi\epsilon_0} \sum_{n=1}^M \rho_n (\beta_n(P_1) - \beta_n(P_2)) \quad (18b)$$

Considering good conductors at low frequencies we can consider $1/\epsilon_0$ much greater than $j\omega/\sigma$, then (14) becomes:

$$\frac{\rho_k g_k}{\epsilon_0} + \frac{1}{4\pi\epsilon_0} \sum_{n=1}^M \rho_n \beta_n(r^+) = - \frac{j\omega\mu_0}{4\pi} \sum_{n=1}^N I_n \alpha_n(r^+) \quad (19)$$

Writing (16) in every elementary volume, (19) on the surface and equations (18) we derive the matrix forms:

$$\underline{\underline{A}}\underline{\underline{I}} + \underline{\underline{B}}\underline{\underline{\rho}} = 0$$

$$\underline{\underline{D}}\underline{\underline{I}} + \underline{\underline{E}}\underline{\underline{\rho}} = \underline{\underline{V}}$$

These systems can be used in order to have an unknown set only, currents or charges.

Analogously, in the time domain equations, $\rho\sigma/\epsilon_0$ can be considered much greater than $\partial\rho/\partial t$. Therefore, we can use (10) to express the charges as a function of currents, obtaining an expression in the current unknowns only.

The accuracy of the presented procedure and the computational cost of the matrix set up is determined by the coefficients (15). As for the high frequency problems, several kinds of basis function and patches can be proposed, and an exhaustive analysis of their numerical characteristics in several kinds of applications is not easy to be determined.

We begin implementing pulse functions as subsectional bases in order to have a quick matrix set-up. In fact, when Ω_n have particular shapes, such as parallelepipeds or cylinder sectors, the evaluation of the surface and volume integrals in (14) can be quickly and accurately obtained by means of analytical expressions [6], [7]. This choice causes the presence of fictitious surface charges at the boundary among adjacent elementary volume elements, since adjacent currents have different values as shown in fig. 2.

Nevertheless, the evaluation of integral quantities in the examined low frequency benchmark problem, has shown a good agreement between our results and results obtained with other numerical methods. Furthermore, the computational times were analogous to those obtained with

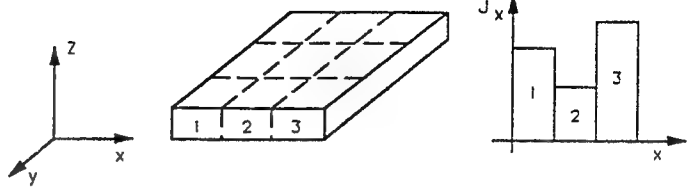


Fig. 2 Pulse function decomposition of a plate

IV. RESULTS

In order to test the frequency domain formulation of the method, we analyse the TEAM problem 3 [8] (Bath plate with two holes) which geometry, shown in fig. 3, consists of a conducting ladder having two holes with a current coil above. The conductivity of the ladder is $\sigma = 0.3278c8$ (S/m), and the driving field originates in the coil. The coil carries a current equivalent to 1260 Amp turns at 50 and 200 Hz, and it is placed at two positions. Position 1 is directly above the center of the ladder, position 2 is directly above the center of one of the holes.

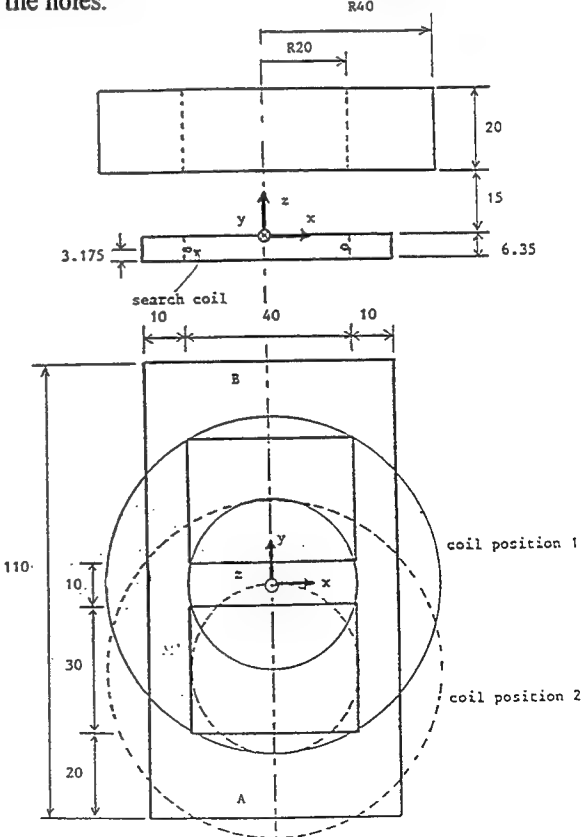


Fig. 3 Geometry of the frequency domain problem.

We calculate the magnitude and phase of the field normal to the ladder for the coil position 2, frequency of 50Hz, along a center line of the geometry 0.5 mm above the conducting ladder between +55mm and -55mm. The calculated data have been obtained considering the decomposition shown in Fig. 4. We adopted parallelepiped volumes and rectangular surfaces as subsectional bases.

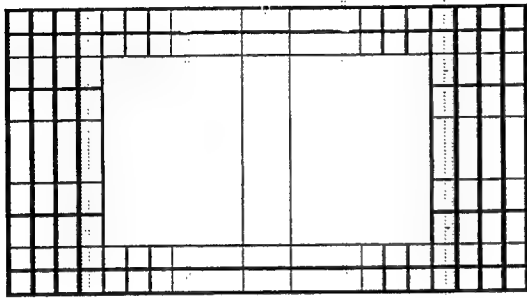


Fig. 4 Decomposition of the geometry.

Fig. 5 shows a good agreement between calculated results obtained with the proposed method and experimental data.

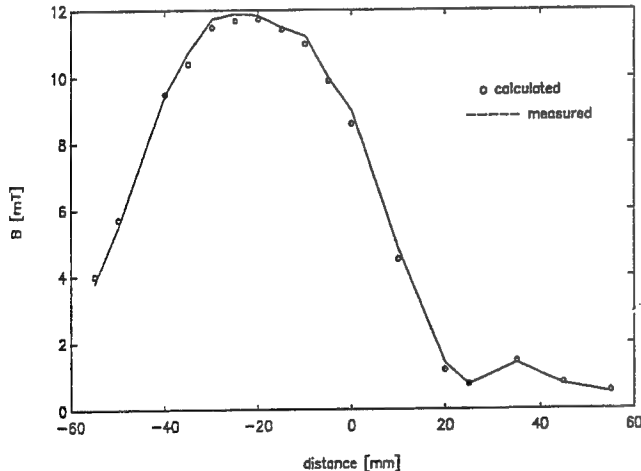


Fig. 5 Comparison between calculated and experimental data of B along the center line

The table I and II report the current in the lateral limbs for positions 1 and 2 for $f=50$ Hz and $f=200$ Hz respectively.

Table I

| | Position 1 | | Position 2 | |
|---------------|-------------|--------|------------|--------|
| | Ia = Ib [A] | Ia [A] | Ib [A] | Ib [A] |
| Kameari [10] | 68.05 | 81.68 | 38.45 | |
| Takahashi [9] | 71.63 | 85.41 | 41.23 | |
| M.O.M. | 69.6 | 82.61 | 40.42 | |

Table II

| | Position 1 | Position 2 | |
|---------------|-------------|------------|--------|
| | Ia = Ib [A] | Ia [A] | Ib [A] |
| Kameari [10] | 153.89 | 190.48 | 80.14 |
| Takahashi [9] | 155.89 | 191.52 | 83.12 |
| M.O.M. | 154.91 | 192.55 | 82.95 |

The time domain formulation has been tested considering a problem [10] where a uniform magnetic field in the Z direction, having a constant rate $B' = 1$ T/sec, is applied to a square plate (20cm x 20cm) with thickness 1cm shown in fig. 6. The resistivity of the plate is $2\mu\Omega\text{cm}$.

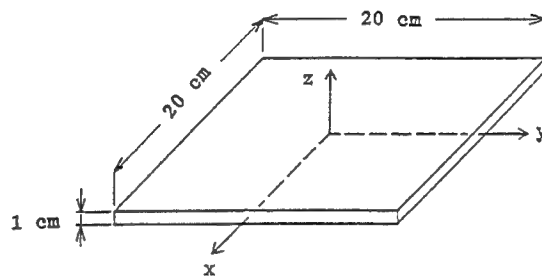


Fig. 6 Geometry of the time domain problem

The square plate has been decomposed by means of elements having different size as shown in Fig. 7.

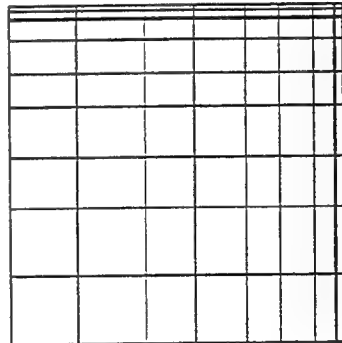


Fig. 7 Decomposition of the geometry.

The figures 8 and 9 show the current density J_y at $t=10$ msec and, varying the x -coordinate, at $y=1\text{cm}$ and $y=x$. The figures show a good agreement among the calculated data by a Finite Element method [10] and the proposed M.O.M. formulation.

The larger disagreement is obtained near the external surface of the plate, where the method [10] forces $J_n=0$, while the proposed formulation gives the average value in the parallelepiped nearby the corner. In the considered low frequency tests we considered point matching and Galerkin

testing procedures, obtaining nearly equal numerical results.

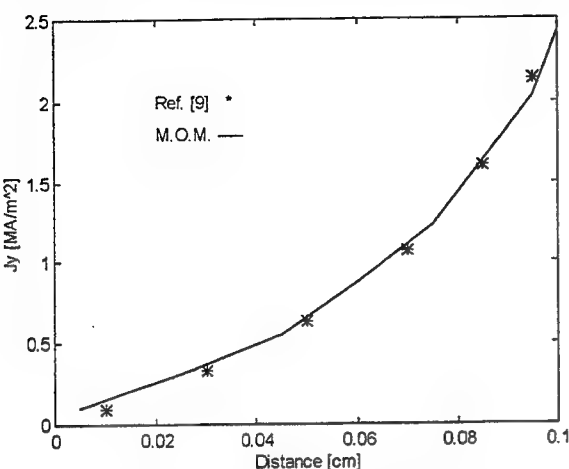


Fig. 8 Eddy current distribution at $t=10\text{msec}$ along the line $y=1\text{cm}$.

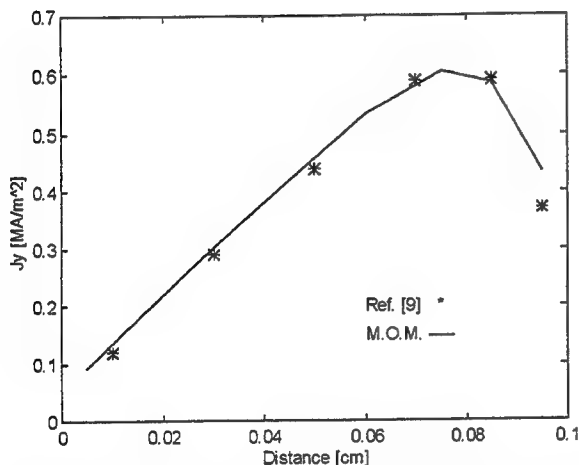


Fig. 9 Eddy current distribution at $t=10\text{msec}$ along the line $y=x$.

V. CONCLUSIONS

Time and frequency domain formulations of the method of moments for the analysis of low frequency problems have been presented.

The two formulations have been tested analysing linear benchmark problems obtaining a good agreement with experimental data and results obtained with other numerical methods.

The use of pulse functions as subsectional basis has allowed a quick matrix set-up with respect to numerical integration.

REFERENCES

- [1] R.F. Harrington: "Field Computation by Method of Moments". New York; Mac Millan, 1968
- [2] C.L. Bennett, L.W. Weeks: "Transient scattering from conducting cylinders", Radi Sci. Vol 16. Nov-Dec 1991
- [3] S.M. Rao, D.R. Wilton: "Transient scattering by conducting surfaces of arbitrary shape IEEE Trans. Antennas and Propag. Vol AP-39 n.1 Jan 1991 pp 56-61
- [4] S.M. Rao, T.K. Sarkar: "An alternative version of the time-domain electric field integral equation for arbitrary shaped conductors" IEEE Trans. Antennas and Propag. Vol AP-41 n.6 June 1993 pp 831-834
- [5] A. Djordjevic, T.K. Sarkar, S.M. Rao, "Analysis of finite conductivity cylindrical conductors excited by axially independent electromagnetic fields" IEEE Trans. M.T.T.Oct.1985 pp 960-966
- [6] B. Azzerboni, E. Cardelli, M. Raugi, A. Tellini, G. Tina: "Analytic expression for magnetic fields from finite curved conductors" IEEE Trans. on Mag. Vol 27 Mar. 1991.
- [7] B. Azzerboni, E. Cardelli, M. Raugi, A. Tellini, G. Tina: "Magnetic fields evaluation for thick annular conductors". IEEE Trans. on Mag., Vol. 29, n. 3 May 1993.
- [8] L.R. Turner et al. " Problems and workshops for eddy current code comparison" IEEE Trans. on Mag. Vol 24 Jan. 1988.
- [9] T. Nakata, N. Takahashi, K. Fujiwara, Y. Okada: " Calculation of Bath plate(Problem 3)" Proceedings of the International workshop for eddy current code comparison, Tokio, 54, 1986.
- [10] A. Kameari " 3-D eddy current calculation using finite element method with A-V in conductor and in vacuum" IEEE Trans. on Mag. Vol 24 Jan. 1988.

A STUDY OF A RECENT, MOMENT-METHOD ALGORITHM THAT IS ACCURATE TO VERY LOW FREQUENCIES

M. Burton and S. Kashyap
Electronic Warfare Division
Defence Research Establishment Ottawa
Ottawa, Ontario, Canada K1A 0Z4

Abstract—We give an alternative description of a recently published moment-method algorithm, which uses divergence-free and rotation-free basis functions to maintain accuracy down to very low frequencies. The basic algorithm is restricted to simply-connected and non-self-intersecting surfaces. But this restriction has little practical impact—we show how multiply-connected surfaces, self-intersecting surfaces, and one-sided surfaces can easily be converted to the required topology without changing the solution. We examine a claim that the impedance matrix is diagonally dominant, which implies a guaranteed-to-converge Jacobi type of iterative solution of the matrix equation. Finally, we show how to control catastrophic-cancellation errors that occasionally appear in the voltage vector.

INTRODUCTION

In moment-method algorithms finite computer memory and CPU time impose a high-frequency limit at about the first or second resonance of the body being tested. Typically, $W/\lambda_{\min} \approx 1$, where W is some representative linear dimension of the body. A popular algorithm for finding the current on arbitrarily shaped conductors was described by Rao, Wilton and Glisson over ten years ago [1]. With this algorithm, a finite computer resource of another kind—word length—sets a *low*-frequency limit. Typically, $W/\lambda_{\max} \approx 10^{-3}$, which limits the usefulness of the algorithm as a tool for studying electrostatic or magnetostatic problems.

Wilton, Lim, and Rao have recently described a new algorithm that has a much smaller low-frequency limit [2,3]. It is very effective and has an appealing structure. We think it deserves wide exposure and, therefore, we present here our own description of it and of the problem that it cures.

The basic algorithm is restricted to surfaces that are simply-connected and not self-intersecting. But this restriction has little practical impact—we show that multiply-connected surfaces, self-intersecting surfaces, and even one-sided surfaces can easily be converted into the required topological form without altering the solutions obtained for them.

The new algorithm also has a feature that may make it superior over the entire moment-method bandwidth. Its impedance matrix is closer to being diagonally dominant than the one from the earlier, Rao-Wilton-Glisson algorithm. This makes the matrix equation more likely to yield to an iterative method of solution. We discuss this possibility.

Finite word-length can occasionally corrupt some of the voltage vector of this new algorithm. We present a simple and effective fix based on the Faraday law.

THE CAUSES OF THE LOWER LIMIT

In the Rao-Wilton-Glisson algorithm a set of “rooftop” functions approximates the \mathbf{J} field on a triangulated surface of the body [1]. There is a rooftop function for each interior edge of the triangulation. The domain of a rooftop is restricted to the pair of faces that share the interior edge. See Figure 1. The definition for the rooftop anchored to the i^{th} interior edge is

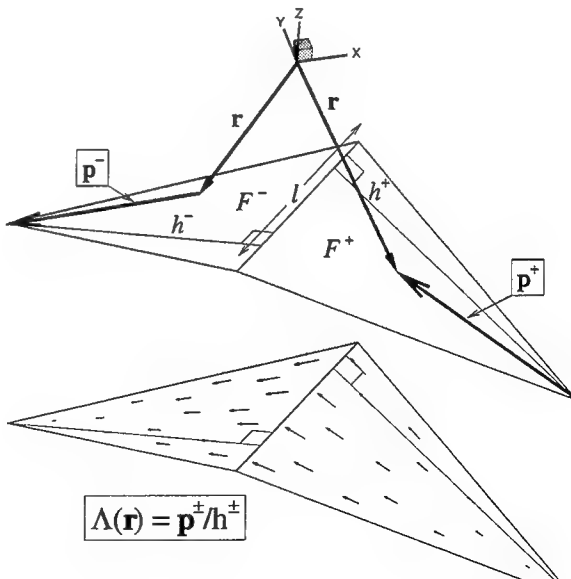


Figure 1 Parameters for defining a rooftop function.

$$\Lambda_i(\mathbf{r}) = \begin{cases} \frac{\mathbf{p}_i^*}{h_i^*}, & \mathbf{r} \in F_i^* \\ 0, & \text{otherwise} \end{cases} \quad (1)$$

where h_i^* is the height of face F_i^* , when measured from the anchor edge to the free vertex; and \mathbf{p}^* is $(\pm 1) \times$ (the vector from the free vertex to \mathbf{r}). The area of face F_i^* is a_i^* . The length of the anchor edge is l_i .

The rooftop function has four nice features: (1) it automatically satisfies Kirchhoff's current law at the anchor edge; (2) there is a charge density of $\rho_i^* = \pm l_i / (-j\omega a_i^*)$ on each face, yet there is no *net* charge deposited—no need to test for conservation of charge on the body; (3) it is simple enough to permit efficient, robust, and accurate computation of the potential integrals [4]; (4) it imposes no restriction on the topology of surface—the surface can be open, closed, simply-connected, disjoint, multiply-connected, one-sided, two-sided, or self-intersecting.

There is a testing integral associated with each rooftop function. Its domain is an *open* path, beginning at the centroid of F^+ and following a streamline of $\Lambda(\mathbf{r})$ across the anchor edge to the centroid of F^- . Figure 2 shows the set of paths from a typical triangulation of a square plate. For each path there is a corresponding equation in the moment-method matrix equation $Zx = b$ stating that the tested scattered field $\int \mathbf{E}_{\text{scat}} \cdot d\mathbf{l}$ is equal to the negative of the tested incident field $-\int \mathbf{E}_{\text{inc}} \cdot d\mathbf{l}$.

But the scattered field is computed in two parts: $\mathbf{E}_{\text{scat}} = -\nabla V(\rho) - j\omega \mathbf{A}(J)$. The first part, $\nabla V(\rho)$, is

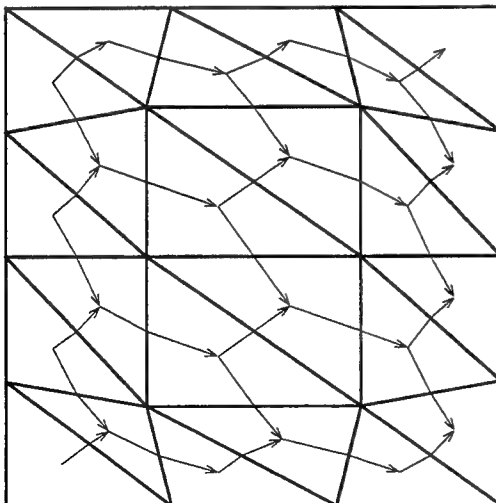


Figure 2 Integration paths for testing a rooftop model of a square plate.

inversely proportional to the frequency, because $\rho_i^* = \pm l_i / (-j\omega a_i^*)$. The second part, $j\omega \mathbf{A}$, is directly proportional to the frequency. So, as the frequency goes lower, the \mathbf{E}_{scat} field becomes more dominated by ∇V and testing integrals of \mathbf{E}_{scat} become more path-independent (because ∇V is a conservative vector field). Ultimately, an integral over any given path in Figure 2 becomes identical to one over any concatenation of other paths having the same endpoints. The corresponding effect on Z is that any row becomes identical to a linear combination of other rows. In other words, as the frequency goes lower, Z becomes more ill-conditioned. Ultimately, it becomes singular.

Increasing condition number is one cause of the poor accuracy at low frequencies. Another cause is the loss of information about $j\omega \mathbf{A}$, due to insufficient word length.

As the frequency goes lower, the two quantities ∇V and $j\omega \mathbf{A}$ become increasingly different in magnitude, yet *their sum is stored in the same word*. The recoverable precision of the smaller quantity, $j\omega \mathbf{A}$, is inversely proportional to the square of the frequency.

But $j\omega \mathbf{A}$ is no less important than ∇V , even at extremely low frequencies. Although all of the paths in Figure 2 are open there are linear combinations of them that form *closed* paths. This implies that there are linear combinations of equations in $Zx = b$ stating that the *closed-path* integral $\oint \mathbf{E}_{\text{scat}} \cdot d\mathbf{l}$ is equal to the *closed-path* integral $-\oint \mathbf{E}_{\text{inc}} \cdot d\mathbf{l}$. But ∇V has no curl (because it is a gradient of a scalar). By Stokes theorem it contributes nothing to a closed-path integral. The only contributor is $j\omega \mathbf{A}$.

The algorithm ignores this. While numerically computing the integrals $-\int \mathbf{E}_{\text{inc}} \cdot d\mathbf{l}$, it needlessly computes the *theoretically vanishing* integrals $\int \nabla V \cdot d\mathbf{l}$. The influence of $j\omega \mathbf{A}$ is lost in the resulting, unnoticed, catastrophic cancellations.

An ill-conditioned Z and loss of precision in $j\omega \mathbf{A}$ are the two causes of poor low-frequency accuracy. They, and the cure, were first described in [2] and [3].

HOW THE LOW-FREQUENCY ERRORS ARE REMOVED

To prevent catastrophic cancellations Wilton, Lim, and Rao *explicitly* create each closed path, which allows them to replace the numerical integration of $\int \nabla V \cdot d\mathbf{l}$ with the exact value of zero. They finesse each closed-path integral into existence by designing a basis function with that integral as its testing integral. The new basis function is a superposition of original rooftop functions so that the new testing integral is a superposition of original testing integrals.

In this way, most of the original algorithm, and its corresponding computer code, stay the same.

But how to find *all possible* closed paths? The answer is to make a set of generator loops, that is, a set of closed paths from which all other closed paths can be assembled. Then, avoiding (numerical computation of) $\oint \nabla V \cdot d\mathbf{l}$ integrals on every loop in the set will avoid them on all possible loops. Making a set of generators is easy. A set of rooftop functions sharing a common node will, if they have the proper reference directions, have a testing integral whose path is a generator. To see this, pick an interior node in Figure 2 and reverse some of the nearby integration paths so that they all have the same sense of rotation around the node. This is a “loop function”.

Loop functions do an excellent job of preserving the information contained in the $j\omega \mathbf{A}$ field. But they are an incomplete cure for low-frequency errors. There are two reasons. First, loop functions do not address the condition-number issue. Second, the charges deposited on each face of a loop function tend to cancel. In fact a body with equilateral triangulation would produce *complete* cancellation. (Recall that $p_i^* = \pm l_i / (-j\omega a_i^*)$.)

A second basis function needs to be invented; one whose testing path cannot become part of a concatenation of paths in a path-independent integral, and thereby increase the condition number. And the second function should be *guaranteed* to contribute to the charge—the charges from contributing rooftop functions should *accumulate* rather than cancel. The set of rooftop functions sharing a common face will do both of these things, if their reference directions are properly chosen. As an illustration, pick a face in Figure 2 and reverse some of its integration paths so that they all have the same sense, outward or inward. The charges on the chosen face will accumulate because they all have the same sign. This is a “star function”. Notice that the testing paths of star functions cannot be concatenated to form a non-reversing path around a loop.

Star functions anchored to interior faces are made from three rooftop functions. Those anchored to faces on boundaries are made from fewer rooftop functions.

Loop functions describe most of the rotation $\oint \mathbf{J} \cdot d\mathbf{l}$ of the \mathbf{J} field. Star functions describe most of the divergence $\nabla \cdot \mathbf{J}$ of the \mathbf{J} field. The duties of rotation and divergence usually would be shared by both functions, since the triangulation is rarely equilateral. Wilton, Lim, and Rao remove this awkward feature by adjusting the intensity of the contributing rooftop functions to compensate for unequal edge lengths. They define the loop function anchored to the i^{th} interior node as follows:

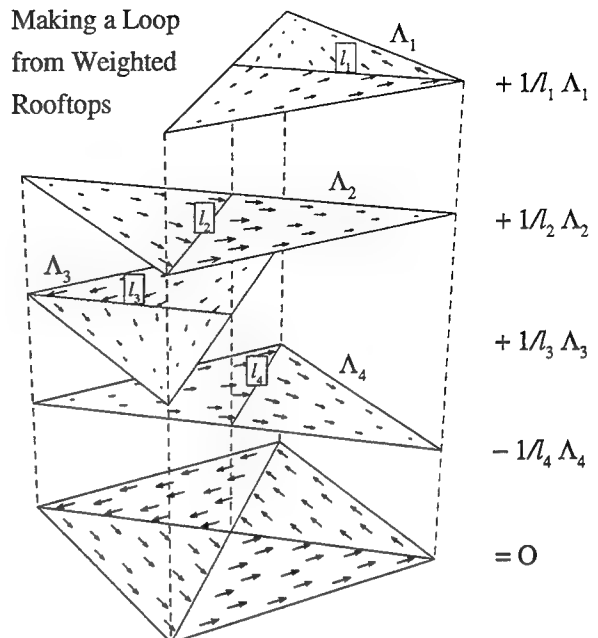


Figure 3 Making a loop function from weighted rooftop functions.

$$\mathbf{O}_i(\mathbf{r}) = \sum_{n_i \in \text{loop}_i} \frac{\sigma_{n_i}}{l_{n_i}} \Lambda_{n_i}(\mathbf{r}) \quad (2)$$

where Λ_{n_i} is the n^{th} member of the set of rooftop functions whose common node is the anchor node of \mathbf{O}_i ; $\sigma = \pm 1$; and l_{n_i} is the length of the n^{th} edge attached to the anchor node. On each face there are two contributions to the charge density; $1/l_{n_i}$ gives them identical magnitudes; σ_{n_i} makes them cancel. In doing so, σ_{n_i} also forces each rooftop current to have the same direction as the loop orientation. The $1/l$ weighting causes the \mathbf{J} streamlines to form closed paths around the anchor node (rotational flow). See Figure 3.

Wilton, Lim, and Rao define the star function anchored to the i^{th} face as follows:

$$\star_i(\mathbf{r}) = \sum_{n_i \in \text{face}_i} \frac{v_{n_i}}{l_{n_i}} \Lambda_{n_i}(\mathbf{r}) \quad (3)$$

where Λ_{n_i} is the n^{th} of the set of rooftop functions whose common face is the anchor face of \star_i ; $v = \pm 1$; and l_{n_i} is the length of the n^{th} edge of the anchor face. On the anchor face there are (usually) three contributions to the charge; $1/l_{n_i}$ gives them equal magnitudes; v_{n_i} makes them accumulate. In doing so, v_{n_i} also forces all rooftop currents to flow out of the face. The $1/l$ weighting causes the \mathbf{J} streamlines to emanate from the *centroid* of the anchor

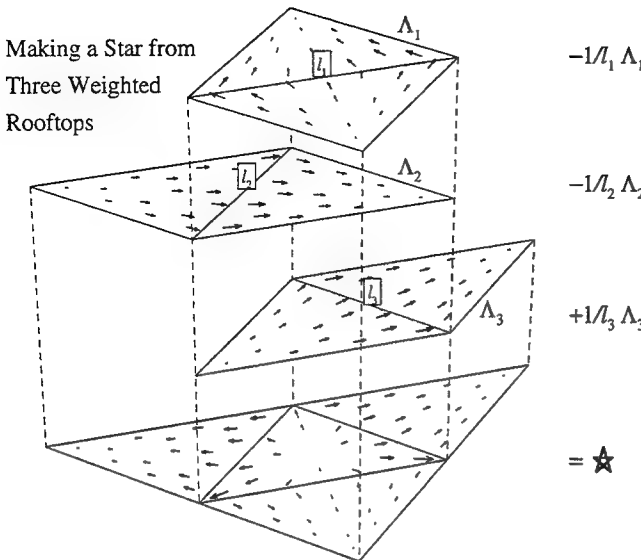


Figure 4 Making a star function from weighted rooftop functions.

face (but only when there are *three* contributing rooftop functions). See Figure 4.

HELMHOLTZIAN COMPLEMENTARITY

When defined this way, loop and star functions have pure Helmholtzian complementarity [5]. Loop functions describe only the rotation of the \mathbf{J} field; star functions describe only the divergence of the \mathbf{J} field. This feature is unaffected by the triangulation of the surface. A loop function's contributions to a star function's irrotational flow come in self-cancelling pairs. Hence, no superposition of loop functions can produce an irrotational flow of current. Similarly, a star function's contributions to a loop function's rotational flow also come in self-cancelling pairs. Hence, no superposition of star functions can produce a rotational flow of current.

There is no coupling via $\int \nabla V \cdot d\mathbf{l}$ between the two kinds of functions; star-to-loop coupling is zero because the path is a loop; loop-to-star coupling is zero because the integrand is zero. The only vehicle for mutual influence between loops and stars is the integral $j\omega \int \mathbf{A} \cdot d\mathbf{l}$. Hence, the two sets of functions become mutually independent as the frequency goes to zero.

Loops and stars form a complete description of the \mathbf{J} field on a simply-connected surface, as does the original set of rooftop functions from which they were assembled. Hence, a moment-method equation $Zx = b$ will have the same number of unknowns

whether it is based on a loop-and-star model or on a rooftop model. But only if the surface is simply-connected. This is the source of a lingering difficulty with the definition of the loop function. (See MULTIPLY-CONNECTED SURFACES below.)

PERFECTLY CONDUCTING SPHERE IN A MAGNETOSTATIC FIELD

Figure 5 shows a perfectly conducting sphere of 1 m radius immersed in a static magnetic field of 1 A/m. The exact, analytical solution for this problem is $\mathbf{J}_\phi = -1.5 H_{inc} \sin\theta \mathbf{u}_\phi$ [6].

To do a numerical simulation we illuminated the sphere with a 377 V/m plane wave at 30 kHz. We then sampled the current that crossed the dashed line. The results show that the loss of information in $j\omega \mathbf{A}$ and the large condition number of Z have made the rooftop model useless, and that the loop-and-star model suffers from neither of these ailments.

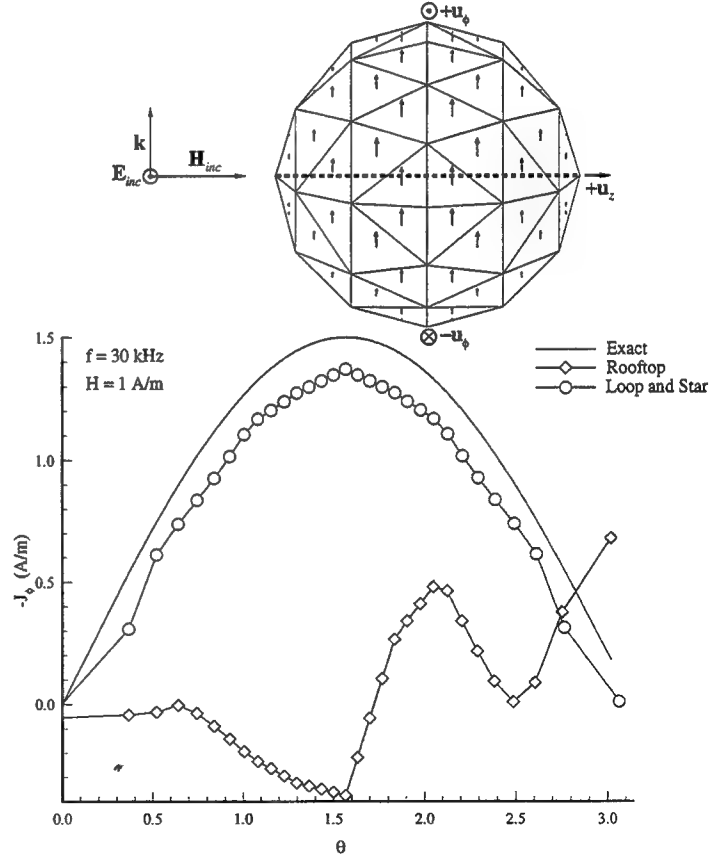


Figure 5 Comparison of surface currents computed by rooftop and loop-and-star models of a conducting sphere.

CONDITION NUMBER

Figure 6 shows the LINPACK estimate [7] of the condition number from a rooftop model and from a loop-and-star model of the sphere in Figure 5. The condition number from the rooftop model is inversely proportional to the square of the frequency, down to about 100 kHz. Below 100 kHz the curve becomes more complicated. We suspect that the roundoff error in the entries in Z actually prevent the straight $1/f^2$ trend towards total dependence below 100 kHz.

The condition number from the loop-and-star model is frequency independent down to at least 3 Hz, showing how effectively the condition number has been controlled.

The LINPACK estimate of the condition number is most accurate when all entries in Z have the same absolute error. Since the error in each z_{ij} is roughly proportional to its magnitude, we meet this requirement by scaling the rows and columns of Z so that all entries on the diagonal have unit magnitude. (Both rows and columns were scaled to preserve the near symmetry of the matrix.)

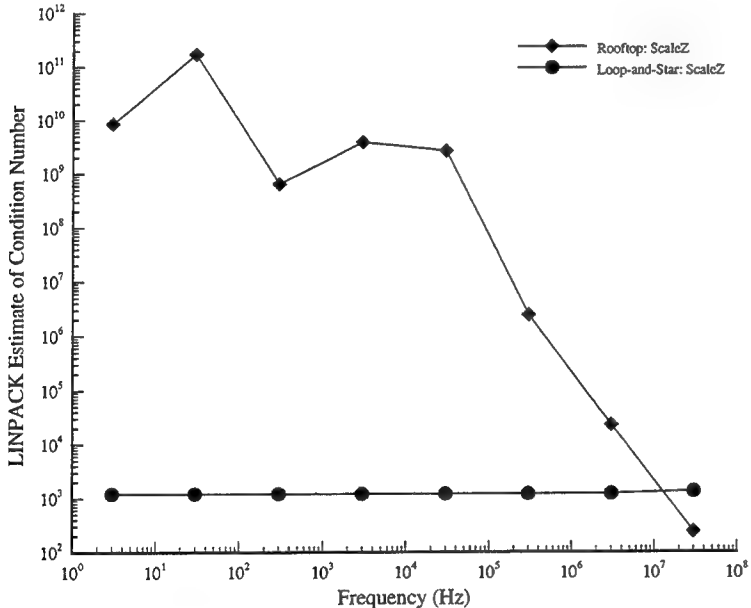


Figure 6 Comparison of condition numbers from the rooftop and loop-and-star models.

SIMPLY-CONNECTED OPEN AND CLOSED SURFACES

When the surface is simply-connected there is no difficulty with the loop-and-star model. The loop function definition (2) forms a complete set of generator loops. There is a loop function at each interior node if the surface is open; one

less if the surface is closed (to avoid making a redundant generator).

The number of star functions is whatever is needed to make the total number of unknowns equal to the number of unknowns from a rooftop model.

DISJOINT BODIES

Both the original Rao-Wilton-Glisson rooftop model and the new loop-and-star model compute the mutual influence between sources on *arbitrarily located* faces. It does not matter that those faces might reside on disjoint surfaces. (However, each surface must be simply-connected if the loop-and-star model is to be used).

MULTIPLY-CONNECTED SURFACES

When the surface is multiply-connected the loop function definition (2) yields an incomplete set of generator loops. As examples, it misses a loop for every aperture, and on a torus it misses two loops.

The most obvious solution would be to broaden the definition in some manner to include the missing loops. But each missing loop is just one of a large set of topologically equivalent loops; any one of them can be used. It might not be possible to design software that reliably and efficiently finds the required sets of topologically equivalent loops and then picks only one of them.

A workable alternative would be to supply the missing loops by hand after inspecting a three-dimensional view of the triangulated surface. Each loop could then be supplied to the program in the form of the set of faces that are traversed. The software would need to be capable of assembling the faces into a loop function, which would then be processed the same as the original loop functions.

Another alternative also involves some manual labor. It is based on the fact that loop functions and star functions are assembled from rooftop functions. Suppose there was some way to change the topology to simply-connected without, in any way, changing the set of rooftops. The solution would then be identical to that produced by either of the previous alternatives, because the *same* set of rooftops would be used to assemble the loops and stars.

Exactly that happens when the surface is “cut” along a selected sequence of edges in such a way that the

CUTTING A MULTIPLY-CONNECTED SURFACE

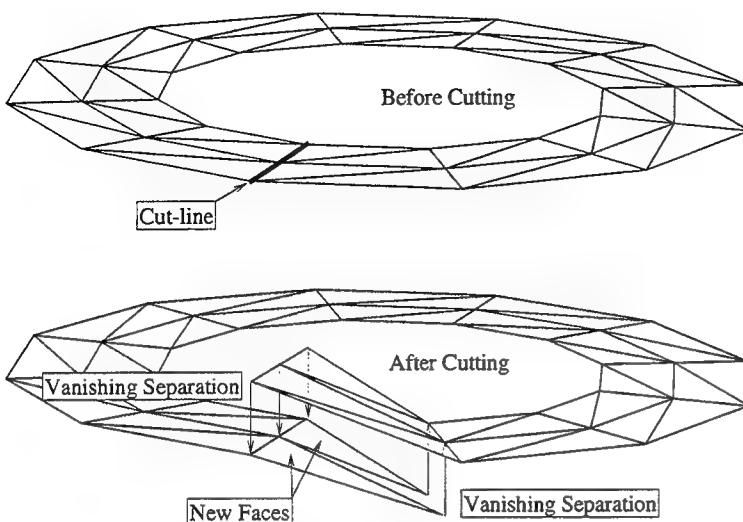


Figure 7 Cutting a multiply-connected surface into a simply-connected surface.

overlapping rooftop functions on each face become topologically, *but not physically*, delaminated. See Figure 7. The surface becomes simply-connected yet the size, shape, and position of its rooftops are not changed.

Three new edges, and one new face, are added for each edge in the cut. But the number of *interior* edges is not changed. There are new nodes but no new node coordinates.

We use the cutting option because it changes only the *triangulation* of the surface; the *algorithm* remains in its basic form. Cutting involves manual work, which takes time. But creating the triangulated surface itself usually involves manual work, and sometimes a lot of it. This is at least as time consuming as the cutting.

SELF-INTERSECTING SURFACES

When a self-intersecting body is triangulated, some edges will have more than two faces attached to them. There are (at least) two methods that could handle this situation, both of which satisfy Kirchhoff's current law at each edge.

In one method, each edge at a self-intersection could be treated as a generalized edge: an edge with f faces attached to it would be assigned $f-1$ rooftop functions. No special care would be needed when choosing which pair of faces to assign to which rooftop function—rooftop currents could even pass *through* each other at a generalized edge. The

number of unknowns in the matrix equation would be *greater* than the number of interior edges in the triangulation. This method would leave the triangulation intact and would change the code.

The original Rao-Wilton-Glisson rooftop algorithm could easily be encoded to use this method but the loop-and-star algorithm might present some trouble. It might be hard to write code that reliably assembles loop-and-star functions in the vicinity of a generalized edge.

For us, a better method is to cut the self-intersecting surface into surfaces that are not self-intersecting. See Figure 8. The cut surface is then disjoint and can be treated by *the basic forms* of either the rooftop model or the loop-and-star model. (See DISJOINT SURFACES above.) As with multiply-connected surfaces, cutting a self-intersecting surface does not change

CUTTING A SELF-INTERSECTING SURFACE

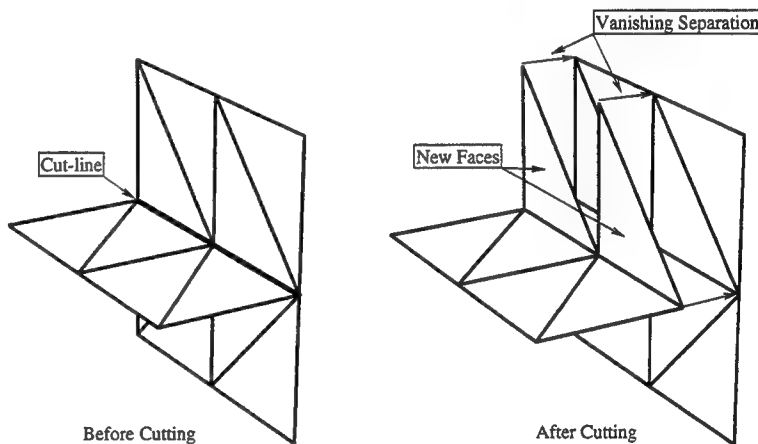


Figure 8 Cutting a self-intersecting surface into a disjoint surface.

in any way the fundamental set of rooftops, so the solution does not change either.

ONE-SIDED SURFACES

A one-sided (non-orientable) surface, like a Moebius strip, can always be cut into a two-sided surface in the manner already shown in Figure 7. Once cut, the surface becomes simply-connected, allowing the basic loop-and-star model to be used. As always, cutting changes the triangulation and leaves the encoded algorithm intact.

Although the encoded version of the original rooftop algorithm of Rao, Wilton, and Glisson is not the main topic of this paper, its popularity and the present heading make it appropriate to now discuss some pertinent details.

The original Rao-Wilton-Glisson rooftop code cannot be applied to a one-sided surface; nor was it intended to be. Its authors chose to give the user another way to check the integrity of the triangulation: they designed the code to compute the volume whenever a closed surface was encountered. So a consistent normal had to be assigned to every face. For simplicity this was done for every type of surface, even open ones. It then seemed convenient to use the normal to help set a reference direction for each rooftop function. Each rooftop current was made to cross its anchor edge in the same direction as $\hat{\mathbf{e}} \times \hat{\mathbf{n}}$, where $\hat{\mathbf{e}}$ is the (arbitrarily defined) direction of the anchor edge.

But a basis function's reference direction is arbitrary in any algorithm. (In the Rao-Wilton-Glisson algorithm it depends on an arbitrary choice of the direction of $\hat{\mathbf{e}}$.) There is no need to involve the surface normal in an arbitrary decision. By removing it from the decision process, the rooftop model of Rao, Wilton, and Glisson immediately can be applied to one-sided surfaces (and it can still compute the volume of closed surfaces).

Finally, we note that the subroutine that sets the surface normals (and, hence, the reference directions) is quite complex and contains a subtle bug, which takes effect only on some triangulations.

DIAGONAL DOMINANCE AND ITERATIVE SOLUTIONS OF $Zx = b$

It turns out that a matrix from a loop-and-star model is closer to being diagonally dominant than one from a rooftop model. Z is said to be diagonally dominant when the "diagonal-dominance" ratio (DDR)

$$\frac{|z_{ii}|}{\sum_{j:j \neq i} |z_{ij}|} \quad (4)$$

is greater than 1 for all $i=1,\dots,N$ [12].

The explanation for the greater DDR lies in the shape of the paths of the testing integrals: in loop-and-star modeling the paths are made from directed line-segments whose orientations tend to cancel; in rooftop modeling the orientations tend to accumulate. This makes the off-diagonal integrals smaller, relative to the diagonal integral, than those in a rooftop model.

PLATE180.GEO

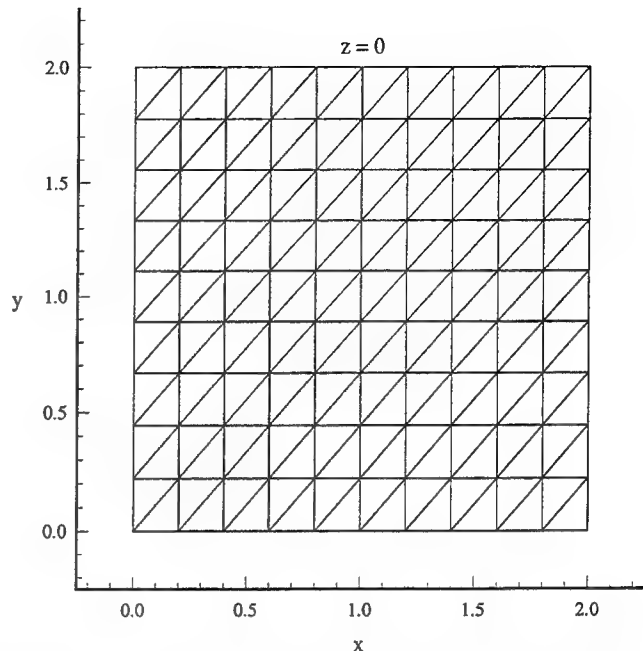


Figure 9 The square plate used to study diagonal dominance.

Figure 10 compares the DDR from a rooftop model to the DDR from a loop-and-star model. (The device-under-test is the square plate in Figure 9.) The rows that test the loops (rows 1 to 72) have DDRs consistently greater than 1. The DDRs of the rows that test stars are about half as big and are usually less than one. Other structures that we have studied also show this behavior. (Perhaps star functions could be redesigned to produce DDRs as high as those of loop functions.)

The DDR is insensitive to the frequency as long as the triangulation is dense enough to allow an adequate description of the sources on the surface. See Figure 11. Also, it is totally independent of the direction and polarization of the incident field, because Z itself is totally independent of these parameters.

Wilton, Lim, and Rao claim that the Z matrix is diagonally dominant [2,3]. We have found no geometries where this is so. We can only say that the Z from a loop-and-star model is closer to being diagonally dominant than one from a rooftop model.

In any case, the improved diagonal dominance may have a practical benefit at all frequencies (below the upper limit). The standard method for solving $Zx = b$ is by LU decomposition, for which the required CPU time is proportional to N^3 . (N is the number of unknowns). The

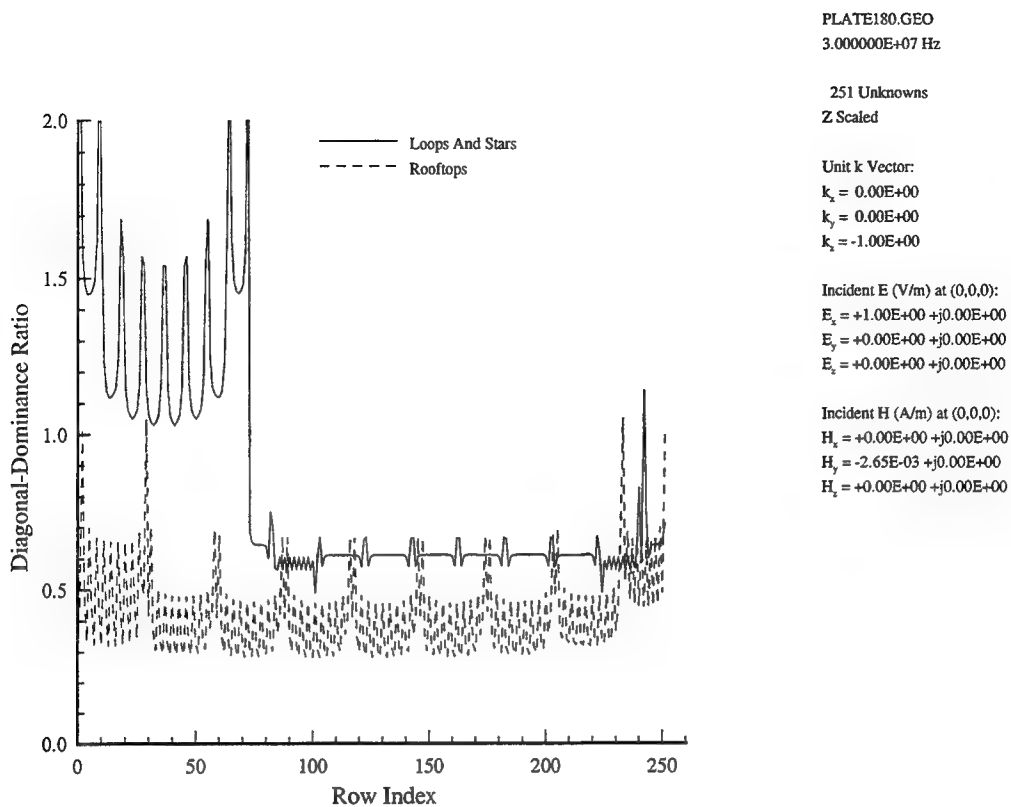


Figure 10 Comparison of diagonal-dominance ratios for a square plate.

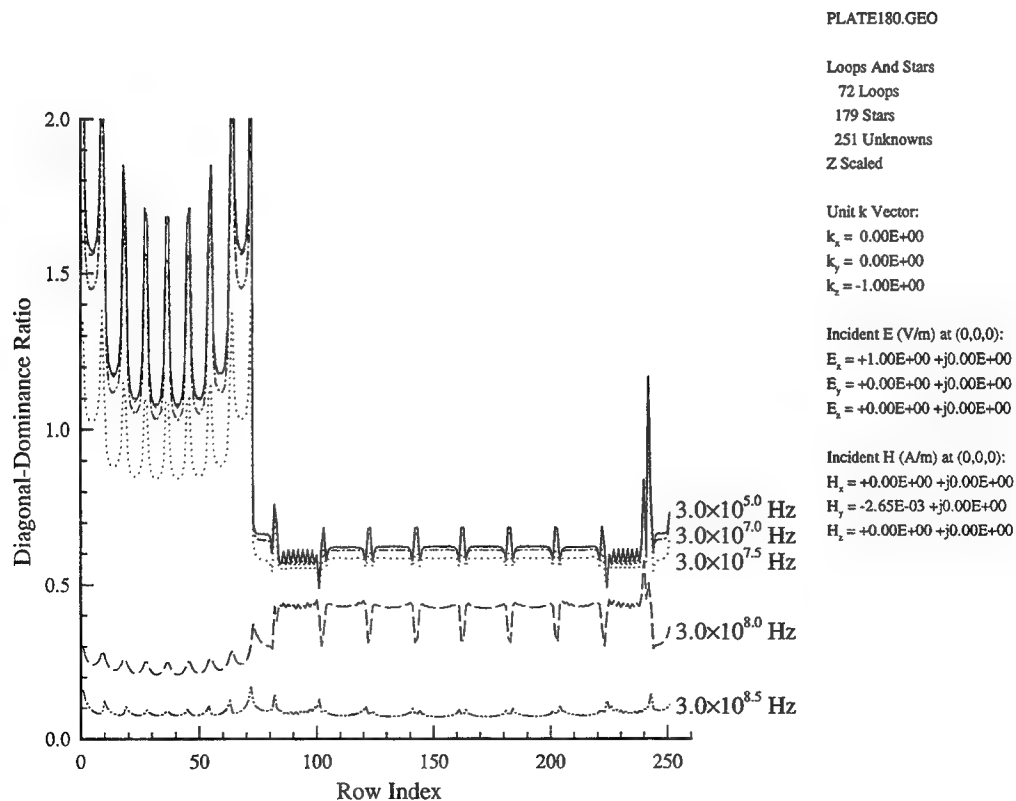


Figure 11 The effect of frequency on the diagonal-dominance ratio.

CPU time for an iterative solution, such as Jacobi iteration, is proportional to N^2 , a great advantage when N is large. Solution by point Jacobi iteration is *guaranteed* to converge when Z is diagonally dominant [8,9,10,11]. A matrix equation in which Z is not diagonally dominant can *sometimes* permit a converging Jacobi iteration. Intuition suggests the closer Z is to diagonal dominance the more likely the iteration will converge and, if it does converge, the faster it will converge.

The number of iterations needed to get a solution depends on the initial guess. Hence, an iterative solution has an extra advantage when doing a sweep of a spectrum since each solution is a good initial guess for the next.

$Zx = b$ could also be solved by *block* Jacobi iteration. Loop-and-star analysis permits a natural way to divide Z into submatrices, if the loops are numbered from 1 to N_{loops} and the stars are numbered from $N_{loops}+1$ to N . The equation then becomes

$$\begin{bmatrix} Z^{00} & Z^{*\circ} \\ Z^{0\star} & Z^{\star\star} \end{bmatrix} \begin{bmatrix} x^0 \\ x^\star \end{bmatrix} = \begin{bmatrix} b^0 \\ b^\star \end{bmatrix} \quad (5)$$

which can be solved by block Jacobi iteration, if Z is well behaved. Good behaviour is guaranteed at 0 Hz because $Z^{*\circ}$ and $Z^{0\star}$ are then filled with zeroes. (See HELMHOLTZIAN COMPLEMENTARITY above.) It may be that the Helmholtzian complementarity of loop functions and star functions will guarantee the convergence of this iteration at higher frequencies.

The potential speed-up is not as great as that for point Jacobi iteration because both Z^{00} and $Z^{\star\star}$ need to be LU decomposed. The required time, relative to an LU decomposition of Z , is $(1/3)^3 + (2/3)^3 = 1/3$ (since the numbers of loops and stars are approximately $N/3$ and $2N/3$, respectively).

CATASTROPHIC CANCELLATIONS IN MAKING b^0

Each entry in b^0 in equation (5) is the integral $\oint \mathbf{E}_{inc} \cdot d\mathbf{l}$ around the closed testing path of a loop function. Sometimes the orientation of the surface and polarization of the illumination can combine so that the integral vanishes. This will happen, for example, when a uniform plane wave is normally incident on a flat plate. Since the integral is computed numerically, the zero is crudely approximated by catastrophic cancellations. To avoid this, we use Faraday's

law to replace the closed-path integral $\oint \mathbf{E}_{inc} \cdot d\mathbf{l}$ with the surface integral $-j\omega \int_S \mathbf{B}_{inc} \cdot \hat{n} da$, where S is some surface bounded by the path. A convenient choice for S is the part of the triangulated surface enclosed by the testing path. We do the numerical integration by sampling \mathbf{B}_{inc} at the centroids of the four-sided "facelets" inside the testing path. See Figure 12. The centroid of each facelet is at $5/12 \mathbf{r}_i + 7/12 \mathbf{r}_{n_i}^c$. The area of the n^{th} facelet is one-third the area of the n^{th} face.

There are some path integrals for which the Faraday alternative is hard to implement. They are the testing integrals of those loop functions that are lost whenever the surface is multiply-connected. The paths of these integrals will not enclose any triangulated surfaces at all! In these cases the Faraday alternative would require the construction of special (non-conducting) surfaces on which to sample \mathbf{B}_{inc} . Also the basic loop-and-star model would have to be modified to handle multiply-connected surfaces. We avoid these problems by cutting the multiply-connected surface into a simply-connected one. (See MULTIPLY-CONNECTED SURFACES above.) Then no testing path will enclose an untriangulated surface.

It is conceivable that a numerical evaluation of the Faraday surface integral can also suffer from catastrophic cancellation. It could happen when the loop function is anchored at the tip of a very sharp cone or at a very sharp edge on the surface. But cases like these will not occur if the surface is triangulated so that there are no acute angles between adjacent faces. The no-acute-angle rule is implied by the standard rule for a good triangulation: it must be

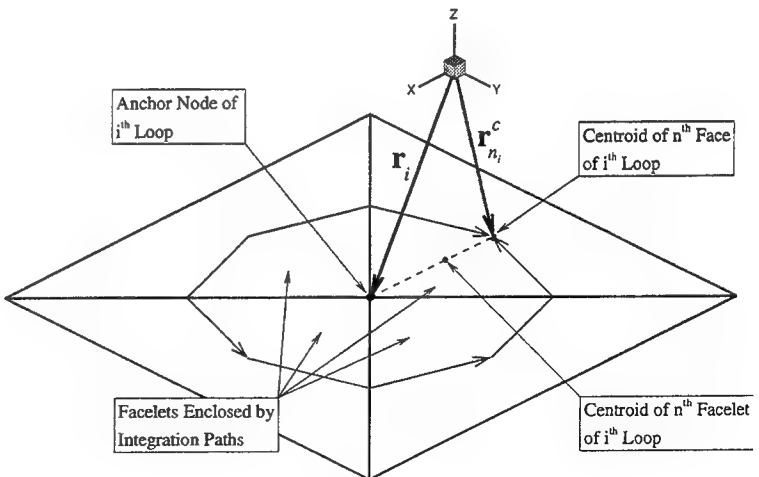


Figure 12 Computing the centroid of a facelet inside an integration loop.

dense enough to adequately describe the surface and the sources on it.

The CPU times needed to compute the \mathbf{b}^o vector by either side of the Faraday equation are roughly the same and are minuscule when compared to the time needed to fill Z .

PROGRAMMING

Each entry z_{ij} in Z is the integration of \mathbf{E}_{ext} , due to the j^{th} basis function, over the testing path of the i^{th} basis function. The most straightforward way to fill Z is to compute an integral for each permutation of i and j encountered in a column-wise scan of Z . (Row-wise if the language is not FORTRAN.) But this is not the most time-efficient way. Each integration calls a potential-integral routine [4], which computes the potentials at a *single* field point due to a source on a *single* face. Because basis functions overlap and testing paths overlap, a scan of Z would actually call this routine many times with the *same combination of source face and field point*. It is therefore much faster to do the computation for a given combination *only once* and to then *add* the result to *all* the z_{ij} that are affected by that combination. This requires a scan of the geometry for all permutations of faces taken two at a time (since there is a field point at the centroid of each face.)

Notice that the scan is independent of the choice of model; the faces of loop functions, star functions, and rooftop functions all carry the same Rao-Wilton-Glisson source function (to within a weighting factor). Hence, it is natural to design the program to do either loop-and-star modeling or rooftop modeling. There is only a small amount of code that actually depends on the choice of basis function. It determines which z_{ij} (and which b_i) are to receive an accumulation. It also determines the weighting of each accumulation.

In our program this basis-function-specific code is executed *before* any entries in Z or b are computed. It simply fills two identically dimensioned arrays. One array links each edge of each face to the weighting factors, $\pm 1/l$, of the four possible functions (two loops and two stars) that cross that edge. The other array supplies the corresponding indices, $i = 1, N$, of the loops or stars. The inner dimension of each array is four because there can be up to four basis functions that can cross each interior edge.

The rest of the code operates without any knowledge of the type of basis function being used. It simply uses the two generic arrays of weighting factors and indices to fill Z and b , and then solves $Zx = b$. For example, if the program is to do rooftop modeling then there is only one weighting factor, ± 1 , and one index per edge. The remaining three

locations along the inner dimension are simply filled with zeroes so that the other accumulations amount to nothing.

The time to execute the basis-function-specific code is very insignificant when compared to the $O(N^3)$ time needed to solve $Zx = b$ and the $O(N^2)$ time needed to fill Z .

CONCLUSIONS

The loop-and-star algorithm of Wilton, Lim, and Rao effectively controls the catastrophic cancellation errors and condition number that corrupt the low-frequency results from the rooftop algorithm of Rao, Wilton, and Glisson. The high-frequency limit of the loop-and-star algorithm is as large as that of the rooftop algorithm, $W/\lambda \approx 1$; and the low-frequency limit is much smaller, at least $W/\lambda \approx 2 \times 10^{-8}$. Electrostatic and magnetostatic simulations can now be done with confidence.

The basic loop-and-star algorithm can treat only simply-connected surfaces. But this restriction has little practical impact because multiply-connected surfaces, self-intersecting surfaces, and one-sided surfaces can be readily "cut" into the required topology without altering the set of rooftop functions that they carry.

The impedance matrix from a loop-and-star model is not diagonally dominant. But it is more so than one from a rooftop model. In fact, the rows of Z that test the loop functions all have a diagonal-dominance ratio greater than one. It is only the rows that test the star functions that have a diagonal-dominance ratio less than one. It might be possible to redesign the star function so that all rows of Z are diagonally dominant. In any case, the matrix equation $Zx = b$ from a loop-and-star model is more likely to be solved by a converging Jacobi iteration.

Catastrophic cancellations can corrupt those entries in the b vector that participate in loop testing. This can be avoided by using the Faraday law to replace the closed-path integral $\oint \mathbf{E}_{inc} \cdot d\mathbf{l}$ with the surface integral $-j\omega \int_S \mathbf{B}_{inc} \cdot \hat{n} da$, where S is some surface bounded by the testing path.

REFERENCES

- [1] S. M. Rao, D. R. Wilton, and A. W. Glisson, "Electromagnetic Scattering by Surfaces of Arbitrary Shape," *IEEE Trans. Antennas Propagat.*, vol. AP-30, no. 3, May 1982, pp. 409-418.
- [2] D. R. Wilton, J. S. Lim, and S. M. Rao, "A Novel Technique to Calculate the Electromagnetic Scattering by Surfaces of Arbitrary Shape," *URSI*

Radio Science Meeting, University of Michigan,
June 1993, page 322.

- [3] J. S. Lim, *Electromagnetic Scattering from Arbitrarily Shaped Bodies at Very Low Frequency Range Using Triangular Patch Modelling*, Ph. D. dissertation, Auburn University, Auburn, AL 36849, March 1994.
- [4] D. R. Wilton, S. M. Rao, A. W. Glisson, D. H. Schaubert, O. M. Al-Bundak, and C. M. Butler, "Potential Integrals for Uniform and Linear Source Distributions on Polygonal and Polyhedral Domains," *IEEE Trans. Antennas Propagat.*, vol. AP-32, no. 3, March 1984, pp. 276-281.
- [5] R. Plonsky and R. E. Collin, *Principles and Applications of Electromagnetic Fields*, International Student Edition, McGraw-Hill Book Co. and Kogakusha Co., 1961, pp.29-38.
- [6] J. Van Bladel, *Electromagnetic Fields*, revised printing, Hemisphere Publishing Corporation, New York, 1985, pp. 275-279.
- [7] J. J. Dongarra, C. B. Moler, J. R. Bunch, and G. W. Stewart, *LINPACK Users' Guide*, SIAM, Philadelphia, 1979, pp. 1.11-1.22.
- [8] L. A . Hageman and D. M. Young, *Applied Iterative Methods*, Academic Press, 1981, pp. 23-26.
- [9] G. E. Forsythe and C. B. Moler, *Computer Solution of Linear Algebraic Equations*, Prentice-Hall, 1967, p. 130.
- [10] W. H. Press, S.A. Teukolsky, W. T. Vetterling, and B. P. Flannery, *Numerical Recipes in FORTRAN, The Art of Scientific Computing*, Cambridge University Press, 1992, p. 856.
- [11] K. Kalbasi and K. Demarest, "A Multilevel Formulation of the Method of Moments," *IEEE Trans. Antennas Propagat.*, vol. AP-41, no. 5, May 1993, pp. 589-599.
- [12] G. H. Golub, C. F. van Loan, *Matrix Computations*, Second Edition, The Johns Hopkins University Press, 1989, p. 119.

A Study of Two Numerical Solution Procedures for the Electric Field Integral Equation at Low Frequency

Wen-Liang Wu, Allen W. Glisson, and Darko Kajfez

Dept. of Electrical Engineering

University of Mississippi

University, MS 38677

Abstract - The numerical solution of the Electric Field Integral Equation (EFIE) using two different low frequency formulations is investigated. The two procedures are implemented for the triangular patch modeling procedure and results obtained for both methods are compared with the original triangular patch EFIE solution. The comparisons are made on the basis of the computed current values and the inverse condition number of the moment matrix. It is observed that the condition number of the matrix can be significantly different between the two low frequency formulations and that the method used to evaluate the forcing function can affect the results both in the low and high frequency ranges.

I. Introduction

The commonly used numerical solution procedure for the Electric Field Integral Equation (EFIE) has been found to become inaccurate in the frequency range where the maximum dimension of the surface is much smaller than a wavelength [1,2]. The problem arises in the evaluation of the elements of the impedance matrix in the moment method solution procedure, because, if the mixed potential form of the EFIE is used as an example, one observes that $|j\omega A| \ll |\nabla\Phi|$, as $\omega \rightarrow 0$. Thus, for a fixed precision computation, the information on the magnetic vector potential A is lost when the frequency is low enough, and the remaining information from the electric scalar potential is not sufficient to determine the surface current distribution. Consequently, the solution is numerically unstable.

This problem may be partially overcome by simply increasing the numeric precision used in the computer code. However, to obtain an EFIE solution that has the potential to be stable at any frequency, a special method of moments solution procedure must be used.

In the following sections, two low-frequency

formulations, referred to here as the Loop/Tree and Loop/Star formulations, are presented. These two formulations have been previously studied and have been applied to different method of moments solution procedures [1-5]. Wilton and Glisson first observed the low-frequency problem of the EFIE and applied the Loop/Tree approach as the new testing procedure for a rectangular-patch model of a perfectly electrically conducting plate [1]. Mautz and Harrington explored in greater detail why the numerical solution becomes inaccurate in the low frequency range, and they applied a procedure equivalent to the Loop/Star formulation to their body of revolution code [2]. Lim, Rao, and Wilton applied the Loop/Star procedure to their triangular patch model [3]. Recently, Wu, Glisson, and Kajfez applied both the Loop/Tree and Loop/Star formulations to another triangular patch model and compared results obtained using the two procedures [4,5].

This paper is an extension of [4,5] and sums up our recent research on this topic. A new version of the patch code, referred to here as LFPATCH, has been developed to apply either the Loop/Tree or Loop/Star formulation to extend a version of the patch code [6] to the low frequency range. The modifications for both formulations require the use of different expansion and testing functions that tend to decouple the electrostatic and magnetostatic portions of the solution. A Galerkin testing procedure is used to obtain the system of linear equations. The two different formulations are compared with each other and with the original triangular patch code with regard to accuracy. The two low-frequency formulations, the Loop/Tree and Loop/Star, are described in Section II. The influence of the form of the forcing function on the solution for the low-frequency formulations is discussed in Section III. The numerical results are shown in Section IV to demonstrate the improvement of the stability of the impedance matrix and the accuracy of the computed current density. A summary is provided in Section V.

II. Low-Frequency Formulations

The scattering problem of a perfectly electrically conducting (PEC) body subject to illumination by a time harmonic incident plane wave can be formulated via the EFIE as

$$\mathbf{E}_{tan}^i(\mathbf{r}) = [j\omega \mathbf{A}(\mathbf{r}) + \nabla \Phi(\mathbf{r})]_{tan}, \quad \mathbf{r} \text{ on } S \quad (1)$$

where \mathbf{E}^i represents the incident electric field, S is the surface of the scatterer, and the subscript tan denotes the component of a quantity tangential to the surface S . \mathbf{A} and Φ are the magnetic vector potential and the electric scalar potential defined by

$$\mathbf{A}(\mathbf{r}) = \mu \int_s J(r') G(r, r') dS' , \quad r' \text{ on } S \quad (2)$$

$$\Phi(\mathbf{r}) = \frac{1}{\epsilon} \int_s \sigma(r') G(r, r') dS' , \quad r' \text{ on } S \quad (3)$$

where

$$G(r, r') = \frac{e^{-jk|r-r'|}}{4\pi|r-r'|} \quad (4)$$

and where $k = \omega(\mu\epsilon)^{1/2}$, and μ and ϵ are the permeability and permittivity of the surrounding medium. The surface charge density σ is related to the surface divergence of \mathbf{J} through the equation of continuity

$$\nabla \cdot \mathbf{J} = -j\omega\sigma \quad (5)$$

Many method of moments [7] schemes have been developed to obtain the numerical solution for equation (1). One of these is the triangular patch model [6], which is based on a method of moments solution of the EFIE in conjunction with a planar triangular patch model of the scatterer and a special set of basis functions. In this section, for completeness, we first describe the basis function used in the original patch code [6]; then the two other vector basis function sets that are suitable for low-frequency use are described.

In the method of moments solution procedure, the surface current density \mathbf{J} is approximated as

$$\mathbf{J} \cong \sum_{n=1}^N I_n \mathbf{u}_n(\mathbf{r}) \quad (6)$$

where N is the number of unknowns, I_n is an unknown coefficient to be determined, and \mathbf{u}_n is a vector basis function. For the formulation described here, \mathbf{u}_n in (6) is chosen from one of three different sets of basis functions:

$\{f_n\}$, $\{J_n^L$ and $J_n^S\}$, or $\{J_n^L$ and $J_n^T\}$. These three sets of basis functions are briefly described in following.

The original vector basis function f_n

As in [6], f_n is a vector basis function defined on a pair of adjacent triangles T_n^\pm associated with the n^{th} non-boundary edge of the model, as shown in Figure 1 and defined by equation (7), where l_n is the length of n^{th} edge and A_n^\pm is the area of triangle T_n^\pm .

$$f_n(\mathbf{r}) = \begin{cases} \frac{l_n}{2A_n^+} \mathbf{p}_n^+ & , \quad \mathbf{r} \text{ in } T_n^+ \\ \frac{l_n}{2A_n^-} \mathbf{p}_n^- & , \quad \mathbf{r} \text{ in } T_n^- \\ 0 & , \quad \text{otherwise} \end{cases} \quad (7)$$

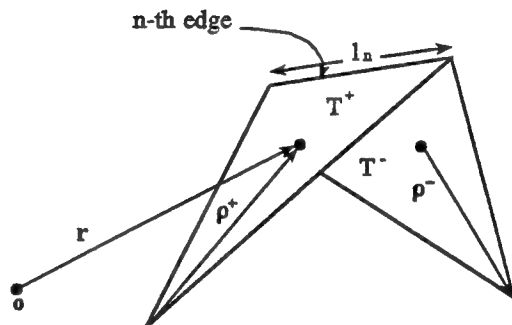


Figure 1. Local coordinates associated with an edge.

To extend the original patch code [6] to the low frequency range, vector basis functions are presented based on the work in [1-3]. These new vector basis functions J_n are divided into two types, J_n^L and either J_n^S or J_n^T , with the following properties which make them suitable for use in the magnetic vector and electric scalar potentials at low frequencies:

- J_n^L is associated with interior nodes and is divergenceless;
- J_n^S is associated with faces and is curl-free;
- J_n^T is equivalent to f_n , but is only associated with the interior edges of the model that lie along a tree structure connecting the centroids of the triangular patches.

The combination of J_n^L and J_n^S is subsequently referred to as the Loop/Star basis function set, and the combination of J_n^L and J_n^T is referred to as the Loop/Tree basis function set. Each of the basis functions J_n^L , J_n^S , and J_n^T can be constructed as a linear combination of the vector basis functions f_n defined in (7).

The vector basis function J_n^L

Figure 2 illustrates in a simplified form the "Loop" basis function J_n^L associated with an interior node n^L . Within each triangle attached to node n^L , J_n^L has vector direction parallel to the edge opposite to node n^L and, therefore, J_n^L forms a loop around node n^L . In Figure 2(a), aside from the edges which are opposite node n^L , all the other edges are connected to node n^L . The currents at these edges connected to node n^L would be unknowns in the original patch code and each would be associated with an original vector basis functions f_n . To obtain the vector basis function J_n^L associated with the interior node n^L , basis functions f_n are first associated with the edges connected to node n^L and are then combined together in a particular manner, so that only a single basis function having zero divergence remains. Figure 2(b) shows the edges and local coordinates associated with one of the triangles in Figure 2(a). In Figure 2(b), if node 1 corresponds to node n^L in Figure 2(a), then J_n^L in this triangle is parallel to edge 1. As indicated in [6], a constant vector of arbitrary magnitude and direction within the triangle may be synthesized by a linear combination of two of the original vector basis functions. Thus, in conjunction with the definition of the vector basis function in equation (7), a vector L_1 within the triangle of Figure 2(b) can be formed as

$$L_1 = \frac{2A}{l_2} f_2 - \frac{2A}{l_3} f_3 \quad (8)$$

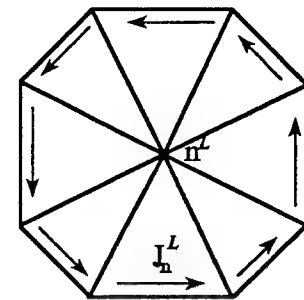
where l_2 and l_3 are the lengths of edges 2 and 3, respectively, and A is the triangle area.

The basis function J_n^L in the triangle of Figure 2(b) is then defined to be

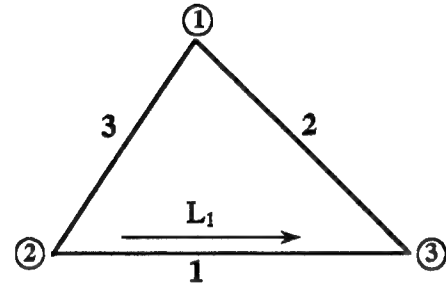
$$J_n^L = \frac{L_1}{A} \quad (9)$$

This definition holds for all triangles attached to interior node n^L by using the local coordinate notation in Figure 2(b) for each triangle attached to node n^L . Then the basis function J_n^L associated with interior node n^L is defined as

$$J_n^L = \sum_{j=1}^{N_t} \frac{L_j}{A_j} \quad (10)$$



(a)



(b)

Figure 2. A representation of the vector basis function J_n^L associated with an interior node n^L .

where N_t is the number of triangles attached to node n^L , L_j is the vector parallel to the edge opposite to node n^L in the j^{th} triangle, and A_j is the area of the j^{th} triangle. We note that the triangular patch loop basis function of (10) has been previously used in the computation of polarizabilities for conducting disks and apertures [8] and for magnetostatic solutions for arbitrarily shaped bodies [9].

The vector basis function J_n^S

The "Star" vector basis function J_n^S of [3] is associated with faces and is shown in a simplified representation in Figure 3. The domain of the basis function J_n^S associated with the n^{th} triangular face consists of the n^{th} face itself and all of the faces attached to the n^{th} face. The new basis function is constructed by first placing an original basis function f_n on the triangle pair associated with each edge of

the n^{th} face and orienting these f_n 's so that current flows out of the n^{th} face for each one. Finally, the "Star" basis function is formed by summing over the f_n 's to obtain

$$J_n^S = \sum_{i=1}^3 \frac{S_{ni} f_{ni}}{\ell_{ni}} \quad (11)$$

where f_{ni} is an original vector basis function associated with edge i of the n^{th} face, and S_{ni} is a sign and magnitude coefficient chosen from the set $\{-1, 0, 1\}$ to provide current flow out of the n^{th} face for a non-boundary edge i or to eliminate contributions from boundary edges.

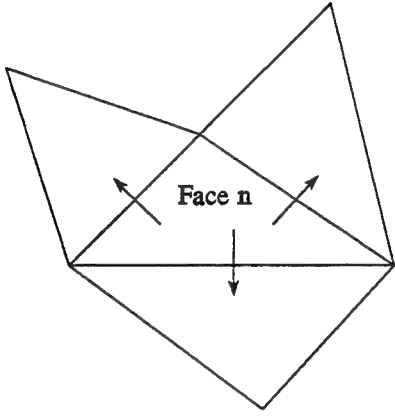


Figure 3. A representation of the vector basis function J_n^S associated with a triangular patch.

The vector basis function J_n^T

The "Tree" basis function J_n^T consists of the f_n 's for the interior edges of the model that lie along a tree structure connecting the centroids of adjacent triangular patches. The definition of *tree* and *branch* for the rectangular-patch model in [Ch. 8, 10] is also applied for the triangular patches used here. A possible choice of the tree for a triangular patch model is shown in Figure 4. Once a tree is obtained, J_n^T can be defined as

$$J_n^T = \begin{cases} f_t, & \text{if edge } t \text{ intersects a tree branch} \\ 0, & \text{otherwise} \end{cases} \quad (12)$$

where f_t is the original vector basis function associated with a non-boundary edge t .

With these definitions, three simple approaches are used to form a complete set of basis functions. The surface current density J is then approximated by either of the three basis function sets. If the set of original vector basis functions f_n is chosen, i.e., if the same basis set as in [6] is

used, then

$$J(r) \cong \sum_{n=1}^N I_n f_n(r) \quad (13)$$

where N is the number of interior (non-boundary) edges in the triangular patch model. If the Loop/Star basis function set is chosen, then J is represented as

$$J(r) \cong \sum_{n=1}^{N^L} I_n J_n^L(r) + \sum_{n=N^L+1}^N I_n J_n^S(r) \quad (14)$$

where N^L is the number of interior nodes, and $N - N^L + 1$ is the number of faces in the triangular patch model. If the Loop/Tree basis function set is chosen instead, then

$$J(r) \cong \sum_{n=1}^{N^L} I_n J_n^L(r) + \sum_{n=N^L+1}^N I_n J_n^T(r) \quad (15)$$

where $N - N^L$ is the number of tree branches in the triangular patch model.

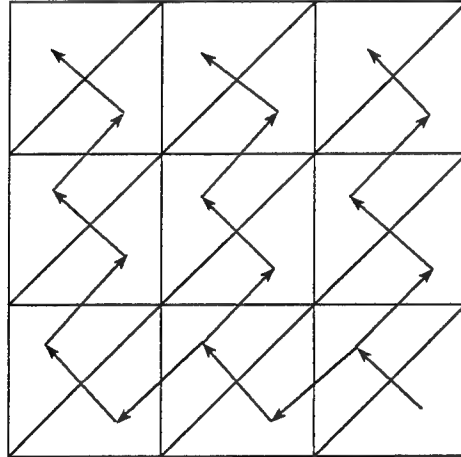


Figure 4. A tree structure connecting the centroids of adjacent triangular patches.

The basis function set J_n^L must include an additional type of element if the body being modeled is not simply connected, as shown in Figure 5. The connectivity of the body can be determined from the triangular patch model for some classes of geometries by noting, for example, that the triangular patch model of a simply connected open surface without any "handles" will have either no "aperture" or only one "aperture," i.e., either there will be no boundary edge or the union of all of the boundary edges in the patch model will form a single closed curve. For each additional aperture in the model it is necessary to include a "super-loop" basis function of form similar to J_n^L . These

additional basis functions will form loops around apertures rather than around interior nodes of the model. In Figure 5, the surface modeled by triangular patches has two apertures; therefore, an additional "super-loop" basis function is needed if one uses one of the low-frequency formulations to determine the surface current. Additional "super-loop" basis functions are also needed if a body modeled by triangular patches has any "handles," as is the case for a closed body that is not simply connected, such as a torus, or for the general open-body geometry illustrated in [6]. The definition and topological properties of a "handle" can be found in [11]. The construction of a "super-loop" basis function is similar to that of Loop basis function J_n^L . The only difference is that the Loop basis function J_n^L is formed by all f_n 's attached to node n^L , while a "super-loop" basis function can be formed by all the f_n 's associated with edges that are attached to an appropriate aperture (either aperture 1 or aperture 2 in Figure 5, for example).

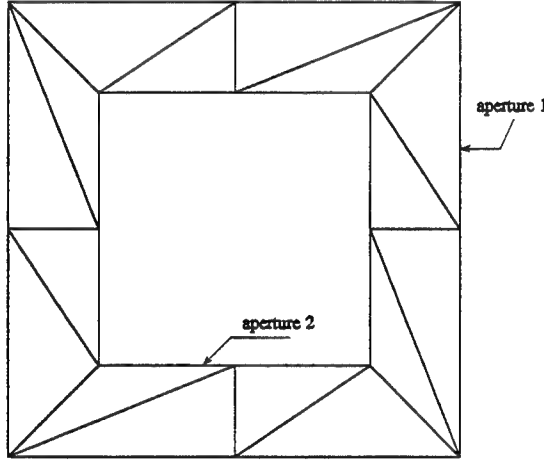


Figure 5. An object with two apertures.

With a Galerkin testing procedure, the impedance matrix elements for the three different basis function sets may be represented as

$$[Z_{orig}]_{mn} = j\omega \langle A(f_n), f_m \rangle + \langle \frac{j}{\omega} \nabla \Phi(\nabla_s \cdot f_n), f_m \rangle \quad (16)$$

$$[Z_{L/S}]_{pq} = \begin{bmatrix} B_{nm}^{LL} & B_{nm}^{SL} \\ B_{nm}^{LS} & B_{nm}^{SS} + C_{nm}^{SS} \end{bmatrix} \quad (17)$$

$$[Z_{L/T}]_{pq} = \begin{bmatrix} B_{nm}^{LL} & B_{nm}^{TL} \\ B_{nm}^{LT} & B_{nm}^{TT} + C_{nm}^{TT} \end{bmatrix} \quad (18)$$

with

$$B_{nm}^{st} = j\omega \langle A(J_n^s), J_m^t \rangle$$

$$C_{nm}^{st} = \langle \frac{j}{\omega} \nabla \Phi(\nabla_s \cdot J_n^s), J_m^t \rangle$$

where the superscripts s, t may be either L , S , or T and indicate the source and testing function types, and $\langle \rangle$ denotes the symmetric product. The brackets on the right side of (17) and (18) indicate that the matrix element is given by one of the expressions for the four different subtypes of matrix elements arising due to the two different basis and testing function types, the local subscripts m and n in (17) and (18) are assumed to be mapped appropriately into the global matrix indices p and q , and the subscripts $orig$, L/S , and L/T on Z denote the basis and testing function types. Equation (16) uses the original basis and testing functions; equation (17) uses the Loop/Star basis and testing functions; and equation (18) uses the Loop/Tree basis and testing functions.

If one compares equations (17) and (18) with (16), it is evident that the magnetic vector potential contribution to the elements of the impedance matrix appears alone in the upper portions of $Z_{L/S}$ and $Z_{L/T}$, and, therefore, is not lost in comparison with $|\nabla \Phi|$ during matrix element computation. We also note that the low-frequency formulations described in this section are valid in principle at any non-zero frequency.

III. The Forcing Function for Low-Frequency Formulations

When a Galerkin testing procedure is applied to equation (1), the left side yields the forcing function, or excitation vector $|V\rangle$ for the system of equations. Four different types of excitation vector elements can be obtained by using f_n , J_n^L , J_n^S , or J_n^T , as described in the last section. If the original basis function f_n is used as the testing function, the same excitation vector as in [6] is obtained

$$V_m^{orig} = \langle E^{inc}, f_m \rangle = \int_S E^{inc} \cdot f_m dS \quad (19)$$

where $m = 1, 2, \dots, N$, and N is the number of interior (non-boundary) edges in the triangular patch model. For simplicity in the numerical calculation, E^{inc} is often approximated by the corresponding value of E^{inc} at the centroid of each triangle. If J_n^T is used as the testing function, then

$$V_p^T = \begin{cases} V_t^{\text{orig}} , & \text{if edge } t \text{ intersects a tree branch} \\ 0 , & \text{otherwise} \end{cases} \quad (20)$$

where $p = 1, 2, \dots, N - N^L$ is the p^{th} tree branch, and N^L is the number of interior nodes in the triangular model. If J_n^S is used as the testing function, then

$$V_q^S = \sum_{i=1}^3 \frac{S_{qi} V_{qi}^{\text{orig}}}{\ell_{qi}} \quad (21)$$

where $q = 1, 2, \dots, N^{\text{star}}$, N^{star} is the number of unknowns associated with the Star basis function, and S_{qi} is a sign coefficient chosen in the same manner as for (11).

It is evident that we use the same strategy to form the excitation vectors $|V^T\rangle$ and $|V^S\rangle$ as we did in last section to develop the *Tree* and *Star* basis functions. But when J_n^L is used as the testing function, there are two ways to evaluate the excitation vector $|V^L\rangle$. In the first approach, we use a linear combination of the V_m 's given in equation (19) to construct the excitation vector $|V^L\rangle$. Applying the same procedure as for the construction of the *Loop* basis function in last section, we obtain

$$V_i^{\text{Lei}} = \sum_{j=1}^{N_t} \left(\frac{2V_2^{\text{orig}}}{l_2} - \frac{2V_3^{\text{orig}}}{l_3} \right) \quad (22)$$

where V^{orig} is given in equation (19), $i = 1, 2, \dots, N^L$, N_t is the number of triangles attached to i^{th} the interior node n^L in the triangular patch model, and the subscripts 2 and 3 refer to local edge numbers as in Figure 2. The superscript *Lei* denotes the testing function is a *Loop* testing function, and that the incident electric field is used in the calculation. In the second approach, we start with the symmetric product expression for the excitation vector with the *Loop* as the testing function:

$$V_i^{\text{Lhi}} = \langle E^{\text{inc}}, J_i^L \rangle = \sum_{j=1}^{N_t} \int_S E^{\text{inc}} \cdot J_i^L \, dS \quad (23)$$

Using a vector calculus identity [12], equation (23) can be written as

$$V_i^{\text{Lhi}} = \sum_{j=1}^{N_t} \int_S \psi_j \, \hat{n} \cdot (\nabla \times E^{\text{inc}}) \, dS \quad (24)$$

which can be further manipulated to

$$V_i^{\text{Lhi}} = -j\omega\mu \sum_{j=1}^{N_t} \int_S \psi_j (\hat{n} \cdot H^{\text{inc}}) \, dS \quad (25)$$

where ψ_j is a scalar function [9] defined over the j^{th} triangle attached to node n^L (cf. Figure 2), and H^{inc} is the incident magnetic field. If H^{inc} is approximated by the corresponding values of H^{inc} at the centroids of each triangle attached to node n^L , then

$$V_i^{\text{Lhi}} = -j\omega\mu \frac{2}{3} \sum_{j=1}^{N_t} A_j \, \hat{n} \cdot H^{\text{inc}}(\mathbf{r}_j^c) \quad (26)$$

where A_j is the area of the j^{th} triangle attached to node n^L and \mathbf{r}_j^c is the position vector to the centroid of the j^{th} triangle. The superscript *Lhi* denotes that the testing function is a *Loop* testing function, and that the incident magnetic field is used in the calculation. This result is similar to that obtained by Arvas *et al* [9], where the magnetostatic problem was solved. It is apparent from (23) to (25) that testing the incident field with the *Loop* testing function is equivalent to performing a curl operation. Comparing $|V^{\text{Lei}}\rangle$ of (22) with $|V^{\text{Lhi}}\rangle$ of (26), one notes that $|V^{\text{Lei}}\rangle$ effectively evaluates the curl of E^{inc} numerically, while for $|V^{\text{Lhi}}\rangle$ the curl operation is performed through the analytic procedure (23) to (25). In principle, either $|V^{\text{Lei}}\rangle$ or $|V^{\text{Lhi}}\rangle$ can serve as the excitation vector. However, the numerical results have demonstrated that computational advantages can be gained by using $|V^{\text{Lei}}\rangle$ in the higher frequency range and by choosing $|V^{\text{Lhi}}\rangle$ when the operation frequency is in the lower frequency range (i.e., when the scatterer is very small in terms of wavelength). This is not surprising, since evaluation of $|V^{\text{Lei}}\rangle$ over a loop results in substantial cancellation of the electric field vector over the testing path and a subsequent loss of precision when the testing path is small in terms of wavelength. Numerical results demonstrating these effects and further discussion are presented in the next section.

IV. Numerical Results

The two low-frequency vector basis functions described in the previous sections have been incorporated in a version of the patch code [6]. This new version of the patch code is referred to here as LFPATCH, which stands for Low Frequency triangular patch code. To study the behavior of the code for the different approaches, several structures have been studied over a wide frequency range. Numerical results are presented in this section comparing the inverse of the condition numbers [13] of the impedance matrix and current distributions obtained using the different basis

function sets. All the scatterers studied are modeled by triangular patches and subject to illumination by an incident plane wave.

To observe the effects of numerical precision of different computers, the examples are computed on different platforms with different precision. The two platforms used for the numerical computations are an IBM 3084QXC Mainframe and a Cray Y-MP8D/464 Supercomputer. The Cray single precision computation is effectively equivalent to the double precision computation on the IBM mainframe.

Flat Square Plate Scatterer

The first example problem considered is a square, flat plate PEC scatterer illuminated by an incident wave with the H component normal to the surface of scatterer, as shown in Figure 6. The inverse condition number obtained for the

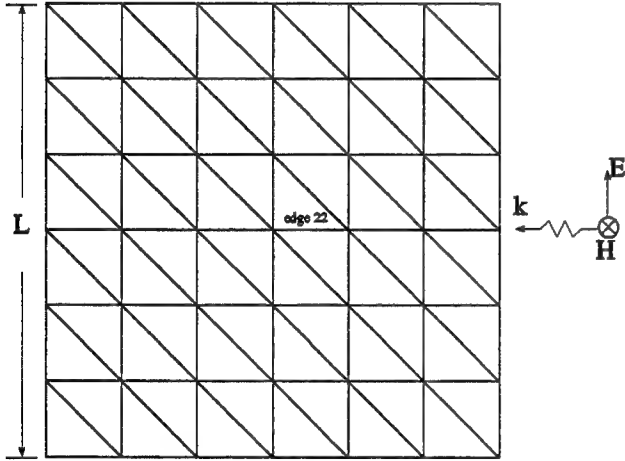


Figure 6. A triangular patch model of a flat square plate scatterer.

impedance matrix using the original, Loop/Tree, and Loop/Star basis function sets are shown in Figure 7. Figure 7(a) shows the inverse condition number for the three basis function sets obtained by running the code on the IBM mainframe using single precision, and Figure 7(b) shows the same case, but running on the Cray supercomputer. The inverse condition number for the impedance matrix using the original basis function set is found to start oscillating wildly when L/λ is smaller than about 10^{-3} for the IBM single precision result. When the impedance matrix is evaluated on the Cray, there is no oscillation, but there is a clear change in the behavior of the curve at $L/\lambda = 10^{-6}$. The inverse condition numbers for the two low-frequency formulations are essentially constant as a function of

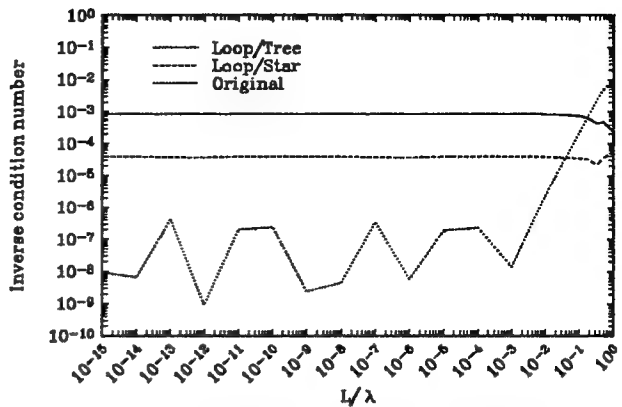


Figure 7(a). Inverse condition number for a square plate scatterer obtained using single precision on the IBM mainframe.

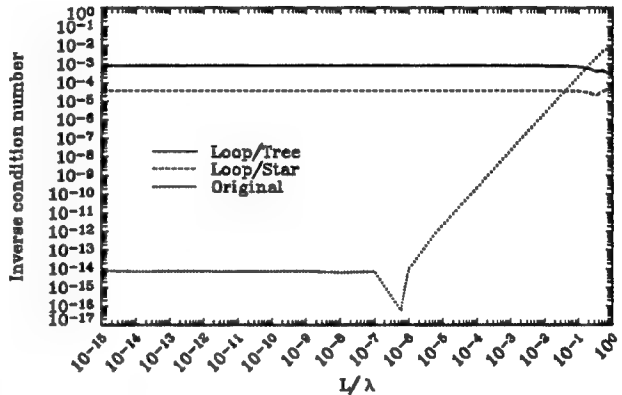


Figure 7(b). Inverse condition number for a square plate scatterer obtained using single precision on the Cray supercomputer.

frequency for L/λ smaller than about 10^{-2} regardless of the platform used. It is also noticed that the condition number obtained with the Loop/Tree basis function is more than an order of magnitude better than that obtained with the Loop/Star basis function.

The effect of using either $|V^{Lei}\rangle$ or $|V^{Lhi}\rangle$ on the computed current distribution for the flat plate scatterer is shown in Figures 8 and 9. The data for both Figures 8 and 9 were generated on the Cray supercomputer. Figures 8(a) and 9(a) show the absolute value of the real and imaginary parts of the current coefficient for edge 22 of the model (Figure 6) over a wide frequency range, while Figures 8(b) and 9(b) show an expanded plot over the higher portion of the frequency range. One observes from Figure 8(a), for which $|V^{Lei}\rangle$ is used, that good agreement is obtained for

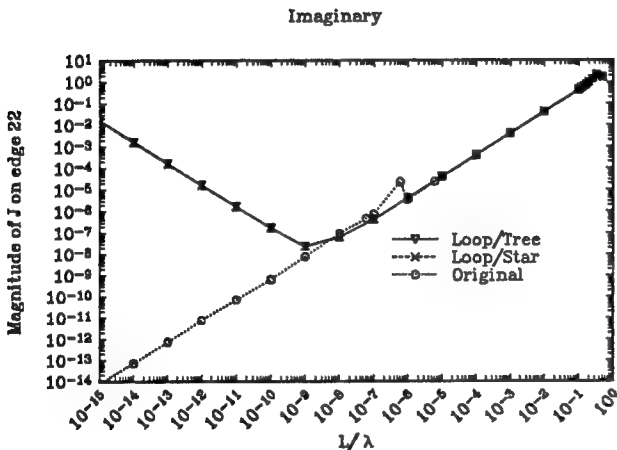
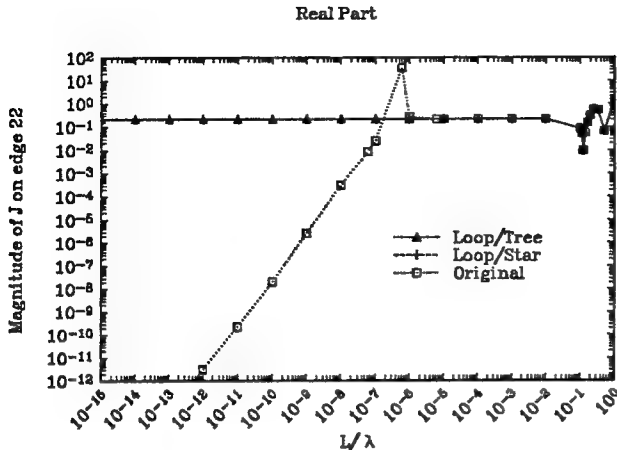


Figure 8(a). Current density at edge 22 for the flat plate scatter obtained using the excitation vector $|V^{Lei}\rangle$.

the real part of the current using the two low-frequency formulations; however, the result obtained using the original basis function becomes erratic at the frequency where the impedance matrix becomes unstable (see Figure 7(b)). The imaginary part of the current obtained with the two low-frequency approaches, on the other hand, becomes inaccurate for L/λ smaller than about 10^{-8} , where one notes that the computed current begins to rise as the frequency decreases. If we use $|V^{Lhi}\rangle$ instead, the result obtained is shown in Figure 9(a). For frequencies such that L/λ less than about 10^{-1} , the real part of the current compares well with the results in Figure 8(a); however, the imaginary part of the current for Loop/Tree and Loop/Star basis functions behaves correctly over this same frequency range, unlike the results of Figure 8(a). Expanded plots of the current

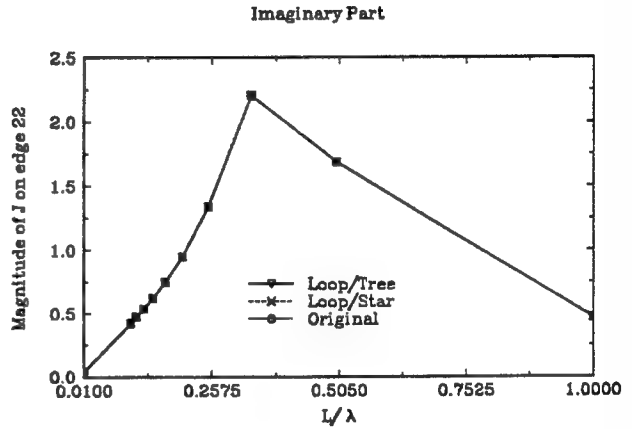
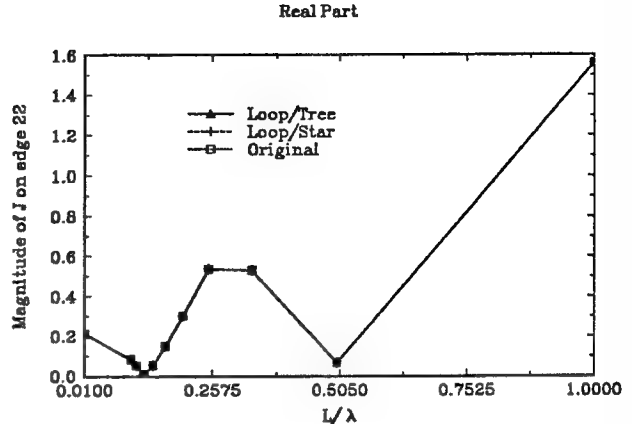


Figure 8(b). Current density at edge 22 for the flat plate scatter obtained using the excitation vector $|V^{Lei}\rangle$ (high frequency range).

obtained using the excitation vectors $|V^{Lei}\rangle$ and $|V^{Lhi}\rangle$ for the two low-frequency approaches over the higher portion of the frequency range are compared with the original EFIE procedure in Figures 8(b) and 9(b). Over the part of the frequency range shown in Figure 9(b), one observes that the currents computed using $|V^{Lhi}\rangle$ do not agree with each other or with the original EFIE. For the same frequency range, the currents obtained using $|V^{Lei}\rangle$ for the two low-frequency approaches, shown in Figure 8(b), are in excellent agreement for both the real and imaginary parts of the current for the three different solution procedures. The results shown in these figures suggest that a different *Loop* testing procedure should be used for the excitation vector calculation for the high and low frequency range. If we consider Figures 8 and 9 again, we can roughly divide the entire frequency range into three

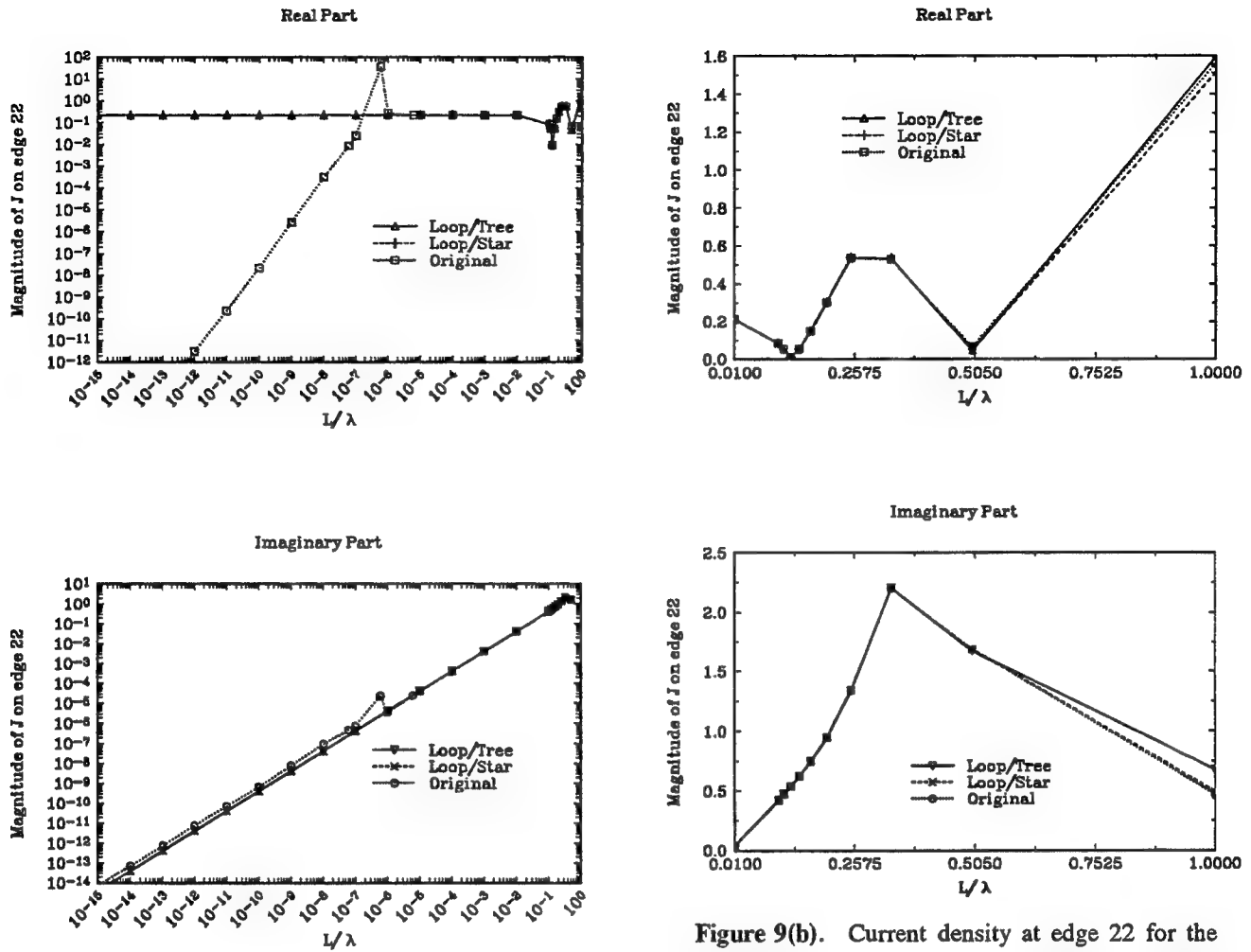


Figure 9(a). Current density at edge 22 for the flat plate scatter obtained using the excitation vector $|V^{Lhi}\rangle$.

convenient regions: region A, where L/λ varies from 10^0 to 10^{-2} ; region B, where L/λ varies from 10^{-2} to 10^{-7} ; and region C, where L/λ is smaller than 10^{-7} . In region A, the size of a triangle ($A=0.0139\lambda^2$ at $L/\lambda = 1$) is comparable in size with the wavelength. To understand the failure of $|V^{Lhi}\rangle$ in this region, we note that when $|V^{Lhi}\rangle$ was derived in the previous section, an analytic curl operation was performed around the interior node n^L via a vector calculus identity. If one recalls that the integral definition of the curl operation evaluates a vector field as an area tends to zero, which implies the field does not change rapidly around node n^L , it is recognized that the numerical application for this definition may not be appropriate in region A. As the frequency decreases, especially in region C, the size of triangle becomes very small in terms of

Figure 9(b). Current density at edge 22 for the flat plate scatter obtained using the excitation vector $|V^{Lhi}\rangle$ (high frequency range).

wavelength, and the value of $|V^{Lhi}\rangle$ becomes quite accurate. The good agreement between all of the approaches in region A for the results obtained when using $|V^{Lei}\rangle$ for two the low-frequency approaches is because all the quantities (A , Φ , E^{inc}) are evaluated at the same points, the triangle centroids, and because there is little loss of numerical accuracy due to cancellation when the triangles are not small with respect to the wavelength. When the frequency falls into region C, the variation of E^{inc} is very small over the domain of the loop basis function ($A=1.39\times10^{-16}\lambda^2$ at $L/\lambda = 10^{-7}$), and the testing procedure leads to the subtraction of very similar field quantities, causing a loss of precision in the computation of $|V^{Lei}\rangle$ for the two low-frequency approaches, which leads to unacceptable results. In region B, both $|V^{Lei}\rangle$ and $|V^{Lhi}\rangle$ for two the low-frequency approaches provide essentially the same result. For the results shown

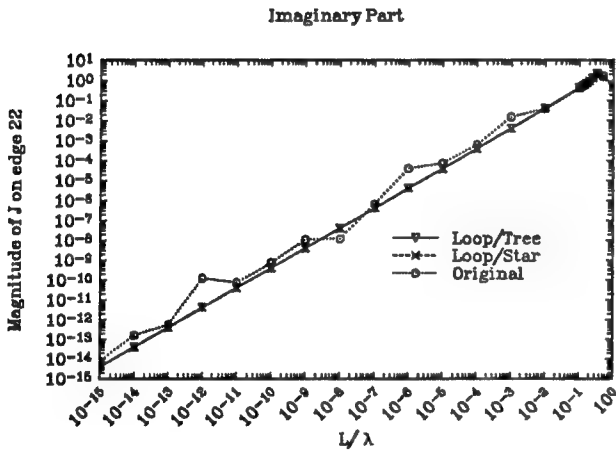
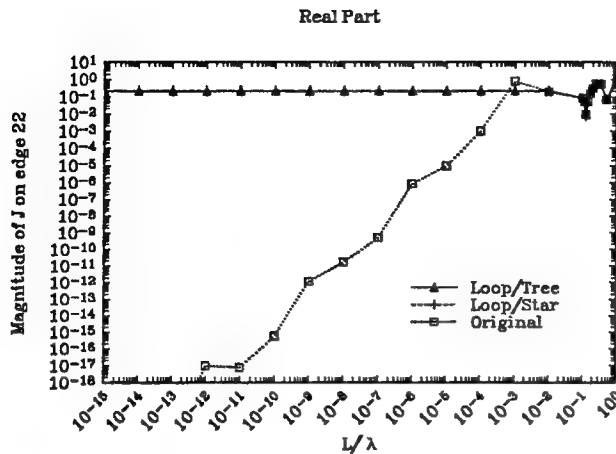


Figure 10(a). Current density at edge 22 for the flat plate scatter obtained using the excitation vector $|V^{Leh}\rangle$ on the IBM mainframe using single precision.

subsequently, we use $|V^{Lei}\rangle$ in region A, $|V^{Lhi}\rangle$ in region C for the two low-frequency approaches, and switch between the two excitation vectors in region B according to the size of triangle respect to the wavelength. We refer to this as the combined Loop testing procedure, and the corresponding excitation vector is denoted as $|V^{Leh}\rangle$. Figures 10(a) and 10(b) show the current density at edge 22 in Figure 6 obtained using the three basis function sets and on different platforms. Since the $|V^{Leh}\rangle$ is used for the Loop testing function, the results obtained with the two low-frequency approaches now agree with each other over the entire frequency shown and are stable even computed on the IBM mainframe in single precision.

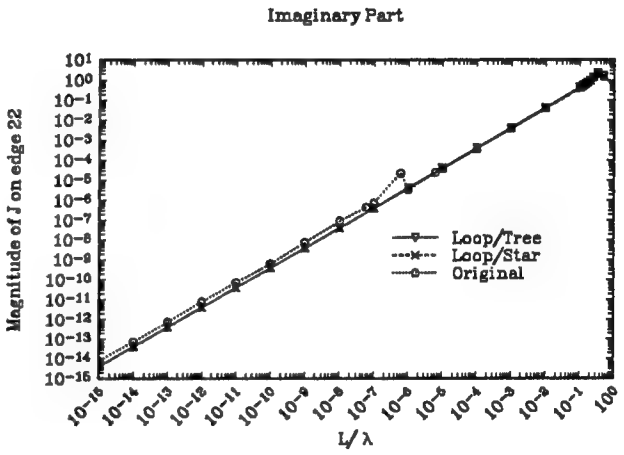
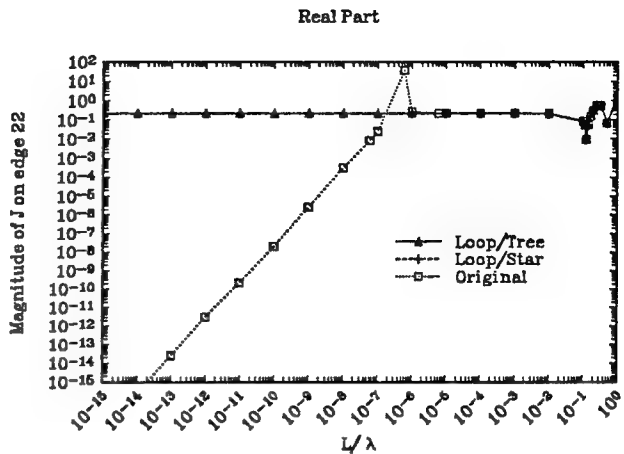


Figure 10(b). Current density at edge 22 for the flat plate scatter obtained using the excitation vector $|V^{Leh}\rangle$ on the Cray supercomputer using single precision.

Long Narrow Bent Strip

The next example presented is a long narrow ($L=30W$) strip which forms a square, open loop, as shown in Figure 11. In this example, to make a simple model with relatively few unknowns for this shape of scatterer, the sizes of triangular patches in the model are not made uniform. Results are shown in Figure 12 for the inverse condition number in this case, and they are similar to those of the previous case, except that the inverse condition number for the Loop/Tree basis function set is now about two orders of magnitude better than that of the Loop/Star basis function set. Consequently, one might expect for this case that the Loop/Tree procedure is the only one likely to provide a reasonable solution with single precision on the IBM

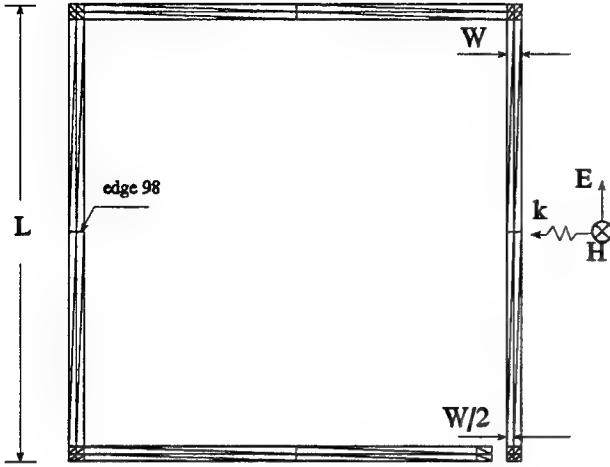


Figure 11. A long narrow bent strip ($L=30W$).

mainframe. From Figure 12(b), it can be observed that, as the precision is increased, the the inverse condition number results obtained using both procedures are large enough relative to the machine precision to expect accurate solutions, while that obtained using the original basis function set shows improvement for L/λ larger than about 10^{-6} , but again deteriorates when L/λ becomes smaller than about 10^{-6} . The results for the current on one of the edges shows behavior similar to that of in previous case.

It should be noted here, however, that scaling of the basis functions may affect the matrix conditioning [14]. Indeed, we have observed, for example, that if the edge length factor in the denominator of (11) is omitted, the Loop/Star results are worse by almost an order of magnitude. The Loop basis and testing functions are the same in both low frequency methods. Nevertheless, application of a scaling factor to the Loop functions may improve the Loop/Star and/or the Loop/Tree condition numbers and is a subject for further research.

V. Summary and Discussion

Two special method of moments solution procedures used to improve the accuracy of the numerical solution for the Electric Field Integral Equation (EFIE) in the low frequency range have been studied. Two alternate vector basis functions have been implemented in a version of the triangular patch code [6] to extend its usefulness to the low frequency range. Numerical results have been presented for two different types of structures over a wide frequency range. The inverse condition numbers of the impedance matrix and the computed current values as a function of frequency have been presented to illustrate the improvement

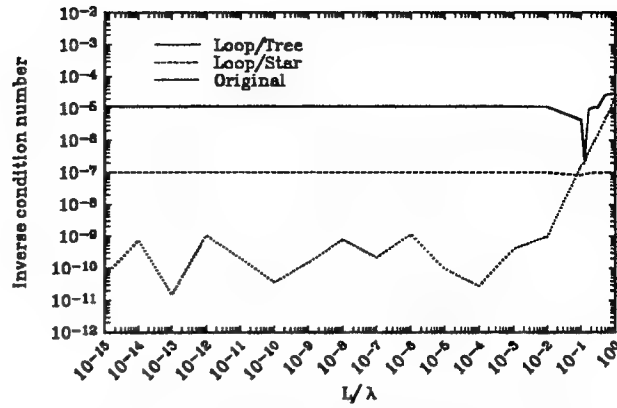


Figure 12(a). Inverse condition number for a long narrow bent strip obtained using single precision on the IBM mainframe.

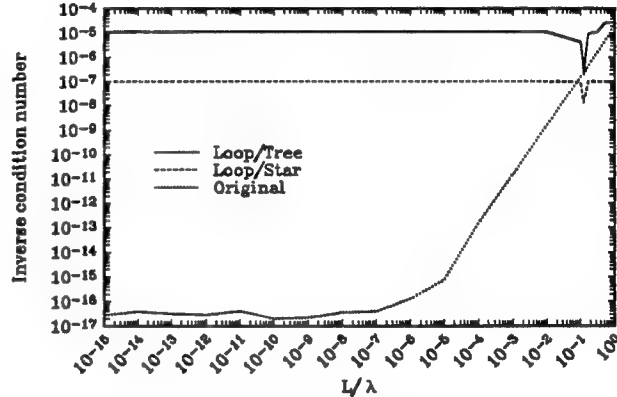


Figure 12(b). Inverse condition number for a long narrow bent strip obtained using single precision on the Cray supercomputer.

of the EFIE solution in the low-frequency range. It has been found in our implementations that using the Loop/Tree basis and testing functions usually yields a more stable impedance matrix (i.e., one with a larger inverse condition number). This is very useful when modeling a resonant structure that is small in terms of wavelength, since near the resonant frequency, the inverse condition number of the impedance matrix usually drops several orders of magnitude from that of the off-resonance case. This is also helpful when the code is running on a computer with lower precision. Additional study of scaling procedures may result in further improvements of the inverse condition numbers of one or both of the low frequency methods.

References

- [1] D. R. Wilton and A. W. Glisson, "On improving the electric field integral equation at low frequencies," *1981 Spring URSI Radio Science Meeting Digest*, p. 24, Los Angeles, CA, June 1981.
- [2] J. R. Mautz and R. F. Harrington, "An E-field solution for a conducting surface small or comparable to the wavelength," *IEEE Antennas Propagat.*, vol. AP-32, pp. 330-339, April 1984.
- [3] J. S. Lim, S. M. Rao, and D. R. Wilton, "A novel technique to calculate the electromagnetic scattering by surfaces of arbitrary shape," *1993 URSI Radio Science Meeting Digest*, p. 322, Ann Arbor, Michigan, June 1993.
- [4] W. Wu, A. W. Glisson, and D. Kajfez, "A comparison of two low-frequency formulations for the electric field integral equation," *Proceedings of the 10th Annual Review of Progress in Applied Computational Electromagnetics*, vol. II, pp. 484-491, Monterey, California, March 1994.
- [5] W. Wu, A. W. Glisson, and D. Kajfez, "Electromagnetic scattering by resonant low-frequency structures," *1994 URSI Radio Science Meeting Digest*, p. 137, Seattle, Washington, June 1994.
- [6] S. M. Rao, D. R. Wilton, and A. W. Glisson, "Electromagnetic scattering by surfaces of arbitrary shape," *IEEE Trans. Antennas Propagat.*, vol. AP-30, pp. 409-418, May 1982.
- [7] R. F. Harrington, *Field Computation by Moment Methods*. New York: Macmillan, 1968.
- [8] E. Arvas and R. F. Harrington, "Computation of the magnetic polarizability of conducting disks and the electric polarizability of apertures," *IEEE Trans. Antennas Propagat.*, vol. AP-31, pp. 719-724, Sept. 1983.
- [9] E. Arvas, R. F. Harrington, and J. R. Mautz, "Radiation and scattering from electrically small conducting bodies of arbitrary shape," *IEEE Trans. Antennas Propagat.*, vol. AP-34, pp. 66-77, Jan. 1986.
- [10] C. M. Butler, D. R. Wilton, and A. W. Glisson, *A Short Course on Fundamentals of Numerical Solution Methods in Electromagnetics*, University of Mississippi, October 1984.
- [11] S. M. Rao, "Electromagnetic scattering and radiation of arbitrarily-shaped surfaces by triangular patch modeling," Ph.D. dissertation, University of Mississippi, 1980.
- [12] J. Van Bladel, *Electromagnetic Fields*. New York: McGraw-Hill, 1964.
- [13] R. Mittra and C. A. Klein, "Stability and Convergence of Moment Method Solutions," Chapter 5 in *Topics in Applied Physics*, Volume 3, edited by R. Mittra, Springer-Verlag, 1975.
- [14] D. R. Wilton, private communication.

ELECTROMAGNETIC SCATTERING FROM TWO DIMENSIONAL ANISOTROPIC IMPEDANCE OBJECTS UNDER OBLIQUE PLANE WAVE INCIDENCE

Ahmed A. Kishk and Per-Simon Kildal*

Department of Electrical Engineering
University of Mississippi, University, MS 38677, USA

*Department of Microwave Technology
Chalmers University of Technology, S-412 96 Gothenburg, Sweden

ABSTRACT. The surface integral equations of a two dimensional (2D) anisotropic impedance object is formulated to obtain the electromagnetic scattered fields due to oblique plane wave incidence. The surface impedance is anisotropic with arbitrary principle directions. The moment method with pulse basis functions and point matching is used to reduce the surface integral equations to a matrix equation. Four different formulations are generated for the problem. The surface current distributions and the scattered far fields are verified against the analytical series solutions of circular impedance cylinders. Very good agreement between the numerical and the analytical solutions is obtained. A rectangular cylinder made of four soft surfaces is analyzed for oblique incidence to verify that the results behave as expected. The computer code is also verified by comparing the solutions of the different formulations against each other.

impedance concept, if the periods of the corrugations or strips are smaller than half the wavelength. The advantage with the surface impedance concept is that the numerical analysis of the object becomes simpler and takes shorter time. This is because the exact geometry of the loads do not need to be modelled so the problem description becomes easier and the number of unknowns can be significantly reduced.

The impedance boundary conditions (IBC) is a valid approximation under certain conditions [1], more references on the IBC can be found in [2]. The use of the IBC can simplify the analysis of some classes of complex electromagnetic problems, but it must be used with care as it may sometimes give erroneous results [3]. In order to widen the applicability of the IBC, generalized impedance boundary conditions (GIBC) was proposed in [4] and later improved for coated 2D structures [5] at the expense, however, of considerable analytical complications which requires specialized researchers to work with such problems. So far, the GIBC has only been used in connection with coated metallic surfaces without corrugations. On the other hand, the IBC has been used successfully to analyze corrugated horns and waveguides [6].

Anisotropic surface impedances have also been used to define soft and hard surfaces [7] that theoretically provides polarization independent soft and hard boundary conditions for electromagnetic waves of known propagation direction. The concept of soft and hard surfaces is also a way of thinking that can help to generate ideas for improved electromagnetic designs. Analysis tools based on the IBC are very important also to verify such thought models initially before the accurate analysis including all surface details is performed for the final design optimization. An example of how to use the concept of soft and hard surfaces to reduce the forward scattering from two dimensional (2D) structures is described in [8].

1 INTRODUCTION

Some complicated structures can be modeled approximately using the concept of surface impedance, such as e.g. corrugated objects or objects coated with lossy material or thin dielectric layers, which can even be loaded with metal strips. The surface impedance model deals with the outer boundary of the structure in terms of an equivalent surface impedance, which can be obtained from the expected local relation between the tangential components of the electric and magnetic fields on the outer boundary. This relation can be found approximately at any surface point from the solution of a canonical problem which is similar to the local geometry around this point. The equivalent surface impedance is generally anisotropic, even if the coating is isotropic, in particular at an outer surface that has two different principle curvatures. Also, structures with periodic surface discontinuities such as corrugations or strip loaded coatings can be modeled using the anisotropic surface

This work was performed while Professor Kishk was on sabbatical leave at Chalmers University of Technology.

Previous papers have formulated the problem of electro-

magnetic scattering from 2D impedance structures due to a normally incident plane wave [9-10]. Oblique incidence is considered in [11-12] for the case of an isotropic surface impedance. In [11], the finite element method is used for an arbitrary cross-section, and in [12] the finite difference method in the frequency domain is used for elliptic cross-sections. In [13] the method of moment is used for bodies of revolution with anisotropic surface impedance. In the present paper the problem of scattering from a two dimensional object of arbitrary cross-section and anisotropic surface impedance is formulated for oblique plane wave incidence.

The present formulation is based on the surface integral equation and solved using the method of moment with pulse basis functions and point matching. With the proper implementation of this simple expansion and testing, accurate numerical solutions are obtained. The numerical solution is verified with the exact solution of a circular cylinder [14]. Different surface integral formulations are generated and found useful in the verification of the numerical solutions for arbitrary objects. In addition a theoretical example is constructed for which the E-field solution for TM_z incidence should be equal to the H-field solution for TE_z incidence. The example is a 2D object with rectangular cross section made of four surfaces which are soft as defined in [7] for the given oblique incidence. Finally, it should be mentioned that the formulations in the present paper describe what in [15] is referred to as a harmonic 2D solutions, and that these can be extended to an arbitrary incident field, i.e. three dimensional sources, by considering a spectrum of 2D solutions [15].

2 IMPEDANCE BOUNDARY CONDITION

The impedance boundary condition (IBC) for exterior fields E_0 and H_0 at a surface S with surface normal \hat{u}_n can generally be stated in vector form as

$$E_0 - (E_0 \cdot \hat{u}_n) \hat{u}_n = \eta_0 \tilde{\eta} \cdot (\hat{u}_n \times H_0) \quad (1)$$

where η_0 is the free space intrinsic impedance and

$$\tilde{\eta} = \eta_{\xi\xi} \hat{u}_\xi \hat{u}_\xi + \eta_{\xi\xi} \hat{u}_\xi \hat{u}_\xi + \eta_{\xi\xi} \hat{u}_\xi \hat{u}_\xi + \eta_{\xi\xi} \hat{u}_\xi \hat{u}_\xi \quad (2)$$

is the anisotropic surface impedance dyad, given in terms of its components in a local surface coordinate system defined by the unit vectors \hat{u}_ξ , \hat{u}_ξ and \hat{u}_n with $\hat{u}_\xi \perp \hat{u}_\xi$ and $\hat{u}_n = \hat{u}_\xi \times \hat{u}_\xi$. We can also express this in a matrix form

as

$$\begin{bmatrix} E_\xi \\ E_\xi \end{bmatrix} = \eta_0 [\eta] \begin{bmatrix} H_\xi \\ -H_\xi \end{bmatrix} \quad (3)$$

with

$$[\eta] = \begin{bmatrix} \eta_{\xi\xi} & \eta_{\xi\xi} \\ \eta_{\xi\xi} & \eta_{\xi\xi} \end{bmatrix} \quad (4)$$

where E_ξ , E_ξ (H_ξ , H_ξ) are the components of the E-field (H-field) along \hat{u}_ξ and \hat{u}_ξ , respectively. The IBC is based on the fact that we in some cases know exactly or approximately the field solution inside the surface, and that this solution is the same or approximately the same for all excitations (incidences) considered. The inner field solution can then be characterized by the relations between its E- and H-fields at the surface, i.e. the surface impedances $\eta_{\xi\xi}$, $\eta_{\xi\xi}$, $\eta_{\xi\xi}$ and $\eta_{\xi\xi}$. The IBC applied to the exterior fields thereby means that the continuity of the E- and H-fields are enforced over the surface S (when the form of the inner field solution is given).

When the surface impedance is anisotropic, we can normally find two principle directions \hat{u}_ξ and \hat{u}_ξ which make η diagonal, according to

$$\tilde{\eta} = \eta_{\xi\xi} \hat{u}_\xi \hat{u}_\xi + \eta_{\xi\xi} \hat{u}_\xi \hat{u}_\xi \quad (5)$$

From now on we will let \hat{u}_ξ and \hat{u}_ξ denote these principle directions of η . The following example will explain how \hat{u}_ξ and \hat{u}_ξ are related to the surface structure. Let us assume a corrugated surface with the corrugations parallel with \hat{u}_ξ . Then, the \hat{u}_ξ component of the E-field will be shorted by the thin ridges between the corrugations, so that $\eta_{\xi\xi} = 0$, and the \hat{u}_ξ component E_ξ of the E-field will couple to a TE to \hat{u}_n mode in each corrugation, which acts as a shorted parallel plate waveguide if the corrugation are straight. The E_ξ inside the parallel plate waveguide is related to H_ξ according to (see e.g. [7])

$$\eta_0 \eta_{\xi\xi} = - \frac{E_\xi}{H_\xi} = - j \eta_c \tan(k_n d) \quad (6)$$

where k_n is the component of the wave number in the \hat{u}_n direction inside the corrugations, d is the corrugation depth, and η_c is the intrinsic impedance inside the corrugation. This assumption is good when k_n is known and independent of the angle of incidence. This is the case for corrugations that are transverse to the direction of incidence of the wave.

We can transform η in (5) to any coordinate system defined by vectors $\hat{u}_\tau \perp \hat{u}_n$ and $\hat{u}_z = \hat{u}_n \times \hat{u}_\tau$ according to

$$\eta = \eta_{zz} \hat{u}_z \hat{u}_z + \eta_{z\tau} \hat{u}_z \hat{u}_\tau + \eta_{\tau z} \hat{u}_\tau \hat{u}_z + \eta_{\tau\tau} \hat{u}_\tau \hat{u}_\tau \quad (7)$$

where

$$\begin{aligned}\eta_{zz} &= \eta_{\xi\xi} (\hat{u}_\xi \cdot \hat{u}_z) (\hat{u}_\xi \cdot \hat{u}_\tau) - \eta_{\xi\xi} (\hat{u}_\xi \cdot \hat{u}_z) (\hat{u}_\xi \cdot \hat{u}_\tau) \\ \eta_{\tau z} &= \eta_{\xi\xi} - \eta_{\xi\xi} (\hat{u}_\xi \cdot \hat{u}_z) (\hat{u}_\xi \cdot \hat{u}_z) \\ \eta_{z\tau} &= (\eta_{\xi\xi} - \eta_{\xi\xi}) (\hat{u}_\xi \cdot \hat{u}_\tau) (\hat{u}_\xi \cdot \hat{u}_\tau) \\ \eta_{\tau\tau} &= \eta_{\xi\xi} (\hat{u}_\xi \cdot \hat{u}_z) (\hat{u}_\xi \cdot \hat{u}_\tau) - \eta_{\xi\xi} (\hat{u}_\xi \cdot \hat{u}_z) (\hat{u}_\xi \cdot \hat{u}_\tau)\end{aligned}\quad (8)$$

3 FORMULATION

Consider a two dimensional (2D) anisotropic impedance scatterer of infinite extent in the z -direction and with arbitrary cross section (Fig. 1). For this geometry, there are two distinct regions V_1 and V_0 , where V_1 constitutes the impedance body which is bounded by the surface S and V_0 is the unbounded region outside S . The surface S is described by the contour C in the xy -plane and has an outward surface normal \hat{u}_n which is orthogonal to \hat{u}_z . The surface is characterized by the anisotropic surface impedance dyad η , as defined in the previous section, where $\eta_{\xi\xi}$, $\eta_{\xi\xi}$, \hat{u}_ξ and \hat{u}_τ are allowed to vary around C .

V_0 is the exterior region characterized by the permittivity and permeability of the free space (ϵ_0 , μ_0). The total electric and magnetic fields in region V_0 are denoted by E_0 and H_0 , respectively. The excitation is assumed to be an obliquely incident plane wave propagating in the x -direction

$$\begin{aligned}\hat{k} &= -\hat{u}_r(\theta_{inc}, \phi_{inc}) = -\cos\phi_{inc} \sin\theta_{inc} \hat{u}_x \\ &\quad - \sin\phi_{inc} \sin\theta_{inc} \hat{u}_y - \cos\theta_{inc} \hat{u}_z\end{aligned}\quad (9)$$

making an angle θ_{inc} with the z -axis and ϕ_{inc} measured from

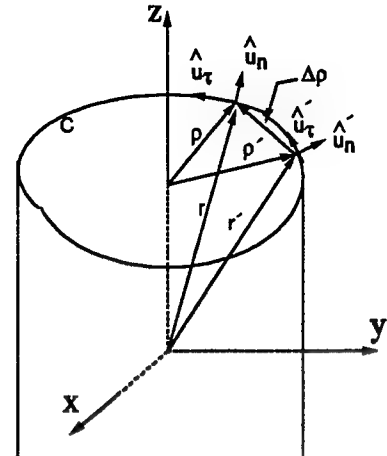


Fig. 1 Geometry of the original problem.

the x -axis in the xy -plane. The incident field at a point r is therefore described by

$$E^{inc} = E_m (E^p \cos\alpha_{inc} + E^n \sin\alpha_{inc}) e^{-jk_0 \hat{k} \cdot r} \quad (10)$$

$$H^{inc} = (\hat{k} \times E^{inc}) / \eta_0 \quad (11)$$

where

$$r = x \hat{u}_x + y \hat{u}_y + z \hat{u}_z = \rho + z \hat{u}_z \quad (12)$$

$$\begin{aligned}E^p &= -\hat{u}_\theta(\theta_{inc}, \phi_{inc}) = -\hat{u}_x \cos\theta_{inc} \cos\phi_{inc} \\ &\quad - \hat{u}_y \cos\theta_{inc} \sin\phi_{inc} + \hat{u}_z \sin\theta_{inc}\end{aligned}\quad (13)$$

$$E^n = -\hat{u}_\phi(\phi) = \hat{u}_x \sin\phi_{inc} - \hat{u}_y \cos\phi_{inc} \quad (14)$$

E^p and E^n are the unit vectors corresponding to polarizations parallel (TM_z case) and normal (TE_z) to the plane defined by the z -axis and \hat{k} . The polarization angle α_{inc} is the angle the incident electric field makes with the plane of incidence. If $\alpha_{inc}=0$, the plane wave is TM_z polarized (θ -polarized), and if $\alpha_{inc}=\pi/2$ the plane wave is TE_z polarized (ϕ -polarized). k_0 is the wave number in the free space, \hat{u}_x , \hat{u}_y and \hat{u}_z are the unit vectors in the direction of x , y , and z , respectively and $\hat{u}_r(\theta_{inc}, \phi_{inc})$, $\hat{u}_\theta(\theta_{inc}, \phi_{inc})$, and $\hat{u}_\phi(\phi_{inc})$ are the unit vectors in the direction of r , θ_{inc} , and ϕ_{inc} in the spherical coordinate system. The complex constant E_m is the amplitude of the plane wave.

Using the equivalence principle the object can be replaced by the material of the region V_0 and the equivalent electric surface current J and the equivalent magnetic surface current M on the surface, which produce zero fields in the region V_1 and $(E_0 - E^{\text{inc}})$ and $(H_0 - H^{\text{inc}})$ in the region V_0 , where

$$J = \hat{u}_n \times H_0 \quad \text{and} \quad M = E_0 \times \hat{u}_n \quad \text{on } S \quad (15)$$

For infinite cylindrical structures the electric and magnetic currents are assumed to be of the form

$$J(r') = J(\rho') e^{jk_z z} \quad (16)$$

and correspondingly for M , where $k_z = k \cos \theta_{\text{inc}}$. These assumptions are evident for isotropic surface boundaries as explained in [15], and we see no reason why it should not apply to anisotropic impedance surfaces as well. The magnetic and electric vector potentials, A and F , due to the equivalent currents J and M can be written as

$$\begin{Bmatrix} A(r) \\ F(r) \end{Bmatrix} = \begin{Bmatrix} \mu_0 \\ \epsilon_0 \end{Bmatrix} \int_{-\infty}^{\infty} \int_C G(r, r') \begin{Bmatrix} J(r') \\ M(r') \end{Bmatrix} d\tau' dz' \quad (17)$$

where $G(r, r')$ is the three-dimensional free space Green's function and $d\tau'$ is the integration increment along the contour C in the cross-sectional plane. The three-dimensional Green's function can be written as

$$G(r, r') = \frac{e^{-jk(|\rho - \rho'|^2 + (z-z')^2)^{1/2}}}{(|\rho - \rho'|^2 + (z-z')^2)^{1/2}} \quad (18)$$

where r and r' are the position vectors of the observation and source points, respectively. ρ and ρ' are the cylindrical vector coordinates of the field and source points, respectively. After performing the known z integral we get

$$\begin{Bmatrix} A(r) \\ F(r) \end{Bmatrix} = \frac{e^{jk_z z}}{4j} \begin{Bmatrix} \mu_0 \\ \epsilon_0 \end{Bmatrix} \int_C H_0^{(2)}(k_\rho |\rho - \rho'|) \begin{Bmatrix} J(\rho') \\ M(\rho') \end{Bmatrix} d\tau' \quad (19)$$

where $k_\rho = \sqrt{k^2 - k_z^2}$, $k_z = -k \cos \theta_i$, and $H_0^{(2)}()$ is the Hankel function of zeroth order and second type. This

indicates that the magnetic vector potential of the three dimensional form is the same as the two dimensional form multiplied by $\exp(jk_z z)$ [15]. Both $J(\rho')$ and $M(\rho)$ have components both in the longitudinal \hat{u}_z direction and in the transverse \hat{u}_τ direction, i.e.

$$\begin{Bmatrix} J \\ M \end{Bmatrix} = \begin{Bmatrix} J_z \\ M_z \end{Bmatrix} \hat{u}_z + \begin{Bmatrix} J_\tau \\ M_\tau \end{Bmatrix} \hat{u}_\tau \quad \text{on } S, \quad (20)$$

where the transverse unit tangent is defined by

$$\hat{u}_\tau = \hat{u}_z \times \hat{u}_n \quad (21)$$

where \hat{u}_n is the unit normal to S .

We can now obtain the electric and magnetic fields $E(\rho)$ and $H(\rho)$ due to the electric current $J(\rho')$ by using

$$H(r) = \frac{1}{\mu_0} \nabla \times A(r) \quad \text{and} \quad E(r) = -\frac{j}{\omega \epsilon_0} \nabla \times H(r) \quad (22)$$

where the ∇ operator in our case can be expressed as

$$\nabla = \nabla_\tau \hat{u}_\tau - jk_z \hat{u}_z \quad \text{and} \quad \nabla_\tau = \frac{\partial}{\partial x} \hat{u}_x + \frac{\partial}{\partial y} \hat{u}_y. \quad (23)$$

After some mathematical manipulations the electric and magnetic fields due to the electric currents can be expressed in operator form as shown in Appendix A. Expressions are given for $E_{zz}(J_z)$, $E_{tz}(J_z)$, $E_{zt}(J_\tau)$, and $E_{tt}(J_\tau)$ which are each of the components of the vector operator $E_{\tan}(J)$ for the tangential E-field at a point ρ on S , and similarly for the tangential H-field vector operator $H_{\tan}(J)$, i.e.

$$E_{\tan}(J) = [E_{zz}(J_z) + E_{zt}(J_\tau)] \hat{u}_z + [E_{tz}(J_z) + E_{tt}(J_\tau)] \hat{u}_\tau \quad (24)$$

$$H_{\tan}(J) = [H_{zz}(J_z) + H_{zt}(J_\tau)] \hat{u}_z + [H_{tz}(J_z) + H_{tt}(J_\tau)] \hat{u}_\tau$$

The fields due to the magnetic current $M(\rho')$ can be obtained using duality (ch. 3, sec. 3-2 [16]).

We will now apply the impedance boundary condition in Eq. (1) to the field at S . The result is an integral equation

in terms of the unknown electric and magnetic currents of the form

$$\begin{aligned} -\frac{1}{\eta_0} E_{\tan}(J) - \frac{1}{\eta_0} E_{\tan}(M) + \hat{\eta} \cdot (\hat{u}_n \times \{H_{\tan}(J) \\ + H_{\tan}(M)\}) = \frac{1}{\eta_0} E_{\tan}^{inc} - \hat{\eta} \cdot (\hat{u}_n \times H_{\tan}^{inc}) \quad \text{on } S \end{aligned} \quad (25)$$

We will now use (1) to express M_z and M_τ in terms of J_z and J_τ , as follows. We cross multiply both sides of (1) with \hat{u}_n and use (15) to obtain

$$M = \eta_0 (\hat{\eta} \cdot J) \times \hat{u}_n \quad (26)$$

We substitute (20) for J and multiply both sides with \hat{u}_z and \hat{u}_τ to get

$$\begin{aligned} M_z = M \cdot \hat{u}_z &= \eta_0 [\hat{\eta} \cdot (J_z \hat{u}_z + J_\tau \hat{u}_\tau)] \times \hat{u}_n \cdot \hat{u}_z \\ &= -\eta_0 (\eta_{\tau\tau} J_\tau + \eta_{zz} J_z) \\ M_\tau = M \cdot \hat{u}_\tau &= \eta_0 [\hat{\eta} \cdot (J_z \hat{u}_z + J_\tau \hat{u}_\tau)] \times \hat{u}_n \cdot \hat{u}_\tau \\ &= \eta_0 (\eta_{zz} J_z + \eta_{\tau\tau} J_\tau) \end{aligned} \quad (27)$$

respectively, with η_{zz} , $\eta_{z\tau}$, $\eta_{\tau z}$ and $\eta_{\tau\tau}$ defined in (8). By inserting (27) in (24) and (24) in (25) we get the final integral equation

$$\begin{aligned} -\frac{1}{\eta_0} [E_{zz}(J_z) + E_{z\tau}(J_\tau) + E_{\tau z}(M_\tau)] + \eta_{zz} [H_{\tau z}(J_z) \\ + H_{\tau\tau}(J_\tau) + H_{z\tau}(M_z) + H_{\tau z}(M_\tau)] - \eta_{z\tau} [H_{z\tau}(J_\tau) + \\ H_{zz}(M_z) + H_{z\tau}(M_\tau)] = \frac{1}{\eta_0} (E_z^{inc} - \eta_{zz} H_\tau^{inc} + \eta_{z\tau} H_z^{inc}) \end{aligned} \quad (28)$$

$$\begin{aligned} -\frac{1}{\eta_0} [E_{\tau z}(J_z) + E_{\tau\tau}(J_\tau) + E_{z\tau}(M_\tau)] + \eta_{\tau z} [H_{\tau z}(J_z) \\ + H_{\tau\tau}(J_\tau) + H_{z\tau}(M_z) + H_{\tau z}(M_\tau)] - \eta_{\tau\tau} [H_{z\tau}(J_\tau) + \\ H_{zz}(M_z) + H_{z\tau}(M_\tau)] = \frac{1}{\eta_0} (E_\tau^{inc} - \eta_{\tau z} H_\tau^{inc} + \eta_{\tau\tau} H_z^{inc}) \end{aligned} \quad (29)$$

where

$$\begin{aligned} E_{z\tau}(M_\tau) &= -\eta_{z\tau} H_{z\tau}(J_\tau) - \eta_{zz} H_{\tau z}(J_z) \\ E_{\tau z}(M_z) &= \eta_{\tau z} H_{\tau z}(J_\tau) + \eta_{\tau\tau} H_{z\tau}(J_z) \\ E_{\tau\tau}(M_\tau) &= -\eta_{\tau\tau} H_{\tau\tau}(J_\tau) - \eta_{zz} H_{\tau z}(J_z) \\ H_{zz}(M_z) &= -\eta_{\tau\tau} E_{zz}(J_\tau) - \eta_{\tau z} E_{z\tau}(J_z) \\ H_{z\tau}(M_\tau) &= \eta_{z\tau} E_{z\tau}(J_\tau) + \eta_{zz} E_{\tau z}(J_z) \\ H_{\tau z}(M_z) &= -\eta_{\tau z} E_{\tau z}(J_\tau) - \eta_{\tau\tau} E_{\tau\tau}(J_z) \\ H_{\tau\tau}(M_\tau) &= \eta_{\tau\tau} E_{\tau\tau}(J_\tau) + \eta_{zz} E_{\tau z}(J_z) \end{aligned} \quad (30)$$

Following the method of moments, the object contour C is divided into N linear segments with length ΔC^i as in [9], $i = 1, 2, \dots, N$ and each current component is expanded into N unknown constant coefficients multiplied by the pulse basis function P^i . In an equation form, the unknown currents can be expressed as

$$J_{\{z\}} = \sum_i^N I_{\{z\}}^i P^i \quad (31)$$

where $I_{\{z\}}^i$ are the unknown current coefficients and $P^i =$
1 on the subdomain i and zero else where. Substituting (31) into the operators defined in the Appendix A and then substitute the operators in (28) and (29) and satisfy (28) and (29) at the match point (middle of the segments), the integral equation reduces to a matrix of order $2N$, which can be written in the form

$$\begin{aligned} \{[Z] + [Y][\eta_s] + [\eta_f]([Y] + [Z][\eta_s])\}[I] \\ = [E] + [\eta_f][H] \end{aligned} \quad (32)$$

here the different matrices and column vectors are defined as in the following. The matrices $[Z]$ and $[Y]$ consist of four submatrices according to

$$[Z] = \begin{bmatrix} Z_{zz}^{ij} & Z_{z\tau}^{ij} \\ Z_{\tau z}^{ij} & Z_{\tau\tau}^{ij} \end{bmatrix} \quad \text{and} \quad [Y] = \begin{bmatrix} Y_{zz}^{ij} & Y_{z\tau}^{ij} \\ Y_{\tau z}^{ij} & Y_{\tau\tau}^{ij} \end{bmatrix} \quad (33)$$

The elements of the Z and Y matrices are given in Appendix B. The first suffix of the subscript refers to the field component and the second suffix refers to the electric current component. The superscript ij is the element order

in the submatrix; i for the matching field point in the middle of the segment i and j for the j 's unit pulse. $[E]$ and $[H]$ are the excitation vectors due to the electric and magnetic fields, respectively defined by

$$[E] = \begin{bmatrix} E_z^{i \text{ inc}} \\ E_\tau^{i \text{ inc}} \end{bmatrix} \quad \text{and} \quad [H] = \begin{bmatrix} H_\tau^{i \text{ inc}} \\ -H_z^{i \text{ inc}} \end{bmatrix} \quad (34)$$

where i denotes the matching field point in the middle of the segment i . The expressions of these elements are given in Appendix B. The column vector containing the unknowns can be expressed as

$$[I] = \begin{bmatrix} I_z^j \\ I_\tau^j \end{bmatrix} \quad (35)$$

The matrices $[\eta_f]$ and $[\eta_s]$ each consists of four submatrices according to

$$[\eta_s] = \begin{bmatrix} \eta_{zz}^{ij} & \eta_{z\tau}^{ij} \\ \eta_{\tau z}^{ij} & \eta_{\tau\tau}^{ij} \end{bmatrix} \quad \text{and} \quad [\eta_f] = \begin{bmatrix} \eta_{rz}^{ij} & \eta_{r\tau}^{ij} \\ -\eta_{zr}^{ij} & -\eta_{z\tau}^{ij} \end{bmatrix} \quad (36)$$

where each submatrix is a diagonal matrix with $\eta_{\gamma\nu}^{ij}$ = the value of the surface impedance $\eta_{\gamma\nu}$ at the middle of the segment i when $i = j$ and zero otherwise, where the subscripts γ and ν refer to z and τ . Once the matrices Z and Y are created and the excitation vectors $[E]$ and $[H]$ are filled and substituted in equation (32), the moment matrix system (32) can be solved to obtain the unknown current coefficients in (35).

4 DIFFERENT FORMULATIONS

In order to account for different formulations, one may use the E-field integral equation ($E_{\tan} = 0$), or H-field integral equation ($H_{\tan} = 0$), both applied just inside the surface S with the equivalent currents defined in (15). Then combining them to obtain the combined field integral equations or use the IBC as an integral equation as described above. The moment matrix of these integral equations can be obtained if the matrix equation (32) is written in the following form

$$\begin{aligned} & \{\alpha([Z] + [Y][\eta_s]) + \beta[\eta_f]([Y] + [Z][\eta_s])\}[I] \\ & = \alpha[E] + \beta[\eta_f][H] \end{aligned} \quad (37)$$

where α and β are, respectively, the combination parameters weighing the electric field and the magnetic field just inside the surface S [2]. Thus different field formulations can be obtained by different selections of α and β . These formulations can be obtained according to Table I.

Table I
Generation of different formulations

| Formulation type | α | β |
|------------------|----------|------------------|
| IBCE | 1. | 0. |
| IBCH | 0. | $-[\eta_f]^{-1}$ |
| IBCC | 1. | $-[\eta_f]^{-1}$ |
| IBC | 1. | 1. |

IBCE (IBCH) implies that the E-field (H-field) boundary condition is applied, i.e. the tangential electric (magnetic) field is assumed zero just inside the surface of the object, using the implementation of the IBC approximation for the magnetic current, i.e. the magnetic current is related to the electric current via the surface impedance as in Eqn (27). The third formulation IBCC denotes the combination of IBCE and IBCH on the impedance surface. The fourth formulation, IBC implies that the IBC is implemented explicitly on the equivalent currents and the tangential fields. The solutions from the IBCE and IBCH formulations are not unique where there are internal structure resonance frequencies. These cases can be treated by using the IBCC or IBC formulations. The solution of the IBC formulation is also not unique when the impedance is zero (perfect conducting case) or inductive. The problem of nonuniqueness will not be investigated in this paper. Interested readers may find this treated in [2] and [17].

5 SCATTERED FIELDS

Once any of the above formulations is solved the scattered field can be computed from the obtained electric current distribution. The field will be scattered along a cone of half angle $\theta = \pi - \theta_{\text{inc}}$ around the structure. In the cylindrical coordinate system it is sufficient to compute the z-components of the electric and magnetic fields in the far zone when r and ρ are much larger than the wavelength and the maximum cross sectional diameter of the object. This can be obtained, first, by using the large argument approxima-

tion of the Hankel functions in the field operators defined in Appendix A and also in their dual operators due to the magnetic currents, Second, neglect the high order terms of $1/\rho$. Third, substitute the magnetic current by the electric current and the surface impedance using (27). It can be found that in the cylindrical coordinate system, only z and ϕ components of the fields are contributing to the far field. The spherical components of the electric field E_θ and E_ϕ , which are more appropriate to use in the oblique incidence case, can be obtained from the cylindrical field components E_z and H_z , respectively. Therefore, by using simple transformations the spherical electric field components can be written as

$$E_\phi^{sc}(\theta, \phi) = \eta \sqrt{\frac{j}{8\pi k_\rho \rho}} e^{-j(k_\rho \rho - k_z z)} \sum_{i=1}^N \Delta C^i e^{jk_\rho (\hat{u}_\rho \cdot \hat{p}_i)} \times I_{r_i} [k_\rho \eta_{rr} - k_0 (\hat{u}_\rho \cdot \hat{u}_{n_i}) - k_z \eta_{zr} (\hat{u}_\rho \cdot \hat{u}_{r_i})] + I_{z_i} [k_\rho \eta_{rz} - k_z \eta_{zz} (\hat{u}_\rho \cdot \hat{u}_{r_i})] \quad (38)$$

$$E_\theta^{sc}(\theta, \phi) = \sqrt{\frac{j}{8\pi k_\rho \rho}} e^{-j(k_\rho \rho - k_z z)} \sum_{i=1}^N \Delta C^i e^{jk_\rho (\hat{u}_\rho \cdot \hat{p}_i)} \times I_{z_i} [k_0 (\hat{u}_\rho \cdot \hat{u}_{n_i}) \eta_{zz} - k_\rho] + I_{r_i} [k_0 (\hat{u}_\rho \cdot \hat{u}_{n_i}) \eta_{zr} - k_z (\hat{u}_\rho \cdot \hat{u}_{r_i})] \quad (39)$$

In this paper the scattered fields are computed and normalized to $\sqrt{2j/\pi k_\rho \rho}$.

6 RESULTS

First, to verify the code, a circular cylinder with an arbitrary anisotropic impedance is considered. The parameters are $ka=3.0$, with arbitrary surface impedance of $\eta_{zz}=0.5+j0.1$, $\eta_{zr}=0.3+j0.6$, $\eta_{rz}=0.3+j0.5$ and $\eta_{rr}=0.7-j0.3$ (these values are chosen arbitrarily) and the plane wave parameters are $\theta_{inc}=45^\circ$, $\phi_{inc}=180^\circ$, and $\alpha_{inc}=45^\circ$. The surface electric current components are plotted in Fig. 2a (against the exact solution obtained from the series solution in [14]), ten and twenty segments per wavelength are used in the numerical solution based on the IBC formulation. Acceptable results are obtained with 10 segments per wavelength and more accurate results are obtained when 20 segments are used. Also the scattered far fields are computed and plotted in Fig. 2b and compared with the exact solutions. It is obvious that the solution using 20 segments per wavelength gives more accurate results within the whole ϕ -range. Notice that neither the fields nor the currents

distribution are symmetric around the plane of incidence because the incident wave is chosen to have both TE_z and TM_z incident polarizations simultaneously and also because of the inequality of the surface impedances values η_{zz} and η_{rz} .

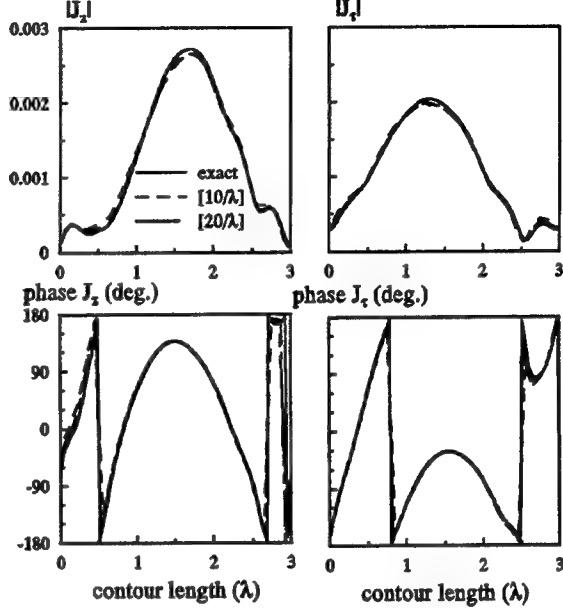


Fig. 2a Exact and numerical current distribution on a circular cylinder with, $ka=3.0$, $\eta_{zz}=0.5+j1$, $\eta_{zr}=0.3+j6$, $\eta_{rz}=0.3+j5$ and $\eta_{rr}=0.7-j3$, illuminated by a plane wave with $\theta_i=45^\circ$, $\phi_i=180^\circ$, and $\alpha_i=45^\circ$.

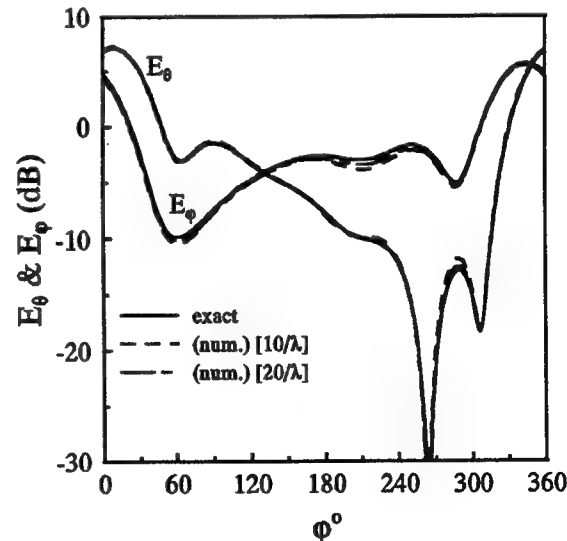


Fig. 2b Exact and numerical scattered far fields of the example in Fig. 2a.

Now we consider some practical configurations. The first example is again a circular cylinder, but now with $\eta_{zz} = -j50.0$, $\eta_{zr} = \eta_{rz} = \eta_{rr} = 0.0$, $\theta_{inc} = 45^\circ$, $\phi_{inc} = 180^\circ$, and $\alpha_{inc} = 45^\circ$. This surface impedance represents transverse corrugations. The actual corrugated surface is very difficult to analyze [18]. The impedance model is much simpler and easier to analyze and an exact solution can be found as considered in [14]. The exact solution is compared with the present moment method solution using the IBC formulation with 20 segment per wavelength. The current distributions are plotted in Fig. 3a. Very good agreement can be noticed between both solutions. Also, one must notice that the current component J_z normal to the corrugations is almost zero. This is expected as J must flow entirely along the corrugations. This is a good verification that the surface impedance considered in this example is a good approximation of the transverse corrugated cylinder. The scattered far fields are given in Fig. 3b. The exact and the numerical solutions are indistinguishable. Notice also, the skew symmetry between E_θ and E_ϕ components which is also expected for oblique incidence and 45 degree polarization. For normal incidence E_θ and E_ϕ could be equal for all ϕ for 45 degree incident polarization if the impedance $\eta_{zz} = \infty$.

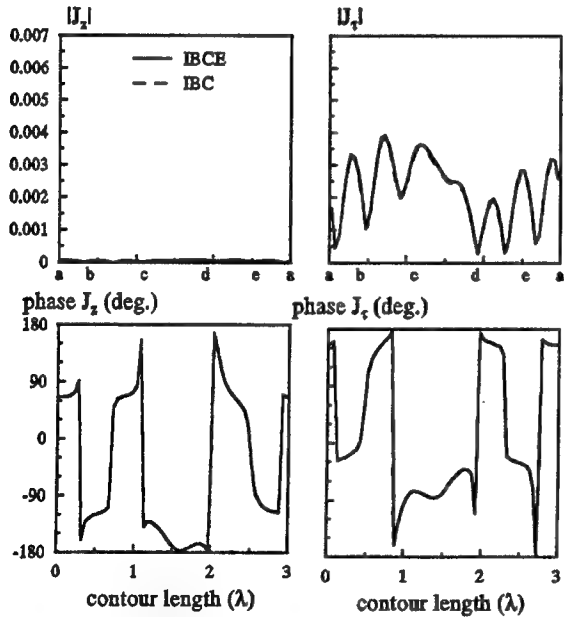


Fig. 3a Exact and numerical current distribution on a circular cylinder with, $ka=3.0$, and $\eta_{zz}=-j50.0$, $\eta_{zr}=\eta_{rz}=\eta_{rr}=0.0$, illuminated by a plane wave with $\theta_{inc}=45^\circ$, $\phi_{inc}=180^\circ$, and $\alpha_{inc}=45^\circ$.

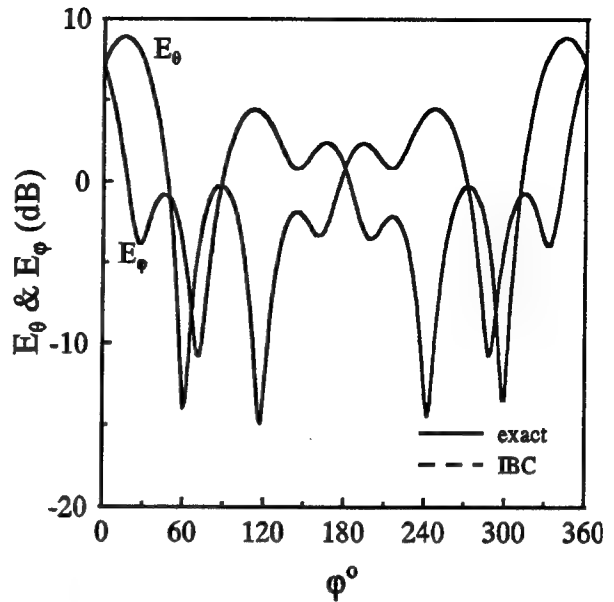


Fig. 3b Exact and numerical scattered far fields of the example in Fig. 3a.

An impedance cylinder with square cross-section is considered as shown in Fig. 4a. This geometry has no analytic solution. The surface impedance is used to model soft corrugated surfaces. The corrugations of the sides A and C are considered to be along the transverse direction parallel to the xy -plane with an equivalent surface impedance assumed to be $\eta_{zz}=-j50.0$, $\eta_{zr}=\eta_{rz}=\eta_{rr}=0.0$. The

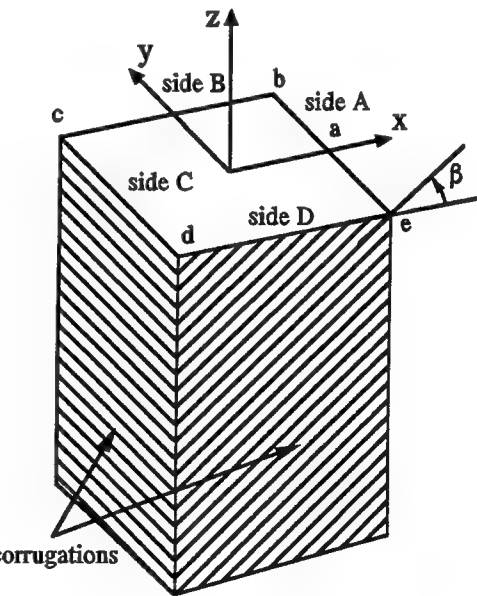


Fig. 4a Geometry of a corrugated square cylinder.

corrugations on the sides B and D are assumed to be of the same parameters as that on sides A and C (i.e. has the same surface impedance with respect to the coordinates of the corrugations with $\eta_{zz} = -j50.0$, $\eta_{zr} = \eta_{rz} = \eta_{rr} = 0.0$), but tilted by an angle $\beta = 45^\circ$ with the x-axis. The equivalent surface impedance with respect to the object surface coordinates using (8) is given as $\eta_{zz} = \eta_{zr} = \eta_{rz} = \eta_{rr} = -j25.0$ on the side D and $\eta_{zz} = \eta_{rr} = -j25.0$, $\eta_{zr} = \eta_{rz} = +j25.0$ on the side B. The electric surface current components and the scattered far fields are computed due to a plane wave with $\theta_i = 45^\circ$, $\alpha_i = 0^\circ$ (TM_z polarization) and $\phi_i = 180^\circ$. The current distributions are plotted in Fig. 4b from the IBCE and IBC formulations. Notice that the x-axis of the upper two figures (current magnitude) are indicated by the letters a, b, c, d, e, and a which are corresponding to the surface positions given in Fig. 4a. In the lower two figures (current phase) the x-axis is indicated by the contour length starting from the point a on Fig. 4a. The scattered far fields are plotted in Fig. 4c. In these figures the solution from the IBCE and IBC formulations are presented and compared against each other. It can be noticed that the solutions obtained from both formulations are in good agreement with each other. It is clear that the scattered fields are symmetric around the xz-plane (plane of incidence) when $\phi_i = 180^\circ$ because of the object symmetry around this plane and because of the pure TM_z polarization of the wave incident. The ϕ -component of the scattered field is zero along the plane of incidence in the forward and the back scattered directions because of the skew symmetry of the J_r component which is obvious from the phase distribution of the current. When the incident wave is TE_z polarized, the current distributions and the scattered far fields are given in Figs. 5a and 5b, respectively. One should notice that the scattered E-field E_θ and E_ϕ for TM_z polarization of the incident wave is nearly equal to the E_ϕ and E_θ , respectively for TE_z polarization of the incident wave. This corresponds to E-field for TM_z polarization being equal to H-field for TE_z polarization, which is expected as the cylinder is close to soft (it would have been ideally soft if $\eta_{zz} = \infty$) and therefore has polarization independent scattering characteristics according to [7]. The electric current component normal to the corrugations must be zero. To check this for our example the electric current components along and normal to the corrugations are computed from the currents in Fig. 4b and 5a and plotted in Figs. 6a and 6b, respectively. One should notice that the current components normal to the corrugations are nearly zero for both TM_z and TE_z incidence as expected. This can also be considered as a verification of the code.

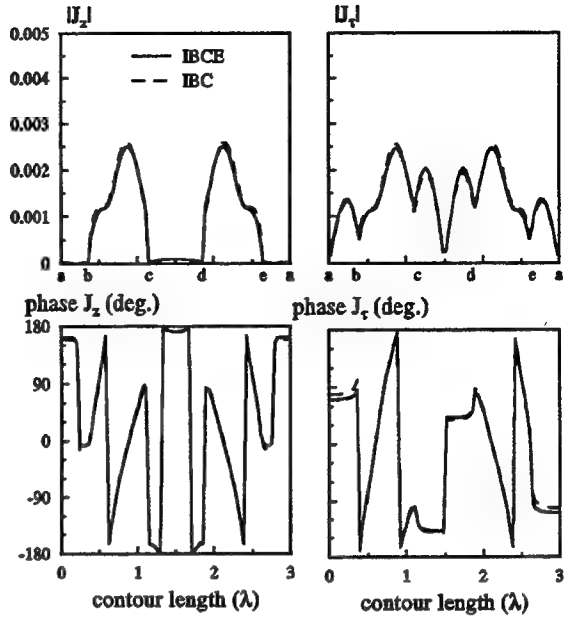


Fig. 4b Electric current distribution of the geometry in Fig. 4a with, $\eta_{zz} = -j50.0$, $\eta_{zr} = \eta_{rz} = \eta_{rr} = 0.0$ on side A and C, $\eta_{zz} = \eta_{zr} = \eta_{rz} = \eta_{rr} = -j25.0$ on the side D and $\eta_{zz} = \eta_{rr} = -j25.0$, $\eta_{zr} = \eta_{rz} = +j25.0$ on the side B. The cylinder side length = 0.75λ . The plane wave with $\theta_{inc} = 45^\circ$, $\alpha_{inc} = 0^\circ$, and $\phi_{inc} = 180^\circ$.

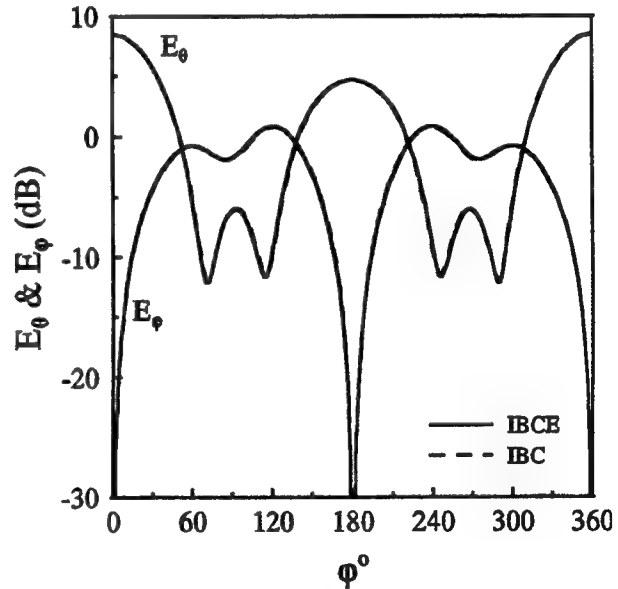


Fig. 4c, numerical scattered far field of the object in Fig. 4a with the parameters in Fig. 4b.

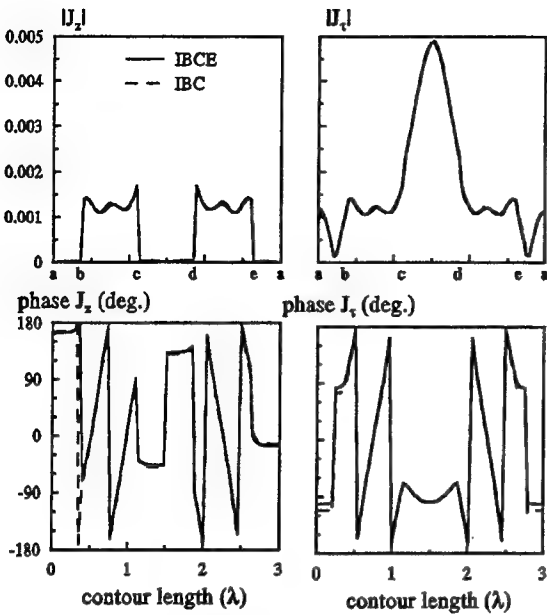


Fig. 5a Electric current distribution of the geometry in Fig. 4a with the same parameters in Fig. 4a and the plane wave with $\theta_{\text{inc}} = 45^\circ$, $\alpha_{\text{inc}} = 90^\circ$, and $\phi_{\text{inc}} = 180^\circ$.

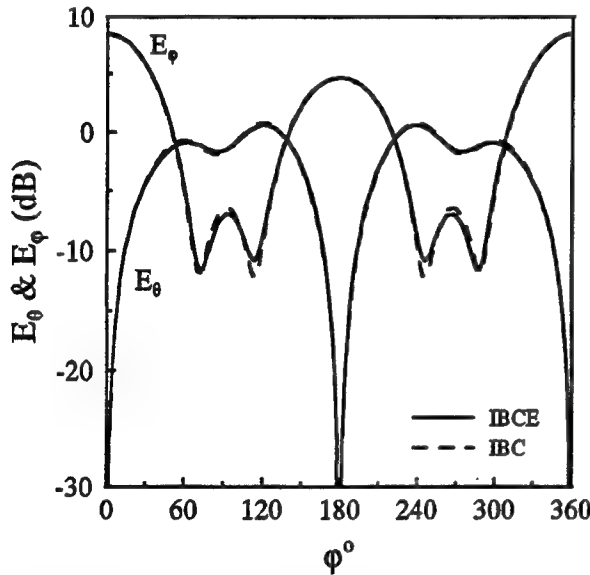


Fig. 5b, numerical scattered far field of the object in Fig. 4a with the parameters in Fig. 5a.

7 CONCLUSIONS

The integral equation for the problem of electromagnetic scattering from arbitrary 2D objects with anisotropic surface impedance due to obliquely incident plane wave with arbitrary linear polarization is derived. The surface impedance is anisotropic with an arbitrary principal direction.

The integral equations are solved by the method of moments with pulse basis functions and point matching. Four different surface integral equations are actually implemented. In the numerical evaluation of the matrix elements four point Gaussian quadrature is used. It is also found that 10 basis functions per wavelength gives reasonable results, but 20 segments per wave length is enough for most applications to obtain accurate results in the near and far fields. For objects with large cross sections in terms of wavelength more segments may be needed in order to get full convergence in weak field regions or in regions of rapidly varying currents. The numerical solutions are verified against the analytical solutions of circular cylinders. A theoretical example is constructed for which the E-field solution for TM_z incidence should be equal to the H-field solution for TE_z incidence. The example is a cylinder with square cross section with soft surfaces, such as corrugations that are tilted to become normal to the k vector for the given oblique incidence. The results are found to behave as expected. This example illustrates the significance of the present solution in order to simplify complex structures that may be very difficult to solve using other models. The IBC is valid for perfectly electric conducting surfaces where the surface impedance is zero as well as to all

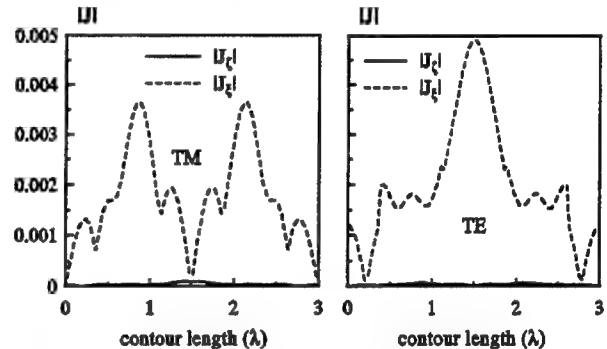


Fig. 6. The amplitude of the current distribution along and normal to the corrugation in Fig. 4a. (a) for the case in Fig. 4b and (b) for the case in Fig. 5a.

surfaces of finite surface impedances. If the impedance is infinite (perfect magnetic conductor) one must use another formulation based on the surface admittance which can be obtained from applying duality on (1) (not presented here). We may refer to this boundary condition as the admittance boundary condition (ABC). Therefore, it is expected that the numerical accuracy will deteriorate when the surface impedance values are much larger than the values used in this paper. To improve that one may use the ABC formulation, which is expected to be more accurate in such cases. This subject and this formulation will be considered in a future study with some discussions on the accuracy and limitations on these formulations.

REFERENCES

- [1] T. B. A. Senior, "Approximate boundary conditions," *IEEE Trans. Antennas Propagat.*, vol. 29, pp. 826-829, 1981.
- [2] A. A. Kishk, "Electromagnetic scattering from composite objects using a mixture of exact and impedance boundary conditions," *IEEE Trans. Antennas Propagat.*, vol. AP-39, pp. 826-833, 1991.
- [3] J. R. Wait, "Use and misuse of impedance boundary conditions in electromagnetics", *Proc. PIERS Symposium*, Boston, MA, p. 358, July 1989.
- [4] T. B. A. Senior and J. L. Volakis, "Derivation and application of a class of generalized boundary conditions," *IEEE Trans. Antennas Propagat.*, vol. AP-37, pp. 1566-1572, 1989.
- [5] D. J. Hoppe and Y. Rahmat-Sami, "Scattering by superquadric dielectric-coated cylinders using higher order impedance boundary conditions," *IEEE Trans. Antennas Propagat.*, vol. 40, pp. 1513-1523, 1992.
- [6] K. A. Iskander, L. Shafai, A. Frandsen, and J. E. Hansen, "Application of impedance boundary conditions to numerical solution of corrugated circular horns, *IEEE Trans. Antennas Propagat.*, vol. 30, pp. 366-372, 1982.
- [7] P.-S. Kildal, "Artificially soft and hard surfaces in electromagnetics," *IEEE Trans. Antennas Propagat.*, vol. 38, pp. 1537-1544, 1990.
- [8] P.-S. Kildal, A. A. Kishk, and A. Tengs, "Reduction of forward scattering from cylindrical objects using hard surfaces," submitted to *IEEE Trans. Antennas Propagat.*, April 1995.
- [9] P. M. Goggans, "A combined method-of-moments and approximate boundary condition solution for scattering from a conducting body with a dielectric-filled cavity," *Ph.D. Dissertation*, Auburn University, 1990.
- [10] A. A. Kishk, and P. M. Goggans, "Electromagnetic scattering from two-dimensional composite objects," *ACES Journal*, vol. 9, no. 1, pp.32-39, 1994.
- [11] Gordon, R., and A. A. Kishk, "An efficient finite element method for determining the scattering from lossy cylinders using the impedance boundary condition and an absorbing boundary condition due to oblique incident," *9th Annual Review of Progress in Applied Comput. Electromagnetics, Conf. Proc.*, pp. 871-878, 1993.
- [12] Yan, Jun, R.K. Richard, and A. A. Kishk, "Electromagnetic scattering from impedance elliptic cylinders using finite difference method (oblique incidence), *Journal of Electromagnetics*, vol. 15, pp. 157-173, 1995.
- [13] A. W. Glisson, M. Orman, and D. Koppel, "Electromagnetic scattering by a body of revolution with a general anisotropic impedance boundary condition," *IEEE Antennas Propagat. Soc. Int. Symp. Dig.*, vol. 4, pp. 1997-2000., June 1992.
- [14] A. A. Kishk, and P.-S. Kildal, "Electromagnetic scattering from a circular cylinder with an anisotropic surface impedance due to an obliquely incident plane wave," *Microwave and Optical Technology Letters*, vol. 10, no. 3, 1995.
- [15] P.-S. Kildal, S. Rengarajan, and A. Moldsvor, Analysis of nearly cylindrical antennas and scattering problems using a spectrum of two-dimensional solutions," submitted to *IEEE Trans. Antennas Propagat.*, April 1995.
- [16] R. F. Harrington, *Time-Harmonic Electromagnetic fields*, McGraw-Hill Book Company, 1961.
- [17] J. M. Putnam and L. N. Medgyesi-Mitschang, "Combined field integral equation formulation for inhomogeneous two- and three-dimensional bodies: The junction problem," *IEEE Trans. Antennas Propagat.*, vol. AP-39, pp. 667-672, No. 5, 1991.
- [18] G. Manara, G. Pelosi, A. Monorchio, and R. Cocciali, "Plane-wave scattering from cylinders with transverse corrugations," *Electronics Letters*, vol. 31, pp. 437-438, 1995.

APPENDIX A

Electric and magnetic field operators due to the electric current components are expressed as

$$E_{zz}(J_z) = -\frac{k_p^2}{4\omega\epsilon_0} \int_C J_z H_0^{(2)}(k_p\Delta\rho) dl' \quad (A-1)$$

$$E_{rz}(J_z) = \frac{-jk_p k_z}{4\omega\epsilon_0} \int_C J_z H_1^{(2)}(k_p\Delta\rho) (\hat{u}_r \cdot \Delta\hat{\rho}) dl' \quad (A-2)$$

$$E_{rz}(J_r) = \frac{-jk_z k_p}{4\omega\epsilon_0} \int_C J_r H_1^{(2)}(k_p\Delta\rho) (\hat{u}_r' \cdot \Delta\hat{\rho}) dl' \quad (A-3)$$

$$\begin{aligned} E_{rr}(J_r) = & -\frac{1}{4\omega\epsilon_0} \int_C k^2 J_r \{ (\hat{u}_r' \cdot \hat{u}_r) H_0^{(2)}(k_p\Delta\rho) \\ & - \frac{k_p}{\Delta\rho} H_1^{(2)}(k_p\Delta\rho) (\hat{u}_r' \cdot \hat{u}_r) - k_p [k_p H_0^{(2)}(k_p\Delta\rho) \\ & - \frac{2}{\Delta\rho} H_1^{(2)}(k_p\Delta\rho)] (\hat{u}_r' \cdot \Delta\hat{\rho}) (\hat{u}_r \cdot \Delta\hat{\rho}) \} dl' \end{aligned} \quad (A-4)$$

$$H_{zz}(J_z) = 0 \quad (A-5)$$

$$H_{rz}(J_z) = -\frac{1}{4} \int_C J_z H_1^{(2)}(k_p\Delta\rho) (\hat{u}_n \cdot \Delta\hat{\rho}) dl' \quad (A-6)$$

$$H_{rz}(J_r) = -\frac{k_p}{4j} \int_C J_r H_1^{(2)}(k_p\Delta\rho) (\hat{u}_n' \cdot \Delta\hat{\rho}) dl' \quad (A-7)$$

$$H_{rr}(J_r) = -\frac{k_z}{4} \int_C J_r H_0^{(2)}(k_p\Delta\rho) (\hat{u}_r \cdot \hat{u}_n') dl' \quad (A-8)$$

here the first suffix of the subscript denotes field component and the second suffix denotes the current component. $H_1^{(2)}(\rho)$ is the Hankel function of the first order and second type and $\Delta\rho = |\rho - \rho'|$ as shown in Fig. 1. The hat is used to indicate the unit vectors. In the above equations the prime is used to indicate the source coordinates. The field operators due to the magnetic currents can be obtained using the duality.

APPENDIX B

The matrix elements of the impedance Z and Y are given below as

$$Z_{zz}^{ij} = -\frac{k_\rho^2}{4k_0} \int_{\Delta C^j} H_0^{(2)}(k_\rho \Delta\rho^{ij}) d\tau' \quad (B-1a)$$

$$Z_{zz}^{ii} = -\frac{k_\rho^2}{4k_0} \Delta C^j [1 - \frac{2j}{\pi} (\ln(\frac{\Delta C^j \gamma k_\rho}{4}) + 1)] \quad (B-1b)$$

$$Z_{rz}^{ij} = \frac{-jk_\rho k_z}{4\omega \epsilon_0} \int_{\Delta C^j} H_1^{(2)}(k_\rho \Delta\rho^{ij}) (\hat{u}_r^i \cdot \Delta\hat{\rho}^{ij}) d\tau' \quad (B-3)$$

$$Z_{rz}^{ii} = 0 \quad (B-2b)$$

$$Z_{zr}^{ij} = -\frac{j k_z k_\rho}{4\omega \epsilon_0} \int_{\Delta C^j} H_1^{(2)}(k_\rho \Delta\rho^{ij}) (\hat{u}_r^j \cdot \Delta\hat{\rho}^{ij}) d\tau' \quad (B-3a)$$

$$Z_{zr}^{ii} = 0 \quad (B-3b)$$

$$\begin{aligned} Z_{rr}^{ij} &= -\frac{1}{4k_0} \int_{\Delta C^j} \{ k^2 (\hat{u}_r^j \cdot \hat{u}_r^i) H_0^{(2)}(k_\rho \Delta\rho^{ij}) \\ &\quad - \frac{k_\rho}{\Delta\rho^{ij}} H_1^{(2)}(k_\rho \Delta\rho^{ij}) (\hat{u}_r^j \cdot \hat{u}_r^i) - k_\rho [k_\rho H_0^{(2)}(k_\rho \Delta\rho^{ij}) \\ &\quad - \frac{2}{\Delta\rho^{ij}} H_1^{(2)}(k_\rho \Delta\rho^{ij})] (\hat{u}_r^j \cdot \Delta\hat{\rho}^{ij}) (\hat{u}_r^i \cdot \Delta\hat{\rho}^{ij}) \} d\tau' \end{aligned} \quad (B-4a)$$

$$Z_{rr}^{ii} = \frac{2k_\rho}{4k_0} H_1^{(2)}(\frac{k_\rho \Delta C^i}{2}) + \frac{k_0^2 \Delta C^i}{4k_0} [1 - \frac{2j}{\pi} \ln(\frac{\Delta C^i \gamma k_\rho}{4}) - 1] \quad (B-4b)$$

$$Y_{zz}^{ij} = 0 \quad (B-5)$$

$$Y_{rz}^{ij} = -\frac{jk_\rho}{4} \int_{\Delta C^j} H_1^{(2)}(k_\rho \Delta\rho^{ij}) (\hat{u}_n^i \cdot \Delta\hat{\rho}^{ij}) d\tau' \quad (B-6a)$$

$$Y_{rz}^{ii} = \frac{1}{2} \quad (B-6b)$$

$$Y_{zr}^{ij} = -\frac{k_\rho}{4j} \int_{\Delta C^j} H_1^{(2)}(k_\rho \Delta\rho^{ij}) (\hat{u}_n^j \cdot \Delta\hat{\rho}^{ij}) d\tau' \quad (B-7a)$$

$$Y_{zr}^{ii} = -\frac{1}{2} \quad (B-7b)$$

$$Y_{rr}^{ij} = -\frac{k_z}{4} \int_{\Delta C^j} H_0^{(2)}(k_\rho \Delta\rho^{ij}) (\hat{u}_r^i \cdot \hat{u}_n^j) d\tau' \quad (B-8a)$$

$$Y_{rr}^{ii} = 0 \quad (B-8b)$$

The above integrals are performed numerically using Gausquadra-ture method of 4 points where $\Delta\rho^{ij} = |\rho^i - \rho'|$ and ρ' for the segment j . The excitation matrix elements are given as

$$E_z^{i inc} = \frac{E_m}{\eta_0} \sin \theta_{inc} \cos \alpha_{inc} e^{jk_\rho (\hat{u}_\rho \cdot \rho^i)} \quad (B-9)$$

$$E_r^{i inc} = \frac{E_m}{\eta_0} (E^p \cos \alpha_{inc} + E^n \sin \alpha_{inc}) \cdot \hat{u}_r^i e^{jk_\rho (\hat{u}_\rho \cdot \rho^i)} \quad (B-10)$$

$$H_z^{i inc} = \frac{1}{\eta_0} \sin \theta_{inc} \sin \alpha_{inc} e^{jk_\rho (\hat{u}_\rho \cdot \rho^i)} \quad (B-18)$$

$$H_r^{i inc} = \frac{E_m}{\eta_0} \cos \theta_i (E^p \sin \alpha_{inc} - E^n \cos \alpha_{inc}) \cdot \hat{u}_r^i e^{jk_\rho (\hat{u}_\rho \cdot \rho^i)} \quad (B-19)$$

where the superscript i denotes the middel of the segment i .

Electromagnetic Scattering by an Arbitrarily Shaped Surface with an Anisotropic Impedance Boundary Condition

Allen W. Glisson

Department of Electrical Engineering
University of Mississippi
University, MS 38677

Mark Orman, Frank Falco, and Donald Koppel
Riverside Research Institute
330 West 42nd St.
New York, NY 10036

Abstract - The problem of electromagnetic scattering from arbitrarily shaped, imperfectly conducting surfaces that can be represented by an anisotropic impedance boundary condition is solved numerically using the electric field integral equation and a triangular patch model for the surface. The anisotropic impedance boundary condition function is described by a constant surface dyadic within each triangular face. The procedure is validated by comparison of numerical results obtained with the triangular patch model with body of revolution model results for problems involving scattering by spheres and cylinders having uniform or anisotropic impedance boundary conditions.

I. Introduction

Many problems of interest in electromagnetic scattering involve imperfectly conducting bodies. The impedance boundary condition (IBC) [1] is often used to model specific classes of such bodies in electromagnetic scattering problems. The IBC is an approximate boundary condition that relates the tangential electric and magnetic fields at the body surface via an impedance parameter, which is a dyadic in the case of an anisotropic surface impedance. When the approximation is valid, it can be used effectively to reduce the number of unknowns required in the numerical solution process by a factor of two. Senior has examined the conditions for which the IBC is valid [2], and Mitzner has presented a surface integral equation formulation for scattering by bodies that are represented by an IBC [3]. The impedance relationship is often obtained through the solution of a canonical problem, such as scattering of a plane wave from an imperfectly conducting ground plane having the constitutive parameters of the scatterer of

interest, and the relationship is then assumed to apply locally to the nonplanar surface of the scatterer. The IBC represents a good approximation in such cases if the magnitude of the complex refractive index of the scatterer material is much greater than unity and if the radius of curvature of the scatterer is sufficiently large. The impedance boundary condition has been used to model high-conductivity scatterers, absorbing coatings, plasma coatings, corrugated surfaces, rough surfaces, and other configurations [4-8]. The applicability of various types of integral equations in modeling IBC problems has been studied by various investigators [9-14]. Numerical solutions for scattering by arbitrarily shaped bodies having isotropic IBC's have been presented using a pulse expansion, point matching procedure by Sebak and Shafai [15] and using the triangular patch modeling method by Glisson [16]. The use of more accurate generalized impedance boundary conditions in the numerical solution of two-dimensional electromagnetic scattering problems has also been demonstrated [17] and higher order IBC's applied to bodies of revolution have been presented [18]. Anisotropic surface impedances have been employed in frequency selective surfaces by Orta *et al* [19]. Numerical solutions for bodies of revolution with anisotropic IBC's have been presented in [20], and a comparison of different integral equation formulations for bodies of revolution with anisotropic IBC's has been presented in [21].

In this work the solution of electromagnetic scattering problems involving an arbitrarily shaped body with an anisotropic impedance boundary condition is formulated and implemented. The triangular patch model described by Rao *et al* [22] serves as the basis for the development. The triangular patch code originally employed the electric field integral equation (EFIE) formulation and was applicable only to scattering problems involving perfectly conducting

bodies, which could be either closed bodies or thin open surfaces. In this work the anisotropic IBC model is included in the EFIE to represent an approximate model for specific classes of imperfectly conducting closed bodies. The implementation permits modeling of objects that are relatively thin in terms of wavelength [23]. Results are validated by comparison of patch code results with results obtained with a body of revolution solution procedure. The formulation of the surface integral equation is presented briefly in Section II, and the numerical implementation is described in Section III. Numerical results are given in Section IV.

II. Integral Equation Formulation

The electric field integral equation for a body having an impedance boundary condition can be developed from the equivalence principle [24] by first removing the scatterer from the medium in which it resides and placing equivalent electric and magnetic surface currents \mathbf{J} and \mathbf{M} along the surface forming the boundary of the scatterer in the original problem. The equivalent currents radiate in an infinite homogeneous region and are defined by the relations $\mathbf{J} = \hat{\mathbf{n}} \times \mathbf{H}$ and $\mathbf{M} = \mathbf{E} \times \hat{\mathbf{n}}$, where \mathbf{E} and \mathbf{H} are the total electric and magnetic fields at the surface of the scatterer in the original problem. With the equivalent currents defined in this manner, they will radiate the correct scattered field for the original problem in the region exterior to the scatterer, and will radiate the negative of the incident field in the region interior to the scatterer surface. The EFIE for the impedance body can therefore be written as

$$-\hat{\mathbf{n}} \times \hat{\mathbf{n}} \times \mathbf{E}^i = \hat{\mathbf{n}} \times \hat{\mathbf{n}} \times \mathbf{E}^s, \quad \mathbf{r} \rightarrow S^- \quad (1)$$

where \mathbf{E}^i is the incident electric field, \mathbf{E}^s is the scattered electric field, and $\hat{\mathbf{n}}$ is the outward directed unit normal at the surface of the scatterer. Eq. (1) is valid in the limit as the observation point \mathbf{r} approaches the surface from the interior, denoted by S^- . A similar equation valid in the limit as \mathbf{r} approaches the surface from the exterior may be obtained from the definition of the equivalent magnetic current. The equation which results after the limit operations are performed is the same in both cases.

The scattered electric field \mathbf{E}^s may be represented in terms of potential functions as

$$\mathbf{E}^s(\mathbf{r}) = -j\omega \mathbf{A}(\mathbf{r}) - \nabla \Phi(\mathbf{r}) - \frac{1}{\epsilon} \nabla \times \mathbf{F}(\mathbf{r}) \quad (2)$$

where

$$\mathbf{A}(\mathbf{r}) = \mu \int_S \mathbf{J}(\mathbf{r}') G(\mathbf{r}, \mathbf{r}') dS' \quad (3a)$$

$$\Phi(\mathbf{r}) = \frac{1}{\epsilon} \int_S \sigma(\mathbf{r}') G(\mathbf{r}, \mathbf{r}') dS' \quad (3b)$$

$$\mathbf{F}(\mathbf{r}) = \epsilon \int_S \mathbf{M}(\mathbf{r}') G(\mathbf{r}, \mathbf{r}') dS' \quad (3c)$$

and where

$$G(\mathbf{r}, \mathbf{r}') = \frac{e^{-jk|\mathbf{r}-\mathbf{r}'|}}{4\pi|\mathbf{r}-\mathbf{r}'|} \quad (4)$$

In (3) and (4) \mathbf{r} and \mathbf{r}' represent the observation and source coordinates, respectively, ϵ , μ , and k are the permittivity, permeability, and the wavenumber of the exterior region, respectively, and σ is the equivalent electric surface charge density, which is related to \mathbf{J} through the continuity equation. A harmonic time variation $\exp(j\omega t)$ is assumed and suppressed.

The scattered electric field given by (2) is evaluated in the limit as \mathbf{r} approaches the scatterer surface from the interior. The scattered field expression resulting from the limit process is valid just inside the scatterer surface, and it may be substituted into (1) to represent the boundary condition just inside the scatterer surface as an integral equation in the unknown surface currents \mathbf{J} and \mathbf{M} . Additional boundary condition information must be enforced to uniquely determine both equivalent current sets, however. When applicable, the impedance boundary condition, which relates the tangential components of the electric and magnetic fields at the scatterer surface, may be enforced to provide the necessary additional information. The IBC considered in this work is the anisotropic impedance boundary condition, which relates the surface electric and magnetic fields by any one of several equivalent expressions:

$$\begin{aligned} \mathbf{E} - (\mathbf{E} \cdot \hat{\mathbf{n}}) \hat{\mathbf{n}} &= \eta \underline{\mathbf{Z}}_s \cdot (\hat{\mathbf{n}} \times \mathbf{H}) \\ -\hat{\mathbf{n}} \times \hat{\mathbf{n}} \times \mathbf{E} &= \eta \underline{\mathbf{Z}}_s \cdot (\hat{\mathbf{n}} \times \mathbf{H}) \\ \hat{\mathbf{n}} \times \mathbf{E} &= \eta \hat{\mathbf{n}} \times [\underline{\mathbf{Z}}_s \cdot (\hat{\mathbf{n}} \times \mathbf{H})] \end{aligned} \quad (5)$$

where the anisotropic IBC surface impedance dyadic is normalized by the intrinsic impedance of free space η and is defined by

$$\begin{aligned} \underline{\mathbf{Z}}_s &= Z_{11}\hat{\mathbf{a}}_1\hat{\mathbf{a}}_1 + Z_{12}\hat{\mathbf{a}}_1\hat{\mathbf{a}}_2 + Z_{21}\hat{\mathbf{a}}_2\hat{\mathbf{a}}_1 + Z_{22}\hat{\mathbf{a}}_2\hat{\mathbf{a}}_2 \\ &= \begin{bmatrix} Z_{11}\hat{\mathbf{a}}_1\hat{\mathbf{a}}_1 & Z_{12}\hat{\mathbf{a}}_1\hat{\mathbf{a}}_2 \\ Z_{21}\hat{\mathbf{a}}_2\hat{\mathbf{a}}_1 & Z_{22}\hat{\mathbf{a}}_2\hat{\mathbf{a}}_2 \end{bmatrix} \end{aligned} \quad (6)$$

and where $\hat{\mathbf{a}}_1$ and $\hat{\mathbf{a}}_2$ are unit vectors in an orthogonal

coordinate system defined on the surface S . The orientation of these unit vectors is assumed to satisfy $\hat{a}_2 = \hat{n} \times \hat{a}_1$, where \hat{n} is the outward-directed unit surface normal. In terms of the equivalent electric and magnetic surface currents, the anisotropic IBC may be represented by

$$\mathbf{M} = -\eta \hat{n} \times [\underline{\underline{Z}}_s \cdot \mathbf{J}] \quad (7)$$

Thus, one finally obtains the EFIE for a scatterer with an anisotropic impedance boundary condition:

$$\begin{aligned} \mathbf{E}_{tan}^i(\mathbf{r}) &= [j\omega\mu \int_S \mathbf{J}\mathbf{G}(\mathbf{r}, \mathbf{r}')dS' + \frac{1}{\epsilon} \nabla \int_S \sigma \mathbf{G}(\mathbf{r}, \mathbf{r}')dS']_{tan} \\ &- \int_S \eta \{\hat{n} \times [\underline{\underline{Z}}_s \cdot \mathbf{J}]\} \times \nabla \mathbf{G}(\mathbf{r}, \mathbf{r}')dS']_{tan}, \quad \mathbf{r} \rightarrow S^- \end{aligned} \quad (8)$$

where $\mathbf{r} \rightarrow S^-$ denotes that the equation is valid in the limit as the observation point approaches S from the interior of S . The equivalent electric surface current \mathbf{J} is then the only unknown quantity and (8) may be solved for \mathbf{J} via the method of moments [25].

III. Numerical Solution Procedure

The triangular patch modeling method developed by Rao, Wilton, and Glisson [22] is employed to solve (8) for the unknown electric surface current density \mathbf{J} . A suitable triangular patch model of the geometry of the impedance body is first developed. The electric surface current density \mathbf{J} on S is then approximated in terms of basis functions \mathbf{f}_n

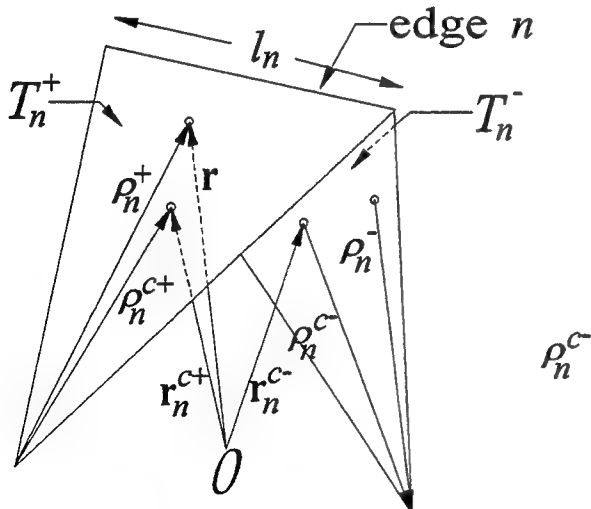


Figure 1. Geometrical parameters associated with a triangle pair.

defined on pairs of triangles as

$$\mathbf{J}(\mathbf{r}) = \sum_{n=1}^N I_n \mathbf{f}_n(\mathbf{r}) \quad (9)$$

where N is the number of interior edges in the model. Various geometrical quantities associated with a triangle pair with common edge n are illustrated in Figure 1. The two triangles attached to the common edge are denoted as T_n^+ and T_n^- . Points within triangle T_n^+ may be defined by a position vector \mathbf{r} with respect to a global coordinate origin O , or by a local position vector ρ_n^+ defined with respect to the free vertex of T_n^+ . Quantities in T_n^- are defined similarly except that the vector ρ_n^- is directed toward the free vertex of T_n^- rather than away from it. The vector basis function \mathbf{f}_n representing the electric surface current density associated with the n^{th} edge is then defined as

$$\mathbf{f}_n(\mathbf{r}) = \begin{cases} \frac{\ell_n}{2A_n^+} \rho_n^+, & \mathbf{r} \in T_n^+ \\ \frac{\ell_n}{2A_n^-} \rho_n^-, & \mathbf{r} \in T_n^- \\ \mathbf{0}, & \text{otherwise} \end{cases} \quad (10)$$

where ℓ_n is the length of edge n and A_n^\pm is the area of triangle T_n^\pm .

The method of moments is applied by next testing (8) with suitable testing functions. The testing functions are chosen to be the expansion functions \mathbf{f}_m defined in the preceding paragraph. Thus, (8) is tested with \mathbf{f}_m , $m=1,2,\dots,N$, and the result can be represented as

$$\begin{aligned} \langle \mathbf{E}^i, \mathbf{f}_m \rangle &= j\omega \langle \mathbf{A}, \mathbf{f}_m \rangle + \langle \nabla \Phi, \mathbf{f}_m \rangle \\ &+ \frac{1}{\epsilon} \langle \nabla \times \mathbf{F}, \mathbf{f}_m \rangle \end{aligned} \quad (11)$$

where the symmetric product is defined as

$$\langle \mathbf{f}, \mathbf{g} \rangle \equiv \int_S \mathbf{f} \cdot \mathbf{g} dS \quad (12)$$

and where the curl term in (11) is understood to be evaluated in the limit as the observation point approaches the surface from the interior, as indicated in (8). The Galerkin solution procedure implied by (11) when the basis and testing functions are the same has often been approximated in previous triangular patch code implementations. In this work the expressions for the terms in (11) are presented without these approximations. Appropriate approximations may be made to reduce the amount of numerical integration required if desired.

The evaluation of the magnetic vector potential term and the electric scalar potential term as they appear in (11) is discussed in [22]. However, in this work the vector potential is evaluated directly in terms of its vector integrand rather than expressing the result as a sum of scalar integrals times constant vectors as in [22]. This is done to simplify the implementation of the full Galerkin testing procedure, which involves double surface integration. As in previous work, however, integrations are performed on source triangle, observation triangle pairs rather than on source basis function, observation basis function pairs. One then finds that the vector potential integrations are all of the form

$$\begin{aligned} A_{ij}^{pq} &= \mu \int_{T^p} \frac{\ell_i}{2A^p} (\mathbf{r} - \mathbf{r}_i) \cdot \int_{T^q} \frac{\ell_j}{2A^q} (\mathbf{r}' - \mathbf{r}_j) G dS' dS \\ &= \frac{\mu \ell_i \ell_j}{16\pi A^p A^q} \left\{ \int_{T^p T^q} (\mathbf{r} - \mathbf{r}_i) \cdot (\mathbf{r}' - \mathbf{r}_j) \frac{e^{-jkR} - I_s}{R} dS' dS \right. \\ &\quad \left. + I_s \int_{T^p} (\mathbf{r} - \mathbf{r}_i) \cdot \left[\int_{T^q} (\mathbf{r}' - \mathbf{r}_j) \frac{1}{R} dS' \right] dS \right\}, \quad \mathbf{r} \in T^p, \mathbf{r}' \in T^q \end{aligned} \quad (13)$$

where $R = |\mathbf{R}| = |\mathbf{r} - \mathbf{r}'|$, the indices p and q refer to the observation and source face numbers, respectively, and the indices i and j are local indices referring to the three different testing and basis functions, respectively, that exist within the testing and source faces. Then, for example, ℓ_j refers to the length of the edge with local edge number j and is associated with the j^{th} (local) basis function, while the position vector \mathbf{r}_j locates the vertex opposite the edge with local edge number j in face q . The quantity I_s in (13) is a control variable that is set to 1 if extraction of the singular term in the integrand is to be performed, and that is set to 0 if no singularity extraction procedure is to be performed. When the singularity extraction procedure is performed, the integration of the singular term over the source region can be evaluated analytically as

$$\begin{aligned} \int_{T^q} (\mathbf{r}' - \mathbf{r}_j) \frac{1}{R} dS' &= \int_{T^q} \frac{\rho' - \rho}{R} dS' + (\rho - \rho_j) \int_{T^q} \frac{1}{R} dS' \\ &= \mathbf{b}^q(\mathbf{r}) + (\rho - \rho_j) \mathbf{a}^q(\mathbf{r}) \end{aligned} \quad (14)$$

where the integrals for $\mathbf{b}^q(\mathbf{r})$ and $\mathbf{a}^q(\mathbf{r})$ have been evaluated in [26]. The cylindrical coordinate vectors ρ in (14) represent the projections of the corresponding global position vectors \mathbf{r} onto the plane of the source triangle as described in and as indicated in Fig. 2, where a local coordinate system has been illustrated for use in evaluating a variety of integrals [26]. The definitions for $\mathbf{b}^q(\mathbf{r})$ and

$\mathbf{a}^q(\mathbf{r})$ are repeated here for completeness:

$$\begin{aligned} \mathbf{a}^q(\mathbf{r}) &= \sum_j \hat{\mathbf{P}}_j^0 \cdot \hat{\mathbf{u}}_j \left[P_j^0 \ln(G_j) \right. \\ &\quad \left. - |d| \left(\tan^{-1}(F_j^+) - \tan^{-1}(F_j^-) \right) \right] \end{aligned} \quad (15)$$

$$\mathbf{b}^q(\mathbf{r}) = \frac{1}{2} \sum_j \hat{\mathbf{u}}_j \left[(R_j^0)^2 \ln(G_j) + \ell_j^+ R_j^+ - \ell_j^- R_j^- \right] \quad (16)$$

where

$$G_j = \frac{R_j^+ + \ell_j^+}{R_j^- + \ell_j^-} = \frac{R_j^- - \ell_j^-}{R_j^+ - \ell_j^+} \quad (17)$$

$$F_j^\pm = \frac{P_j^0 \ell_j^\pm}{(R_j^0)^2 + |d|R_j^\pm} \quad (18)$$

The remaining quantities appearing in (15)-(18) are defined as indicated by Fig. 2.

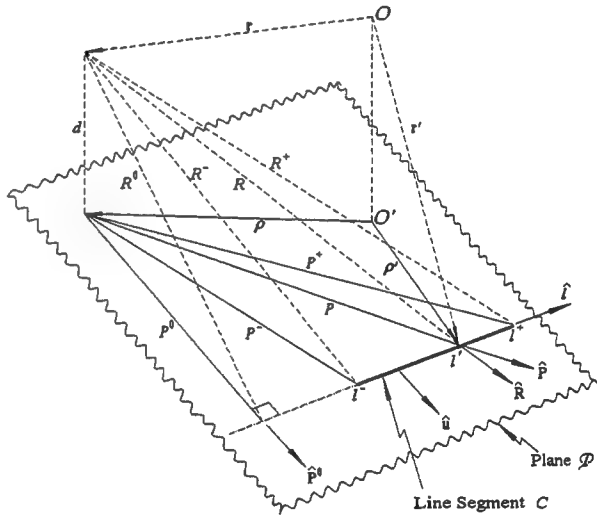


Figure 2. Geometrical quantities associated with the line segment C lying in plane P and the arbitrary observation point \mathbf{r} .

The first step in the evaluation of the scalar potential term in (11) involves the use of a vector calculus identity for surface integration [27] and the particular properties of the basis function or testing function at the edges of its domain of support. The scalar potential term is thus re-expressed as

$$\langle \nabla \Phi, \mathbf{f}_m \rangle = - \int_S \Phi (\nabla_s \cdot \mathbf{f}_m) dS \quad (19)$$

When the integration process is performed on a face-by-face basis, the integrals which must be evaluated are of the form

$$\Phi_{ij}^{pq} = \frac{\ell_i \ell_j}{4\pi j \omega e A^{pq}} \int_{T^p T^q} \int \frac{e^{-jkR}}{R} dS' dS \quad (20)$$

where, as in the vector potential term, the source region integration can be expressed in terms of bounded and singular integrand portions as

$$\int_{T^q} \frac{e^{-jkR}}{R} dS' = \int_{T^q} \frac{e^{-jkR} - I_s}{R} dS' + I_s \int_{T^q} \frac{1}{R} dS' \quad (21)$$

The last integral on the right in (21) contains the singular integrand and can be evaluated analytically. The result is simply $a^q(\mathbf{r})$ as given by (15).

The singularity extraction process described above for the magnetic vector potential and the scalar potential terms was performed for all source-face, testing-face combinations in the original implementation of the triangular patch computer code (i.e., I_s was set to 1 for all source-face, testing-face combinations). This seems unnecessary for the general case and it may lead to numerical inaccuracies in matrix element computations when the source face and testing face are far removed from each other and the testing face also lies near the linear extension of one of the edges of the source triangle. The errors appear to result from the evaluation of G_j as given by (17) when the ℓ_j^\pm tend to cancel the R_j^\pm terms. For widely separated source and testing faces, these errors can be eliminated by setting $I_s=0$. Similar errors may also occur for nearby source and testing faces when the subdomain scheme is not completely regular. Therefore, two forms for G_j are given in (17). The first should be used when the ℓ_j^\pm are both positive, the second when the ℓ_j^\pm are both negative, and in other cases either expression may be used.

The accurate evaluation of the electric vector potential term in (11) using singularity extraction procedures has been previously addressed for the isotropic case [23, 28]. For this term, if the source face and the testing face are not the same (i.e., for a non-self term) the curl operator may be carried under the source integral and appropriate vector identities may be applied. Thus, the integration required for a source face q and an observation face p becomes

$$\begin{aligned} \left[\frac{1}{\epsilon} \langle \nabla \times \mathbf{F}(\mathbf{r}), \mathbf{f}_m \rangle \right]^{pq} &= - \int_{T^p T^q} \int \mathbf{f}_m \cdot \mathbf{M} \times \nabla G dS' dS \\ &= \eta \int_{T^p T^q} \int \hat{\mathbf{n}}' [\mathbf{f}_m \cdot (\underline{\mathbf{Z}}_s \cdot \mathbf{J})] \cdot \nabla G dS' dS \quad (22) \\ &\quad + \eta \int_{T^p T^q} \int (\mathbf{f}_m \cdot \hat{\mathbf{n}}') (\underline{\mathbf{Z}}_s \cdot \mathbf{J}) \cdot \nabla' G dS' dS \end{aligned}$$

where the magnetic surface current \mathbf{M} has been related to the electric surface current \mathbf{J} through the IBC relationship, and where \mathbf{f}_m is the portion of the m th testing function within face p . The result in (22) has been expressed in a form in which the terms representing field components normal and tangential to the plane of the source are easily separated.

We consider first the field component tangential to the plane of the source triangle. For this component the contribution to a matrix element for the portion of the testing function \mathbf{f}_i residing in face p and the basis function \mathbf{f}_j in face q is

$$\begin{aligned} \eta \int_{T^p} \mathbf{f}_i^p \cdot \underline{\mathbf{Z}}_s \cdot \mathbf{I}_j^q dS &= - \frac{\eta}{4\pi} \left[\frac{\ell_i \ell_j}{4A^{pq}} \right] \\ &\quad \left\{ \int_{T^p} d \int_{T^q} (\mathbf{r} - \mathbf{r}_i) \cdot \underline{\mathbf{Z}}_s \cdot (\mathbf{r}' - \mathbf{r}_j) K(R) dS' dS \right. \\ &\quad \left. + I_s \int_{T^p} (\mathbf{r} - \mathbf{r}_i) \cdot \underline{\mathbf{Z}}_s \cdot \mathbf{A}_j^q dS \right\} \quad (23) \end{aligned}$$

with

$$K(R) = \frac{(1+jkR)e^{-jkR} - I_s(1+\frac{1}{2}k^2 R^2)}{R^3}$$

where ℓ_n is the length of edge n , A^n is the area of face n , $d = \hat{\mathbf{n}}' \cdot \mathbf{R}$, \mathbf{r}_n is the position vector to the triangle vertex opposite edge n , and where I_s is either one, if singularity extraction is to be performed, or zero, if not. The vector function \mathbf{A}_j^q in (23) which results when singularity extraction is performed is defined by

$$\begin{aligned} \mathbf{A}_j^q &= -d \mathbf{U}^q(\mathbf{r}) + (\rho - \rho_j) \frac{d}{|d|} V^q(\mathbf{r}) \\ &\quad + \frac{1}{2} dk^2 \mathbf{b}^q(\mathbf{r}) + \frac{1}{2} dk^2 (\rho - \rho_j) \mathbf{a}^q(\mathbf{r}) \quad (24) \end{aligned}$$

where \mathbf{U}^q , and V^q are defined as:

$$\mathbf{U}^q(\mathbf{r}) = \sum_j \hat{\mathbf{u}}_j \ln(G_j) \quad (25)$$

$$V^q(\mathbf{r}) = \sum_j \hat{\mathbf{P}}_j^0 \cdot \hat{\mathbf{u}}_j [\tan^{-1}(F_j^+) - \tan^{-1}(F_j^-)] \quad (26)$$

Other quantities appearing in (24) are defined in (15) through (18). The details of the evaluations leading to (24) through (26) are given in [29] and [30]. Evaluation of the electric vector potential integrals has been performed via a similar procedure in [28]. Another alternate procedure has been described in [31].

The source-region integration appearing on the right side in (23) is performed numerically. The term in (23) containing the source-region integration can be rewritten as

$$-\frac{\eta}{4\pi} \left(\frac{\ell_i \ell_j}{4A^P A^q} \right) \int_{T^P} \sum_{r=1}^2 \sum_{s=1}^2 [(\mathbf{r}-\mathbf{r}_i) \cdot \hat{\mathbf{a}}_r Z_{rs} \hat{\mathbf{a}}_s \cdot \mathbf{I}_{bj}^q] dS \quad (27)$$

where

$$\mathbf{I}_{bj}^q = \int_{T^q} (\mathbf{r}'-\mathbf{r}_j) d \left[\frac{(1+jkR)e^{-jkR} - I_s(1+\frac{1}{2}k^2 R^2)}{R^3} \right] dS' \quad (28)$$

which has been previously evaluated numerically in the isotropic IBC case [29, 30]. The double dot product with the IBC dyadic in (23) has been represented as a double summation in (27). The portion of (23) resulting from analytical integration over the source region can be expressed similarly as

$$\begin{aligned} & -I_s \frac{\eta}{4\pi} \left(\frac{\ell_i \ell_j}{4A^P A^q} \right) \int_{T^P} (\mathbf{r}-\mathbf{r}_i) \cdot \underline{\mathbf{Z}}_s \cdot \mathbf{A}_j^q dS \\ & = -I_s \frac{\eta}{4\pi} \left(\frac{\ell_i \ell_j}{4A^P A^q} \right) \int_{T^P} \sum_{r=1}^2 \sum_{s=1}^2 Z_{rs} b_{i,r}^A b_{j,s}^B dS \end{aligned} \quad (29)$$

where

$$b_{i,r}^A = (\mathbf{r}-\mathbf{r}_i) \cdot \hat{\mathbf{a}}_r \quad (30)$$

and

$$b_{j,s}^B = \hat{\mathbf{a}}_s \cdot \mathbf{A}_j^q(\mathbf{r}) \quad (31)$$

No new numerical or analytical integral evaluations are required for the field component tangential to the plane of the source in the anisotropic case. The terms obtained for the isotropic case are merely combined with different coefficients.

The component of the scattered electric field normal to the plane of the source triangle and arising from the magnetic current contribution in (22) is

$$\eta \int_{T^P} (\mathbf{f}_i^P \cdot \hat{\mathbf{n}}') \int_{T^q} (\underline{\mathbf{Z}}_s \cdot \mathbf{f}_j^q) \cdot \nabla' G dS' dS \quad (32)$$

The dyadic notation in (32) can be rewritten using the double summation as

$$\begin{aligned} & \frac{\eta}{4\pi} \left(\frac{\ell_i \ell_j}{4A^P A^q} \right) \int_{T^P} [(\mathbf{r}-\mathbf{r}_i) \cdot \hat{\mathbf{n}}'] \int_{T^q} [\underline{\mathbf{Z}}_s \cdot (\mathbf{r}'-\mathbf{r}_j)] \cdot \nabla' G dS' dS \\ & = -\frac{\eta}{4\pi} \left(\frac{\ell_i \ell_j}{4A^P A^q} \right) \int_{T^P} N_i(\mathbf{r}) \sum_{r=1}^2 \sum_{s=1}^2 [Z_{rs} \hat{\mathbf{a}}_r \cdot \mathbf{I}_{sj}(\mathbf{r})] dS \end{aligned} \quad (33)$$

where $N_i(\mathbf{r}) = (\mathbf{r}-\mathbf{r}_i) \cdot \hat{\mathbf{n}}'$ and

$$\mathbf{I}_{sj}(\mathbf{r}) = - \int_{T^q} [\hat{\mathbf{a}}_s \cdot (\mathbf{r}'-\mathbf{r}_j)] \nabla' G dS' \quad (34)$$

The integral for $\mathbf{I}_{sj}(\mathbf{r})$ can be expressed in a more convenient form for implementation by using the identity $a\nabla b = \nabla(ab) - b\nabla a$ and the fact that $\hat{\mathbf{a}}_s$ is tangential to the source plane. One then obtains

$$\begin{aligned} \mathbf{I}_{sj}(\mathbf{r}) & = - \int_{T^q} \nabla_{s'} \{ [\hat{\mathbf{a}}_s \cdot (\mathbf{r}'-\mathbf{r}_j)] G \} dS' + \int_{T^q} G \nabla_{s'} [\hat{\mathbf{a}}_s \cdot (\mathbf{r}'-\mathbf{r}_j)] dS' \\ & = - \int_{\partial T^q} [\hat{\mathbf{a}}_s \cdot (\mathbf{r}'-\mathbf{r}_j)] G \hat{\mathbf{u}} d\ell' + \int_{T^q} G \mathbf{H}_{sj} dS' \\ & = -\mathbf{I}_{sj}^L + \mathbf{I}_{sj}^A \end{aligned} \quad (35)$$

where $\hat{\mathbf{u}}$ is the outward-directed unit normal to the triangle boundary lying in the plane of the triangle and \mathbf{H}_{sj} is a constant vector obtained by evaluating the gradient operation in the second term of (35):

$$\begin{aligned} \mathbf{H}_{sj} & = \nabla_{s'} \{ \hat{\mathbf{a}}_s \cdot [\xi_{j+1}(\mathbf{r}_{j+1}-\mathbf{r}_j) + \xi_{j-1}(\mathbf{r}_{j-1}-\mathbf{r}_j)] \} \\ & = \hat{\mathbf{a}}_s \cdot \ell_{j-1} \left(\frac{-\hat{\mathbf{h}}_{j+1}}{h_{j+1}} \right) - \hat{\mathbf{a}}_s \cdot \ell_{j+1} \left(\frac{-\hat{\mathbf{h}}_{j-1}}{h_{j-1}} \right) \\ & = -\frac{1}{2A^q} [(\hat{\mathbf{a}}_s \cdot \ell_{j-1})(\ell_{j+1} \times \hat{\mathbf{n}}') - (\hat{\mathbf{a}}_s \cdot \ell_{j+1})(\ell_{j-1} \times \hat{\mathbf{n}}')] \end{aligned} \quad (36)$$

This result is obtained by expressing the vector basis

function variation ($\mathbf{r}' - \mathbf{r}_j$) in area coordinates [28], as indicated in the first line of (36), where ξ_j is the area coordinate having value one at the vertex \mathbf{r}_j and value zero at the vertices \mathbf{r}_{j+1} and \mathbf{r}_{j-1} . The gradient operation on the j th area coordinate variable is then conveniently expressed in terms of the height of the j th vertex, h_j , and a vector directed normal to the j th edge, $\hat{\mathbf{n}}_j$ ($= \hat{\mathbf{u}}_j$). Thus, $\mathbf{I}_{sj}(\mathbf{r})$ can be expressed as

$$\begin{aligned}\mathbf{I}_{sj}(\mathbf{r}) &= \mathbf{H}_{sj} \int_{T^q} G^b dS' + \mathbf{H}_{sj} \int_{T^q} G^u dS' \\ &\quad - \int_{\partial T^q} [\hat{\mathbf{a}}_s \cdot (\mathbf{r}' - \mathbf{r}_j)] G^b \hat{\mathbf{u}} d\ell' - \int_{\partial T^q} [\hat{\mathbf{a}}_s \cdot (\mathbf{r}' - \mathbf{r}_j)] G^u \hat{\mathbf{u}} d\ell' \\ &= \mathbf{H}_{sj} I_q^{Ab} + \mathbf{H}_{sj} I_q^{Au} - \mathbf{I}_{sj}^{Lb} - \mathbf{I}_{sj}^{Lu}\end{aligned}\quad (37)$$

In (37) the superscript b indicates a term which is bounded or has a bounded integrand (when I_s is appropriately chosen), while the superscript u indicates a term which may be unbounded or may have an unbounded integrand. The superscript L indicates a line integral term, while the superscript A indicates an area integral term. The bounded and unbounded kernel terms are given by

$$G^b = \frac{e^{-jkR} - I_s}{R} \quad (38)$$

and

$$G^u = \frac{I_s}{R} \quad (39)$$

Thus, the terms involving the field component normal to the plane of the source triangle can be expressed as

$$\begin{aligned}-\frac{\eta}{4\pi} \left(\frac{\ell_i \ell_j}{4A^P A^q} \right) \left\{ \sum_{r=1}^2 \sum_{s=1}^2 [Z_{rs} \mathbf{H}_{sj} \cdot \hat{\mathbf{a}}_r] \int_{T^P} N_i(\mathbf{r}) [I_q^{Ab} + I_q^{Au}] dS \right. \\ \left. - \sum_{r=1}^2 \sum_{s=1}^2 Z_{rs} \int_{T^P} N_i(\mathbf{r}) \hat{\mathbf{a}}_r \cdot [\mathbf{I}_{sj}^{Lb}(\mathbf{r}) + \mathbf{I}_{sj}^{Lu}(\mathbf{r})] dS \right\}\end{aligned}\quad (40)$$

where the area integrations over the source region are defined by

$$I_q^{Ab}(\mathbf{r}) = \int_{T^q} \frac{e^{-jkR} - I_s}{R} dS' \quad (41)$$

and

$$I_q^{Au}(\mathbf{r}) = a^q(\mathbf{r}) \quad (42)$$

while the line integrations around the source triangle are given by

$$\begin{aligned}\mathbf{I}_{sj}^{Lb}(\mathbf{r}) &= [\hat{\mathbf{a}}_s \cdot \ell_{j-1}] \sum_{k=j-1}^{j+1} \hat{\mathbf{u}}_k \int_{\partial_k T^q} \xi_{j+1} G^b d\ell' \\ &\quad - [\hat{\mathbf{a}}_s \cdot \ell_{j+1}] \sum_{k=j-1}^{j+1} \hat{\mathbf{u}}_k \int_{\partial_k T^q} \xi_{j-1} G^b d\ell'\end{aligned}\quad (43)$$

and

$$\begin{aligned}\mathbf{I}_{sj}^{Lu}(\mathbf{r}) &= I_s [\hat{\mathbf{a}}_s \cdot \ell_{j-1}] \sum_{k=j-1}^{j+1} \hat{\mathbf{u}}_k \int_{\partial_k T^q} \frac{\xi_{j+1}}{R} d\ell' \\ &\quad - I_s [\hat{\mathbf{a}}_s \cdot \ell_{j+1}] \sum_{k=j-1}^{j+1} \hat{\mathbf{u}}_k \int_{\partial_k T^q} \frac{\xi_{j-1}}{R} d\ell'\end{aligned}\quad (44)$$

The area integration terms given in (41) and (42) were evaluated in the isotropic case and are again simply combined with different coefficients in the anisotropic case. The line integrations indicated in (43) and (44), however, did not appear in the same form in the isotropic case. Therefore, new numerical and analytical line integral evaluations are required for the anisotropic IBC case. The new analytical integral evaluations required are indicated in (45) below.

$$\begin{aligned}\int_{\partial_i T^q} \frac{\xi_i}{R} d\ell' &= 0 \\ \int_{\partial_{i+1} T^q} \frac{\xi_i}{R} d\ell' &= \frac{1}{\ell_{i+1}} [R_{i+1}^+ - R_{i+1}^- - \ell_{i+1}^- \ell n(G_{i+1})] \\ \int_{\partial_{i-1} T^q} \frac{\xi_i}{R} d\ell' &= -\frac{1}{\ell_{i-1}} [R_{i-1}^+ - R_{i-1}^- - \ell_{i-1}^+ \ell n(G_{i-1})]\end{aligned}\quad (45)$$

The line integral term in (40) that may have an unbounded integrand can then be succinctly expressed as

$$\begin{aligned}\mathbf{I}_{sj}^{Lu}(\mathbf{r}) &= I_s [\hat{\mathbf{a}}_s \cdot \ell_{j-1}] \sum_{k=j-1}^{j+1} \hat{\mathbf{u}}_k L_k^{j+1} \\ &\quad - I_s [\hat{\mathbf{a}}_s \cdot \ell_{j+1}] \sum_{k=j-1}^{j+1} \hat{\mathbf{u}}_k L_k^{j-1}\end{aligned}\quad (46)$$

where

$$L_k^\alpha = \begin{cases} -\frac{1}{\ell_k} [R_k^+ - R_k^- - \ell_k^+ \ell n(G_k)] & , \quad k=\alpha-1 \\ \frac{1}{\ell_k} [R_k^+ - R_k^- - \ell_k^- \ell n(G_k)] & , \quad k=\alpha+1 \\ 0 & , \quad k=\alpha \end{cases}\quad (47)$$

The special case in which the source and observation triangles are the same must also be reevaluated for the anisotropic case. The self term for the anisotropic case may be written as

$$\begin{aligned} \langle \mathbf{f}_i^q, \frac{1}{2}\hat{\mathbf{n}} \times \mathbf{M}_j^q \rangle &= \frac{1}{2}\eta \langle \mathbf{f}_i^q, \underline{\mathbf{Z}}_s \cdot \mathbf{f}_j^q \rangle \\ &= \frac{\ell_i \ell_j}{8(A^q)^2} \int_{T^q} (\rho' - \rho_i) \cdot \underline{\mathbf{Z}}_s \cdot (\rho' - \rho_j) dS' \end{aligned} \quad (48)$$

If the vector variation of the basis functions is expressed in terms of the area coordinates and the dyadic dot products are given in double summation form, the self term becomes

$$\begin{aligned} &\frac{\ell_i \ell_j}{8(A^q)^2} \int_{T^q} \sum_{r=1}^2 \sum_{s=1}^2 Z_{rs} \{ [\xi_{i+1}(\mathbf{r}_{i+1} - \mathbf{r}_i) + \xi_{i-1}(\mathbf{r}_{i-1} - \mathbf{r}_i)] \cdot \hat{\mathbf{a}}_r \} \\ &\quad \cdot \{ \hat{\mathbf{a}}_s \cdot [\xi_{j+1}(\mathbf{r}_{j+1} - \mathbf{r}_j) + \xi_{j-1}(\mathbf{r}_{j-1} - \mathbf{r}_j)] \} \\ &= \frac{\ell_i \ell_j}{4(A^q)^2} \sum_{r=1}^2 \sum_{s=1}^2 Z_{rs} [\alpha_{i-1,r} \alpha_{j-1,s} I_{i+1,j+1} \\ &\quad - \alpha_{i-1,r} \alpha_{j+1,s} I_{i+1,j-1} \\ &\quad - \alpha_{i+1,r} \alpha_{j-1,s} I_{i-1,j+1} \\ &\quad + \alpha_{i+1,r} \alpha_{j+1,s} I_{i-1,j-1}] \end{aligned} \quad (49)$$

where

$$\alpha_{mn} = \ell_m \cdot \hat{\mathbf{a}}_n \quad (50)$$

and

$$I_{mn} = \int_{\xi_1=0}^1 \int_{\xi_2=0}^{1-\xi_1} \xi_m \xi_n d\xi_2 d\xi_1 = \begin{cases} \frac{1}{12}, & m=n \\ \frac{1}{24}, & m \neq n \end{cases} \quad (51)$$

The preceding expressions have been implemented in the evaluation of the impedance matrix for the triangular patch scattering code. The resulting system of linear equations is solved in the usual manner for the surface current distribution. Once the surface current distribution on the scatterer has been computed, the far scattered electric field may be determined from

$$\mathbf{E}^s = -C(r) \eta \int_S G_f [\mathbf{J} - \hat{\mathbf{r}}(\mathbf{J} \cdot \hat{\mathbf{r}})] dS' + C(r) \int_S G_f (\hat{\mathbf{r}} \times \mathbf{M}) dS' \quad (52)$$

where

$$C(r) = \frac{jk}{4\pi r} e^{-jkr} \quad (53)$$

and

$$G_f = e^{jk(\hat{\mathbf{r}} \cdot \mathbf{r}')} \quad (54)$$

After substitution of the IBC relating the electric and magnetic current, the θ and ϕ components of the far scattered electric field can be represented as

$$E_\theta = -\eta C(r) \int_S G_f \mathbf{J} \cdot \{ \hat{\theta} - \sum_{r=1}^2 \sum_{s=1}^2 [(\hat{\phi} \times \hat{\mathbf{n}}') \cdot \hat{\mathbf{a}}_r] Z_{rs} \hat{\mathbf{a}}_s \} dS' \quad (55)$$

and

$$E_\phi = -\eta C(r) \int_S G_f \mathbf{J} \cdot \{ \hat{\phi} + \sum_{r=1}^2 \sum_{s=1}^2 [(\hat{\theta} \times \hat{\mathbf{n}}') \cdot \hat{\mathbf{a}}_r] Z_{rs} \hat{\mathbf{a}}_s \} dS' \quad (56)$$

The far scattered electric field may then be represented conveniently in terms of pattern integrals P_θ and P_ϕ as

$$\mathbf{E}^s = -\eta C(r) [P_\theta \hat{\theta} + P_\phi \hat{\phi}] \quad (57)$$

where the pattern integral due to a single source face q is given by

$$\begin{aligned} P_\alpha^q &= \sum_{i=1}^3 s_i \frac{I_i \ell_i}{2A^q} \int_{T^q} G_f (\mathbf{r}' - \mathbf{r}_i) \cdot \{ \hat{\alpha} \\ &\quad + \sum_{r=1}^2 \sum_{s=1}^2 [(\hat{\alpha} \times \hat{\mathbf{r}}) \times \hat{\mathbf{n}}'] \cdot \hat{\mathbf{a}}_r Z_{rs} \hat{\mathbf{a}}_s \} dS' \end{aligned} \quad (58)$$

with α replaced by either θ or ϕ . In (58), $s_i = \pm 1$, the plus sign being chosen if the basis function for edge i is directed away from vertex i in face q , and the minus sign being chosen if the basis function is directed toward the vertex. The integration over the source region in (58) can be performed analytically to obtain

$$\begin{aligned} P_\alpha^q &\approx \sum_{i=1}^3 s_i \frac{I_i \ell_i}{2A^q} e^{jk(\hat{\mathbf{r}} \cdot \mathbf{r}^{cq})} \gamma \cdot \int_{T^q} (\mathbf{r}' - \mathbf{r}_i) dS' \\ &= \frac{1}{2} \sum_{i=1}^3 s_i I_i \ell_i e^{jk(\hat{\mathbf{r}} \cdot \mathbf{r}^{cq})} \gamma \cdot (\mathbf{r}^{cq} - \mathbf{r}_i) \end{aligned} \quad (59)$$

where

$$\gamma = \hat{\alpha} + \sum_{r=1}^2 \sum_{s=1}^2 [(\hat{\alpha} \times \hat{\mathbf{r}}) \times \hat{\mathbf{n}}'] \cdot \hat{\mathbf{a}}_r Z_{rs} \hat{\mathbf{a}}_s \quad (60)$$

Thus, the final result may also be expressed as

$$P_{\alpha}^Q = \frac{1}{2} \sum_{i=1}^3 s_i I_i \ell_i e^{jk(\hat{r} \cdot \mathbf{r}^Q)} [\hat{\alpha} \cdot (\mathbf{r}^Q - \mathbf{r}_i) + (\hat{\alpha} \times \hat{r}) \cdot \sum_{r=1}^2 \sum_{s=1}^2 (\hat{n}' \times \hat{a}_r) Z_{rs} \hat{a}_s \cdot (\mathbf{r}^Q - \mathbf{r}_i)] \quad (61)$$

IV. Numerical Results

The procedures described in the previous section were initially implemented into a modified version of the original triangular patch code [22] and were subsequently incorporated into the more sophisticated IBC3D scattering code [30]. Numerical results are presented here for several spherical and cylindrical geometries with isotropic or anisotropic surface impedance boundary conditions. Results obtained using the triangular patch code and body of revolution codes are compared.

We first consider a cylindrical scatterer geometry with geometrical parameters as shown in Fig. 3. The cylinder is assumed to have length L and radius a . A standard

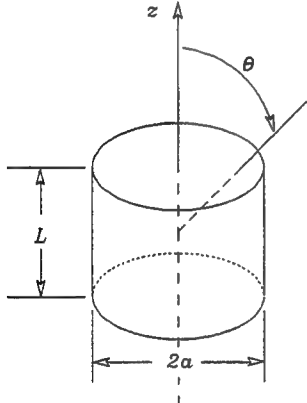


Figure 3. Geometrical parameters for cylinder.

cylindrical coordinate system is used for the body of revolution model with the z axis being the axis of revolution. For the triangular patch code, the axis of the cylinder was oriented along the y axis. Data obtained in the rotated coordinate system of the patch code model, however, are presented relative to the coordinate system of Fig. 3 in each case.

The first example considered is that of a small cylinder with length $L=0.2\lambda$ and radius $a=0.1\lambda$. The triangular patch model used to obtain the results presented is shown in Fig. 4. This triangular patch model uses 16 linear segments to model the geometry in the azimuthal direction, 4

segments along the cylinder radius, and 6 segments along the cylinder length. The quadrilateral patches formed by the azimuthal and generating contour segmentations are then divided by a line segment to form the triangular patches. The resulting patch model has 624 unknowns. The monostatic radar cross section results obtained with the triangular patch code and a body of revolution code modified to solve the anisotropic IBC problem [20] are shown in Fig. 5. For this case a θ -polarized plane wave is the excitation and the anisotropic surface impedance is defined by $Z_s = \hat{t}\hat{\phi}$, corresponding to a single non-zero, off-diagonal element in the impedance dyadic (6). Results are shown for the co-polarized and cross-polarized components of the radar cross section. The agreement between the results obtained by the two different methods is excellent.

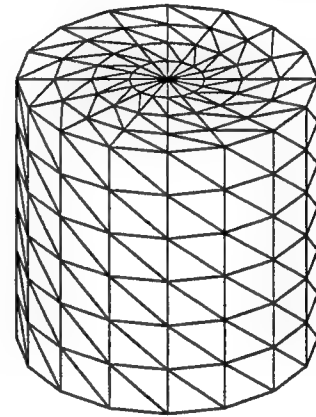


Figure 4. Triangular patch model for a cylinder of length $L=0.2\lambda$ and radius $a=0.1\lambda$.

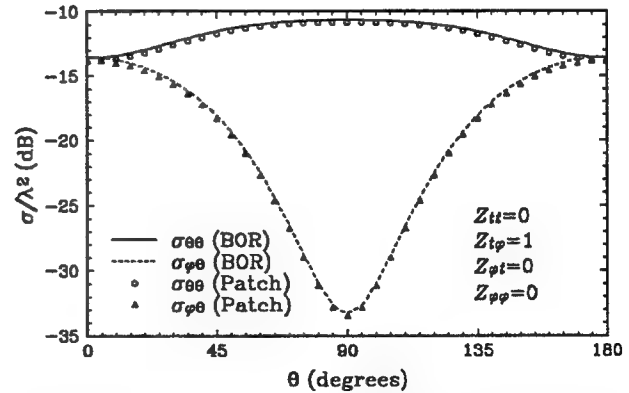


Figure 5. Comparison of monostatic radar cross section results for a small cylinder with an anisotropic impedance boundary condition.

Results were also obtained for a larger, resonant length

cylinder of length $L=\lambda$ and radius $a=0.1\lambda$. One triangular patch model used for this cylinder is shown in Fig. 6. A second model with more unknowns is shown in Fig. 7. The model of Fig. 6 has 220 triangular faces and 330 unknowns. The model is generated using 10 linear segments to model the surface in the azimuthal direction, 2 segments in the radial direction, and 8 segments along the length of the



Figure 6. Triangular patch model of a cylinder with 330 unknowns ($L=\lambda$, $a=0.1\lambda$).

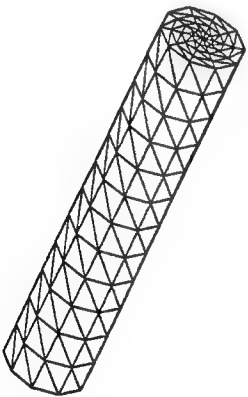


Figure 7. Triangular patch model of a cylinder with 570 unknowns ($L=\lambda$, $a=0.1\lambda$).

cylinder. The model of Fig. 7 has 570 unknowns. It is generated using 10 linear segments to model the surface in the azimuthal direction again, but with 4 segments in the radial direction and 12 segments along the length of the cylinder. Results obtained for the triangular patch model of Fig. 6 are compared with those obtained from the modified body of revolution formulation in Figs. 8 and 9 for the co-polarized and cross polarized radar cross section components, respectively. For the body of revolution model, the generating contour was modeled by 32 linear segments, resulting in 126 unknowns. The anisotropic

surface impedance is again defined by $Z_s = i\hat{\phi}$. The agreement of the results is generally very good except for near-axial incidence and, for $\sigma_{\phi\theta}$, in the case of broadside incidence. The disagreement between the data obtained by the two different methods for axial incidence is believed to indicate slow convergence (for both approaches) due to discretization error. It seems likely that the error at broadside incidence is partially due to insufficient resolution of the triangular patch model in the azimuthal direction.

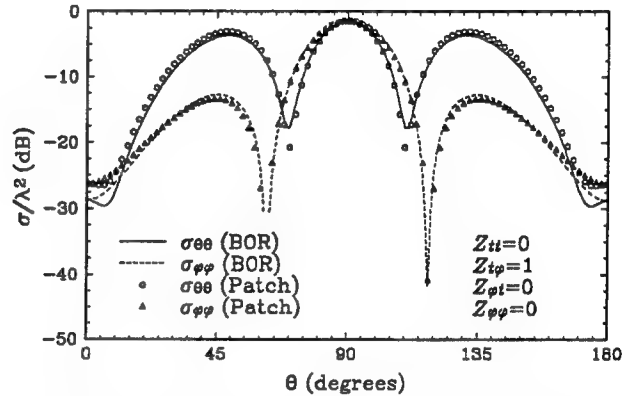


Figure 8. Comparison of co-polarized monostatic radar cross section results obtained with body of revolution and triangular patch models.

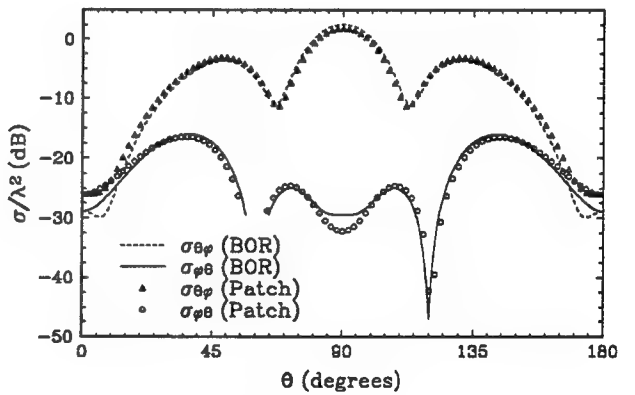


Figure 9. Comparison of cross-polarized monostatic radar cross section results obtained with body of revolution and triangular patch models.

For the triangular patch model of Fig. 7, the results are compared with those obtained from the modified body of revolution formulation in Figs. 10 and 11 for the co-polarized and cross-polarized radar cross section components, respectively. The generating contour for the body of revolution model in this case was defined by 56 linear segments, resulting in 222 unknowns. The agreement

between the results obtained by the two different methods is generally very good, and it is clear that the increased number of unknowns in both methods has improved the agreement between the two methods for axial and broadside illumination.

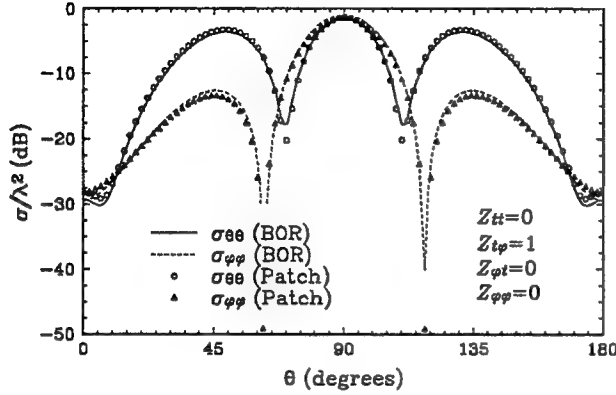


Figure 10. Comparison of co-polarized radar cross section results obtained with body of revolution and triangular patch models.

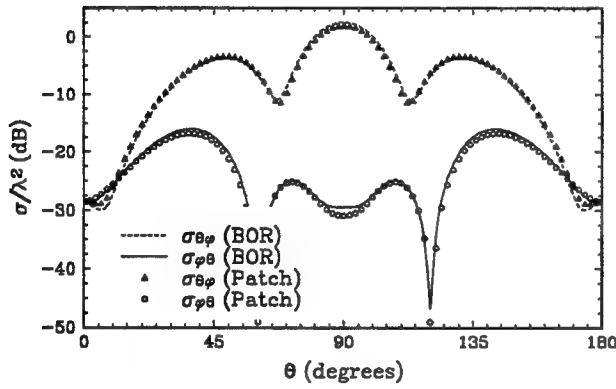


Figure 11. Comparison of cross-polarized radar cross section results obtained with body of revolution and triangular patch models.

We next consider the case of a sphere, both with an isotropic IBC and with an anisotropic IBC. In both cases, the results obtained using the IBC3D patch code are compared with an independent IBC body of revolution code (JRMBOR [32]). Comparisons are also made with the predictions of Weston's theorem [33] for the anisotropic IBC case. Three different triangular patch models, with 260, 570, and 1616 unknowns, were used to represent the sphere for the isotropic IBC case. The two models with the larger number of unknowns are shown in Fig. 12. Calculated backscatter cross-sections, normalized by πa^2 ,

where a is the sphere radius, are shown in Fig. 13 for the isotropic IBC case (i.e., in (6) $Z_{11}=Z_{22}=0.1+j0.1$, and $Z_{12}=Z_{21}=0$) as a function of $ka=2\pi a/\lambda$, where λ is the excitation wavelength. For $ka=3$, the segmentations of the three IBC3D models correspond to about 7, 11, and 18 triangles per wavelength. The JRMBOR result used at least 25 triangles per wavelength, and consequently, was reasonably well converged. The plotted IBC3D results have been radius-corrected to account for the difference in surface area of the inscribed triangle model of the sphere and the actual sphere. The radius correction factors for the 260, 570, and 1616 patch models were 0.988, 0.991, and 0.998, respectively. The IBC3D results are observed to converge to the JRMBOR solution as the triangle segmentation is increased. For the 1616, patch model, the agreement is nearly precise for $ka=2$, with differences no greater than a small fraction of a dB for $ka=3$.

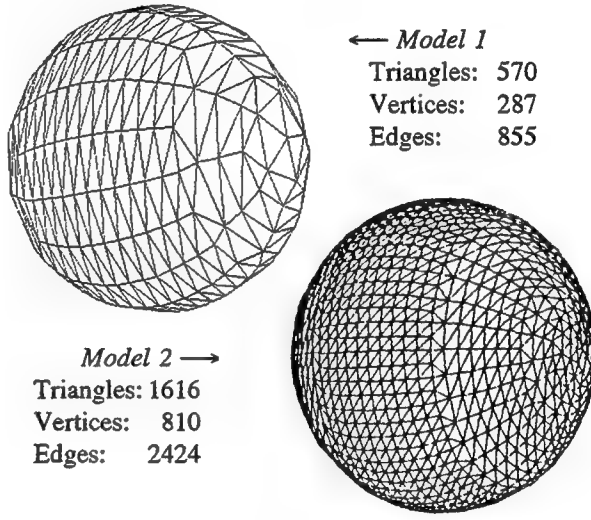


Figure 12. Triangulated sphere models.

Note that the 260 triangle patch model has spikes at $ka=2.75$ and $ka=3.9$. The spikes are an artifact of the EFIE formulation used, and they appear at the internal resonance frequencies of a perfect electric conductor (PEC) scatterer having the same surface. The width of the spike decreases as the number of patches increases, and, due to the finite sampling in frequency, the 570 triangle model shows only a small kink near $ka=3.9$. The JRMBOR code result was obtained with a combined field integral equation (CFIE) formulation using equal weightings of the EFIE and MFIE, which tends to suppress the spurious internal resonances [34].

IBC3D results and the JRMBOR results have also been compared for the case of a sphere with an anisotropic IBC

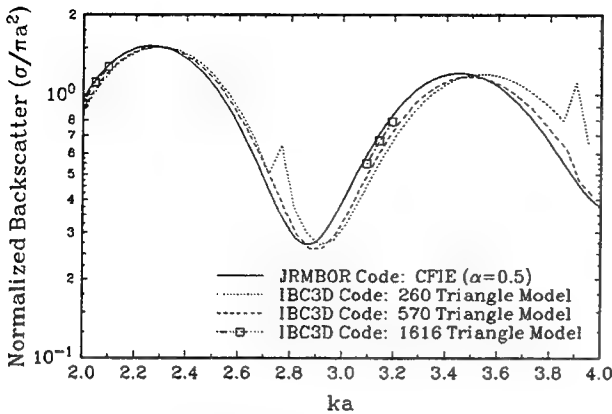


Figure 13. Comparison of IBC3D and JRMBOR for an isotropic impedance sphere ($Z_s = 0.1 + j0.1$).

and size $ka=1$ in Fig. 14. The geometry is shown in the figure, where the dashed line represents an axis of symmetry of the body, and \hat{k} is a unit vector in the direction of propagation of the incident plane wave. The plane of scattering is defined by these two lines, and the angle θ between them is the scattering angle plotted in Fig. 14. Vertical polarization (V) corresponds to the case where the electric field is perpendicular to the plane of scattering, while horizontal polarization (H) has the electric field in the plane of scattering. The intersection section of the axis of symmetry (dashed line) with the surface of the sphere defines one pole of the sphere. The unit vectors \hat{a}_1 in (6) are chosen to be everywhere tangential to the surface of the sphere and directed toward the pole, while the unit vectors \hat{a}_2 are in the azimuthal direction on the sphere surface. The surface impedance for the case is then defined as

$$\underline{Z}_s = \begin{bmatrix} 4.0 & 0 \\ 0 & 0.25 \end{bmatrix}$$

Results for the PEC sphere case are also shown (dashed curve) in Fig. 14, and the IBC3D and JRMBOR results are virtually indistinguishable. For the anisotropic IBC case, the surface impedance is defined so that the product of the diagonal matrix elements is unity. As a consequence, a generalization of Weston's theorem [33] to anisotropic BORs [35] is applicable, and the backscatter RCS along the axis of symmetry should vanish. It can be seen in Fig. 14 that the RCS along the axis of symmetry ($\theta=0^\circ, 180^\circ$) is 45 dB lower than the PEC case. Also shown is the comparison between JRMBOR and IBC3D results (dotted and solid lines, respectively). The agreement between the two codes is quite good except for the smallest cross-section regions of

the curve, where increased model segmentation is required to obtain more precise agreement. The generalized Weston theorem also requires that the VV and HH polarization results should be the same [35]. Both sets of numerically computed results exhibit this behavior except over the region of the curve where the cross section is small. The JRMBOR results were obtained using a segmentation equivalent to 40 triangles per wavelength, while the IBC3D results were obtained using about 27 triangles per wavelength.

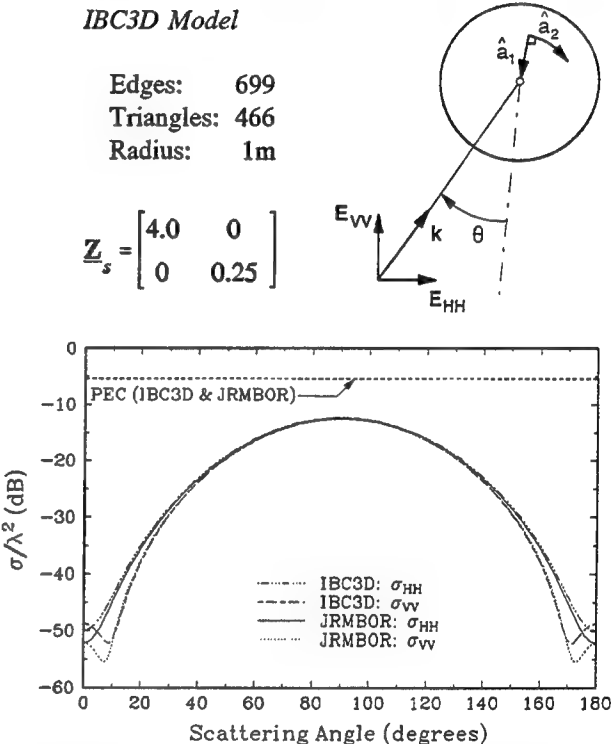


Figure 14. Comparison of IBC3D and JRMBOR bistatic scattering cross section for an anisotropic impedance sphere.

As a final example, we consider the case of another cylinder with an anisotropic IBC. The cylinder model is the same as that shown in Fig. 6, with length $L=\lambda$ and radius $a=0.1\lambda$. The unit vectors \hat{a}_1 and \hat{a}_2 that define the dyadic surface impedance are chosen to correspond to the azimuthal unit vector $\hat{\phi}$ and the generating arc unit vector \hat{t} commonly used in BOR representations. Thus, \hat{a}_1 is on the cylinder surface and azimuthally directed with respect to the axis of symmetry of the cylinder. Along the length of the cylinder, the vector \hat{a}_2 is parallel to the axis of symmetry, but on the endcaps, \hat{a}_2 is radially directed. The cylinder has roughly 8.5 triangles per wavelength. The JRMBOR results were obtained using the CFIE formulation

with equal weight to the EFIE and MFIE. Fourier modes zero through five and a Gaussian quadrature order of 30 were used. There were about 25 triangles per wavelength for the JRMBOR model. Thus, one might expect the JRMBOR calculations to be more accurate than those of IBC3D for this case.

Fig. 15 shows the comparison between the predictions of IBC3D and JRMBOR when the cylinder has an anisotropic surface IBC with unequal diagonal elements. The plane of scattering and the horizontal and vertical polarizations are defined in the same manner as in the preceding case of the sphere. The HH results shown in Fig. 15 for a horizontally polarized transmitter and receiver are almost coincident, while there is a worst-case discrepancy of less than 2 dB for the VV polarization result at about 45°. This agreement seems quite reasonable considering the rather crude segmentation of the IBC3D patch model.

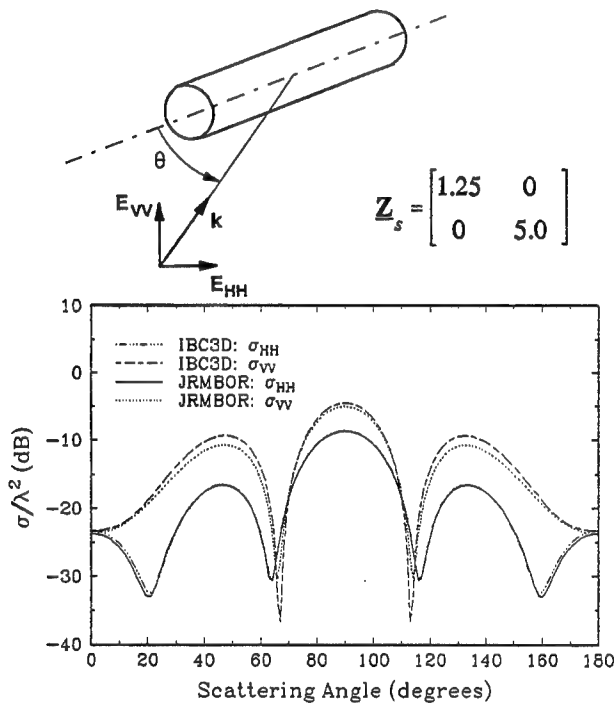


Figure 15. Comparison of IBC3D and JRMBOR monostatic RCS results for a cylinder with an anisotropic impedance boundary condition.

V. Summary

In this work the problem of electromagnetic scattering from arbitrarily shaped, imperfectly conducting surfaces modeled by an anisotropic impedance boundary condition has been considered. The numerical solution has been implemented using the electric field integral equation and a

triangular patch model for the scatterer surface. The anisotropic impedance boundary condition function has been specified by a constant surface dyadic within each triangular face. Good agreement between numerical results obtained with the triangular patch model and a body of revolution model has been observed for the scattering cross sections of spheres and cylinders for both isotropic and anisotropic impedance boundary conditions.

References

- [1] M. A. Leontovich, "Approximate boundary conditions for the electromagnetic field on the surface of a good conductor," *Investigations on Radiowave Propagation, Part II*, pp. 5-12, Printing House of the Academy of Sciences, Moscow, 1948.
- [2] T. B. A. Senior, "Impedance boundary conditions for imperfectly conducting surfaces," *Appl. Sci. Res.*, Sect. B, no. 8, pp. 418-436, 1960.
- [3] K. M. Mitzner, "An integral equation approach to scattering from a body of finite conductivity," *Radio Sci.*, vol. 2, no. 12, pp. 1459-1470, 1967.
- [4] R. D. Graglia and P. L. E. Uslenghi, "Surface currents on impedance bodies of revolution," *IEEE Trans. Antennas Propagat.*, vol. AP-36, no. 9, pp. 1313-1317, September 1988.
- [5] P. L. Huddleston, "Scattering by finite, open cylinders using approximate boundary conditions," *IEEE Trans. Antennas Propagat.*, vol. AP-37, no. 2, pp. 253-256, February 1989.
- [6] K. A. Iskander, L. Shafai, A. Fransen, and J. E. Hansen, "Application of impedance boundary conditions to numerical solution of corrugated circular horns," *IEEE Trans. Antennas Propagat.*, vol. AP-30, no. 3, pp. 366-372, May 1982.
- [7] T. B. A. Senior, "Impedance boundary conditions for statistically rough surfaces," *Appl. Sci. Res.*, Sect. B, no. 8, pp. 437-462, 1960.
- [8] J. R. Wait and C. M. Jackson, "Calculations of the bistatic scattering cross section of a sphere with an impedance boundary condition," *Radio Sci. J. Res. Nat. Bur. Stand./USNC-URSI*, vol. 69D, no. 2, pp. 299-315, 1965.
- [9] G. E. Heath, "Impedance boundary condition integral equations," *IEEE AP-S International Symposium Digest, Vol. II*, pp. 697-700, IEEE, Piscataway, 1984.
- [10] A. A. Kishk, "Electromagnetic scattering from composite objects using a mixture of exact and impedance boundary conditions," *IEEE Trans. Antennas Propagat.*, vol. AP-39, no. 6, pp. 826-833, June 1991.
- [11] L. N. Medgyesi-Mitschang and J. M. Putnam,

- "Integral equation formulations for imperfectly conducting scatterers," *IEEE Trans. Antennas Propagat.*, vol. AP-33, no. 2, pp. 206-214, February 1985.
- [12] J. R. Rogers, "On combined source solutions for bodies with impedance boundary conditions," *IEEE Trans. Antennas Propagat.*, vol. AP-33, no. 4, pp. 462-464, April 1985.
- [13] W. V. T. Rusch and R. J. Pogorzelski, "A mixed-field solution for scattering from composite bodies," *IEEE Trans. Antennas Propagat.*, vol. AP-34, no. 7, pp. 955-958, July 1986.
- [14] A. Sebak and L. Shafai, "Performance of various integral equation formulations for numerical solution of scattering by impedance objects," *Can. J. Phys.*, vol. 62, pp. 605-615, 1984.
- [15] A. Sebak and L. Shafai, "Scattering from arbitrarily-shaped objects with impedance boundary conditions," *IEE Proc., Part H*, vol. 136, no. 5, pp. 371-376, 1989.
- [16] A. W. Glisson, "Electromagnetic scattering by arbitrarily shaped surfaces with impedance boundary conditions," *Radio Science*, vol. 27, no. 6, pp. 935-943, 1992.
- [17] T. B. A. Senior and J. L. Volakis, "Generalized impedance boundary conditions in scattering," *Proc. IEEE*, vol. 79, no. 10, pp. 1413-1420, October 1991.
- [18] D. J. Hoppe and Y. Rahmat-Samii, "Higher order impedance boundary conditions applied to scattering by coated bodies of revolution," *IEEE Trans. Antennas Propagat.*, vol. AP-42, no. 12, pp. 1600-1611, December 1994.
- [19] R. Orta, R. Tascone, G. Tessitore, and R. Zich, "Frequency selective surfaces made of anisotropic material (antennas)," *Proc. Int. Conf. Electromagnetics in Aerospace Applications*, Torino, Italy, pp. 341-345, 1989.
- [20] A. W. Glisson, Mark Orman, Frank Falco, and Donald Koppel, "Electromagnetic scattering by a body of revolution with a general anisotropic impedance boundary condition," *IEEE AP-S International Symposium Digest*, Vol. IV, pp. 1997-2000, Chicago, IL, 1992.
- [21] A. H. Chang, K. S. Yee, and J. Prodan, "Comparison of different integral equation formulations for bodies of revolution with anisotropic surface impedance boundary conditions," *IEEE Trans. Antennas Propagat.*, vol. AP-40, no. 8, pp. 989-991, August 1992.
- [22] S. M. Rao, D. R. Wilton, and A. W. Glisson, "Electromagnetic scattering by surfaces of arbitrary shape," *IEEE Trans. Antennas Propagat.*, vol. AP-30, no. 3, pp. 409-418, May 1982.
- [23] A. W. Glisson and M. Orman, "Implementation of the impedance boundary condition in the triangular-patch scattering code for thin scatterers," *IEEE AP-S International Symposium Digest*, Vol. III, pp. 1756-1759, London, Ontario, Canada, 1991.
- [24] R. F. Harrington, *Time Harmonic Electromagnetic Fields*. New York: McGraw-Hill, 1961.
- [25] R. F. Harrington, *Field Computation by Moment Methods*, 229 pp., Macmillan, New York, 1968.
- [26] D. R. Wilton, S. M. Rao, A. W. Glisson, D. H. Schaubert, O. M. Al-Bundak, and C. M. Butler, "Potential integrals for uniform and linear source distributions on polygonal and polyhedral domains," *IEEE Trans. Antennas Propagat.*, vol. AP-32, no. 3, pp. 276-281, March 1984.
- [27] J. Van Bladel, *Electromagnetic Fields*. New York: McGraw-Hill, 1964, p. 502.
- [28] S. V. Yesantharao, *EMPACK-A software toolbox of potential integrals for computational electromagnetics*. M. S. Thesis, University of Houston, Houston, Texas, December 1989.
- [29] A. W. Glisson, "Technical considerations for the implementation of the impedance boundary condition in the triangular-patch electromagnetic scattering code," Report No. FR-1, Subcontract No. C95-AWG, for Riverside Research Institute, New York, NY, December 1990.
- [30] F. Falco, D. Koppel, N. Erlbach, and M. Orman, "Anisotropic impedance boundary condition 3D scattering code (IB3D): Vol. I -- User's manual and programmer's guide," Technical Report, Riverside Research Institute, November 1991.
- [31] R. D. Graglia, "On the numerical integration of the linear shape functions times the 3-D Green's function or its gradient on a plane triangle," *IEEE Trans. Antennas Propagat.*, vol. AP-41, no. 10, pp. 1448-1455, October 1993.
- [32] J. R. Rogers, "JRMBOR - Program description and user's guide," Technical Report, Atlantic Aerospace Electronics Corporation, Greenbelt, Maryland, June 1989.
- [33] V. H. Weston, "Theory of absorbers in scattering," *IEEE Trans. Antennas Propagat.*, vol. AP-11, no. 5, pp. 578-584, September 1963.
- [34] J. R. Mautz and R. F. Harrington, "Electromagnetic scattering from a homogeneous material body of revolution," *Arch. Elek. Übertrag.*, vol. 33, no. 2, pp. 71-80, 1979.
- [35] K. S. Yee and A. H. Chang, "Scattering theorems with anisotropic surface boundary conditions for bodies of revolution," *IEEE Trans. Antennas Propagat.*, vol. AP-39, no. 7, pp. 1041-1043, July 1991.

Parametric mapping of vector basis functions for surface integral equation formulations

*Andrew F. Peterson and Keith R. Aberegg
School of Electrical and Computer Engineering
Georgia Institute of Technology
Atlanta, GA 30332-0250
peterson@ee.gatech.edu*

Abstract: A parametric mapping of vector basis functions is presented for curved-patch discretizations of surface integral equations. The mapping of the vector basis function maintains the normal continuity of the surface current density at cell boundaries, and is therefore suitable for use with the electric-field integral equation. Expressions for the matrix elements associated with the electric and magnetic field integral equations are developed.

1. Introduction

During the past two decades, the approximate solution of surface integral equations by the method of moments has matured into a well-accepted process. However, the most widely-used procedures tend to employ flat-cell models of curved structures and relatively low-order basis functions to represent surface currents and fields. Specifically, the Rao-Wilton-Glisson (RWG) triangular-rooftop basis functions [1] commonly used to model currents on surfaces in 3D provide only a constant normal and linear tangential representation of the surface current density. If higher accuracy in the results is desired, a low-order representation is likely to prove inefficient. Furthermore, flat cells limit the modeling resolution. In this article, we discuss the use of a higher-order vector basis set with continuity properties similar to the RWG functions, in conjunction with a curved-cell scatterer model.

The incorporation of curved cells into moment-method discretizations, although uncommon, has been discussed by a number of authors [2-8]. However, a critical issue in the discretization of surface integral equations such as the electric-field equation (EFIE) is the need to maintain continuity of the normal surface current density at cell junctions [1]. The existing literature on curved-cell representations fails to adequately address this issue. References [2] and [3] assumed a piecewise-constant

representation for the current density, while [4] investigated both piecewise-constant and piecewise-linear representations. Thus, these studies did not always impose normal continuity because of the nature of the basis functions. In addition, [2] and [4] only consider the magnetic field integral equation (MFIE), which is less sensitive to discontinuities in the current density. References [5] and [6] employed mixed-order vector basis functions on curved triangular and quadrilateral cells, respectively, and a similar approach has been reported in [7]. These articles consider the use of low-order basis functions similar to the RWG functions and do not specifically discuss the continuity properties of the curved-cell representation.

Higher-order scalar polynomial basis functions have been investigated by numerous researchers in the context of finite element solutions [9-10]. Higher-order vector functions are less well known, but have also been studied [11-13]. In general, if the scatterer model incorporates curvature, there is little additional effort required to implement higher-order basis functions (other than the additional unknowns for a given number of cells, which may be offset by improved accuracy).

In this paper, we briefly review the scalar transformation required to treat the EFIE and MFIE applied to two-dimensional scatterers. We then consider the mapping necessary to define curved-cell vector basis functions compatible with 3D surface integral equations. The development is based on a cell-by-cell coordinate mapping obtained via Lagrangian interpolation polynomials. Other specific representations of the surface (e.g., splines) could be implemented in a similar manner. For illustration, we present preliminary results for a curved-cell implementation using vector basis functions one polynomial order greater than the RWG functions.

2. Discretization of 2D surface integral equations using an isoparametric quadratic representation

To motivate the use of higher-order basis functions and curved-cell models, this section briefly reviews their application in 2D. Two-dimensional method-of-moments discretization schemes employing flat-cell models of the scatterer contours and piecewise-constant or piecewise-linear basis functions have been widely used [14]. The scatterer models can be improved by using cells with parabolic curvature. Suppose t is a parametric variable with the interval $-1 \leq t \leq 1$ used to describe a single cell. The cell can be defined by the three points (x_1, y_1) , (x_2, y_2) , and (x_3, y_3) , and the mapping

$$x(t) = x_1 B_1(t) + x_2 B_2(t) + x_3 B_3(t) \quad (1)$$

$$y(t) = y_1 B_1(t) + y_2 B_2(t) + y_3 B_3(t) \quad (2)$$

where

$$B_1(t) = \frac{t(t-1)}{2} \quad (3)$$

$$B_2(t) = 1 - t^2 \quad (4)$$

$$B_3(t) = \frac{t(t+1)}{2} \quad (5)$$

are quadratic Lagrangian interpolation functions. It is convenient to also use quadratic Lagrangian interpolation polynomials to represent the surface current density, which is known as an isoparametric expansion. For a smooth scatterer, and the TM polarization, the current density within a cell can be replaced by

$$J_z(t) \equiv \sum_{n=1}^3 j_n B_n(t) \quad -1 \leq t \leq 1 \quad (6)$$

Thus, within each cell there are three overlapping basis functions that contribute to the representation. Each basis function interpolates to the current density at one of the three "nodes" that define the cell shape, according to (1)–(2).

Consider the TM EFIE, and the use of Dirac delta testing functions (located at the interpolation nodes) to complete the discretization. The entries of the system matrix involve integrals of the form

$$I_{mn}^{cell\ p} = \frac{k\eta}{4} \int_{cell\ p} B_n(t') H_0^{(2)}(kR_m) J(t') dt' \quad (7)$$

where m and n now denote global indices,

$$R_m = \sqrt{[x_m - x(t')]^2 + [y_m - y(t')]^2} \quad (8)$$

and J is the Jacobian

$$J(t) = \sqrt{\left(\frac{dx}{dt}\right)^2 + \left(\frac{dy}{dt}\right)^2} \quad (9)$$

The Jacobian can be evaluated using the mapping in (1)–(2), which yields

$$\frac{dx}{dt} = \left(\frac{x_3 - x_1}{2}\right) + (x_1 - 2x_2 + x_3)t \quad (10)$$

$$\frac{dy}{dt} = \left(\frac{y_3 - y_1}{2}\right) + (y_1 - 2y_2 + y_3)t \quad (11)$$

within a particular cell. In general, the integrals defined by (7) must be evaluated by numerical quadrature. In the case where R_m vanishes within the interval of integration, the Hankel function singularity can be extracted, splitting the integral into two parts. The first integral can be computed by quadrature; the second can be evaluated analytically over a flat cell. As an alternative approach, the original integral can be evaluated using a quadrature rule that specifically incorporates the logarithmic singularity [15–16].

For the TE MFIE, a similar discretization can be developed, using an expansion similar to (6) for the transverse component of the current. The off-diagonal matrix entries involve integrals of the form

$$I_{mn}^{cell\ p} = \frac{k}{4j} \int_{cell\ p} B_n(t') \left\{ \sin\Omega(t') \frac{x_m - x(t')}{R_m} - \cos\Omega(t') \frac{y_m - y(t')}{R_m} \right\} H_1^{(2)}(kR_m) J(t') dt' \quad (12)$$

where the Jacobian J is defined in (9), R_m is defined in (8), and Ω denotes the continuous angle between the x -axis and the tangent vector to each point on the cell. If node m lies at an intercell node, the diagonal matrix entries for the MFIE have the form

$$Z_{mm} = -\frac{\Gamma_m}{2\pi} + I_{mm}^{cell\ p} + I_{mm}^{cell\ q} \quad (13)$$

where Γ_m denotes the total interior wedge angle formed by the conductor at node m , and $I_{mm}^{cell\ p}$ and $I_{mm}^{cell\ q}$ have the form of (12), except that a small region in the vicinity of node m is excluded from the integral. (The integral was

evaluated using an "open" quadrature formula that did not sample at the endpoints of the interval; a region on the order of $10^{-5} \lambda$ is easily excluded by this procedure.) If node m lies in the cell interior, the MFIE diagonal entries are

$$Z_{mm} = -\frac{1}{2} + I_{mm}^{cell p} \quad (14)$$

where again a small region around node m is excluded from the integral.

To illustrate the accuracy of the isoparametric Lagrangian approach, Table 1 shows the TE surface current density induced on a circular cylinder by a uniform plane wave. Results from a curved-cell discretization of the MFIE using piecewise-quadratic basis functions are compared to similar solutions obtained using a flat-cell discretization with piecewise-constant and piecewise-linear representations

of the current density. For a density of 40 unknowns/ λ , there is a consistent improvement in accuracy as the basis function order is increased. The curved-cell results exhibit four decimal places of agreement with the exact solution.

In general, numerical experimentation using a range of cell sizes tends to confirm that the error in the 2D surface current density follows the predicted interpolation error of $O(h^{p+1})$ as $h \rightarrow 0$, where h is the relative cell size and p is the polynomial degree of the basis functions (p=2 denotes quadratic functions, for instance). Thus, it is more efficient to obtain high accuracy by increasing the polynomial order than by reducing the cell sizes. Additional results using this type of mapping with a combined-field formulation are presented in [17].

Table 1

Comparison of the current density induced on a circular cylinder with circumference 1λ by a TE plane wave propagating in the $\phi=0$ direction. MFIE results obtained with pulse, linear, and quadratic basis functions and Dirac delta testing functions are compared with the exact solution, for a 40 unknown discretization. The quadratic case employs parabolic cells defined by (1)–(2); the other results were obtained using flat cells.

| ϕ | MFIE pulse basis, flat cells | MFIE linear basis, flat cells | MFIE quadratic basis, parabolic cells | exact |
|--------|------------------------------------|-------------------------------------|---|---------|
| | | (magnitude) | | |
| 0° | 0.8907 | 0.8891 | 0.8883 | 0.8882 |
| 45 | 0.6733 | 0.6729 | 0.6722 | 0.6722 |
| 90 | 1.1751 | 1.1708 | 1.1714 | 1.1713 |
| 135 | 1.6232 | 1.6201 | 1.6199 | 1.6199 |
| 180 | 1.7094 | 1.7076 | 1.7073 | 1.7071 |
| | | (phase) | | |
| 0° | 66.29° | 66.66° | 66.56° | 66.56° |
| 45 | 113.41 | 113.57 | 113.56 | 113.56 |
| 90 | -164.88 | -164.80 | -164.82 | -164.82 |
| 135 | -125.83 | -125.82 | -125.84 | -125.84 |
| 180 | -110.77 | -110.82 | -110.83 | -110.83 |

3. Mapping vector basis functions to curvilinear cells in 3D

The previous section showed that higher-order basis functions and curved cells can produce improved accuracy in scalar problems. The process of mapping scalar basis functions to curved cells in two and three dimensions is explained in a number of textbooks [9-10], and is widely understood. A transformation defined by a small number of points (nodes) on the curved cell uniquely specifies the mapped functions. Neighboring cells can be defined by independent mappings that share nodes along the common edges. Usually, the continuity of the scalar basis functions is maintained across curved cell boundaries, although derivative continuity is not. (Derivative continuity can be maintained by alternative mappings involving spline functions or Hermitian interpolation polynomials.)

One would expect to realize a similar improvement in accuracy from the use of higher-order functions and curved cells in vector problems, such as the 3D EFIE. When transforming vector basis functions, however, there is an additional degree of freedom embodied in the vector direction of the function that was not present in the scalar case. Thus, the vector mapping process is somewhat different from that used with scalar basis functions. A local mapping that describes the curved cell shape via Lagrangian polynomials will generally not be able to maintain the complete continuity of a vector basis function across cell boundaries. For the treatment of surface integral equations such as the EFIE, the surface current density must maintain normal continuity across cell junctions, in order that the surface divergence of the current remains finite at the cell edges. Therefore, it is critical to define the vector projection in a way that ensures normal continuity. In addition, to treat surface integral equations the mapping involves a two-dimensional surface in three-dimensional space. Crowley has discussed the mapping of a tangentially-continuous vector representation (the complementary case), for application to the vector Helmholtz equation [18]. A covariant mapping preserves tangential continuity. Apparently, no detailed discussion of the appropriate parametric mapping needed for surface integral equations exists at present in the electromagnetics literature. Normal continuity can be preserved by using a contravariant mapping, as described below.

For illustration, the following development considers a curved quadrilateral cell shape; the same expressions apply to triangular cells provided that the limits of integration are modified accordingly. Consider a basis function defined in the 2D reference cell ($-1 < \eta < 1$, $-1 < \xi < 1$). This vector can be represented by its covariant components

$$\bar{B} = (\bar{B} \cdot \bar{\eta}) \bar{\eta}' + (\bar{B} \cdot \bar{\xi}) \bar{\xi}' \quad (15)$$

or its contravariant components

$$\bar{B} = (\bar{B} \cdot \bar{\eta}') \bar{\eta} + (\bar{B} \cdot \bar{\xi}') \bar{\xi} \quad (16)$$

where the base vectors are given by

$$\bar{\eta} = \frac{\partial x}{\partial \eta} \hat{x} + \frac{\partial y}{\partial \eta} \hat{y} + \frac{\partial z}{\partial \eta} \hat{z} \quad (17)$$

$$\bar{\xi} = \frac{\partial x}{\partial \xi} \hat{x} + \frac{\partial y}{\partial \xi} \hat{y} + \frac{\partial z}{\partial \xi} \hat{z} \quad (18)$$

and the reciprocal base vectors are given by

$$\bar{\eta}' = \frac{\partial \eta}{\partial x} \hat{x} + \frac{\partial \eta}{\partial y} \hat{y} + \frac{\partial \eta}{\partial z} \hat{z} \quad (19)$$

$$\bar{\xi}' = \frac{\partial \xi}{\partial x} \hat{x} + \frac{\partial \xi}{\partial y} \hat{y} + \frac{\partial \xi}{\partial z} \hat{z} \quad (20)$$

In a skewed quadrilateral cell, the base vectors are tangential to the cell edges while the reciprocal base vectors are normal to the cell edges. The mapping from the 2D reference cell to the curved patch in 3D can be defined by a transformation of the form

$$x = \sum_n x_n B_n(\eta, \xi) \quad (21)$$

$$y = \sum_n y_n B_n(\eta, \xi) \quad (22)$$

$$z = \sum_n z_n B_n(\eta, \xi) \quad (23)$$

where $\{B_n\}$ represents a set of scalar Lagrangian interpolation functions (of any order), and the nodes (x_n, y_n) specify the specific patch shape. Therefore, the Jacobian relationship is given by

$$\begin{bmatrix} \frac{\partial}{\partial \eta} \\ \frac{\partial}{\partial \xi} \end{bmatrix} = \begin{bmatrix} \frac{\partial x}{\partial \eta} & \frac{\partial y}{\partial \eta} & \frac{\partial z}{\partial \eta} \\ \frac{\partial x}{\partial \xi} & \frac{\partial y}{\partial \xi} & \frac{\partial z}{\partial \xi} \end{bmatrix} \begin{bmatrix} \frac{\partial}{\partial x} \\ \frac{\partial}{\partial y} \\ \frac{\partial}{\partial z} \end{bmatrix} = J \begin{bmatrix} \frac{\partial}{\partial x} \\ \frac{\partial}{\partial y} \\ \frac{\partial}{\partial z} \end{bmatrix} \quad (24)$$

For use with surface integral equations, the basis functions must be tangential to the curved patch at every point within the patch, and ensure normal continuity between adjacent patches. These characteristics can be obtained if the

Cartesian components of the basis function in each cell are defined by the contravariant mapping

$$\begin{bmatrix} B_x \\ B_y \\ B_z \end{bmatrix} = \frac{1}{Q} J^T \begin{bmatrix} B_\eta \\ B_\xi \end{bmatrix} \quad (25)$$

where B_η and B_ξ denote the contravariant components of the basis function in the reference cell,

$$Q = \sqrt{\left(\frac{\partial x}{\partial \eta} \frac{\partial z}{\partial \xi} - \frac{\partial x}{\partial \xi} \frac{\partial z}{\partial \eta}\right)^2 + \left(\frac{\partial x}{\partial \eta} \frac{\partial y}{\partial \xi} - \frac{\partial x}{\partial \xi} \frac{\partial y}{\partial \eta}\right)^2 + \left(\frac{\partial y}{\partial \eta} \frac{\partial z}{\partial \xi} - \frac{\partial y}{\partial \xi} \frac{\partial z}{\partial \eta}\right)^2} \quad (26)$$

is the pseudo-determinant of the 2×3 Jacobian matrix, and we assume that the basis functions B_η and B_ξ maintain normal continuity in the reference cell. The factor Q defines the scaling necessary to write the differential surface area

$$dS = Q d\eta d\xi \quad (27)$$

in terms of the (η, ξ) coordinates.

When working with mapped basis functions, it is convenient to perform the calculations directly in the (η, ξ) system. Thus, we would like to express the integrals arising from the EFIE in terms of η and ξ . For a basis function defined by Equation (25), it is possible to show that the surface divergence operation on a curved cell simplifies to

$$\nabla_s \cdot \bar{B} = \frac{1}{Q} \left\{ \frac{\partial B_\eta}{\partial \eta} + \frac{\partial B_\xi}{\partial \xi} \right\} \quad (28)$$

By combining Equations (27) and (28), the contribution from one cell to the scalar potential integral within the EFIE can be written as

$$\Phi = \frac{1}{j\omega\epsilon} \int \int (\nabla_s \cdot \bar{B}_n) G dS' = \frac{1}{j\omega\epsilon} \int_{\eta'=1}^1 \int_{\xi'=1}^1 \left\{ \frac{\partial B_\eta}{\partial \eta'} + \frac{\partial B_\xi}{\partial \xi'} \right\} G d\eta' d\xi' \quad (29)$$

where G denotes the Green's function. Since the testing functions are also defined by the transformation in (25), a general form for the complete matrix entry is

$$\begin{aligned} & \int \int \bar{T}_m \cdot \nabla \Phi dS \\ &= - \int \int (\nabla \cdot \bar{T}_m) \Phi dS \end{aligned}$$

$$= - \int_{\eta=-1}^1 \int_{\xi=-1}^1 \left\{ \frac{\partial T_{m\eta}}{\partial \eta} + \frac{\partial T_{m\xi}}{\partial \xi} \right\} \Phi d\eta d\xi \quad (30)$$

Using (25) and (27), the matrix entry associated with the magnetic vector potential term in the EFIE can be written in terms of the integral

$$\begin{aligned} & \int \int \bar{T}_m(\bar{r}) \cdot \left\{ \int \int \bar{B}_n(\bar{r}) G dS' \right\} dS \\ &= \int_{\eta=-1}^1 \int_{\xi=-1}^1 \int_{\eta'=-1}^1 \int_{\xi'=-1}^1 [T_{m\eta} \ T_{m\xi}] J J^T \begin{bmatrix} B_{m\eta} \\ B_{m\xi} \end{bmatrix} G d\eta' d\xi' d\eta d\xi \quad (31) \end{aligned}$$

Thus, in these integrals the scale factors arising from the basis and testing functions cancel those arising from the differential surface areas. The matrix entries associated with the MFIE can also be expressed over curved patches; for instance the off-diagonal entries have the form

$$\begin{aligned} & \int \int \bar{T} \cdot \bar{H}^s dS = \\ & \int_{\eta} \int_{\xi} \int_{\eta'} \int_{\xi'} [T_\eta \ T_\xi] J \begin{bmatrix} 0 & -\frac{\partial G}{\partial z} & \frac{\partial G}{\partial y} \\ \frac{\partial G}{\partial z} & 0 & -\frac{\partial G}{\partial x} \\ \frac{\partial G}{\partial y} & \frac{\partial G}{\partial x} & 0 \end{bmatrix} J^T \begin{bmatrix} B_\eta \\ B_\xi \end{bmatrix} d\eta' d\xi' d\eta d\xi \quad (32) \end{aligned}$$

while the diagonal entries differ in the usual way due to the total field term and the Green's function singularity.

The general expressions in (30)–(32) provide a convenient way of computing the matrix entries when a piecewise-parametric representation is used to define the curved surface. All integrals can be performed over the square reference cell in the (η, ξ) coordinate system by numerical quadrature. In the case of a triangular reference cell, the limits of integration in (30)–(32) must be modified to incorporate the triangular cell shape.

4. Higher-order vector basis functions for surface currents

The surface current representation proposed in 1982 by Rao, Wilton and Glisson [1] has a constant normal component and a linear tangential component (CN/LT) around the cell edges. Better accuracy could be obtained with higher-order polynomial functions. Functions have been proposed that provide a linear normal, quadratic-tangent (LN/QT) representation of the surface current density, and exhibit finite divergence throughout the computational domain [13]. As compared with an RWG representation, where three basis functions overlap each cell, eight different

LN/QT basis functions overlap each triangular cell. Six of these functions have support shared by two triangular cells, like the RWG CN/LT functions. Each of these six functions interpolates to the normal vector component of the surface current at one end of a cell edge. These six functions maintain normal-vector continuity with the adjoining cell, and eliminate fictitious charge densities at cell interfaces. Equivalently, the surface divergence of the representation remains finite. Within a single cell, these six edge-based basis functions can be expressed as

$$\hat{z} \times w_{ij} L_i \nabla L_j, \quad i \neq j \quad (33)$$

where $\{L_1, L_2, L_3\}$ denote simplex coordinates [9-10] within a triangle in the x-y plane, and w_{ij} is the length of the edge between nodes i and j . (L_1 and L_2 play the role of the local coordinates η and ξ in the expressions from the preceding section, with L_3 defined by $L_3 = 1 - L_1 - L_2$.) In addition, there are two basis functions in each cell whose support is confined to that cell. These cell-based functions can be expressed in simplex coordinates as

$$\hat{z} \times 4w_{13}\{L_2 L_3 \nabla L_1 - L_1 L_2 \nabla L_3\} \quad (34)$$

and

$$\hat{z} \times 4w_{23}\{L_1 L_3 \nabla L_2 - L_1 L_2 \nabla L_3\} \quad (35)$$

These two functions have zero normal component along all three edges of the cell, and together provide a quadratic representation for the tangential component of the current density. The LN/QT basis functions have been motivated by the development of complementary techniques for discretizing the curl-curl form of the vector Helmholtz equation [19]. The basis functions belong to the mixed-order divergence-conforming spaces originally proposed by Nedelec [11], which include representations for arbitrary polynomial order. For a triangular-cell model, the global LN/QT representation consists of two basis functions per non-boundary edge and two basis functions per cell. Figure 1 depicts these basis functions.

The 8 basis functions in Equations (33)–(35) are linearly independent and can be used as testing functions within a Galerkin implementation, if desired. However, for simplicity we propose the use of piecewise-constant “razor-blade” testing functions defined along linearly independent paths that roughly correspond to the basis function locations, as depicted in Figure 2.

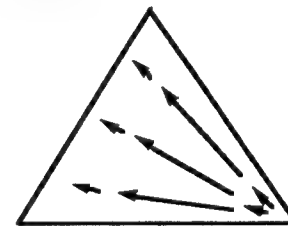
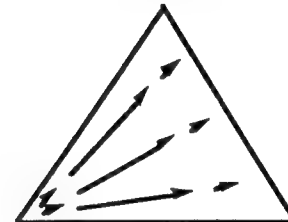
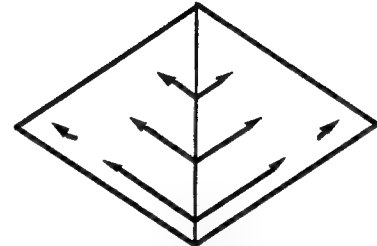
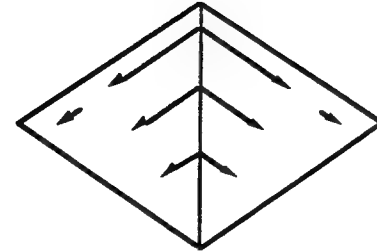


Figure 1. The linear-normal/quadratic-tangential (LN/QT) basis functions defined on a triangular cell. The upper two triangles depict the edge-based functions, while the lower two depict the cell-based functions.

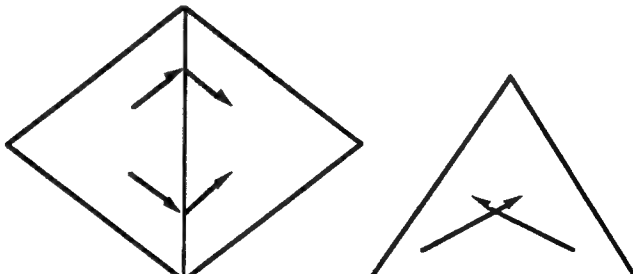


Figure 2. Domain of support for the razor-blade testing functions on triangles. The left cell shows the path for the edge-based functions; the right shows the path for the cell-based functions.

5. Preliminary results

To demonstrate the preceding ideas, we implemented the basis functions in (33)–(35) using a piecewise-parabolic surface representation defined by triangular-cell quadratic Lagrangian polynomials. Each patch is defined by the mapping in (21)–(23), using 6 scalar interpolation polynomials

$$B_{200}(L_1, L_2, L_3) = (2L_1 - 1)L_1 \quad (36)$$

$$B_{020}(L_1, L_2, L_3) = (2L_2 - 1)L_2 \quad (37)$$

$$B_{002}(L_1, L_2, L_3) = (2L_3 - 1)L_3 \quad (38)$$

$$B_{110}(L_1, L_2, L_3) = 4L_1 L_2 \quad (39)$$

$$B_{101}(L_1, L_2, L_3) = 4L_1 L_3 \quad (40)$$

$$B_{011}(L_1, L_2, L_3) = 4L_2 L_3 \quad (41)$$

and 6 coordinate values at the corners and mid-sides of each cell. The first three functions have unity value at one corner node, while the latter three functions have unity value in the center of one of the three sides.

The functions in (36)–(41) define the shape of the curved cells comprising the scatterer, given six points per patch from which to interpolate according to (21)–(23). By converting from simplex coordinates to Cartesian coordinates [10], one readily obtains the entries of the Jacobian matrix defined in (24). The LN/QT basis functions defined in (33)–(35) are mapped to the curved cells using the contravariant projection in (25), and used to represent the vector surface current density. The matrix entries for the EFIE are obtained from (30)–(31), with the integration limits suitably modified for a triangular reference cell. Equations (30)–(31) account for the curved-cell mapping, so the only additional effort needed to implement the curved-cell discretization is the computation of the Jacobian matrix at points needed for the quadrature algorithm used to evaluate (30) and (31). Since the integration is performed in the reference cell, it is not necessary to explicitly define the basis functions within the curved patches.

The evaluation of the matrix entries by numerical quadrature is straightforward except when the source and observation regions overlap, due to the Green's function singularity. In this case, the $1/R$ singularity is extracted and evaluated analytically over a tangent plane, then added back to the result of the quadrature.

For illustration, consider a plane wave illuminating a perfectly conducting sphere of radius 0.2λ , where λ denotes the wavelength. Figures 3a, 3b, 4a, and 4b depict the magnitude and phase of the surface currents around the sphere. The surface current density is normalized to the magnitude of the incident magnetic field. The incident field propagates in the $-z$ direction with the electric field polarized in the $-x$ direction. Exact solutions are compared to EFIE results obtained using curved-cell and flat-cell models, each of which consist of 48 cells and produce a moment-method system of order 240. Both results employed LN/QT basis functions and razor-blade testing functions. Clearly, the curved-cell data more closely approximates the exact solution. Since the basis functions provide normal continuity but not tangential continuity, there are a few places where jump discontinuities can be observed in these plots. These discontinuities occur in places where the tangential component contributes to the current density shown in the plot, and they diminish as the model is refined and the cell sizes are reduced. Figure 5 shows the scattering cross section comparison for the same example. In this case, the flat-cell model is inscribed within the actual sphere and the scattering cross section differs substantially from the true values.

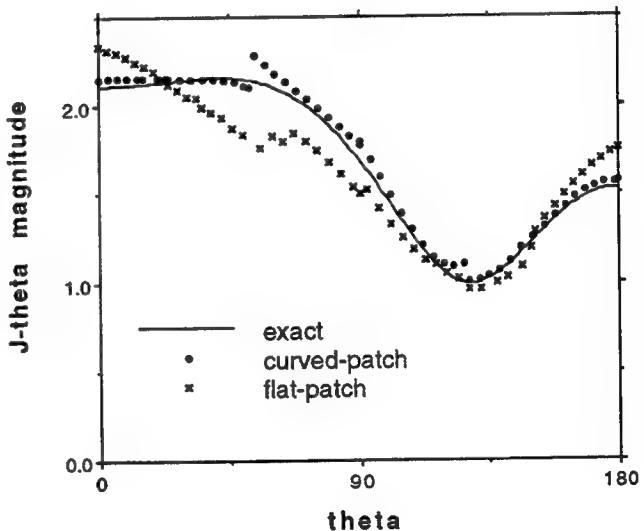


Figure 3(a). The magnitude of the θ -component of the current density induced by a uniform plane wave on a spherical conducting scatterer with radius 0.2 wavelengths. Numerical results produced using LN/QT basis functions with a flat-cell model and a curved-cell model are compared with the exact solutions. The models contained 48 cells and produced a system of order 240.

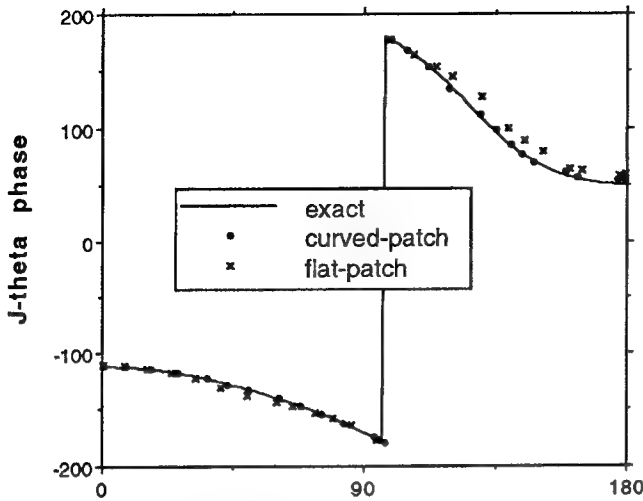


Figure 3(b). The phase of the θ -component of the current density for the example in Figure 3(a).

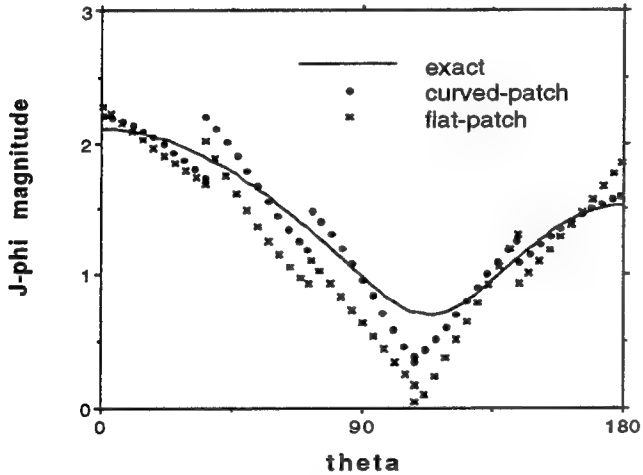


Figure 4(a). The magnitude of the ϕ -component of the current density for the example in Figure 3(a).

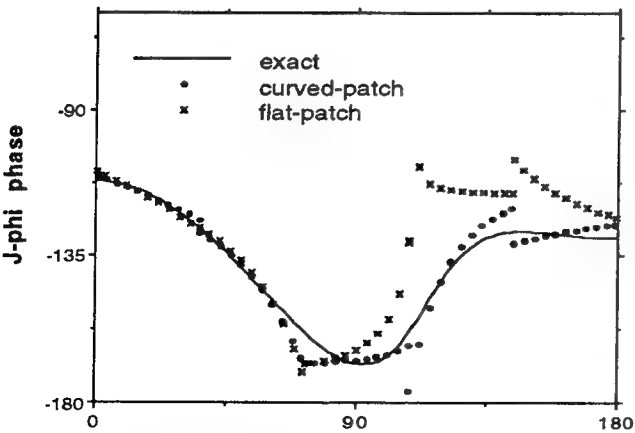


Figure 4(b). The phase of the ϕ -component of the current density for the example in Figure 3(a).

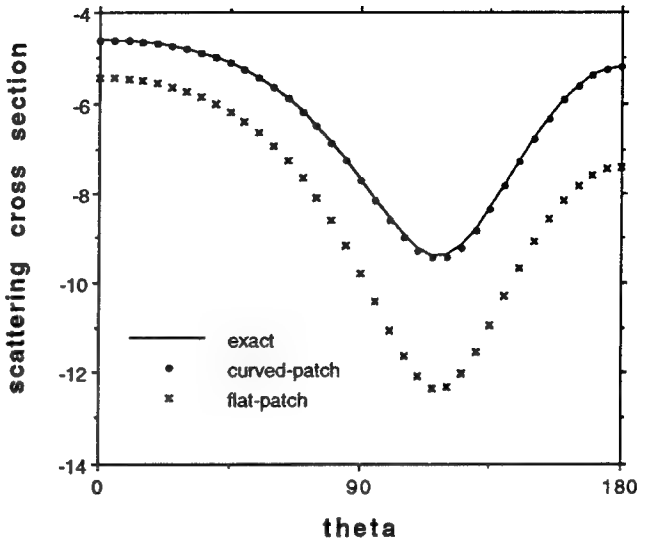


Figure 5. The scattering cross section ($\text{dB } \lambda^2$) for a spherical conducting scatterer with radius 0.2 wavelengths, shown for $\phi=0$. Numerical results obtained using LN/QT basis functions with flat-cell and curved-cell models are compared with the exact solution. The models contained 48 cells and produced a system of order 240. The substantial difference in the accuracy of the numerical results may be due in part to the fact that the flat-cell model was inscribed within the desired sphere.

6. Summary

In practice, the accuracy of most numerical solutions is limited by the interpolation error associated with the expansion, and the use of higher-order functions and curved cells is expected to provide better accuracy and faster convergence. This paper presents a procedure for defining vector basis functions on curved cells, while maintaining the normal-vector continuity of the representation. Expressions for the matrix entries arising from EFIE and MFIE discretizations are presented. The 3D procedure has been implemented using LN/QT basis functions and curved triangular patches defined by a scalar Lagrangian mapping. Additional 3D results based on the EFIE, MFIE, and combined field equation are available in [20].

7. References

- [1] S. M. Rao, D. R. Wilton, and A. W. Glisson, "Electromagnetic scattering by surfaces of arbitrary shape," *IEEE Trans. Antennas Propagat.*, vol. AP-30, pp. 409-418, May 1982.
- [2] D. L. Knepp and J. Goldhirsh, "Numerical analysis of electromagnetic radiation properties of smooth conducting bodies of arbitrary shape," *IEEE Trans. Antennas Propagat.*, vol. AP-20, pp. 383-388, May 1972.
- [3] M. I. Sancer, R. L. McClary, and K. J. Glover, "Electromagnetic computation using parametric geometry," *Electromagnetics*, vol. 10, pp. 85-103, 1990.
- [4] M. S. Ingber and R. H. Ott, "An application of the boundary element method to the magnetic field integral equation," *IEEE Trans. Antennas Propagat.*, vol. 39, pp. 606-611, May 1991.
- [5] N. Y. Zhu and F. M. Landstorfer, "Application of curved parametric triangular and quadrilateral edge elements in the moment method solution of the EFIE," *IEEE Microwave and Guided Wave Letters*, vol. 3, pp. 319-321, Sept. 1993.
- [6] G. E. Antilla and N. G. Alexopoulos, "Scattering from complex three-dimensional geometries by a curvilinear hybrid finite element - integral equation approach," *J. Opt. Soc. Amer. A*, vol. 11, pp. 1445-1457, April 1994.
- [7] D. Wilkes and C. C. Cha, "Method of moments solution with parametric curved triangular patches," *Digest of the 1991 IEEE Antennas and Propagation Society International Symposium*, London, ON, pp. 1512-1515, June 1991.
- [8] J. M. Song and W. C. Chew, "Moment method solutions using parametric geometry," *J. Electromagnetic Waves Applics.*, vol. 9, pp. 73-81, 1995.
- [9] O. C. Zienkiewicz and R. L. Taylor, *The Finite Element Method*. London: McGraw-Hill, 1988.
- [10] P. P. Silvester and R. L. Ferrari, *Finite Elements for Electrical Engineers*. Cambridge: Cambridge University Press, 1990.
- [11] J. C. Nedelec, "Mixed finite elements in R3," *Numer. Math.*, vol. 35, pp. 315-341, 1980.
- [12] S. Wandzura, "Electric current basis functions for curved surfaces," *Electromagnetics*, vol. 12, pp. 77-91, 1992.
- [13] A. F. Peterson, "Higher-order surface patch basis functions for EFIE formulations," *Digest of the 1994 IEEE Antennas and Propagation Society International Symposium*, Seattle, WA, pp. 2162-2165, June 1994.
- [14] R. F. Harrington, *Field Computation by Moment Methods*. Macmillan, 1968.
- [15] S. Wandzura, "Accuracy in computation of matrix elements of singular kernels," *Proceedings of the Eleventh Annual Review of Progress in Applied Computational Electromagnetics*, Monterey, CA, pp. 1170-1176, March 1995.
- [16] J. Ma, V. Rokhlin, and S. Wandzura, "Generalized Gaussian quadrature rules for systems of arbitrary functions," Research Report YALEU/DCS/RR-990, Yale University, October 1993.
- [17] K. R. Aberegg and A. F. Peterson, "Application of the integral equation - asymptotic phase method to two-dimensional scattering," *IEEE Trans. Antennas Propagat.*, vol. 43, pp. 534-537, May 1995.
- [18] C. W. Crowley, *Mixed-order Covariant Projection Finite Elements for Vector Fields*. Ph.D. Dissertation, McGill University, Montreal, Quebec, 1988.
- [19] A. F. Peterson, "Vector finite element formulation for scattering from two-dimensional heterogeneous bodies," *IEEE Trans. Antennas Propagat.*, vol. 43, pp. 357-365, March 1995.
- [20] K. R. Aberegg, "Electromagnetic scattering using the integral equation - asymptotic phase method," Ph.D. dissertation, Georgia Institute of Technology, Atlanta, 1995.

A Technique for Avoiding the EFIE “Interior Resonance” Problem Applied to an MM Solution of Electromagnetic Radiation from Bodies of Revolution

Pierre Steyn and David B. Davidson

Department of Electrical and Electronic Engineering

University of Stellenbosch, Stellenbosch 7600, South Africa

e-mail: davidson@firga.sun.ac.za

Abstract

Various surface integral equation formulations, including the electric (EFIE) and magnetic (MFIE) field integral equations, suffer from what is commonly known as the “interior resonance” problem. There are a number of remedies to this problem of which many involve modifying the integral equation formulation and result in increased computational effort and computer storage requirements. In an attempt to avoid this the application of a remedy, proposed in the literature, which requires no modification to the formulation has been investigated. This involves the detection of interior resonance frequencies and correction of the current by removing the mode responsible for the “interior resonance”. In the literature, the success of the remedy has been demonstrated for two-dimensional scattering problems involving PEC cylinders. In this work it is demonstrated that, while the correction of the MM (moment method) solution is successful when an “interior resonance” has been detected, the detection of the interior resonance frequencies can be extremely difficult in an MM solution of radiation from composite bodies of revolution. In fact, a foolproof computational algorithm for detecting interior resonance frequencies for this class of problems is yet to be developed.

1 Introduction

The electric field integral equation (EFIE) and magnetic field integral equation (MFIE) suffer from what is commonly known as the “interior resonance” problem. The reason for this is that some surface integral equation (SIE) formulations, including the EFIE and MFIE, can be used to represent both an interior and an exterior electromagnetic problem for a closed geometry.

The exterior problem involves fields produced by an applied source whereas the interior, or cavity, problem involves source-free “resonant cavity modes”. The cavity modes of the interior problem occur at discrete frequencies known as eigenfrequencies. Thus, when solving the exterior problem in the region of these eigenfrequencies, the SIE’s solution is not unique because a nontrivial solution exists to the interior problem.

The problem is widely reported in the literature, e.g. [1, 2, 3, 4, 5]. Recently, Peterson presented an excellent review of the problem, along with a survey of various remedies [6]. Numerous references to the literature are included therein.

Many of the remedies to the problem involve modifying the SIE formulation. For example, the combined field integral equation (CFIE) [1], involving a linear combination of the EFIE and MFIE, yields unique solutions at all frequencies. These remedies require more computational effort than the EFIE or MFIE and possibly more computer storage as well.

A remedy proposed by Canning in [7] involves solving the EFIE or MFIE without modifications and correcting the solution near eigenfrequencies. Algorithms that execute this correction, which involves detecting the presence of a cavity mode superimposed on the desired solution and “discarding” it, can be added to existing MM solutions of the EFIE and MFIE without major modifications.

The purpose of the study presented here is to investigate the application of this method to an existing MM/BOR formulation for the solution of scattering [8] and radiation [9] from composite bodies of revolution¹.

¹By composite it is meant here as made up of different homogeneous isotropic material regions, penetrable by electromagnetic waves, and perfectly electrically conducting regions surrounded by free space. The material regions can be lossy.

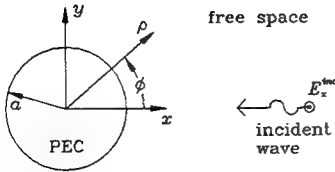


Figure 1: A circular cylinder of infinite length, extending from $z = -\infty$ to ∞ (the z -axis points out of the page), illuminated by a TM plane wave.

For conducting regions the MM/BOR formulation utilizes the EFIE, while for penetrable regions the CFIE is used.

Following this introduction is a demonstration of the “interior resonance” problem in the application of the EFIE to a two-dimensional problem. This is followed by a numerical investigation of the problem, which follows the work presented by Canning in [10] although from a different perspective, wherein the singular value decomposition (SVD) was used to demonstrate why the “interior resonance” problem occurs. The application of Canning’s remedy to the canonical problems is then discussed. Finally, Canning’s remedy is applied to the MM/BOR formulation and subtleties involved in its implementation are demonstrated and discussed.

2 Demonstration of the “Interior Resonance” problem

To illustrate the interior resonance problem it is useful to analyze a problem that can be solved analytically. Such a problem, which has previously been investigated by Peterson [6] and Canning [10], is scattering of a transverse magnetic (TM) plane wave from a perfectly electrically conducting (PEC) circular cylinder of infinite length. It is presented here in a different manner in order to highlight certain points. The problem is illustrated in Figure 1. Here the incident plane wave is assumed to be traveling in the negative x -direction with the incident electric field given by

$$\bar{E}^{inc} = \hat{z} E_0 e^{j k_0 x} \quad (1)$$

where E_0 is a constant, \hat{z} is the unit vector in the z -direction and k_0 is the wave number of free space. This is a two-dimensional problem with the EFIE given by

$$\bar{E}^{inc}|_{\rho=a} = \hat{z} \frac{k_0 a \eta_0}{4} \int_{-\pi}^{\pi} J_z(\phi') H_0^{(2)}(k_0 a |\hat{\rho} - \hat{\rho}'|) d\phi' \quad (2)$$

where unprimed coordinates indicate the field point, primed coordinates the source point, a is the radius of the cylinder, and η_0 is the intrinsic impedance of free

space. The kernel of the integral, $H_0^{(2)}$, is the Hankel function of the second type and order zero, and J_z is the desired surface current.

An MM solution to this problem will be compared with an analytical solution.

An analytical solution for the problem can be obtained by following the MM solution procedure [11, pages 5-6] as follows. The surface current is expanded as a Fourier series that is appropriate to the geometry of the problem, i.e.

$$J_z(\phi) = \frac{a_0}{2} + \sum_{n=1}^{\infty} (a_n \cos n\phi + b_n \sin n\phi) \quad (3)$$

where a_n and b_n are unknown coefficients. The expansion functions are $\{\frac{1}{2}, \cos n\phi, \sin n\phi\}$ with $n = 1, \dots, \infty$, and the testing functions are chosen as $\{1, \cos m\phi, \sin m\phi\}$ with $m = 1, \dots, \infty$. By substituting equation (3) into (2) and forming the inner product with each testing function, equation (2) is transformed into the infinite order matrix equation

$$\begin{bmatrix} \Lambda_0 & 0 & 0 & \cdots & 0 & 0 & \cdots & 0 & 0 \\ 0 & \Lambda_1 & 0 & \cdots & 0 & 0 & \cdots & 0 & 0 \\ 0 & 0 & \Lambda_1 & \cdots & 0 & 0 & \cdots & 0 & 0 \\ \vdots & \vdots & \vdots & \ddots & \vdots & \vdots & \cdots & \vdots & \vdots \\ 0 & 0 & 0 & \cdots & \Lambda_m & 0 & \cdots & 0 & 0 \\ 0 & 0 & 0 & \cdots & 0 & \Lambda_m & \cdots & 0 & 0 \\ \vdots & \vdots & \vdots & \cdots & \vdots & \vdots & \ddots & \vdots & \vdots \\ 0 & 0 & 0 & \cdots & 0 & 0 & \cdots & \Lambda_{\infty} & 0 \\ 0 & 0 & 0 & \cdots & 0 & 0 & \cdots & 0 & \Lambda_{\infty} \end{bmatrix} \begin{bmatrix} a_0 \\ a_1 \\ b_1 \\ \vdots \\ a_n \\ b_n \\ \vdots \\ a_{\infty} \\ b_{\infty} \end{bmatrix} = \begin{bmatrix} v_0 & v_1 & 0 & \cdots & v_m & 0 & \cdots & v_{\infty} & 0 \end{bmatrix}^T \quad (4)$$

where $v_n = 2E_0 j^n J_n(k_0 a)$, with J_n being the Bessel function of order n , and $\Lambda_0, \Lambda_1, \dots, \Lambda_{\infty}$ are the eigenvalues of equation (2) which are given by

$$\Lambda_m = \frac{\eta_0 \pi k_0 a}{2} J_m(k_0 a) H_m^{(2)}(k_0 a) \quad (5)$$

where $H_m^{(2)}$ is the m -th order Hankel function of the second type.

Since the matrix of equation (4) is diagonal, the unknown coefficients can easily be obtained and are, for $n = 0, 1, \dots, \infty$,

$$a_n = \frac{4E_0 j^n}{\eta_0 \pi k_0 a H_n^{(2)}(k_0 a)}, \quad (6)$$

$$b_n = 0. \quad (7)$$

The surface current can then be determined using equation (3) with these coefficients.

For a given $k_0 a$ value the magnitude of the coefficients of equation (6) decreases with increasing n and beyond about $n = k_0 a + 2\pi$ their magnitudes are less than one percent of a_0 . Thus, $J_z(\phi)$ can be computed reasonably accurately using $N_{max} \geq k_0 a + 2\pi$ terms in the summation in equation (3).

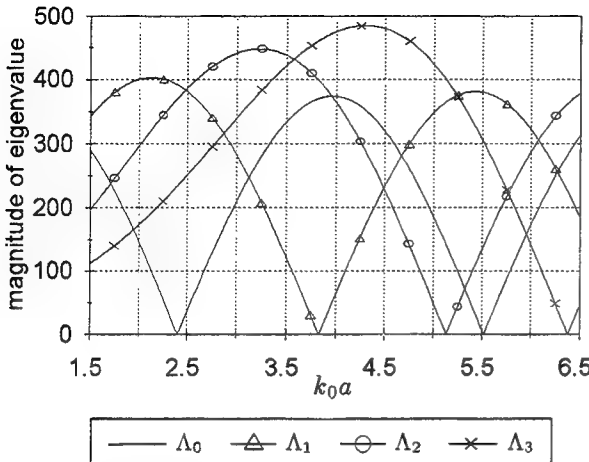


Figure 2: Behavior of the first few eigenvalues versus k_0a for a circular cylinder of infinite length.

The interior problem, i.e. the circular cavity of infinite length formed by the outer boundary of the cylinder, described by equation (2) with the left hand side set to zero, has nontrivial solutions at frequencies where the eigenvalues of equation (5) are zero. These coincide with the zeros of $J_m(k_0a)$ with $m = 0, 1, \dots, \infty$. The behaviour of the first few eigenvalues from $k_0a = 1.5$ to 6.5, computed using equation (5), are plotted in Figure 2. The first few resonances are seen to occur at $k_0a = 2.405, 3.832, 5.136, 5.520$ and 6.380 with the responsible eigenvalues being $\Lambda_0, \Lambda_1, \Lambda_2, \Lambda_0$, and Λ_3 respectively.

An approximate, but more general, MM solution to equation (2) was obtained using pulse basis functions and impulse testing functions as described in [11, pages 42-45]. The circle that generates the circular cylinder was approximated by a regular N -sided polygon, circumscribed by the circle. The pulses coincided with the sides of this polygon and the testing was done at the centres of these sides. The non-diagonal elements of the impedance matrix were found by approximating each integral by the value of the integrand at the middle of the pulse multiplied by the pulse width [11, equation (3-12)]. To avoid the singularity in the self terms, the diagonal elements were obtained by replacing the Hankel functions by their small argument form and integrating analytically [11, equation (3-14)]. The result is a matrix equation

$$\mathbf{ZJ} = \mathbf{E}_i \quad (8)$$

where the vector \mathbf{J} contains the unknown current coefficients, the elements of \mathbf{E}_i are given, with $E_0 = 1$, by

$$E_{im} = \Delta C_m e^{j k_0 x_m} \quad (9)$$

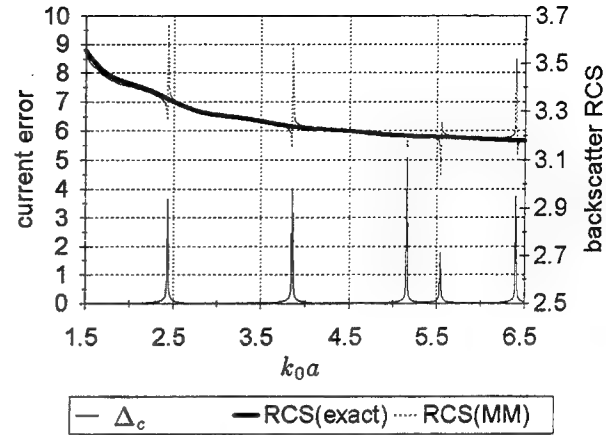


Figure 3: Electric current error Δ_C in the MM solution and backscatter RCS, exact and MM solutions, versus k_0a for scattering by a PEC circular cylinder of infinite length excited by an incident TM plane wave.

and the elements of \mathbf{Z} given by

$$Z_{mn} = \begin{cases} \frac{k_0 \eta_0 \Delta C_m \Delta C_n}{4} H_0^{(2)}[k_0 \sqrt{(x_n - x_m)^2 + (y_n - y_m)^2}] & m \neq n, \\ \frac{k_0 \eta_0 \Delta C_m \Delta C_n}{4} [1 - j \frac{2}{\pi} \log(\frac{\gamma k_0 \Delta C_n}{4e})] & m = n \end{cases} \quad (10)$$

where ΔC_m is the width of pulse m , x_m and y_m are the coordinates of the centre of pulse m , $\gamma = 1.7810724\dots$ such that $\log \gamma$ is Euler's constant and $e = 2.7182818\dots$ is the natural base of logarithms. Here the widths of all the pulses are equal which results in \mathbf{Z} for this problem being complex symmetric (it is, in fact, Toeplitz).

The current, \vec{J}_{MM} , obtained using the formulas of equations (10) and (9) can be compared with the "exact" current, \vec{J}_{exact} , computed using equation (3) by determining the current error, Δ_C , given by [1, equation (30)]

$$\Delta_C = \sqrt{\frac{\iint_S |\vec{J}_{MM} - \vec{J}_{exact}|^2 ds}{|\vec{H}^{inc}|^2 \iint_S ds}}. \quad (11)$$

where S is the surface of the PEC cylinder and \vec{H}^{inc} is the incident magnetic field. A plot of Δ_C for this problem, from $k_0a = 1.5$ to 6.5, is given in Figure 3. The number of unknowns N_{MM} in the MM computation varied with k_0a according to the formula

$$N_{MM} \geq 10k_0a \quad (12)$$

which ensures that there are 10 unknowns per wavelength. It is observed that Δ_C is small except in the vicinity of those values of k_0a that coincide with the interior resonances observed in Figure 2.

Also plotted in Figure 3 is the backscatter radar cross section (RCS) computed by the exact solution and the MM which demonstrates that the anomalies in the current couple to the far field.

3 Investigation of the “Interior Resonance” problem using the SVD

Canning introduced the application of the SVD to the study of MM matrices in [10]. The SVD is discussed in numerous texts related to linear algebra, for example [12]. An SVD of an N -by- N matrix \mathbf{A} is any factorization of the form

$$\mathbf{A} = \mathbf{U}\mathbf{S}\mathbf{V}^h \quad (13)$$

where the superscript h indicates the Hermitian conjugate, \mathbf{U} is an N -by- N unitary matrix, \mathbf{V} is an N -by- N unitary matrix and \mathbf{S} is an N -by- N diagonal matrix with elements $s_{mn} = 0$ if $m \neq n$. The diagonal elements of \mathbf{S} , $s_n = s_{nn}$, are known as the singular values. These are real, nonnegative and arranged in order of decreasing magnitude. The columns of \mathbf{U} are the left singular vectors and the columns of \mathbf{V} are the right singular vectors.

By following the MM procedure, the EFIE is transformed to a matrix equation of the form given by equation (8). Decomposition of \mathbf{Z} to its SVD reduces equation (8) to the diagonal equation

$$\mathbf{S}\tilde{\mathbf{J}} = \tilde{\mathbf{E}}_i \quad (14)$$

where $\tilde{\mathbf{J}} = \mathbf{V}^h\mathbf{J}$ and $\tilde{\mathbf{E}}_i = \mathbf{U}^h\mathbf{E}_i$. Thus, the SVD diagonalizes the MM equation and $\tilde{\mathbf{J}}$ and $\tilde{\mathbf{E}}_i$ are the currents and fields expressed in the bases that diagonalize the problem – the columns of \mathbf{V} and \mathbf{U} respectively. The elements of $\tilde{\mathbf{J}}$, the coefficients of the diagonalizing current bases, are easily obtained by

$$\tilde{j}_m = \frac{\tilde{e}_m}{s_m} \quad (15)$$

where \tilde{e}_m is the m -th element of $\tilde{\mathbf{E}}_i$.

The SVD can be used to reach an understanding of how the interior resonance problem occurs for the problem of scattering of a TM plane wave from a PEC circular cylinder of infinite length. For this particular problem, the singular values of \mathbf{Z} are numerically equal to the magnitude of the eigenvalues of \mathbf{Z} (this may be because the eigenvalues are approximately orthogonal). Thus, the singular values of the approximate MM matrix of order N_{MM} are approximations of the magnitudes of the first $\frac{N_{MM}}{2} + 1$ eigenvalues of equation (5) if N_{MM} is even, or the first $\frac{N_{MM}+1}{2}$ if N_{MM} is odd. This is

| Singular values of MM solution | Magnitudes of eigenvalues of exact solution |
|--------------------------------|---|
| $s_1 = 367.698$ | $ \Lambda_0 = 348.796$ |
| $s_2 = 219.017$ | $ \Lambda_1 = 233.490$ |
| $s_3 = 219.017$ | $ \Lambda_1 = 233.490$ |
| $s_4 = 102.139$ | $ \Lambda_2 = 112.513$ |
| $s_5 = 102.139$ | $ \Lambda_2 = 112.513$ |
| $s_6 = 65.500$ | $ \Lambda_3 = 67.396$ |
| $s_7 = 65.500$ | $ \Lambda_3 = 67.396$ |
| $s_8 = 57.423$ | $ \Lambda_4 = 48.773$ |

Table 1: The singular values of \mathbf{Z} and the magnitudes of the exact eigenvalues for the circular cavity of infinite length with $k_0a = 1$ and $N_{MM} = 8$.

demonstrated in Table 1 where the singular values are compared with the magnitudes of the exact eigenvalues for $k_0a = 1$ and $N_{MM} = 8$.

Further, the columns of \mathbf{U} and \mathbf{V} are approximations of the basis functions of the exact solution, i.e. $\{\frac{1}{2}, \cos n\phi, \sin n\phi\}$. This is demonstrated in Table I of [10] for $k_0a = 1$ and $N_{MM} = 8$.

Thus, the resonance problem should occur whenever the smallest singular value $s_{N_{MM}}$ approaches zero. This is verified in Figure 4 where $s_{N_{MM}}$ is plotted for $k_0a = 1.5$ to 6.5. In the vicinity of a value of k_0a which corresponds to an interior resonance, $s_{N_{MM}}$ is observed to tend rapidly to zero since it corresponds to the eigenvalue responsible for the resonance. Otherwise, away from interior resonances where it corresponds to the eigenvalue with largest index (away from a resonance, for a given value of k_0a , the eigenvalues decrease in magnitude with increasing index), $s_{N_{MM}}$ remains almost constant with increasing k_0a .

Equations (4) to (6) provide a clue as to how the interior resonance problem occurs. In computing the coefficient a_n in the exact solution, the Bessel function, $J_n(k_0a)$, that is present in the eigenvalue Λ_n cancels out as it also occurs in the excitation. It is this factor that becomes zero at an interior resonance making the corresponding eigenvalue zero. Thus it is not present in the exact solution for the exterior problem. However, the discretization error perturbs the MM matrix eigenvalue from the exact eigenvalue [6] and in the vicinity of an interior resonance numerical instability can be expected if the factor in the eigenvalue does not cancel properly with the factor in the excitation.

Using the SVD, the MM matrix equation is diagonal-

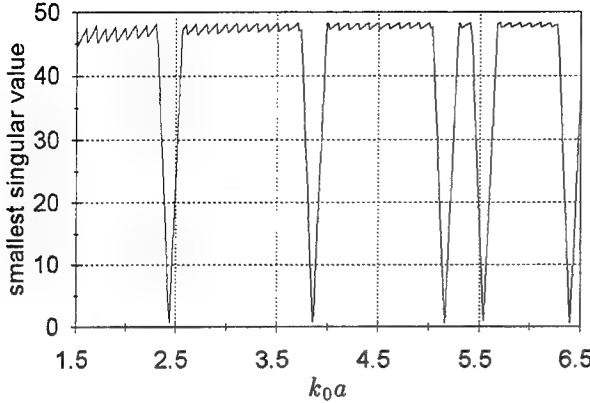


Figure 4: Smallest singular value $s_{N_{MM}}$, versus k_0a , of the MM impedance matrix for a PEC circular cylinder of infinite length.

ized to the form of equation (14). In this form, the coefficients in the diagonalized current vector $\tilde{\mathbf{J}}$ are easily obtained using equation (15). However, in the vicinity of a resonance, $s_{N_{MM}}$ tends toward zero and one can expect problems in computing the corresponding coefficient, i.e.

$$\tilde{j}_{N_{MM}} = \frac{\tilde{e}_{N_{MM}}}{s_{N_{MM}}} \quad (16)$$

since $s_{N_{MM}}$ appears as the denominator. Theoretically, the near-zero term in $s_{N_{MM}}$ should cancel with the corresponding term in the numerator.

Following [10], the quantities $s_{N_{MM}}^{-1}$ and $\tilde{e}_{N_{MM}}$ are plotted in Figure 5, as well as the current J_1 , which is on the segment nearest the incoming plane wave, and the backscatter RCS, σ , in the vicinity of the lowest interior resonance, $k_0a \approx 2.405$, with $N_{MM} = 32$. As expected, $\tilde{e}_{N_{MM}}$ tends to zero very close to $k_0a \approx 2.405$. However, the peak in $s_{N_{MM}}^{-1}$ is shifted up in frequency. Thus, the cancellation that should occur in the product $s_{N_{MM}}^{-1} \tilde{e}_{N_{MM}}$ is not realized. The anomalies in J_1 and σ are seen to occur at the same value of k_0a as the peak in $s_{N_{MM}}^{-1}$.

The desired current vector can be written as

$$\begin{aligned} \mathbf{J} &= \mathbf{V}\tilde{\mathbf{J}} \\ &= \mathbf{V}\mathbf{S}^{-1}\tilde{\mathbf{E}}_i \end{aligned} \quad (17)$$

and since \mathbf{V} is orthogonal equation (17) can be rewritten as

$$\mathbf{J} = \sum_{n=1}^{N_{MM}} \mathbf{V}_n s_n^{-1} \tilde{e}_n \quad (18)$$

where \mathbf{V}_n is the n -th column of \mathbf{V} . With $s_{N_{MM}}$ corresponding to the eigenvalue responsible for the resonance, $\mathbf{V}_{N_{MM}}$ is the basis that supports the resonant

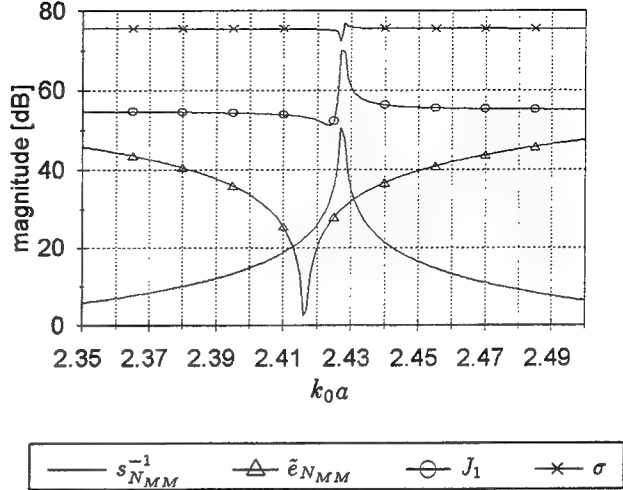


Figure 5: Behavior, in the vicinity of the lowest interior resonance, of the inverse of the smallest singular value $s_{N_{MM}}^{-1}$, the measure of the cavity mode excitation $\tilde{e}_{N_{MM}}$, the current on the near side of the incoming plane wave J_1 and the backscatter RCS σ versus k_0a in the MM solution of scattering by a circular cylinder of infinite length excited by an incident TM plane wave with $N_{MM} = 32$. The curves are vertically shifted from each other for clarity and 0 dB is arbitrary.

mode². Thus, in the MM solution, since $s_{N_{MM}}$ is shifted up in frequency with respect to $\tilde{e}_{N_{MM}}$, the coefficient $s_{N_{MM}}^{-1} \tilde{e}_{N_{MM}}$ of the cavity mode $\mathbf{V}_{N_{MM}}$ in equation (18) is inaccurate in the vicinity of resonance.

For this particular problem, scattering by an infinitely long circular cylinder, more accurate MM matrix elements can be computed with relative ease by modelling the pulse basis functions on segments of the actual, curved, circular cylinder and performing a careful numerical integration. Canning did this in [10] and demonstrated that the shift in frequency of the smallest singular value can be reduced quite substantially. This resulted in a much narrower, in terms of k_0a , anomaly in the current and the disappearance of the anomaly in the RCS. Canning also showed that the condition number increased with the more accurate matrix elements which emphasized that the problem is not due solely to the ill-conditioned matrix since the more ill-conditioned matrix gave more accurate results. Further, since Canning used the same number of unknowns in the computation with more accurate matrix elements as with the less accurate elements, it can be concluded, at least for the circular cylinder considered, that the problem is not entirely due to “truncation error” – the error due to in-

²This is easily verified by comparing $\mathbf{V}_{N_{MM}}$ to combinations of the $+n$ and $-n$ terms of the summation in equation (5-109) of [13]. When $J_n(k_0a) = 0$, these terms are cavity mode currents

troducing a finite number of basis and testing functions and thereby reducing the integral equation to a matrix equation [10] – but at least in part due to “numerical error” – approximations made in calculating the matrix elements in terms of the basis and testing functions [10].

4 Protecting the EFIE using the SVD

In the previous section the amount of the resonant current was not computed accurately in the vicinity of an internal resonance. Furthermore, the computed resonant current should in theory not contribute to the scattered field at the resonance frequency. The cavity mode current is represented by the column of \mathbf{V} of the SVD which corresponds to the smallest singular value, i.e. $\mathbf{V}_{N_{MM}}$. As suggested by Canning in [10], the scattered field could be calculated accurately by discarding the resonant current in the vicinity of its resonant frequency. If the MM equation is being solved via the SVD, the mode is easily discarded by setting $s_{N_{MM}}^{-1}$ to zero in equation (18).

Unfortunately the SVD is computationally expensive and operates on a fully square matrix – thus any advantage is lost if the impedance matrix \mathbf{Z} is symmetric. In [7], Canning proposed a method of performing the correction to the current in which the vector $\mathbf{V}_{N_{MM}}$ and the smallest singular value $s_{N_{MM}}$ are approximated by an iterative technique known as the power method (PM). The desired current \mathbf{J} is approximated by orthogonalizing \mathbf{J}_0 , the current computed directly by the MM, to the resonant mode $\mathbf{V}_{N_{MM}}$ using the formula

$$\mathbf{J} = \mathbf{J}_0 - \mathbf{V}_{N_{MM}} \frac{\langle \mathbf{V}_{N_{MM}}, \mathbf{J}_0 \rangle}{\langle \mathbf{V}_{N_{MM}}, \mathbf{V}_{N_{MM}} \rangle} \quad (19)$$

where $\langle \mathbf{P}, \mathbf{Q} \rangle$ is a vector inner product in which one takes the complex conjugate of the first vector. In the vicinity of an interior resonance the PM converges rapidly [7].

For the infinitely long circular PEC cylinder, the smallest singular value approximated by the PM is compared with the smallest singular value computed directly by the SVD in Figure 6. The current \mathbf{J}_0 was used as the starting vector in the PM and at each frequency the PM was terminated once either the difference between consecutive approximations of the smallest singular value was less than 10^{-8} or 21 iterations had been completed. The approximated value were found to converge quickly, i.e. within 5 iterations, to the exact value in the vicinity of an interior resonance, that is when the smallest singular value corresponds to the eigenvalue responsible for the resonance. Away from resonances, however, the convergence is generally poor and the approximated

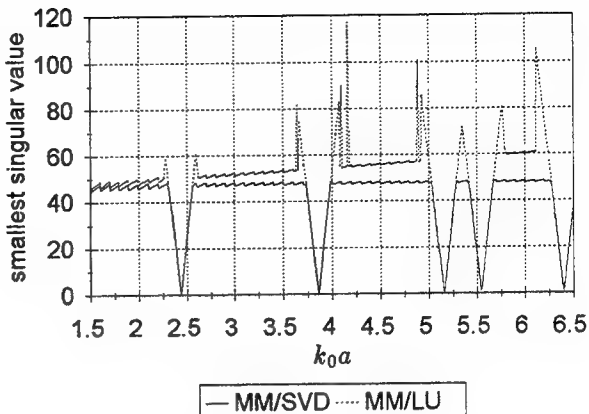


Figure 6: Smallest singular value $s_{N_{MM}}$, exact and approximated, of the MM impedance matrix versus k_0a for a PEC circular cylinder of infinite length. The curve “MM/SVD” is $s_{N_{MM}}$ computed by the SVD while the curve “MM/LU” is $s_{N_{MM}}$ approximated via the power method. The number of unknowns N_{MM} satisfied equation (12).

value is larger – this does not necessarily have a negative consequence since it is still clear from the approximated values where the resonances occur.

Oddly, as a resonance is approached, the power method converges, within at most 20 iterations, prematurely to the mode responsible for that resonance, i.e. before the singular value corresponding with this mode is the smallest one³. This accounts for the sudden increase in the approximated smallest singular value as a resonance is approached.

The wavy nature of the curves away from resonance is probably due to the variation in number of unknowns N_{MM} with frequency.

The interior resonances coincide with frequencies where the smallest singular value becomes small, so this could be used as an indication of the occurrence of problems. But, the question is how small should this singular value be in order to know whether to discard the offending current mode? For the problem involving TM scattering by a PEC circular cylinder of infinite length, this question is easily answered if a frequency sweep is carried out. Then, by observing where the anomalies begin and end, with increasing k_0a , in the current or RCS (for example Figure 3), one can determine the value of the smallest singular value at these frequency points from, for example, Figure 6. A threshold can then be derived and the resonant current mode discarded at all frequencies where the smallest singular value is below this threshold. It is also easy to know beforehand where

³This may be due to the choice of starting vector

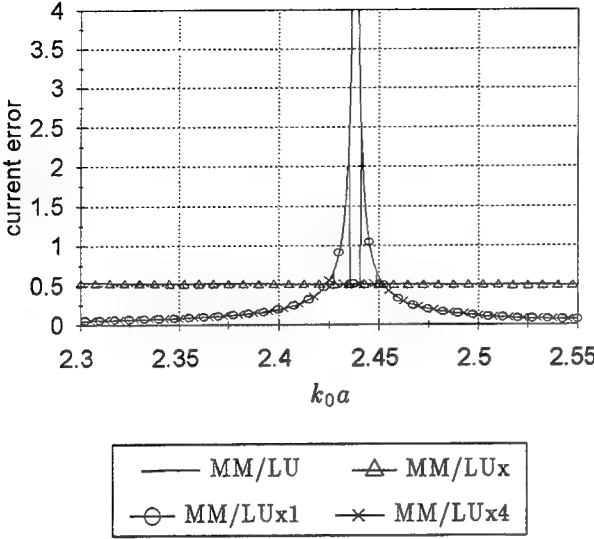


Figure 7: Electric current error Δ_C , without and with current correction versus k_0a in the region of the lowest resonance in the MM solution, computed via the LU decomposition, of a PEC circular cylinder of infinite length excited by an incident TM plane wave. The curve “MM/LU” is with no correction, the curve “MM/LUX” is with equation (19) applied for all k_0a and the curves “MM/LUX1” and “MM/LUX4” are with equation (19) applied where $s_{N_{MM}} \leq 1$ and $s_{N_{MM}} \leq 4$ respectively. The number of unknowns N_{MM} satisfied equation (12). (Maximum in the curve “MM/LU” is approximately 36, off the scale of this figure.)

to expect the interior resonances to occur as analytical formulas exist for the circular cylinder. However, for a more general problem for which analytical solutions do not exist, it may be extremely difficult or impossible to determine where interior resonances may occur before carrying out the MM solution. Also, if the solution is only desired at a specific frequency and it is computationally expensive to compute a frequency sweep, how does one know what the threshold in smallest singular value should be? How dependent is this threshold on the geometry of the problem being solved?

Three possibilities were investigated and their effect on the current error is compared in Figure 7 and on the backscatter RCS in Figure 8.

The first was to discard $\mathbf{V}_{N_{MM}}$ at all frequencies. This seems feasible since away from resonance this vector corresponds to a higher order term in the series expansion, equation (3), of the exact solution which does not make a significant contribution. The anomaly in Δ_C has been suppressed but the error is now increased over the whole range of k_0a where $s_{N_{MM}}$ corresponds to Λ_0 . The latter situation is because the mode represented by $\mathbf{V}_{N_{MM}}$ has been completely removed while part of it should be

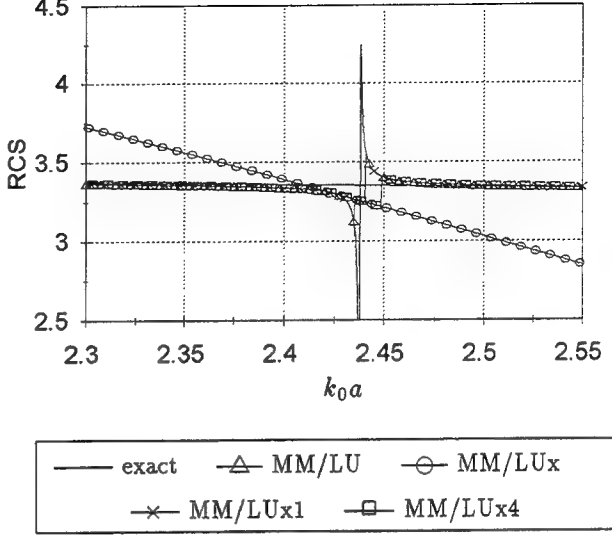


Figure 8: Backscatter RCS, without and with current correction, versus k_0a in the region of the lowest resonance for a PEC circular cylinder of infinite length excited by an incident TM plane wave. The curve “exact” was computed by the Fourier series of equation (3) with equation (6). The remaining curves correspond with those of Figure 7.

contributing to the desired solution for the current even at the precise resonance point and for the scattered field except at the precise resonance point. The current error Δ_C remains constant over the whole range of k_0a where $s_{N_{MM}}$ corresponds to Λ_0 . It is constant here because the exact current contains a constant amount of $V_{N_{MM}}$. There is also a large improvement in the backscatter RCS where the anomaly occurred. However, the deviation becomes larger with decreasing or increasing k_0a away from this point, emphasizing that it is inappropriate to carry out the orthogonalization away from the resonance point and that it is thus important that the resonances be detected.

It is evident from Figures 7 and 8 that one cannot expect to completely solve the problem by suppressing $\mathbf{V}_{N_{MM}}$, however, the anomalies can be drastically reduced. Ideally, away from the anomalies one would like to retain the solution without $\mathbf{V}_{N_{MM}}$ discarded. This was attempted by setting a threshold in $s_{N_{MM}}$ and only discarding $\mathbf{V}_{N_{MM}}$ when $s_{N_{MM}}$ is beneath it. The effect on Δ_C for two thresholds, $s_{N_{MM}} \leq 1$ and $s_{N_{MM}} \leq 4$, is also plotted in Figure 7. These values were arrived at by observing $s_{N_{MM}}$ in the vicinity of the anomalies using Figures 3 to 4. A threshold of 4 brings the error down to almost the best that can be achieved while a threshold of 1 is a bit low, although the anomaly is drastically suppressed.

The backscatter RCS for $s_{N_{MM}}$ with these thresholds

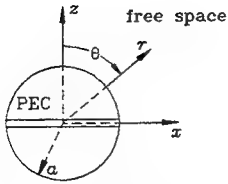


Figure 9: A PEC sphere with a rotationally symmetric equatorial aperture.

is plotted in Figure 8. With the threshold of 1 the maximum deviation in the RCS from the exact solution is about 10% while with a threshold of 4 it is about 4%.

5 Protecting the MM/BOR formulation from interior resonances

In this section the application of Canning's method, presented in [7], to the MM/BOR formulation for the solution of scattering [8] and radiation [9] from composite bodies of revolution is discussed. For penetrable regions the MM/BOR formulation uses the CFIE. However, for conducting regions the EFIE is used which results in a complex symmetric impedance matrix (this would not be the case if the CFIE was used for conducting regions as well). Thus, for problems involving conducting regions, the MM/BOR formulation can suffer from the interior resonance problem.

The method's application is demonstrated here for two problems that can also be solved analytically: firstly, radiation from a rotationally symmetric aperture in a PEC sphere, and secondly, the same problem with the PEC sphere covered by a spherical dielectric shell.

5.1 Radiation from a rotationally symmetric equatorial aperture in a PEC sphere

The problem is illustrated in Figure 9. The PEC sphere has a radius 100 mm and has a rotationally symmetric aperture at its equator. The aperture subtends an angle of 5° in θ and it is assumed that only a θ -directed electric field exists in the aperture. This excitation will produce fields TM to the radial direction. The electric field is constant across the aperture, i.e. a pulse distribution in θ .

An analytical solution for this problem, in terms of a spherical wave function expansion (SWFE), is presented by Harrington in [13, pages 301-303] for the case where the aperture has a small width so that the aperture field is an impulse function in θ . This solution can easily be

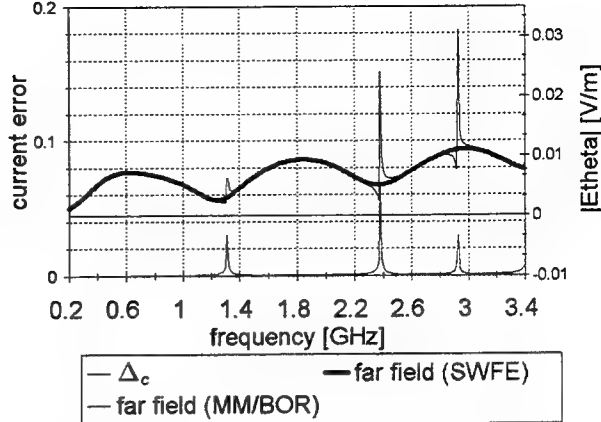


Figure 10: Electric current error Δ_C and the far field, at $\theta = 90^\circ$, in the MM solution of radiation from a rotationally symmetric equatorial aperture in a PEC sphere of radius 100 mm. The number of unknowns provided ten basis functions per wavelength at 3.4 GHz.

modified to solve problems involving an aperture subtending an arbitrary angle in θ [9, Appendix D].

For the radiation problems presented here, the current error is defined as

$$\Delta_C = \sqrt{\frac{\iint_S |\vec{J}_{MM} - \vec{J}_{SWFE}|^2 ds}{\iint_S ds}}. \quad (20)$$

where \vec{J}_{MM} is the current computed by the MM, S is the outer surface of the PEC sphere and \vec{J}_{SWFE} is the current computed by the SWFE using the relationship $\vec{J}_{SWFE} = \hat{r} \times \vec{H}$ where \hat{r} is the unit vector in the r -direction and \vec{H} is the exterior magnetic field.

In Figure 10 the current error in the MM/BOR solution and the radiated far field are plotted from 0.2 to 3.4 GHz. Anomalies occur in the vicinity of resonance frequencies of a spherical cavity [13, pages 269-273].

The smallest singular value approximated using the PM is compared with that computed directly by the SVD in Figure 11. The behaviour of the approximated smallest singular value is similar to that in the problem involving the PEC cylinder (see Figure 6) in that it also converges to the singular value corresponding to the resonant mode away from the resonance as well as at the resonance. As was the case in the PEC cylinder problem, the PM converges to the singular value corresponding to the resonant mode prematurely, i.e. before it is actually the smallest singular value, which results in a sudden increase in the approximated value.

A further observation is that the smallest singular value computed directly by the SVD increases gradually with frequency outside of the resonance region and does not remain approximately constant as was the case

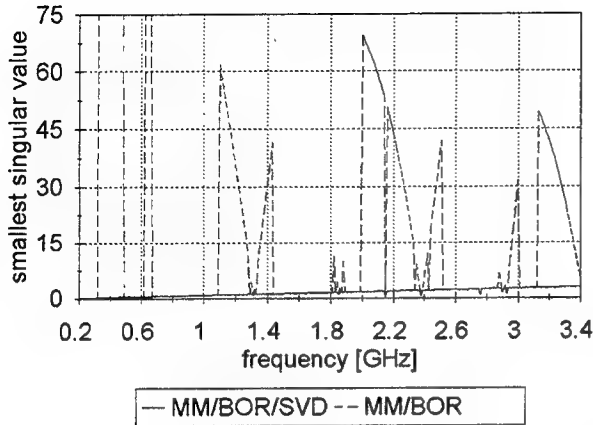


Figure 11: Smallest singular value $s_{N_{MM}}$ of the MM impedance matrix for a PEC sphere of radius 100 mm. The curve “MM/BOR/SVD” is $s_{N_{MM}}$ computed by the SVD while the curve “MM/BOR” is $s_{N_{MM}}$ approximated via the power method. The number of unknowns provided ten basis functions per wavelength at 3.4 GHz.

in the results for the problem involving a PEC circular cylinder (see Figure 4 or 6). The difference here is that the number of unknowns is kept constant, providing ten basis functions per wavelength at 3.4 GHz, whereas in the PEC cylinder computations the number of unknowns was varied with frequency.

It is difficult to determine a suitable smallest singular value threshold from Figure 11 for carrying out the current correction. If one is to carry out the correction across the entire frequency range displayed then the threshold must always be beneath the smallest singular value away from resonance. However, if this is satisfied at the lower frequencies, the resonances at the higher frequencies will not be detected. This problem can possibly be avoided by varying the discretization with frequency, so that there are just ten unknowns per wavelength at each frequency, as was done in Figure 6. Then, away from resonances, the smallest singular value should be larger in magnitude and remain more constant with frequency. Unfortunately, the computer implementation of the MM/BOR method was not at a point where this could readily be done at the time of writing this paper.

In Figure 12 the smallest singular value is plotted in the vicinity of the first interior resonance using two discretizations. The first is as above, which provided ten unknowns per wavelength at 3.4 GHz, and the second provided ten unknowns per wavelength at 1.35 GHz. Indeed, for the coarser discretization, which is sufficient at the resonance, both the exact and approximated singular values are larger. The resonance frequency is also shifted up in frequency due to the increased truncation error.

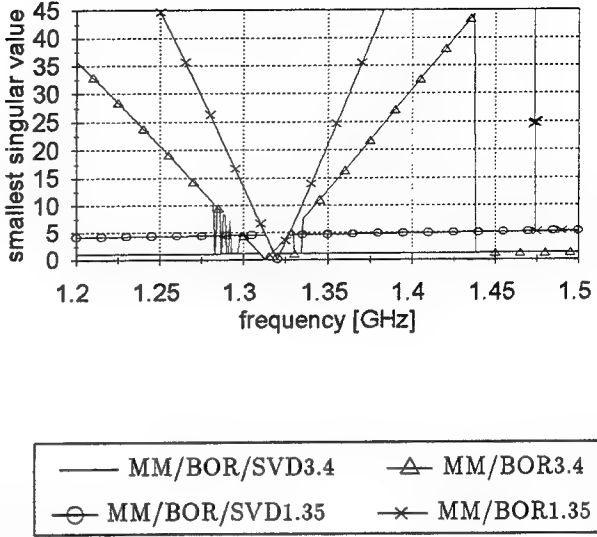


Figure 12: Smallest singular value $s_{N_{MM}}$ of the MM impedance matrix for a PEC sphere of radius 100 mm in the vicinity of the lowest interior resonance. The curves “MM/BOR/SVD3.4” and “MM/BOR/SVD1.35” are $s_{N_{MM}}$ computed by the SVD while the curves “MM/BOR3.4” and “MM/BOR1.35” are $s_{N_{MM}}$ approximated via the power method. The numbers in the labels, i.e. 3.4 and 1.35, refer to the frequency in GHz at which the discretization used to compute the curves provided ten basis functions per wavelength.

Using the curves of the coarser discretization a threshold of 4 in the approximated smallest singular value was chosen to carry out the correction on the current. The current error obtained using equation (19) with the PM at all frequencies as well as with the threshold of $S_{N_{MM}} = 4$ are plotted in Figure 13, as the curves “MM/BORx” and “MM/BORx4” respectively, along with the original current error, the curve “MM/BOR”, in the vicinity of the lowest resonance. The anomaly is completely suppressed for the correction at all frequencies (“MM/BORx”) and in contrast to the results for scattering by the PEC circular cylinder, see Figure 7, the error is now small at all frequencies. The result is also good with the threshold of 4 (“MM/BORx4”).

Far field results at $\theta = 90^\circ$ achieved with the correction at all frequencies, the curve “MM/BORx”, with the threshold of 4, the curve “MM/BORx4”, and with a threshold of 15, the curve “MM/BORx15”, are compared in Figure 14 to the far field computed by the MM/BOR method without correction as well as the SWFE solution. The result obtained with the correction at all frequencies (MM/BORx) is excellent at frequencies below resonance and at the resonance the anomaly is completely suppressed. However, above the resonance

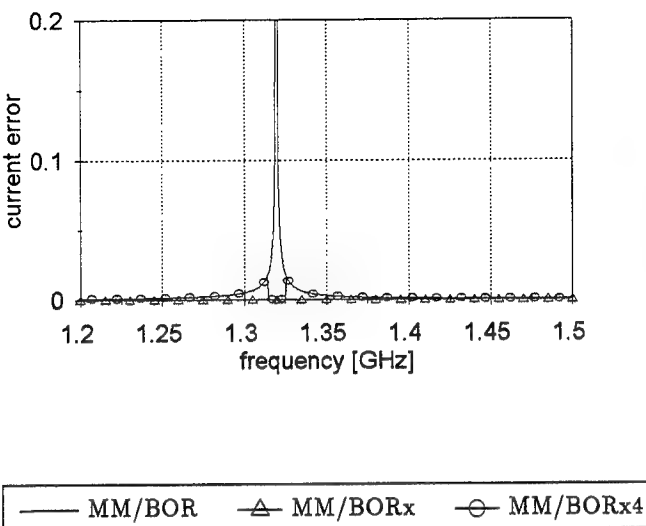


Figure 13: Electric current error Δ_C in the region of the lowest resonance in the MM solution of radiation from a rotationally symmetric equatorial aperture in a PEC sphere of radius 100 mm. The curve "MM/BOR" is with no correction and the curves "MM/BORx" and "MM/BORx4" are with equation (19) applied at all frequencies and at frequencies where $s_{N_{MM}} \leq 4$ respectively. The number of unknowns provided ten basis functions per wavelength at 1.35 GHz.

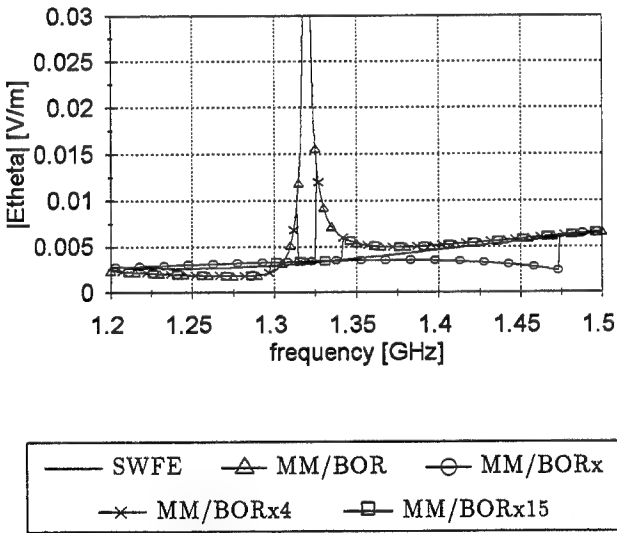


Figure 14: Far field, at $\theta = 90^\circ$, in the region of the lowest resonance of the rotationally symmetric equatorial aperture in a PEC sphere of radius 100 mm computed by the SWFE and the MM. The curve "SWFE" is the SWFE solution, curves "MM/BORx" and "MM/BORx4" correspond to those of Figure 13 and "MM/BORx15" is with a threshold of 15.

this result increasingly deviates with frequency until 1.475 GHz where it jumps to the correct solution. This is the frequency at which the approximated smallest singular value converges to the exact smallest singular value (see Figure 12). With a threshold of 4 the anomaly is reduced drastically in close proximity to the resonance but slightly away the deviation is still relatively large. A far better result is achieved with a threshold of 15 which also does not alter the solution above 1.475 GHz.

From the above results it appears that the current correction procedure using the PM can safely be used at all frequencies where the approximated smallest singular value has converged to the actual smallest singular value – this can be at and in close proximity to the resonant frequency as well as away from resonances. The reason for this is that at a resonance the smallest singular value corresponds to the undesired mode that must be thrown away and away from resonance the smallest singular value corresponds to a mode whose contribution is small if the discretization is sufficiently fine. It is not safe, however, to carry out the current correction at those frequencies at which the approximated smallest singular value is not the actual smallest singular value as the approximated value then corresponds to a mode that makes a desired and necessary contribution.

The problem remains as to how to determine at a discrete frequency, without having done a frequency sweep, whether a resonance occurs especially for a complex geometry. It is evident from the above results that the problem is made a bit easier if the number of unknowns in the solution is just sufficient at that frequency. However, a knowledge of the magnitude of the smallest singular value away from resonance still appears to be necessary.

5.2 Radiation from a rotationally symmetric equatorial aperture in a PEC sphere with a spherical dielectric shell.

This problem is illustrated in Figure 15. An analytical solution, in terms of a spherical wave function expansion (SWFE) [9, Appendix D], can be derived using the methods presented in [13, Chapter 6].

The radius of the PEC sphere is 100 mm and the outer radius of the dielectric shell is 150 mm. The dielectric shell has a relative permittivity $\epsilon_r = 3$ and relative permeability $\mu_r = 1$. As for the problem without the shell, the aperture subtends an angle of 5° in θ and it is assumed that only a θ directed electric field exists in the aperture.

The current error in the MM solution for this problem and the radiated far field are plotted in Figure 16. The interior resonances of the sphere have shifted down in

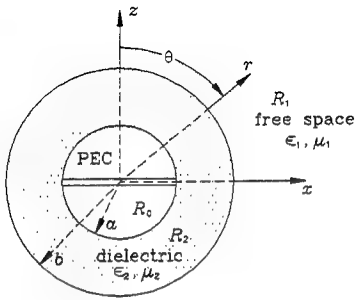


Figure 15: A PEC sphere, coated by a spherical dielectric shell, containing a rotationally symmetric equatorial aperture.

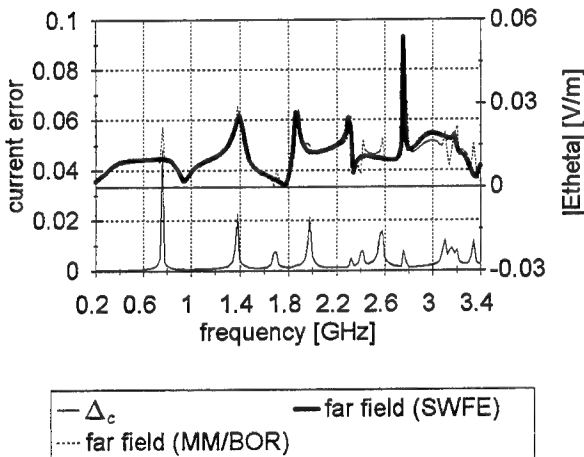


Figure 16: Electric current error Δ_C and the far field, at $\theta = 90^\circ$, in the MM solution of radiation from a rotationally symmetric equatorial aperture in a PEC sphere of radius 100 mm with a spherical dielectric shell of radius 150 mm and relative permittivity $\epsilon_r = 3$. The number of unknowns provided ten basis functions per wavelength at 3.4 GHz.

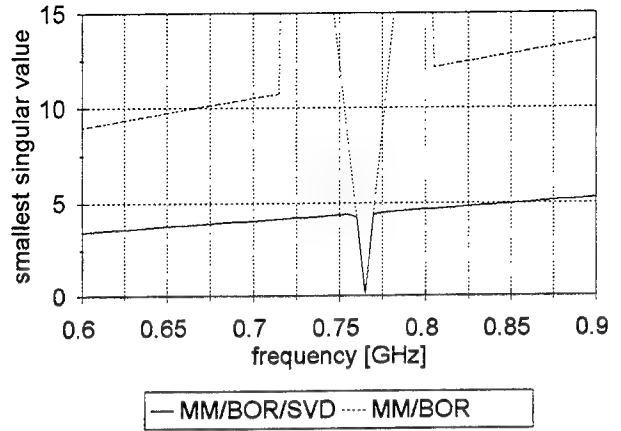


Figure 17: Smallest singular value $s_{N_{MM}}$, in the frequency range 0.6 to 1 GHz, of the MM impedance matrix for a PEC sphere of radius 100 mm with a spherical dielectric shell of radius 150 mm and relative permittivity $\epsilon_r = 3$. The curve “MM/BOR/SVD” is $s_{N_{MM}}$ computed by the SVD while the curve “MM/BOR” is $s_{N_{MM}}$ approximated via the power method. The number of unknowns provided ten basis functions per wavelength at 0.9 GHz.

frequency, as is evident in the positions of the anomalies in the current error, due to the presence of the shell. This is a result of the application of the equivalence principle in the formulation of the EFIE which replaces the interior region with the same material as the surroundings. This also means that there are now more interior resonances in the frequency range shown as some of the higher resonances have shifted down.

It is clear that not all the apparent anomalies in the far field are due to interior resonances as they are also present in the result computed by the SWFE. Some of the anomalies due to interior resonances have merged with actual anomalies in the result computed via the MM/BOR formulation. Thus, the presence of an anomaly in the frequency sweep of a quantity such as the far field is not necessarily an indication of an interior resonance.

The smallest singular value for this problem in frequency subrange 0.6 to 1 GHz is plotted in Figure 17.

Inspection of Figure 17 led to a threshold of 8 being applied to the current orthogonalization procedure in the frequency range 0.6 to 1 GHz. The resultant change in current error is shown in Figure 18 and the change in the field in Figure 19. From these figures it is seen that the method does work; however the problems regarding the detection of interior resonances remain.

6 Conclusions

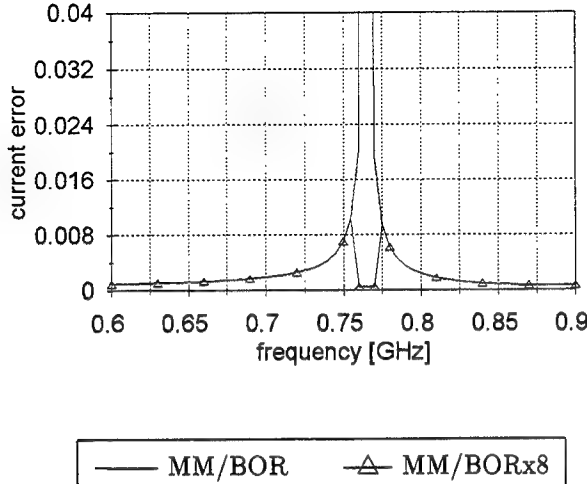


Figure 18: Electric current error Δ_C in the frequency range 0.6 to 0.9 GHz in the MM solution of radiation from a rotationally symmetric equatorial aperture in a PEC sphere of radius 100 mm with a spherical dielectric shell of radius 150 mm and relative permittivity $\epsilon_r = 3$. The curve “MM/BOR” is with no correction and the curve “MM/BORx8” is with equation (19) applied at frequencies where $s_{N_{MM}} \leq 8$. The number of unknowns provided ten basis functions per wavelength at 0.9 GHz.

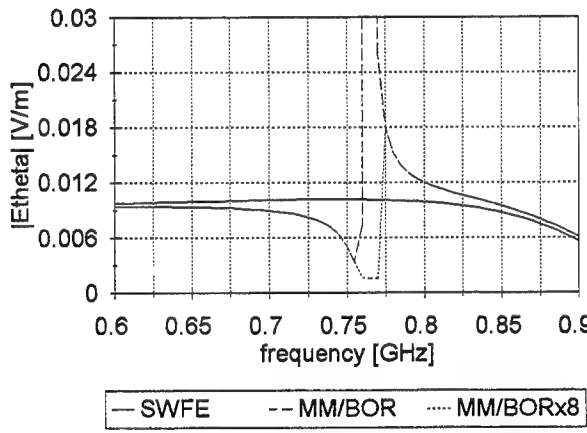


Figure 19: Far field in the frequency range 0.6 to 0.9 GHz, at $\theta = 90^\circ$, of the rotationally symmetric equatorial aperture in a PEC sphere of radius 100 mm with a spherical dielectric shell of radius 150 mm and relative permittivity $\epsilon_r = 3$ computed by the SWFE and the MM. The curve “SWFE” is computed via the SWFE while the remaining curves correspond with those of Figure 18.

The electric field integral equation, which is a surface integral equation, is valid for both the exterior and interior problems as defined in section 1. Although the interior solution should not couple to the exterior solution and vice versa in theory, when solving numerically, anomalies are observed at discrete frequencies that coincide with the eigenfrequencies of the interior solution. This is a well-known result in the literature and is demonstrated here.

A comparison between an analytical solution and a moment method solution for a canonical problem shows how the interior resonance problem arises. In the analytical solution for the electric current, the eigenvector corresponding to the zero eigenvalue is generally present but does not radiate any external field. However, with the aid of the singular value decomposition (SVD), it is seen that in the approximate moment method solution the zero in the eigenvalue, or smallest singular value, shifts in frequency with respect to the zero in the excitation thus the quotient in equation (16), which is the coefficient of the eigenvector corresponding to the zero eigenvalue, is inaccurate. Canning has demonstrated that the problem may be more due to approximations made in calculating the matrix elements in terms of the basis and testing functions, than due to introducing a finite number of basis and testing functions.

The anomalies in the computed results for the exterior field can be suppressed by discarding the eigenvector corresponding to the smallest singular value in the vicinity of an interior resonance. This was demonstrated using the singular value decomposition to solve the moment method matrix equation directly as well as by using the power method to approximate the smallest singular value and the corresponding eigenvector. It was found that the eigenvector corresponding to the smallest singular value can safely be discarded at all frequencies, provided a sufficient number of unknowns is used, as at an interior resonance it makes an undesired contribution and away from resonance its contribution is small. However, the power method does not always converge to the smallest singular value but converges to the eigenvector responsible for a resonance prematurely.

The question still remains on how to detect the occurrence of such resonances in a foolproof manner. The detection is easy for canonical problems as analytical formulas exist for the eigenvalues. However, for general problems the size of the smallest singular value depends on the geometry of the problem. A possible way around this is to do a frequency sweep if it is suspected that an interior resonance is present. However, this could prove computationally very expensive and, it was demonstrated that anomalies in the computed results do

not necessarily indicate interior resonances. More work needs to be done to find a reliable method, if possible, of detecting interior resonances that takes the geometry of the problem into account.

The major contribution of the work presented in this paper is the demonstration that whilst the method used to avoid the interior resonances can work, applying it automatically in a MM code is not as straightforward as was implied by Canning [7]. The major obstacle is that the power method only converges to the smallest singular value in the region of resonance. This has been illustrated in this paper using a number of examples, including rotationally symmetric radiators. The full SVD is unfortunately very expensive computationally, making the direct use thereof most unattractive. A further contribution is the specific investigation of the method with regard to the MM/BOR solution of radiation problems.

Acknowledgements

We gratefully acknowledge the most helpful comments of Dr. Joseph R. Mautz, who drew our attention to several errors in the draft version of this paper.

References

- [1] J. R. Mautz and R. F. Harrington, "H-field, E-field, and combined-field solutions for conducting bodies of revolution," *AEU*, vol. 32, pp. 157-164, 1978.
- [2] J. R. Mautz and R. F. Harrington, "A combined-source solution for radiation and scattering from a perfectly conducting body," *IEEE Trans. Antennas Propagat.*, vol. AP-27, pp. 445-454, July 1979.
- [3] L. N. Medgyesi-Mitschang and D.-S. Wang, "Hybrid solutions for scattering from perfectly conducting bodies of revolution," *IEEE Trans. Antennas Propagat.*, vol. AP-31, pp. 570-583, July 1983.
- [4] L. N. Medgyesi-Mitschang and J. M. Putnam, "Integral equation formulations for imperfectly conducting scatterers," *IEEE Trans. Antennas Propagat.*, vol. AP-33, pp. 206-214, February 1985.
- [5] P. L. Huddleston, L. N. Medgyesi-Mitschang, and J. M. Putnam, "Combined field integral equation formulation for scattering by dielectrically coated conducting bodies," *IEEE Trans. Antennas Propagat.*, vol. AP-34, pp. 510-520, April 1986.
- [6] A. F. Peterson, "The "interior resonance" problem associated with surface integral equations of electromagnetics: numerical consequences and a survey of remedies," *Electromagnetics*, vol. 10, pp. 293-312, 1990.
- [7] F. X. Canning, "Protecting EFIE-based scattering computations from effects of interior resonances," *IEEE Trans. Antennas Propagat.*, vol. 39, pp. 1545-1552, November 1991.
- [8] L. N. Medgyesi-Mitschang and J. M. Putnam, "Electromagnetic scattering from axially inhomogeneous bodies of revolution," *IEEE Trans. Antennas Propagat.*, vol. AP-32, pp. 797-806, August 1984.
- [9] P. Steyn, *A Moment Method Solution of Electromagnetic Radiation from Composite Bodies of Revolution*. PhD thesis, University of Stellenbosch, South Africa, November 1994.
- [10] F. X. Canning, "Singular value decomposition of integral equations of EM and applications to the cavity resonance problem," *IEEE Trans. Antennas Propagat.*, vol. 37, pp. 1156-1163, September 1989.
- [11] R. F. Harrington, *Field Computation by Moment Methods*. Malabar, Florida: Robert E. Krieger, first ed., 1982. Reprint of 1968 edition.
- [12] G. H. Golub and C. F. van Loan, *Matrix Computations*. Baltimore, Maryland: The John Hopkins University Press, first ed., 1983.
- [13] R. F. Harrington, *Time-Harmonic Electromagnetic Fields*. New York: McGraw-Hill, first ed., 1961.

The authors

Pierre Steyn was born in Cape Town, South Africa in 1962. He received the Bachelor and Master degrees in electronic engineering (both cum laude) from the University of Stellenbosch, South Africa in 1986 and 1989 respectively. In 1994 he received the Ph.D. degree in Electronic Engineering from the University of Stellenbosch. His chief research interests are in computational electromagnetics and computer aided antenna design. Pierre is presently pursuing a career in commercial antenna design.

David Bruce Davidson: See biography elsewhere in this issue.

Computation of Multipole Moments for Short Thin Wire Chiral Structures

Isak Petrus Theron, David Bruce Davidson and Johannes Hendrik Cloete

Department of Electrical and Electronic Engineering
University of Stellenbosch
Stellenbosch 7600
South Africa

Abstract

This paper considers the computation of the multipole moments of small chiral wire structures. The multipole moments are reviewed and it is shown that the charge induced on the wire must be accurately computed. A quasistatic thin-wire Galerkin Method of Moments formulation has been developed to numerically compute the charge distribution.

The chiral structures under consideration are on the borderline of "thin" and a Body of Revolution Method of Moments formulation has also been developed for use as a check on the accuracy of the thin-wire approximations. It is shown that the "standard" thin-wire formulation is not sufficiently accurate, but the relatively simple addition of an end-cap greatly improves the convergence and accuracy of the formulation with acceptable computation cost.

Finally, the formulation is extended to include bent wires, permitting the electric and magnetic dipole moments as well as the electric quadrupole moment to be calculated for a small chiral structure.

1 Introduction

In 1979, Jaggard et al. [1] initiated the current interest of the electromagnetic engineering community in artificial chiral media at microwave frequencies. They used approximate electric and magnetic dipole moments to analyse a material composed of single turn helixes randomly distributed and oriented in vacuum. Since this work was published, and in particular over the last several years, there has been a substantial amount of research in this field.

In addition to questions regarding the physical realizability of microwave chiral absorbing materials, there are also questions relating to the theoretical basis of the constitutive relations used to date. In [2] Graham, Pierrus and Raab show that when using magnetic dipoles, one

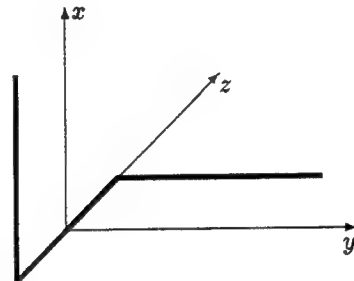


Figure 1: Chiral hook

needs to include the electric quadrupole term to maintain the origin-independence of the Maxwell equations. In [3] Raab and Cloete show that, for chiral elements much smaller than a wavelength, the optical activity of a chiral medium can be described by the electric quadrupole-magnetic dipole approximation. The theory requires the structures to be much smaller than a wavelength as the scattering from the structures is approximated in terms of only the first three multipole moments. It is also required that the spacing between structures is much less than a wavelength — otherwise the composition will be more of a diffraction grating than a continuum.

Construction of a practical medium to validate this theory thus requires chiral structures much smaller than a wavelength. To measure at practical microwave frequencies (eg. 3 GHz) this limits the wire length to a few millimetres, while physical restrictions limit the wire thickness to no less than a few tenths of a millimetre, resulting in "thick" thin wires.

In order to determine the accuracy of the current theoretical models, the contribution of the electric quadrupole term relative to the dipole terms needs to be calculated. This necessitates the calculation of the different multipole moments for a chiral structure. The simplest possible chiral structure, a three dimensional hook as shown in Fig. 1, was chosen such that the calculations — using thin wire approximations — would be as simple

as possible. This structure, at resonance, was also used by Morin for a polarization selective surface [4]. The main advantage of this structure is the ease with which it can be arranged to simulate crystals in the various point groups [5]. This will, however, not be considered in this paper.

To compute the multipole moments, the charges and currents induced on the chiral element are required. Only the simplest structures admit analytical electrodynamic solutions (even the simple half-wave dipole analysis found in most undergraduate electromagnetic textbooks uses an approximation to the current); for an accurate solution of a bent structure such as the chiral hook shown in Fig. 1, numerical methods must be used. The well known method of moments (MoM) will be used in this paper for this purpose. We will show in the next section that a quasi-static formulation suffices for the structures of interest, and that only the induced charge needs to be solved.

Solving for the charge on a quasi-static thin-wire structure appears to be a rather simple problem (it is addressed in many post-graduate texts, for example [6]), but we will show that computing multipole moments requires that the induced charge be very accurately computed. It will be demonstrated that the widely used thin wire approximation must be used with circumspection in this case. Following a brief discussion of the computation of the polarizability tensors, this paper first presents an analysis of a very simple (non-chiral) structure — an electrically short dipole — to test the validity of the techniques. A moderately simple extension to the thin-wire formulation is then used to compute the multipole moments of a chiral structure.

2 The polarizability tensors

In [3] it is shown that the macroscopic electric dipole and quadrupole moments and the magnetic dipole moment are related to the excitation fields and their derivatives via the polarizability tensors

$$\begin{aligned} P_\alpha &= \alpha_{\alpha\beta} E_\beta + \frac{1}{2} a_{\alpha\beta\gamma} \nabla_\gamma E_\beta + \frac{1}{\omega} G'_{\alpha\beta} \dot{B}_\beta + \dots \\ Q_{\alpha\beta} &= a_{\gamma\alpha\beta} E_\gamma + \dots \\ M_\alpha &= -\frac{1}{\omega} G'_{\beta\alpha} \dot{E}_\beta + \dots \end{aligned}$$

from which follow the general form of the constitutive relations for chiral media [3]. In these equations a Greek subscript denotes any of the three Cartesian directions (x , y or z). Repeated subscript notation implies summation over the three components (the Einstein notation) and ∇_β implies the derivative with respect to β . These multipole densities can also be found by spatial averaging

of the multipole moments due to the discrete elements. Thus the polarizability tensors describing a composite medium can be calculated from the multipole moments of the inclusions. From [2] the first three multipole moments for a given charge distribution are given by:

$$p_\alpha = \int_v \rho(r) r_\alpha dv \quad (1)$$

$$q_{\alpha\beta} = \int_v \rho(r) r_\alpha r_\beta dv \quad (2)$$

$$m_\alpha = \frac{1}{2} \int_v [\mathbf{r} \times \mathbf{J}(r)]_\alpha dv \quad (3)$$

where ρ , \mathbf{J} and \mathbf{r} have their normal definitions.

As discussed in the introduction, the underlying theory requires the structures to be much smaller than a wavelength. The problem can thus be approached using electroquasistatic approximations [7, Chapter 3] and is formulated as a boundary value problem in terms of the scalar potential, from which the unknown charges can be solved. (Note that the structure is quasi-static and not static, thus the current is non-zero and can be calculated from the spatial integral of the time derivative of the charge.) Since calculating the charges from the current implies a numeric differentiation process, directly solving for the charges will have a distinct advantage. This is the approach adopted here.

Consider the calculation of the dipole moment. It is tempting to view this “observable” as fundamentally similar to the computation of a radiation pattern or a scattering cross-section, typically the type of output required from a full electrodynamic code, since all involve an integration over the current (or charge in the present case). It is widely accepted that the integration process smoothes the effect of errors in the computed current. However, this is *not* so with the dipole moment calculations. The reason is that the integrand in this case involves the *moment* of the charge, that is the charge weighted by the distance from the centre. Hence, errors at the ends of the wire, which are normally insignificant for the typical electrodynamic observables mentioned above, are magnified in this case; furthermore, the charge is singular at the end of a wire, whereas the current is zero.¹

From this discussion it is obvious that an accurate charge distribution is needed. Before using the thin wire formulation with its desirable properties, the approach must first be carefully validated for this application. This will be done using as a test case a single straight wire in a

¹The electric dipole moment can also be formulated in terms of the integral of the current on the wire, which can be solved dynamically. However, due to the short nature of the wires, significant currents can exist on the end-caps and the axial current cannot be considered to go to zero at the ends of the straight section of wire. The dynamic formulation is thus not a very attractive alternative.

uniform electric field directed along its length, where, as can be seen from Eqs. (1) to (3), only the dipole moment, p , is non-zero when referred to the centre of the dipole. There are no exact analytical solutions available for the charge distribution on a thin wire, and an accurate numerical scheme was thus required to provide reference data. Hence a body of revolution method of moments (BOR MoM) formulation was developed, using the Galerkin approach.

3 Body of revolution method of moments solution

The BOR formulation uses entire domain Fourier modes for the circumferential expansion, and conventional sub-domain basis functions along the generating curve (also known as the generatrix). Mautz and Harrington's work, along with later extensions, has become one of the standard references for the full electrodynamic BOR MoM formulation [8]. The present quasi-static formulation is similar in concept, although the implementation is of course greatly simplified by the quasi-static nature of the problem.

The subdomain basis functions used were triangular functions along the generatrix (generally referred to as the t direction [8]). This provides a first-order basis function in finite element terminology. Since the electric field is purely z -directed, the charge is independent of ϕ , and hence only the zero-order Fourier mode is needed. The charge may be visualised as being expanded in terms of short cylindrical rings around the z -axis. Reflectional symmetry was also exploited and only one half of the wire was discretised.

Due to the singularity of the charge at the end of the wire, the distribution varies more rapidly towards the end of the wire. Thus it is advisable to use a non-uniform discretisation along the vertical part of the generatrix (the side of the dipole). On the end-cap the discretisation is uniform. The basis functions are shown in Fig. 2. The length of the last segment on the dipole side, b_{ZN} , is set as close as possible to that of the segments on the end-cap, and the segments increase linearly in length towards the centre of the dipole.

The quasistatic MoM formulation is given in Appendix A while Appendix B shows some detail on the evaluation of the integrable singularities which are unavoidable in the BOR MoM formulation.

The resulting charge distribution, for a 3 mm long wire of diameter 0.3 mm in a uniform electric field of 1 V/m directed along its axis, on one half of the wire length, is given in Fig. 3. The dipole moment for this wire was calculated using the charges from the BOR MoM code. Doubling the number of segments resulted in less than

0.01% change in the dipole moment. This result was thus taken to be a good reference value and is used to normalise the dipole moments in Fig. 4.

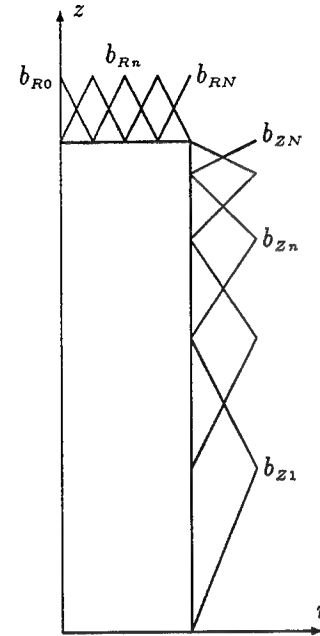


Figure 2: The basis functions on the wire. Note that the whole figure is rotated around the z -axis and is symmetric about the $z = 0$ plane. At the corner, b_{zN} and b_{RN} are joined to form a single basis function such that continuity of the charge is ensured.

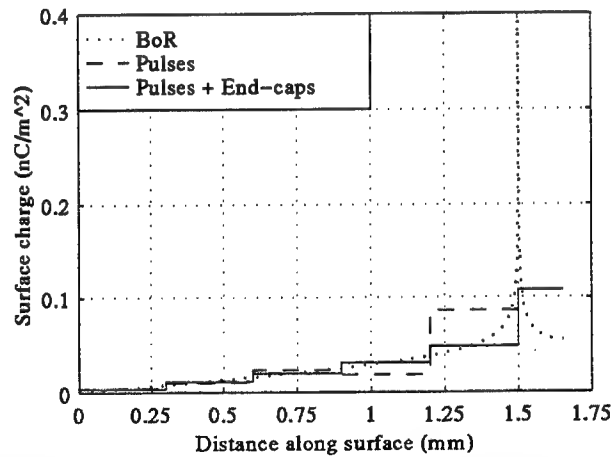


Figure 3: Comparison of the surface charges for the different techniques. The horizontal axis is the t -axis, a length parameter that follows the generatrix. (First it follows the z -axis along the surface of the dipole, then goes inwards along the $-r$ direction on the end-cap.) The 3 mm long wire of diameter 0.3 mm was excited by a uniform field of 1 V/m along its axis.

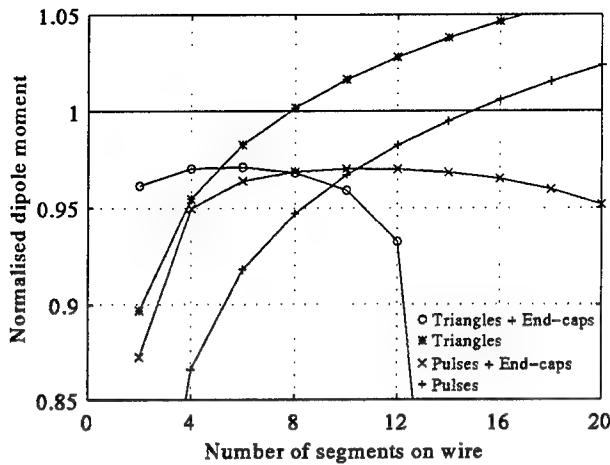


Figure 4: The dipole moments, for a 3 mm long wire with diameter 0.3 mm in a uniform electric field of 1 V/m in the axial direction, plotted against the number of segments. The moments are normalised by $p = 9.305 \times 10^{-20}$ as calculated by the BOR MoM code.

4 The thin wire technique

The electrodynamic solution of thin wires has been extensively studied, initially using analytical techniques (work which reached its peak with the King-Middleton approximate formulas of the 1950's [9]) and more recently using numerical methods, in particular the MoM. The widely used Pocklington formulation is almost 100 years old. Despite the very simple physical structure, sophisticated treatments are required for highly accurate and stable computations. In particular, the following require attention: the end-cap treatment, the source region modelling, and a method for handling thicker wires. All can and have been handled using a BOR MoM formulation, but this a computationally expensive solution, and the BOR MoM formulation is obviously not applicable to bent wires. Janse van Rensburg's doctoral thesis addresses the first two points (end-caps and source region modelling) [10]. Burke and Poggio incorporated an extended thin wire formulation and a simple treatment of wire ends in NEC-2 (this is not a full end-cap treatment) [11, pp. 10-30]; Burke extended this in [12, pp. 28-31]. Popović *et al.* describe a careful treatment of end-caps of flat or hemispherical shape [13, pp. 79-89]. Peterson [14] presents results showing how the careful treatment of end-caps is necessary for a properly converged solution. Fortunately, the source region modelling problem is not a concern with the present scattering formulation.

However, the electroquasistatic solution has received very little attention (certainly in the high-frequency literature). We will now consider the standard thin wire formulation as given by [6, Chapter 12]. A crucial part

of the formulation is the reduction of the problem from a two-dimensional surface charge to a one-dimensional line charge. This is known as the thin-wire approximation and has been widely used in powerful numerical electromagnetic codes such as NEC-2. The thin-wire approximation is very attractive, since it removes a dimension from the problem and also avoids the singularity inherent in the formulation. However, the formulation has some restrictions, not least the obvious requirement that the wire indeed be thin!

It is intuitively obvious that for a "thick" wire, the thin wire approximations are invalid; Collin has presented a very elegant discussion of the *theoretical* reasons for the failure of the approximation [15, p. 67-72]. He showed that the high spatial frequency component of the equivalent line current (which the thin-wire MoM codes compute) grows exponentially if the number of harmonics is such that the spatial period becomes less than about πa , where a is the wire radius. Collin's analysis used entire domain basis functions, but similar caveats apply when using subsectional basis functions; it is important to ensure that the discretisation is *coarse* enough to ensure that these harmonics are kept to a minimum. Of course, the discretisation must also be *fine* enough to adequately sample the actual spatial variation of the current (or charge); for sufficiently thin wires, there is a large stable (converged) region between these two requirements, but for thick wires it is possible to move directly from the under-discretised to the over-discretised regimes without the solution evidencing any form of convergence.

Using too fine a discretisation often results in errors around the end points of the wire; the undesirability of this for polarizability calculations is evident from the discussion in section 2. Generally it is accepted that, for the full electrodynamic formulation, the segment length to wire diameter ratio must be greater than two.

The present formulation was implemented with pulse basis and testing functions (i.e. a Galerkin approach) in a similar fashion to that described in [6]. The charge distribution was approximated as a line charge and the potential matched at the outer radius of the wire. (This is the thin-wire approximation already discussed.) The result for the 3 mm wire, shown in Fig. 3, was done with 10 segments on the wire — hence a segment length equal to the wire diameter. It can be seen that there is a considerable error near the end of the wire due to the over discretisation. This error is clearly unacceptable when computing the multipole moments. However, using fewer segments also resulted in large errors, as long segments cannot follow the charge singularity at the end of the wire. The ratio used here seems to be the optimum: half of the normal dynamic requirement that the minimum segment length must be larger than twice the wire diameter.

The dipole moment for the 3 mm wire was calculated using the charges resulting from this formulation. The charges were also calculated using a formulation implementing triangular basis and testing functions. The dipole moments for these two cases are plotted against the number of segments used in Fig. 4. It is clear that although the results throughout the graph are within 15% of the values computed with the BOR MoM formulation the convergence is poor and, without the reference data, one would be hard pressed to decide which discretisation gave the correct result.

Using the charge calculated by the body of revolution code it is found that the end-cap contributes almost 20% towards the dipole moment for the test case. Thus it can be expected that the thin wire technique will give erroneous results, since the end-cap is explicitly excluded from this formulation. An attractive solution to this problem is the inclusion of an end-cap term, and this will be considered in the next section.

5 Thin wire formulation with an added end-cap

The thin-wire technique was expanded by adding one more basis function — a flat disc of constant charge density to model the end-cap.² With the axis of the wire in the z -direction and the end-cap located at z' , the potential of the end-cap at any position (r, ϕ, z) , given by the inner integral in Eq. (7) of Appendix A, is

$$\Phi(r) = \int_0^{2\pi} \int_0^a \frac{r' dr' d\phi'}{\sqrt{(z - z')^2 + r'^2 + r^2 - 2r'r \cos \phi'}}$$

increasing the complexity of the formulation. One more weighted sample of the field is thus needed. This is obtained by an integral over the end-cap area.

It is important to note that this introduces an asymmetry into the impedance matrix of the moment method formulation.³ Changing from placing the charge on the axis (and sampling on the surface at the radius) to placing charge at the surface (and sampling on the axis) now results in the transposition of the impedance matrix — with a quite significant effect on the charge distribution. (For the standard straight thin-wire formulation the problem is symmetrical and it is irrelevant whether the charge is viewed as on the surface of the wire and the sampling on the axis or *vice versa*). In accordance

with physical principles, the charge is placed on the wire radius and the potential sampled on the axis — thus the outer integral in Eq. (7) of Appendix A reduces to a line integral. Sampling on the axis greatly simplifies the potential of the end-cap to

$$\Phi = 2\pi(\sqrt{a^2 + (z - z')^2} - |z - z'|)$$

where $|z - z'|$ is the distance from the end-cap. Computation of the “self-term” of the end-cap results in similar singularities to those experienced with the “self-term” calculations discussed in Appendix B.

The potential caused by the basis functions on the sides of the wire is reasonably constant on the end-cap, and their contributions are computed by using the value at the centre of the end-cap weighted by its area. (The “self term” is, however, integrated over the full area.) The charge distribution calculated with this technique is also shown in Fig. 3.

The graphs of the dipole moments (Fig. 4) show that incorporating the end-cap does indeed have the desired result of stabilising the convergence — which is now not only stable but also accurate within about 2% of the BOR MoM result. It is interesting to note how neglecting a significant physical feature in the numerical model (the end-cap in the standard thin wire formulation) can impact in unexpected ways, such as in poor convergence. As one would expect, the formulation using pulses converges more slowly than when using triangles.

The most important feature of this graph, however, is that the pulse formulation remains stable for significantly larger number of segments compared to triangular basis functions (up to a segment length equal to wire diameter). The reason for this is presently not clear. Both formulations converge to the same value. Using pulses leads to a much simpler formulation and, even with double the number of segments, shorter computing times than when using triangles. Hence this last formulation — viz. a Galerkin pulse basis function thin wire (with end-cap) MoM approach — was the one finally adopted. The runtime of this technique on a 486 PC was a few minutes compared with a few seconds for the standard thin wire technique (and two hours for the BOR MoM formulation!) For these time scales the added expense of the end-cap is certainly worthwhile, considering the increase in stability, and the computational cost is still much less than that of a full two-dimensional treatment (even one exploiting symmetry).

6 A chiral element

The chiral element is the bent wire shown in Fig. 1. As for the straight wire, sampling for all the wire segments is done on the axis, with the charge placed on the wire

²This is only an approximation as the actual charge distribution on the end-cap is much more complicated.

³This is due to the fact that the testing and basis functions for the end-cap are the same, whilst for the axial segments, the basis functions lie on the wire surface and the testing functions on the axis. For the end-cap, the equivalent of a line charge would be a point charge at its centre.

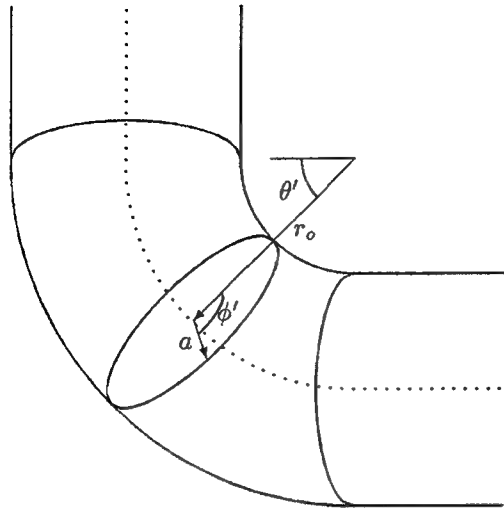


Figure 5: Structure of bend segment.

radius. When sampling on field segments that are not on the same straight section of wire, and are far enough away from the source segments (at least two segments in between them), the source charge was approximated by a line charge on the axis.

The bend requires some special treatment. It is constructed by sweeping the wire cross section along the angle θ' through 90 degrees as shown in Fig. 5, thus joining the two straight wires. The bend is modelled by a single curved segment with the charge placed on the wire surface; this is consistent with the straight segment treatment. When sampling the potential caused by this segment, the integral over the field segment (the outer integral in Eq. (7)) is done analytically,⁴ but the source integrand has to be evaluated numerically. Sampling of the field on the bend is done on the axis by numerical integration over θ (measured in the same way as θ').

This treatment of the bend is much more rigorous (and more complex) than merely having a sharp corner. It was implemented to check the effect of the bend and avoid the uncertainty regarding the position of the surface charge in its immediate vicinity. Increasing the radius, r_o , of the curved segment from $r_o = a$, which is as small as the code will allow, to $r_o = 2a$ decreased q_{zz} for a z -directed field⁵ by about 3%. Hence it does not appear to have a significant contribution to the calculation of the moments.

The end-cap is treated as a disk for the straight wire section that it terminates; for the other wire sections, it is handled as a point charge on the axis. Treating the end-cap as a point charge removes the expensive calculations

⁴Except in the case of the “self-term” or the interaction with the other bend where the field integral is also done numerically — thus requiring three numeric integrations.

⁵This is the moment most sensitive to the radius of the bends.

necessary when integrating over the endcap without significantly affecting its potential at these wire sections.

As an example, the charge is calculated for the structure in Fig. 1 with 3.12 mm long x - and y -axis legs, 3.14 mm z -axis leg and wire diameter 0.3 mm. The radius of curvature at the two bends in the wire is 1.5 times the wire diameter.⁶ The charge distribution for the structure excited by uniform 1 V/m x - and z -directed fields is shown in Fig. 6. Consideration of Fig. 4 led to the conclusion that the optimal segment length is equal to the wire diameter. This required 10 segments on a 3 mm leg. Fig. 6 shows the respective charge distributions calculated with 8 segments on the front leg (27 basis functions including the two bends and the two end-caps⁷) and with 12 segments on the front leg (39 basis functions). It is clear that the charge distribution con-

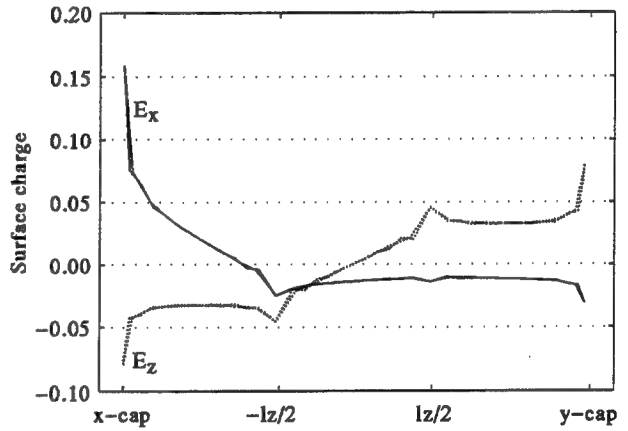


Figure 6: Surface charge in nC m^{-2} for a chiral hook with $l_x = l_y = 3.12 \text{ mm}$, $l_z = 3.14 \text{ mm}$, wire radius $a = 0.15 \text{ mm}$, and $r_o = 1.5a$; in an excitation field of 1 V/m using respectively 27 and 39 basis functions. E_x and E_z in the graph indicate direction of the applied electric field.

verged very well. The graphs lie almost on top of each other, with only a small difference near the ends and bends. This is due to the fact that the field is sampled at different points for different segmentations. As one would expect, the E_z -excited charge is anti-symmetrical around the centre of the z -axis. Note also the small peaks at the bends — which is to be expected as a sharp corner would have caused a singularity.

As the charge distribution is convergent around this point, it was finally calculated using 10 segments on the front leg (33 basis functions in total). This charge distribution was used in Eqs. (1) to (3) to calculate the

⁶These dimensions arose from practical considerations in manufacturing an artificial crystalline medium.

⁷The straight part of the z -leg is shorter due to the two bends subtracting from it, and requires one less segment.

| | E_x -excitation | E_z -excitation |
|-----------------------|-------------------------|-------------------------|
| p_x | 2.12×10^{-19} | -1.81×10^{-19} |
| p_y | -6.79×10^{-20} | 1.81×10^{-19} |
| p_z | -1.81×10^{-19} | 3.88×10^{-19} |
| $\frac{m_x}{j\omega}$ | 5.29×10^{-23} | -1.41×10^{-22} |
| $\frac{m_y}{j\omega}$ | -1.66×10^{-22} | 1.41×10^{-22} |
| q_{xx} | 5.56×10^{-22} | -4.03×10^{-22} |
| q_{xz} | -3.33×10^{-22} | 2.84×10^{-22} |
| q_{yy} | -1.54×10^{-22} | 4.03×10^{-22} |
| q_{yz} | -1.07×10^{-22} | 2.84×10^{-22} |
| q_{zz} | 6.95×10^{-23} | 0 |

Table 1: Multipole moments for a chiral hook with $l_x = l_y = 3.12$ mm, $l_z = 3.14$ mm, wire radius $a = 0.15$ mm, and $r_o = 1.5a$; in a unity uniform field.

multipole moments shown in Table 1. The current density was found by integrating the charge along the wire and differentiating with respect to time. Note that the time derivative of the electric quadrupole moments are of the same order as the magnetic dipole moments.

Formulating the problem without the end-caps and calculating the moments for the same number of segments as used for Table 1 yielded moments within 1% of the values in the table. However decreasing or increasing the number of segments led to poor convergence similar to that shown in Fig. 4. Note that the dipole moments in Fig. 4 are also almost equal at 10 segments which is the number used here. Hence, the advantage of the end-cap is in stabilising the convergence.

With the multipole moments known, the multipole moment densities and medium parameters can be calculated. An artificial crystalline medium was designed with the lattice and orientation of the structures as shown in Fig. 7. The spacings in the plane of the paper are 6.5 and 8 mm respectively and the disks are repeated in the z -direction at intervals of 9.3 mm.

With a host dielectric constant of 1.09 this resulted in dyadic medium parameters [5]

$$\begin{aligned}\epsilon_{xx} &= 1.01 \times 10^{-11} = 1.14 \epsilon_0 \\ \epsilon_{zz} &= 1.06 \times 10^{-11} = 1.20 \epsilon_0 \\ \xi_{xx} &= -\omega 2.54 \times 10^{-16} \\ \xi_{zz} &= \omega 2.55 \times 10^{-16}\end{aligned}$$

for the anisotropic constitutive relations

$$\begin{aligned}\mathbf{D} &= \bar{\epsilon} \cdot \mathbf{E} + j\bar{\xi} \cdot \mathbf{B} \\ \mathbf{H} &= j\bar{\xi}^T \cdot \mathbf{E} + \mu_0^{-1} \mathbf{B}.\end{aligned}$$

These have been rigorously derived [5] and are in the so-called Post-Jaggard form [16].

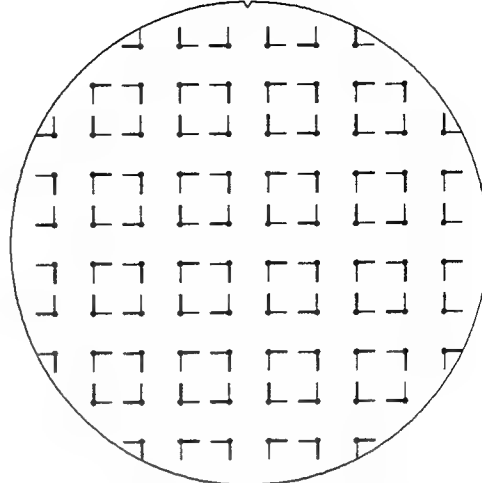


Figure 7: Disklike building element of the crystal. The thick lines are situated in front of the plane of the paper and the thin ones at the back.

At 3 GHz this medium would yield a rotation of 6.5 degrees per metre of the polarization plane of the electric field. The rotation is counter clockwise when viewed in the direction of propagation. The parameters given here were used to predict the rotation inside a waveguide. Agreement of the order of 13% was obtained between predictions and measurements, which is good when considered in the light of probable sources of error [17].

7 Conclusion

This paper has discussed the computation of the multipole moments of an electrically short chiral hook. To obtain the desired result, the charge distribution induced by a uniform electric field was required. It has been obtained via a quasi-static boundary value problem, which was solved using a variety of moment method formulations. A rigorous body of revolution MoM formulation has been presented. Results computed using this BOR MoM code converge rapidly and these computations have been used as a base-line for numerical investigations on thin wire MoM formulations.

The problems arising with the thin-wire formulation for a structure that is on the borderline of “thin” have been discussed. It has been shown that because the observable required from the code is the moment of the charge, the charge must be computed accurately at the ends — precisely where the thin-wire MoM formulations are expected to be least accurate. Results have been presented that show that the conventional thin-wire formulation does not properly converge for these structures. It has been demonstrated that a moderately straightforward extension to the thin-wire approach, viz. adding an

additional basis function to represent the end-cap, gives sufficiently accurate and converged results (within 3% of the BOR MoM result). The code used the same basis and testing functions, i.e. a Galerkin MoM formulation.

The emphasis of this paper has been the accurate computation of multipole moments. These moments can be used to predict medium parameters in the low-frequency regime as briefly described in section 6. The multipole moment calculations are not valid for higher frequencies, but at these frequencies the medium constructed with the chiral elements described here may start behaving more like a diffraction grating than a continuum. The predicted parameters have been experimentally verified.

References

- [1] D. L. Jaggard, A. R. Mickelson, and C. H. Papas, "On electromagnetic waves in chiral media," *Applied Physics*, vol. 18, pp. 211–216, 1979.
- [2] E. B. Graham, J. Pierrus, and R. E. Raab, "Multipole moments and Maxwell's equations," *J Physics B*, vol. 25, pp. 4673–4684, 1992.
- [3] R. E. Raab and J. H. Cloete, "An eigenvalue theory of circular birefringence and dichroism in a non-magnetic chiral medium," *J Electromagnetic Waves and Applications*, vol. 8, no. 8, pp. 1073–1089, 1994.
- [4] G. A. Morin, "A new circular polarization selective surface (CPSS)," in *Antenna Applications Symposium*, Univ. of Illinois, Urbana-Champaign, Illinois, Sept. 1989.
- [5] I. P. Theron, *The Circular Birefringence of Artificial Chiral Crystals at Microwave Frequencies*. PhD dissertation, University of Stellenbosch, submitted, 1995.
- [6] C. A. Balanis, *Advanced Engineering Electromagnetics*. New York: John Wiley and Sons, 1989.
- [7] H. A. Haus and J. R. Melcher, *Electromagnetic Fields and Energy*. Englewood Cliffs, New Jersey: Prentice-Hall, 1989.
- [8] J. R. Mautz and R. F. Harrington, "Radiation and scattering from bodies of revolution," *Journal of Applied Scientific Research*, vol. 20, pp. 405–435, June 1969.
- [9] R. S. Elliott, *Antenna Theory and Design*. Englewood Cliffs, New Jersey: Prentice-Hall, 1981.
- [10] D. J. J. van Rensburg, *On the computation of electromagnetic observables of conducting thin wire radiators*. PhD dissertation, Pretoria University, 1990.
- [11] G. J. Burke and A. J. Poggio, "Numerical Electromagnetics Code (NEC) - Method of Moments; Part I: Program Description - Theory," Jan. 1981.
- [12] G. J. Burke, "Numerical Electromagnetics Code – NEC-4 – Method of Moments; Part II: Program Description - Theory," Jan. 1992.
- [13] B. D. Popović, M. B. Dragović, and A. R. Djordjević, *Analysis and Synthesis of Wire Antennas*. Chichester: Research Studies Press, 1982.
- [14] A. F. Peterson, "Difficulties encountered when attempting to validate thin-wire formulations for linear dipole antennas," *Applied Computational Electromagnetics Society Journal*, Special Issue on Electromagnetics Computer Code Validation, pp. 25–40, 1989.
- [15] R. E. Collin, *Antennas and Radiowave Propagation*. New York: McGraw-Hill, 1985.
- [16] A. Lakhtakia, V. K. Varadan, and V. V. Varadan, *Time-Harmonic Electromagnetic Fields in Chiral Media*. Berlin: Springer-Verlag, 1989.
- [17] I. P. Theron and J. H. Cloete, "Microwave optical activity of an artificial non-magnetic uniaxial chiral crystal" and "Waveguide measurement of an artificial uniaxial chiral crystal in the long wavelength regime," in *Chiral'95. International Symposium on Chiral, Bi-isotropic and Bianisotropic Materials*, Pennsylvania State University, 1995.

A Quasistatic MoM formulation

In this appendix we formulate the quasistatic MoM. In the quasistatic formulation the static free-space Green's function is used. Thus the charge is the solution of the integral equation

$$\Phi(\mathbf{r}) = \Phi_i(\mathbf{r}) + \int_V \frac{\rho(\mathbf{r}')}{4\pi\epsilon_0|\mathbf{r} - \mathbf{r}'|} dV' \quad (4)$$

where $\Phi_i(\mathbf{r})$ is the applied potential in the absence of the scatterer and $\Phi(\mathbf{r})$ is the boundary value for the potential over a given boundary area. In this paper the applied field is uniform; for example $\Phi_i(\mathbf{r}) = -z$ for a z -directed field.

In the method of moments the surface charge distribution, $\rho(\mathbf{r})$, is modelled as the sum of a given set of basis functions, $b_n(\mathbf{r})$, defined on the surface, S ,

$$\rho(\mathbf{r}) = \sum_n a_n b_n(\mathbf{r}) \quad (5)$$

with the unknown coefficients, a_n , determining the distribution. The unknown coefficients can be found by

solving Eq. (4) to yield an approximate charge distribution. This is done by multiplying the equation with a number of testing functions $t_i(\mathbf{r})$ and integrating over the area S . Using N basis and N testing functions this results in a matrix equation

$$\begin{bmatrix} m_{11} & \cdots & m_{1n} & \cdots & m_{1N} \\ \vdots & & \vdots & & \vdots \\ \vdots & & \vdots & & \vdots \\ m_{i1} & \cdots & m_{in} & \cdots & m_{iN} \\ \vdots & & \vdots & & \vdots \\ m_{N1} & \cdots & m_{Nn} & \cdots & m_{NN} \end{bmatrix} \begin{bmatrix} a_1 \\ \vdots \\ a_n \\ \vdots \\ a_N \end{bmatrix} = \begin{bmatrix} v_1 \\ \vdots \\ v_i \\ \vdots \\ v_N \end{bmatrix}$$

where

$$v_i = 4\pi\epsilon_0 \int_S t_i(\mathbf{r}) (\Phi(\mathbf{r}) - \Phi_i(\mathbf{r})) da \quad (6)$$

$$m_{in} = \int_S \int_S \frac{t_i(\mathbf{r}) b_n(\mathbf{r}')}{|\mathbf{r} - \mathbf{r}'|} da' da \quad (7)$$

such that the calculation of m_{in} involves four integrations in total. The inner integral yields the potential due to $b_n(\mathbf{r}')$, while the outer integral samples the potential over a given region.

For a conducting body the boundary potential, $\Phi(\mathbf{r})$, is a constant. For a thin wire, symmetrical about the origin, $\Phi(\mathbf{r}) = 0$ by inspection. In the case of the chiral structure this constant is, however, unknown. As this introduces another variable in the MoM formulation another equation is necessary. This condition is provided for by requiring that the total charge on the wire be zero.

B The BOR MoM formulation

The BOR MoM formulation requires careful attention to certain details and this appendix addresses the computation of the potential and the associated singularity for the self terms of the BOR MoM matrix.

Here these functions are independent of ϕ and can be written as $b_n(z)$ along the dipole side and $b_n(r)$ on the endcap. Because of the non-uniform segmentation, the potential of each basis function must be computed — translational symmetry cannot be used — so it is important to do this efficiently.

The applied potential is required to produce a uniform z -directed field in the absence of the wire thus $\Phi_i(\mathbf{r}) = -z$. As the boundary condition the wire surface must be an equipotential surface. With the structure placed symmetrically about the z -axis the boundary potential is zero. Thus the excitation vector is

$$V_i = 4\pi\epsilon_0 \int_S b_i(l) z da$$

where l is a parameter that can be either z or r depending on where the testing function is located. As discussed earlier, the testing functions are the same as the basis functions and thus denoted $b_i(l)$.

The matrix entry m_{in} for basis functions along the dipole side was determined from the integral

$$\int_S \int_S \frac{b_i(l) b_n(z') a r}{\sqrt{(z - z')^2 + r^2 + a^2 - 2ra \cos \phi'}} dz' d\phi' dl d\phi$$

where l is as defined before. The inner z' integral was done analytically and the ϕ' -integral numerically. The result is proportional to the potential caused by $b_n(z)$ and is independent of ϕ — thus the outer ϕ integration merely results in multiplication by 2π . The outer l -integration was also done numerically.

The m_{in} entry for the basis functions on the cap was calculated from the integral

$$\int_S \int_S \frac{b_i(l) b_n(r') r' r}{\sqrt{(z - z')^2 + r^2 + r'^2 - 2rr' \cos \phi'}} dr' d\phi' dl d\phi \quad (8)$$

where the inner r' -integral was again algebraically evaluated and the ϕ -integral numerically. Here again the outer ϕ integral resulted in multiplication by 2π and the outer l -integration was also done numerically. Note that $z' = \pm L/2$ on the two caps respectively.

In both cases there is a singularity at $\phi' = 0$, when the testing and basis functions coincide (the self-term in MoM parlance). Consider, for example, the inner integral when calculating the self-term for the innermost basis function on the cap — b_{R0} in Fig. 2. If the length of this basis function in the r -direction is d , the basis function can be written as

$$b_{R0}(r) = \frac{d - r}{d}$$

and the inner integral in Eq. (8) becomes

$$\begin{aligned} & \int_0^{2\pi} \int_0^d \frac{(d - r)(d - r') r' r}{d^2 \sqrt{r^2 + r'^2 - 2rr' \cos \phi'}} dr' d\phi' \\ &= 2 \int_0^\pi \int_0^d \frac{(d - r)(d - r') r' r}{d^2 \sqrt{r^2 + r'^2 - 2rr' \cos \phi'}} dr' d\phi' \\ &= \frac{r(d - r)}{d^2} \int_0^\pi \left[r(3r \cos \phi' - 2d) \right. \\ & \quad \left. + (d - 3r \cos \phi') \sqrt{d^2 + r^2 - 2dr \cos \phi'} \right. \\ & \quad \left. + r(2r - 2d \cos \phi' - 3r \sin^2 \phi') \times \right. \\ & \quad \left. \log \frac{r - r \cos \phi'}{d - r \cos \phi' + \sqrt{d^2 + r^2 - 2dr \cos \phi'}} \right] d\phi \end{aligned}$$

where the symmetry of the ϕ' dependence is utilised — the integral between 0 and 2π can be written as two times

the integral between 0 and π . It is clear that the third term in the ϕ' -integrand will be singular at $\phi = 0$. This singularity, present at any value of r , can be removed by subtracting a term

$$r(2r - 2d \cos \phi' - 3r \sin^2 \phi') \log(1 - \cos \phi')$$

which can be integrated algebraically using⁸

$$\begin{aligned} \int_0^\pi \log(1 - \cos \phi) d\phi &= -\pi \log 2 \\ \int_0^\pi \cos \phi \log(1 - \cos \phi) d\phi &= -\pi \\ \int_0^\pi \sin^2 \phi \log(1 - \cos \phi) d\phi &= \frac{1}{2}\pi(\frac{1}{2} - \log 2) \end{aligned}$$

after expanding the factors. The remaining integrand⁹ contains a logarithm that is singular at $r = d$. At this value of r it is simplified to

$$\begin{aligned} \log \frac{r}{d - r \cos \phi' + \sqrt{d^2 + r^2 - 2dr \cos \phi'}} \\ = \log \frac{1}{1 - \cos \phi' + \sqrt{2(1 - \cos \phi')}} \\ = \log \frac{1 + \cos \phi'}{\sin \phi'(\sin \phi' + \sqrt{2(1 + \cos \phi')})} \end{aligned}$$

from which the singular $\log \sin \phi'$ can be extracted and integrated analytically between $0 < \phi' < \frac{\pi}{2}$. The remaining term is then integrated numerically (also between $0 < \phi' < \frac{\pi}{2}$) and the original integrand integrated numerically between $\frac{\pi}{2} < \phi' < \pi$. The analytic integration requires the further integrals

$$\begin{aligned} \int_0^{\frac{\pi}{2}} \log(\sin \phi) d\phi &= -\frac{\pi}{2} \log 2 \\ \int_0^{\frac{\pi}{2}} \cos \phi \log(\sin \phi) d\phi &= -1 \\ \int_0^{\frac{\pi}{2}} \sin^2 \phi \log(\sin \phi) d\phi &= \frac{\pi}{8}(1 - \log 4). \end{aligned}$$

This process unfortunately leads to the subtraction of a large component due to the analytic integration of the singularity from an almost equally large component due to the remaining numeric integral. Thus a few significant digits are lost and the numeric integration has to be done to a very high degree of accuracy. This problem was overcome by dividing the singular component by π , the integration interval, and subtracting it as a constant from the integrand. Thus the two numbers are subtracted before the approximation caused by the numerical integration, requiring much less severe restrictions on the accuracy of the numerical integration to

achieve the same final accuracy. The self-terms for the other segments result in similar singularities, which can be subtracted in a similar fashion.

Numeric integration was done with Simpson's rule and halving the interval each time until the results had converged to within 10^{-3} of the last result. The convergence requirements for the inner integral had to be stricter than for the outer integral to converge properly, and 10^{-4} was chosen. The charge on the test case wire was calculated by this technique using 40 segments on the cap and 44 along the axis. About four decimals of accuracy were used in the numerical integrations and the condition number of the MoM matrix was sufficient to preserve this accuracy when inverting the matrix.

The authors

Isak Petrus Theron was born in 1967 and grew up in Upington, South Africa. He received the B.Eng. and M.Eng. degrees from the University of Stellenbosch in 1989 and 1991 respectively, both cum laude. He is presently a research student in the electromagnetics group at the Department of Electrical and Electronic Engineering at that university. His research is currently directed at modelling anisotropic chiral media by combining optical theories of matter from molecular physics with the analytical, numerical and experimental techniques of classical electromagnetics.

David Bruce Davidson was born in London, England in 1961. He grew up in South Africa. He received the B.Eng., B.Eng. (Honours) and M.Eng. degrees (all cum laude) from the University of Pretoria in 1982, 1983 and 1986 respectively, and in 1991 he received the Ph.D. degree from the University of Stellenbosch. David is presently an Associate Professor of Electrical and Electronic Engineering at the University of Stellenbosch, where he started teaching in 1988 following three years as a research engineer at the national research laboratories. His research interests centre around computational electromagnetics — theory, code development and applications.

Johannes Hendrik Cloete was born in Clocolan, Orange Free State, South Africa in 1945. He received the B.Eng. and Ph.D. (Eng) degrees in Electrical Engineering from the University of Stellenbosch and the MS. degree in Electrical Engineering from the University of California, Berkeley. He has been a professor in the Department of Electrical and Electronic Engineering at the University of Stellenbosch since 1984. His research interests are the electromagnetic properties of microwave materials, experimental methods for characterising them, and antenna engineering.

⁸Calculated with *Mathematica 2.0*.

⁹Note that $\log a + \log b = \log ab$.

APPLICATION OF THE UMOM FOR THE COMPUTATION OF THE SCATTERING BY DIELECTRICS COATED WITH WEAKLY NONLINEAR LAYERS

Salvatore Caorsi*, Andrea Massa**, and Matteo Pastorino**

* Department of Electronics, University of Pavia
Via Abbiategrasso 209, I-27100 Pavia, Italy

** Department of Biophysical and Electronic Engineering
University of Genoa, Via Opera Pia 11, I-16145, Genova, Italy

ABSTRACT. The paper describes an iterative approach to the computation of the electromagnetic scattering by isotropic, dielectric objects partially made of weakly nonlinear materials. The approach is started by using a perturbative moment-method solution based on the Sherman-Morrison-Woodbury formula. The nonlinearity is assumed to be of the Kerr type, i.e., the dielectric permittivity depends on the square amplitude of the electric field. The bistatic scattering width and the field distribution are computed for some test cases, in particular, for infinite cylinders coated and filled with nonlinear materials. The convergence of the medium is numerically evaluated and the results are compared with those obtained by the iterative distorted-wave Born approximation.

1 INTRODUCTION

An interesting perturbational version of the moment method [1] was recently proposed by Yip and Tomas [2]. The approach is aimed at determining the electromagnetic scattering by a slightly perturbed scatterer, after a moment-method solution for the original unperturbed scatterer has already been obtained. The method applies the Sherman-Morrison-Woodbury (SMW) updating formula and allows one to consider changes in both the geometry and the dielectric properties of the scatterer. The above method, called by the authors the UMoM, is one of the various perturbational methods that make it possible to avoid repeating a complete computation when several scatterers, only partially different, have to be considered in the scattering evaluation. An overview of these methods was presented by Newman [3], who also described an efficient combination of the moment method with Green's function.

In this paper, the application of the UMoM, as proposed in [2], is the starting point for the development of an iterative approach to the computation of the electromagnetic scattering by nonlinear dielectric objects. The interest in evaluating the scattering by nonlinear dielectrics is generally related to the possibility of using them as coating materials, for example, in order to obtain apparatus for minimizing and

maximizing scattering cross-sections in camouflage applications.

Here the nonlinearity is assumed to be of the Kerr type, i.e., the relative dielectric permittivity depends on the square amplitude of the internal electric field. As long as the nonlinearity is weak, as for most of nonlinear materials [4], the main effect of the nonlinearity is a modification to the field distribution at the frequency of the incident field, whereas the process of higher-harmonics generation may be neglected. Moreover, if the nonlinearity is weak, from a perturbation point of view, one can assume the effective dielectric permittivity to be approximated by writing it in terms of the linear field. This was done by the authors in a previous work in which they computed the bistatic scattering width for a circular nonlinear cylinder by using an iterative approach based on the distorted-wave Born approximation [5]. The main limitation of this approach is related to the fact that the effective dielectric permittivity must be weak in order that the process may converge. This is a severe limitation, in that a nonlinearity can usually be considered weak but the resulting effective dielectric permittivity is not at all weak. The authors showed that, although the nonlinearity was very weak, it affected the bistatic scattering width in a significant way.

If a nonlinear material is assumed to be only a portion of the scatterer considered, the UMoM can be successfully applied, as the weak nonlinearity can be viewed as a perturbation of the original scattering configuration. At this point, an iterative process is started by applying the SMW formula, or, in a simpler way, by using the approach described in [5], but, at the 0-th step, the linear field (distorted-wave Born approximation) is replaced by the field obtained by the UMoM without iterations.

In the following, the mathematical formulation of the approach is provided. Some test cases are described that involve coated cylinders of circular and irregular cross-sections. We consider infinite cylinders illuminated by transverse-magnetic waves. As $\nabla \cdot \mathbf{E} = 0$, \mathbf{E} being the electric field vector, the problem reduces to a two-dimensional scalar one, for which the notation is simplified.

MATHEMATICAL FORMULATION

Let us consider an infinite dielectric cylinder of arbitrary cross-section, with the cylindrical axis parallel to the z axis (Figure 1). The cylinder is illuminated by a time-periodic transverse-magnetic electromagnetic field, for which $\mathbf{E}^{\text{inc}}(x,y,z,t) = E_z^{\text{inc}}(x,y,t)\mathbf{z}$ and $\mathbf{H}^{\text{inc}}(x,y,z,t) = H_x^{\text{inc}}(x,y,t)\mathbf{x} + H_y^{\text{inc}}(x,y,t)\mathbf{y}$. The propagation medium is assumed to be lossless, homogeneous, and characterized by μ_0 and ϵ_0 . Suppose the region S_2 to be made of a weakly nonlinear material (isotropic and nonmagnetic) whose dielectric permittivity is of the Kerr type [6]:

$$\epsilon_{nl}(x,y) = \epsilon_0[\epsilon_2(x,y) + \xi|E_z(x,y,t)|^2] \quad (1)$$

where $\epsilon_2(x,y)$ is the linear part and ξ is a nonlinear parameter. The medium of the region S_2 is assumed to be inhomogeneous both due to the nonlinearity and in the limit $E_z(x,y,t) \rightarrow 0$ [7]. To simplify the notation, let us assume that also the dielectric permittivity of the region S_1 is expressed by (1), with $\xi = 0$ and $\epsilon_2(x,y)$ replaced by $\epsilon_1(x,y)$.

In order to devise an iterative approach to the computation of the electromagnetic field distribution, let us compute the scattering by an inhomogeneous linear scatterer of section $S = S_1 \cup S_2$, obtained by setting $\xi = 0.0$ everywhere. The electric field integral equation (EFIE) for this problem can be expressed as [8]:

$$\Phi^t(x,y) = \Phi^i(x,y) - j(k_0^2/4) \int_S [\epsilon_{lin}(x,y) - 1] \Phi^t(x',y') \times H_0^{(2)}(k_0\rho) dx' dy' \quad (2)$$

where $\Phi^i(x,y)$ and $\Phi^t(x,y)$ are the space-dependent parts of the incident and the total electric fields (the time-dependence $\exp\{j\omega t\}$ is assumed and suppressed); $H_0^{(2)}(k_0\rho)$ is the Hankel function of the second kind and the zero-th order, ρ is given by: $\rho = [(x - x')^2 + (y - y')^2]^{1/2}$, and $\epsilon_{lin}(x,y) = \epsilon_1(x,y)$ if $(x,y) \in S_1$, $\epsilon_{lin}(x,y) = \epsilon_2(x,y)$ if $(x,y) \in S_2$. By applying the Richmond formulation [9] to (2), the problem solution is reduced to solving the following algebraic system of linear equations:

$$[G]\underline{\Phi}^t = \underline{\Phi}^i \quad (3)$$

where:

$\underline{\Phi}^t$: unknown array of dimensions $P \times 1$, P being the number of subdomains. The p th element of $\underline{\Phi}^t$ is given by: $\phi_p^t = \Phi^t(x_p, y_p)$, where (x_p, y_p) is the center of the p th subdomain;

$\underline{\Phi}^i$: excitation array of dimensions $P \times 1$ whose elements are given by: $\phi_p^i = \Phi^i(x_p, y_p)$, $p = 1, \dots, P$;

$[G]$: Green's matrix of dimensions $P \times P$ whose generic elements are:

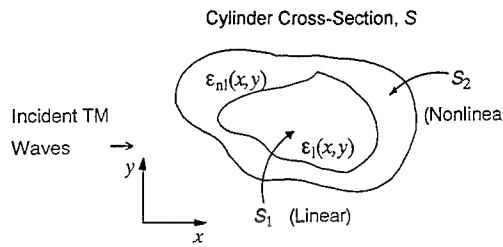


Fig. 1 Problem geometry.

$$g_{pq} = \begin{cases} (j/2)[\epsilon_{lin}(x_q, y_q) - 1][\pi k_0 a_q H_1^{(2)}(k_0 a_q) - 2j] & \text{if } p = q \\ 0 & \text{if } p \neq q \end{cases}$$

$$g_{pq} = \begin{cases} (j/2)[\epsilon_{lin}(x_q, y_q) - 1]\pi k_0 a_q J_1(k_0 a_q) H_0^{(2)}(k_0 \rho_{pq}) & \text{if } p \neq q \\ 0 & \text{if } p = q \end{cases}$$

where $\rho_{pq} = [(x_p - x_q)^2 + (y_p - y_q)^2]^{1/2}$ and $a_q = (S_q/\pi)^{1/2}$, S_q being the area of the q -th subdomain.

Let us now apply the UMoM, considering the perturbed configuration obtained by computing the dielectric permittivity in (1) in terms of the linear field distribution. If we use the same scheme as for the Richmond formulation, the problem turns out to be expressed by:

$$[G']\underline{\Phi}^{nl} = \underline{\Phi}^i \quad (4)$$

where:

$\underline{\Phi}^{nl}$: unknown array of dimensions $P \times 1$;

$[G']$: Green's matrix whose generic elements are:

$$g_{pq} = \begin{cases} (j/2)[\epsilon_{nl}(x_q, y_q) - 1][\pi k_0 a_q H_1^{(2)}(k_0 a_q) - 2j] & \text{if } p = q \\ 0 & \text{if } p \neq q \end{cases}$$

$$g_{pq} = \begin{cases} (j/2)[\epsilon_{nl}(x_q, y_q) - 1]\pi k_0 a_q J_1(k_0 a_q) H_0^{(2)}(k_0 \rho_{pq}) & \text{if } p \neq q \\ 0 & \text{if } p = q \end{cases}$$

As the geometrical properties are kept unperturbed and only the electric properties are made to change, the matrix

$$[\Delta G] = [G] - [G'] \quad (5)$$

has only P_2 non-zero columns, corresponding to the subdomains with perturbed characteristics. For the solution of (4), the UMoM uses the SMW updating formula [10]:

$$[G']^{-1} = [G]^{-1} + [G]^{-1}[U](I - [V]^T[G]^{-1}[U])^{-1}[V]^T[G]^{-1} \quad (6)$$

where $[U]$ and $[V]$ are matrices defined in the following and I is a $P_2 \times P_2$ identity matrix. The problem is the same as for case (a) in [2], so the identification of matrices $[U]$ and $[V]$ is quite immediate. In particular, U is a $P \times P_2$ matrix whose columns are the P_2 non-zero columns of $[\Delta G]$, and $[V]$ is a $P_2 \times P$ matrix whose elements are given by: $v_{ij} = \delta_{ij}$, where δ_{ij}

denotes the Kronecker symbol. It follows that:

$$[\Delta G] = [U][V]^T \quad (7)$$

where $[V]^T$ is the transposed matrix of $[V]$. The use of the SMW is discussed in several papers and books (see the exhaustive list given in [2]; in the Appendix of that paper, the formula is derived for completeness). A discussion of the convergence of the series on which the SMW formula is based, in terms of the matrix eigenvalues, can be found, for example, in [10].

At this point, the nonlinear problem can be solved in two ways. Once the first-order approximation has been obtained, one can start the iterative process by applying the UMoM recursively, according to the following scheme:

- At step $k = 0$, set:

$$\underline{\Phi}^{k=0} = \underline{\Phi}^i; \quad \varepsilon_{nl(k=0)}(x_p, y_p) = \varepsilon_0 [\varepsilon_{lin}(x_p, y_p) + \xi |\phi_p^t|^2]; \quad [G^{k=0}] = [G]$$

- At step k , assume:

$$\begin{aligned} \underline{\Phi}^k &= [G^k]^{-1} \underline{\Phi}^i = \{[G^{k-1}]^{-1} + \\ &+ [G^{k-1}]^{-1} [U]([I]-[V]^T [G^{k-1}]^{-1} [U])^{-1} [V]^T [G^{k-1}]^{-1}\}, \\ \varepsilon_{nl(k)}(x_p, y_p) &= \varepsilon_0 [\varepsilon_{lin}(x_p, y_p) + \xi |\phi_p^k|^2] \end{aligned}$$

In a simplified version of the approach, the nonlinear solution obtained by approximating the solution for $\underline{\Phi}^n$ in (4) by the SMW formula is used to start an iterative process expressed by ($k \geq 1$):

$$\begin{aligned} \Phi_k^t(x, y) &= \Phi^i(x, y) - j(k_0^2/4) \int_S [(\varepsilon_{lin}(x', y') - 1) + \\ &+ \xi |\Phi_{k-1}^t(x', y')|^2] \Phi_{k-1}^t(x', y') H_0^{(2)}(k_0 \rho) dx' dy' \end{aligned} \quad (8)$$

where $\Phi_{k=0}^t(x, y)$ is computed, in an approximate way, by (4) and (6). This simplified version constitutes an improvement over the distorted-wave Born-approximation iterative approach proposed in [5]. In a discretized form, the above iterative process can be written as:

$$\begin{aligned} \phi_q^k &\approx \phi_q^k - j(k_0^2/4) \sum_{p=1}^P [\varepsilon_{lin}(x_p, y_p) + \xi |\phi_p^k|^2] \phi_p^k \\ &\times H_0^{(2)}(k_0 \rho_p) \Delta s_p \end{aligned} \quad (9)$$

where $\rho_p = [(x - x_p)^2 + (y - y_p)^2]^{1/2}$ and $q = 1, \dots, P$.

In a linear case, the possibility of applying the UMoM is related to the convergence of the series for the SMW formula, which in turn is related to the matrix eigenvalues. This sets rigid limits on the validity of the approach for slightly perturbed geometries. When the scatterer's geometry is unperturbed, the above condition can

be satisfied for a weak "excess" of permittivity. Analogously, in the case of nonlinear scatterers, we can expect the process to converge for weak nonlinearities only. Unfortunately, in the present case, convergence depends on various factors: the linear part of the dielectric permittivity, the nonlinear coefficient, and the incident electric field. Unlike linear scattering, for a monochromatic plane-wave TM illumination, the amplitude, phase and frequency values contribute to the process convergence or divergence. At present, this makes it impossible for the authors to define a criterion that establishes whether convergence can be reached or not, for given perturbed and unperturbed configurations. In the Results section, however, this aspect will be discussed by way of several numerical examples.

To this end, let us define the following residual error:

$$\begin{aligned} \Re\{k+1\} [\text{dB}] &= 10 \log_{10} (S^{-1}) \int_S \{ \Phi_{k+1}^t(x', y') - \Phi^i(x', y') + \\ &+ j(k_0^2/4) \int_S [\varepsilon_{nl}(u, v) - 1] \Phi_{k+1}^t(u, v) H_0^{(2)}(k_0 \xi) du dv \} \} \quad (10) \end{aligned}$$

The approach is assumed to be convergent if $\Re\{k\} \rightarrow 0$, as $k \rightarrow \infty$.

3 NUMERICAL RESULTS

Some test cases are now described. In the first example, a homogeneous dielectric cylinder ($\varepsilon_1 = 1.8$), coated with a nonlinear layer ($\varepsilon_2 = 1.1$), was illuminated by a unit uniform plane TM-wave propagating along the x axis (Figure 2(a)). The radii of the two cylinders were such that $k_0 a_1 = 0.49\pi$ and $k_0 a_2 = 0.6\pi$. Figure 2 gives the values of the bistatic scattering width (BSW), defined as [11]:

$$W(\phi) [\text{dB}] = 10 \log_{10} \left[\lim_{\rho \rightarrow \infty} 2\pi\rho \frac{|\Phi'(x, y) - \Phi^i(x, y)|^2}{|\Phi^i(x, y)|^2} \right] \quad (11)$$

The values of the nonlinear parameter were assumed to be (a) $\xi = 0.01$, (b) $\xi = 0.1$, and (c) $\xi = 0.8$. The linear values ($\xi = 0.0$) are also provided. They were analytically computed by using the recursive Richmond formula [12] (slightly corrected in [13]). For comparison, the figure also gives the values obtained by applying the iterative distorted-wave Born-approximation (DWBA) approach [5]. It can be noticed that the behaviours for $\xi = 0.01$, corresponding to a very weak nonlinearity, and for $\xi = 0.1$ are similar. For $\xi = 0.8$, the iterative DWBA solution did not converge, so only the first two iterations are shown. As expected, the iterative UMoM always converged very fast (it should be stressed that the relative high permittivity of the internal cylinder made the convergence of the DWBA problematic, even for very weak nonlinearities). It is worth noting that, for the considered values of the field intensity and of the scatterers' dimensions most of the chosen values for ξ correspond to weak

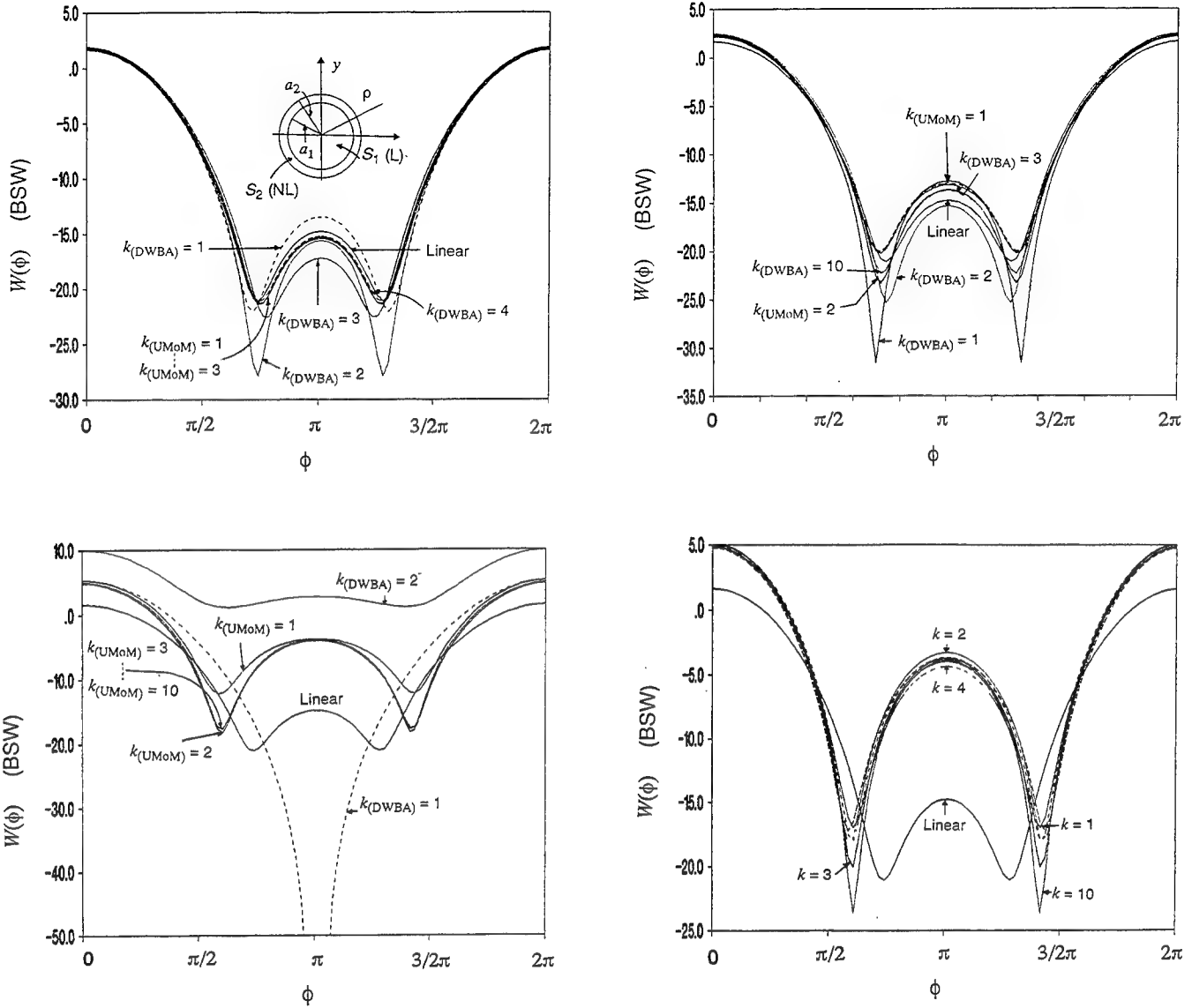


Fig. 2 Bistatic scattering width of a circular cylinder ($\varepsilon_1 = 1.8$) coated with a nonlinear layer ($\varepsilon_2 = 1.1$, $k_0 a_1 = 0.49\pi$; $k_0 a_2 = 0.6\pi$, $P = 121$, $P_2 = 40$). Comparison between the iterative approaches using the distorted-wave Born approximation (DWBA) and the UMoM. (a) $\xi = 0.01$; (b) $\xi = 0.1$; (c) $\xi = 0.8$; (d) $\xi = 0.8$, simplified iterative version (relation (8)).

nonlinearities, in the sense the resulting scatterers are such that the obtained scattering distributions (predicted by the assumed nonlinear electromagnetic model) can be regarded as slight perturbations of those of the corresponding linear cases.

The simplified version of the proposed approach (relation (8)) was also applied. As an example, Figure 2(d) gives the BSW value for $\xi = 0.8$. The solution converged, even though rather slowly, whereas, for the other two values of ξ , the behaviours were similar to that of the iterative DWBA approach.

Figure 3 gives, for the same values of the nonlinear parameter, the amplitude of the total electric field along the x axis [$y = 0$]. Finally, Figure 4 shows the plots of the residual errors (relation (10)) for different numbers of iterations. As long as the nonlinearity was weak (and hence the

configuration was slightly perturbed), the iterative UMoM approach converged independently of the linear permittivity. This is confirmed by Figure 5, which gives the BSW values for a multilayer cylinder equal to that in the previous example, but with an internal dielectric permittivity equal to 5.0. In this example, the nonlinearity was partially blinded by the high value of the nonlinear permittivity. The simplified version of the approach (which exhibited obvious limitations similar to those of the DWBA approach) did not converge

$$(\Re(1) = -36.2, \Re(2) = -31.3, \Re(3) = -24.7, \Re(5) = -2.0, \Re(8) = 40.5).$$

In another example, we considered the effects of the ratio between the wavelength and the scatterer's dimensions by considering a multilayer cylinder with the cross-section shown

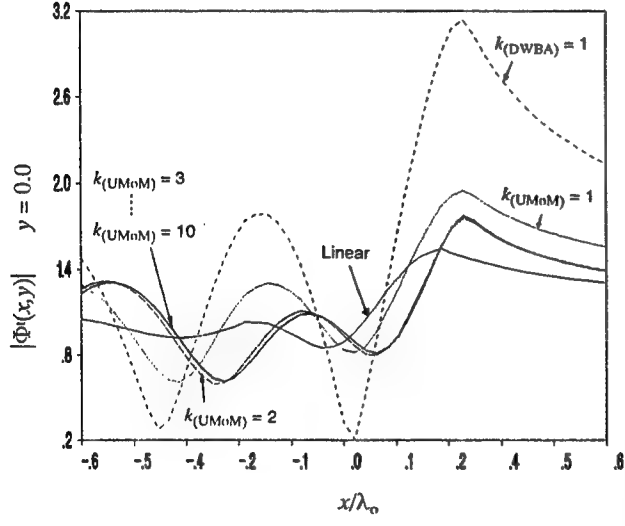
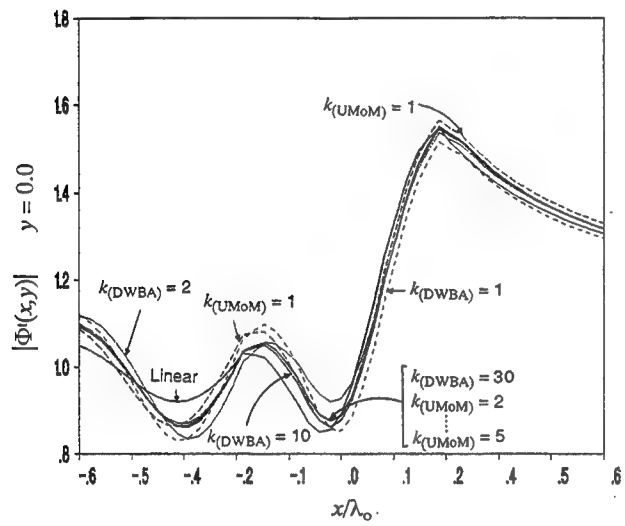
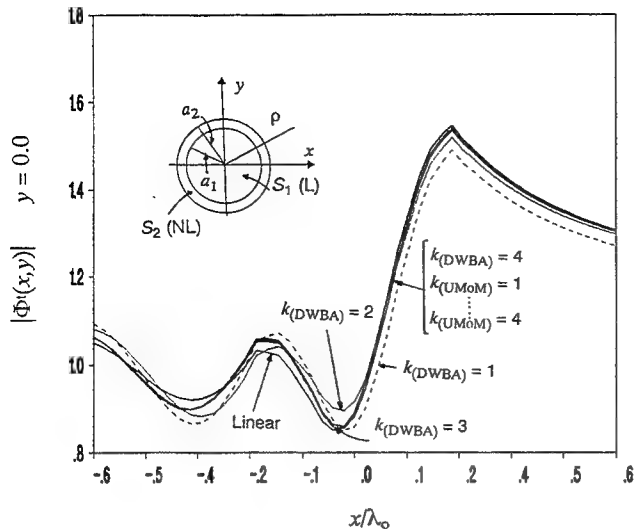


Fig. 3 Scattering by a circular cylinder ($\epsilon_1 = 1.8$) coated with a nonlinear layer ($\epsilon_2 = 1.1$, $k_0 a_1 = 0.49\pi$; $k_0 a_2 = 0.6\pi$, $P = 121$, $P_2 = 40$). Amplitude of $\Phi^t(x,y)$. Comparison between the iterative approaches using the distorted-wave Born approximation (DWBA) and the UMoM. (a) $\xi = 0.01$; (b) $\xi = 0.1$; (c) $\xi = 0.8$.

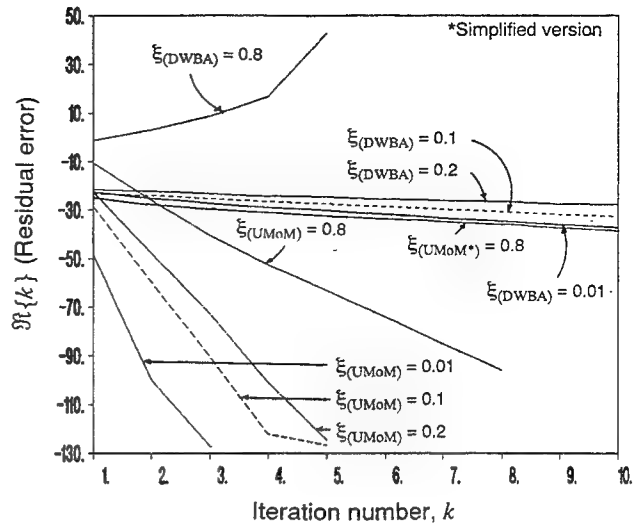


Fig. 4 Residual errors $\Re\{k\}$ (dB) for different numbers of iterations. Simulations in Figs. 2 and 3.

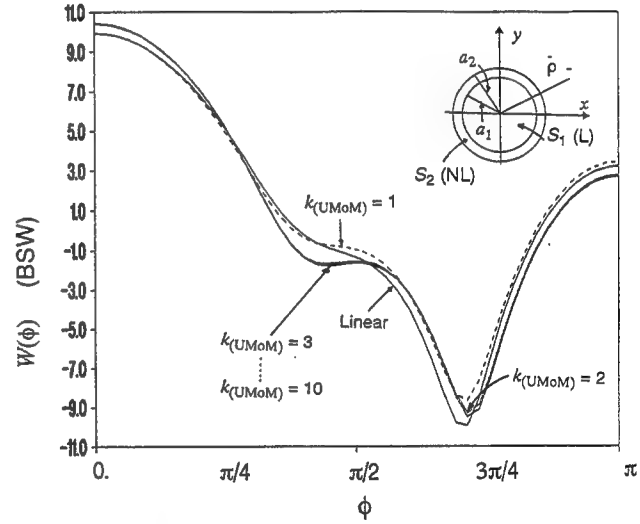


Fig. 5 Bistatic scattering width of a circular cylinder ($\epsilon_1 = 5.0$) coated with a nonlinear layer ($\epsilon_2 = 1.1$, $\xi = 0.1$, $k_0 a_1 = 0.49\pi$; $k_0 a_2 = 0.6\pi$, $P = 121$, $P_2 = 40$). Iterative UMoM.

in Figure 6(a). The internal layer was linear ($\epsilon_1 = 1.5$), whereas the external was nonlinear ($\epsilon_2 = 1.5$, $\xi = 0.2$). The illumination conditions were the same as in the previous examples. The BSW was computed by using the iterative UMoM for (a) $k_0 l = 0.48\pi$, (b) $k_0 l = 0.8\pi$, and (c) $k_0 l = 1.2\pi$. The linear values ($\xi = 0$) are also given in Figure 6, and the residual errors are given in Table I.

A linear circular cylinder ($\epsilon_1 = 3.0$) with a nonlinear nucleus ($\epsilon_2 = 3.0$, $\xi = 0.2$) was then considered. The radii of the two cylinders were such that $k_0 a_1 = 1.27\pi$ and $k_0 a_2 = 1.63\pi$.

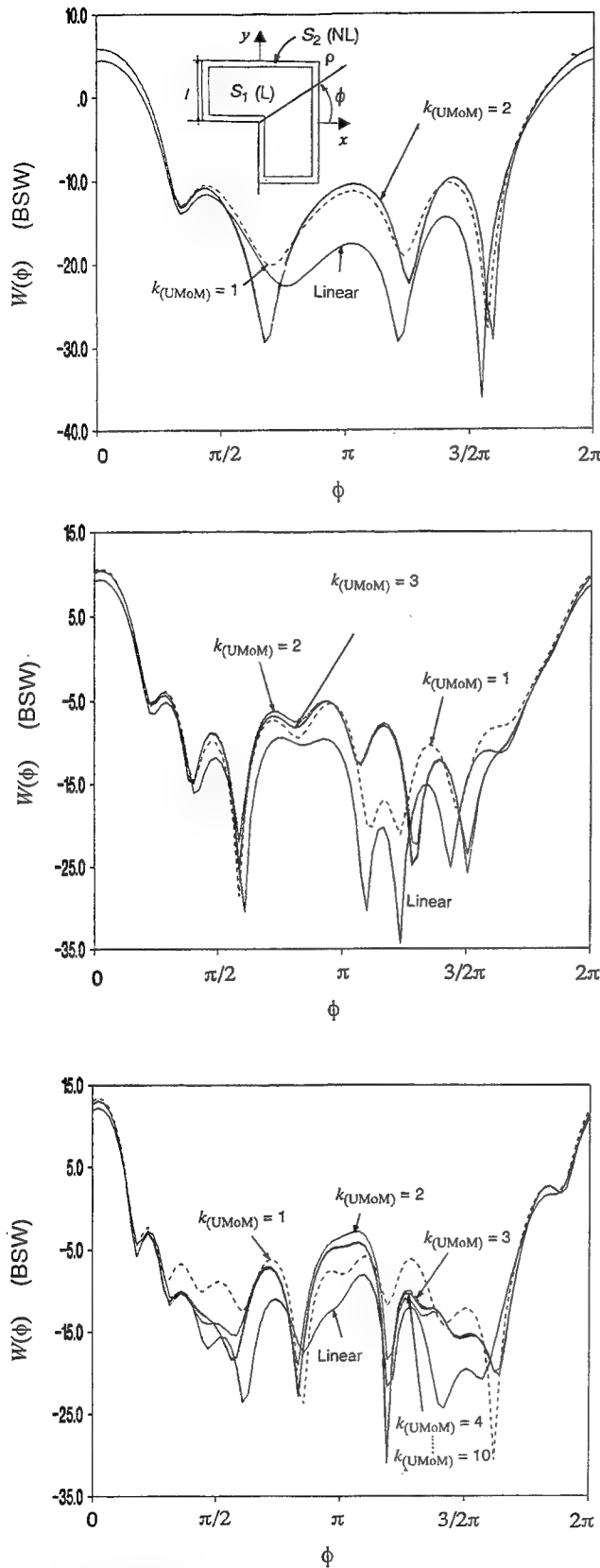


Fig. 6 Bistatic scattering width of a cylinder of irregular cross section ($\epsilon_1 = \epsilon_2 = 1.5$, $\xi = 0.2$, $P = 132$, $P_2 = 52$). (a) $k_0 l = 0.48\pi$; (b) $k_0 l = 0.8\pi$; (c) $k_0 l = 1.2\pi$.

| $\downarrow k_0 l$ | $k=1$ | $k=2$ | $k=3$ | $k=4$ | $k=5$ | $k=6$ | $k=7$ | $k=8$ |
|--------------------|-------|-------|-------|-------|--------|--------|--------|--------|
| 0.48π | -20.4 | -44.6 | -66.2 | -86.5 | -103.2 | -121.1 | -125.5 | -126.0 |
| 0.8π | -15.9 | -36.1 | -51.1 | -67.7 | -81.8 | -95.0 | -109.2 | -121.7 |
| 1.2π | -13.3 | -28.6 | -45.1 | -58.9 | -75.6 | -88.5 | -101.0 | -111.9 |

Table I. Residual errors $\Re\{k\}$ (dB) for different numbers of iterations. Simulations in Fig. 6.

Figure 7 gives the BSW values computed at various iteration steps, and Table II provides the values of the residual errors.

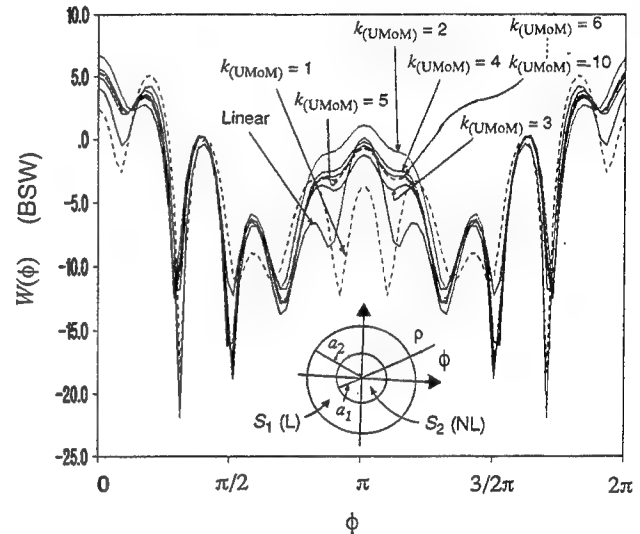


Fig. 7 Bistatic scattering width of a circular cylinder ($\epsilon_1 = 3.0$) with a nonlinear nucleus ($\epsilon_2 = 3.0$, $\xi = 0.2$, $k_0 a_1 = 1.27\pi$; $k_0 a_2 = 1.63\pi$, $P = 81$, $P_2 = 49$). Iterative UMoM.

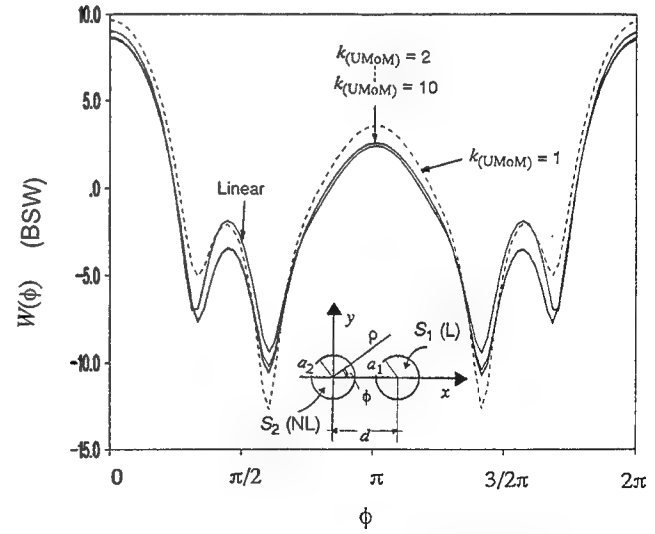


Fig. 8 Bistatic scattering width of two separate circular cylinders ($\epsilon_1 = \epsilon_2 = 4.0$, $\xi = 0.2$, $k_0 a_1 = k_0 a_2 = 0.82\pi$, $P = 162$, $P_2 = 81$). Iterative UMoM.

| k | 1 | 2 | 3 | 4 | 5 | 10 | 15 | 20 |
|-----|-------|-------|-------|-------|-------|-------|--------|--------|
| - | -11.1 | -19.7 | -25.3 | -33.0 | -39.1 | -72.9 | -107.1 | -119.0 |

Table II. Residual errors $\Re\{k\}$ (dB) for different numbers of iterations. Simulations in Fig. 7.

Finally, the plane-wave scattering by two equal, separate, homogeneous, circular cylinders was considered ($\varepsilon_1 = \varepsilon_2 = 4.0$). The cylinders' radii were such that $k_0 a_1 = k_0 a_2 = 0.82\pi$, and the distance between the two centers was such that $k_0 d = 1.2\pi$. As a perturbed configuration, one of the two cylinders was assumed to be nonlinear, with $\xi = 0.2$. Figure 8 gives the BSW values computed for this configuration at various steps. The linear values (numerically computed) are also given for comparison.

4 DISCUSSION AND CONCLUSIONS

In this paper, the perturbational UMoM has been applied to develop an iterative approach to the numerical computation of the electromagnetic scattering by dielectric cylinders of arbitrary shapes, coated with layers made of weakly nonlinear materials (of the Kerr type). Some test cases have been described, including multilayer circular cylinders coated or filled with nonlinear dielectrics, under TM illumination conditions. A comparison with data obtained by the iterative DWBA has been made.

The approach converged very fast as long as the nonlinearity was weak, corresponding to a slightly perturbed configuration. For example, in the example shown in Figure 7, the approach did not converge for $\xi = 2.0$. But this nonlinearity seems too high for the considered simplified electromagnetic model of the nonlinear process (neglecting the harmonics generation) to be realistic [14].

Future work will be devoted to applying the proposed iterative approach to perturbed geometries for which the nonlinearities, although weak, are such that the harmonics generation cannot be neglected. As shown in [14], each field component can then be expressed in integral form by coupling coefficients that take into account the harmonics mixing. From a perturbation point of view, the nonlinear field provided by the UMoM could be used to start an iterative process by which the higher-order harmonics (initially, the third-order harmonic, if a Kerr-like nonlinearity is assumed to be under monochromatic illumination) are first computed in terms of the field of the fundamental frequency, and the effects of the higher-order harmonics on the effective dielectric permittivity are then recursively evaluated. Convergence will of course remain an issue.

The approach has so far been applied only to dielectric infinite cylinders under TM illumination. For these configurations, the Richmond formulation is quite effective. Extensions to the TE-wave case and to the three-dimensional

case are conceptually feasible, even though more accurate testing and weighting functions should be used for the MoM implementation.

The UMoM considered here is not restricted to dielectric configurations (the test case described in [2] actually concerns perfectly conducting scatterers). Therefore, the approach could in principle be applied to conductive objects coated with nonlinear materials. To this end, MoM solutions suitable for heterogeneous structures made of dielectric and conductive materials should be used.

5 REFERENCES

- [1] R. F. Harrington, *Field Computation by Moment Method*, New York: McMillan, 1968.
- [2] E. Yip and B. Tomas, "Obtaining scattering solutions for perturbed geometries and materials from moment method solutions," *ACES Journal*, pp. 95-118, fall 1988.
- [3] E. H. Newman, "An overview of the hybrid MM/Green's function method in electromagnetics," *Proc. IEEE*, March 1988.
- [4] N. D. Bloembergen, *Nonlinear Optics*, New York: Plenum Press, 1960.
- [5] S. Caorsi, A. Massa, and M. Pastorino, "Bistatic scattering width evaluation for nonlinear isotropic infinite circular cylinders," *Microwave and Optical Technology Lett.*, vol. 7, no. 4, pp. 639-642, 1994.
- [6] L. D. Landau, E. M. Lifshits, and L. P. Pitaevskii, *Electrodynamics of Continuous Media*, Oxford: Pergamon Press, 1984.
- [7] M. Miyagi and S. Nishida, "Guided waves in nonlinear medium (II). Dielectric boundaries," *Sci. Rep. Res. Inst. Tohoku Univ. B*, vol. 24, pp. 53-67, 1972.
- [8] J. A. Stratton, *Electromagnetic Theory*, New York: McGraw Hill, 1941.
- [9] J. H. Richmond, "Scattering by a dielectric cylinder of arbitrary cross-section shape," *IEEE Trans. on Antennas Propagat.*, vol. 13, pp. 334-341, 1965.
- [10] A. Jennings, *Matrix Computation for Engineers and Scientists*, New York: Wiley, 1977.
- [11] C. A. Balanis, *Advanced Engineering Electromagnetics*, New York: John Wiley & Sons, 1989.
- [12] H. E Bussey and J. H. Richmond, "Scattering by a lossy dielectric circular cylindrical multilayer, numerical values," *IEEE Trans. on Antennas Propagat.*, vol. AP-23, pp. 723-725, Sept. 1975.
- [13] S. Caorsi and M. Pastorino, "Correction to 'Scattering by a lossy dielectric circular cylindrical multilayer, numerical values,'" *IEEE Trans. on Antennas Propagat.*, in press.
- [14] S. Caorsi, A. Massa, and M. Pastorino, "A numerical solution to full-vector EM scattering by three-dimensional nonlinear bounded dielectrics," *IEEE Trans. Microwave Theory Tech.*, vol. MTT-43, Feb. 1995.

EM Simulation of Packaged MMIC and Microstrip Antennas Using “Microwave Explorer”

Ali Sadigh, Krishnamoorthy Kottapalli, Peter Petre

Compact Software, Inc.
201 McLean Blvd.
Paterson, NJ 07504
Tel: (201) 881 1200 FAX: (201) 881 8361

ABSTRACT. A moment method solution is presented for the full-wave electromagnetics analysis of multi-layered planar structures of arbitrary shape. The mathematical formulation is based on the spectral domain integral equation and the Galerkin's testing procedure. The method is applied to shielded MMIC as well as radiating systems in the open environment. The inclusion of vertical current elements in the solution enables the method to analyze structures with vias and air bridges in both packaged and open environments. Since a periodic structure approach is used in the formulation, extension to the analysis of infinite and finite antenna arrays becomes rather straightforward. Simulated results, obtained from our electromagnetic simulator “Microwave Explorer,” are presented and compared with the available data to demonstrate the versatility and the accuracy of the method. The numerical results presented include S-parameters and far field data.

I Introduction

The integral equation formulation in spectral domain has become the preferred technique for the analysis and simulation of components and discontinuities in microwave and millimeter-wave circuits and radiating systems [1]. This method is the most rigorous and efficient to perform a full-wave analysis of 3-D planar circuits. A typical 3-D planar structure is shown in Fig. 1.

We have developed an efficient and accurate numerical implementation for the analysis of passive microwave circuits and antennas based on an extension of the previous work reported in [2]. The periodic structure approach is utilized to perform efficient analysis of packaged MMIC's and interconnects. This approach has been modified and applied to structures in open environment. The modifications are such that the numerical efficiency in open environment analysis is retained, while the solution represents the results of an isolated unit cell

analysis in the absence of the side walls and the top cover plate. Linear phased arrays can be easily analyzed by making use of a transformation on spectral variables.

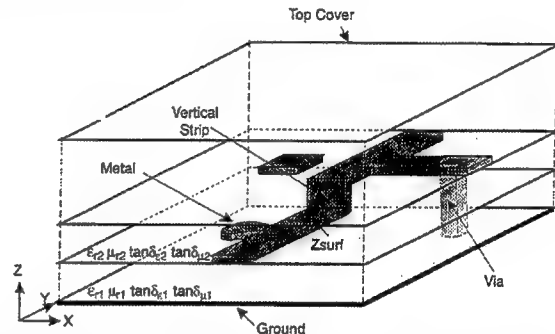


Fig. 1: A typical multi-layered 3-D structure backed by a ground plane.

The article consists of an overview of the formulation in the next section and then the simulated results. Presented simulations are intended to demonstrate sample practical problems which can be analyzed in Microwave Explorer.

II Theory

In this section, an overview of the formulation and the numerical solution which is used in Microwave Explorer is presented. Figure 1 shows a multi-layer structure in a package. The structure can consist of an arbitrary number of homogeneous dielectric layers with different parameters. Metalized traces can run in between layers or from one layer to another through vias or vertical strips. Depending on whether the circuit to be analyzed is a packaged MMIC or a radiating system such as a patch antenna, there could be conducting walls on the top, bottom, and the sides.

The dyadic spectral Green's function for a stratified medium of infinite extent is derived by using

a versatile approach in which a transmission line analogy is employed for each layer [3]-[4]. In this method, fields are decomposed into TE and TM components and the parameters of the transmission line model for each layer take on different values for each mode. This method offers versatility in computation of the Green's function of structures with arbitrary number of layers. The dielectric and magnetic losses of each layer are also included in the Green's function. This is done automatically through the lossy characteristic impedances for the transmission lines corresponding to each layer and for each TE and TM component.

The expressions for a multi-layered structure Green's function are too lengthy to include in this article. However, as an example, we assume a dielectric layer backed by a ground plane and present some of the details regarding the spectral Green's function. Assuming that there are only transverse currents present in the problem, the dyadic Green's function can be written as

$$\overline{\overline{G}}(k_x, k_y, h) = \begin{bmatrix} \hat{x}\hat{x} G_{xx}(k_x, k_y, h) & \hat{x}\hat{y} G_{xy}(k_x, k_y, h) \\ \hat{y}\hat{x} G_{yx}(k_x, k_y, h) & \hat{y}\hat{y} G_{yy}(k_x, k_y, h) \end{bmatrix} \quad (1)$$

where

$$G_{xx} = -\left(\frac{k_x^2}{k_p^2} Q_{TM} + \frac{k_y^2}{k_p^2} Q_{TE}\right) \quad (2)$$

$$G_{xy} = G_{yx} = -\frac{k_x k_y}{k_p^2} (Q_{TM} - Q_{TE}) \quad (3)$$

$$G_{yy} = -\left(\frac{k_y^2}{k_p^2} Q_{TM} + \frac{k_x^2}{k_p^2} Q_{TE}\right) \quad (4)$$

Here $k_p^2 = k_x^2 + k_y^2$ and k_x and k_y are the spectral variables. Q_{TM} and Q_{TE} are the equivalent TM and TE impedances seen at the dielectric junction looking into the two transmission lines representing the free space and the dielectric layer. The characteristic (wave) impedances for each region is given by

$$Z_{TM} = \frac{\eta_0 k_z}{\epsilon_r k_0} \quad (5)$$

$$Z_{TE} = \frac{\mu_r \eta_0 k_0}{k_z} \quad (6)$$

where k_0 and η_0 are the free space wave number and impedance, respectively. ϵ_r and μ_r represent the relative permittivity and the permeability of the free

space or the material layer. While complex ϵ_r and μ_r account for material losses, an imperfect conducting ground plane affects the input impedance looking into the transmission line which represents the dielectric layer.

The electric field integral equation (EFIE) formulation of the problem is given by

$$\hat{n} \times [\overline{E}^s(x, y, z) - Z_s \bar{J}(x, y, z)] = -\hat{n} \times \overline{E}^i(x, y, z) \quad (7)$$

where \hat{n} is the normal vector to the metalized surfaces, \overline{E}^i is the incident field, Z_s is the surface impedance, and \bar{J} is the surface current density which can have transverse \bar{J}_t and vertical J_z components. The electric field due to the surface current \overline{E}^s is given by the integral

$$\overline{E}^s = \iiint \overline{\overline{G}}(x, y, z, x', y', z') \cdot \bar{J}(x', y', z') dx' dy' dz' \quad (8)$$

where $\overline{\overline{G}}$ is the dyadic Green's function for a general multi-layer structure.

Note that metalization losses are accounted for in Eq. (7). If a perfect or lossy conductor top or bottom plate or both are present, the Green's function will satisfy those boundary conditions. For packaged microwave circuits, where the circuit is enclosed in a rectangular box, the boundary conditions on the side walls are satisfied by employing a periodic structure approach.

The method of moments is utilized to solve Eq. (7) for the unknown surface electric current \bar{J} . The electric current in transverse direction is approximated by rooftop basis functions in the x and y directions [5]. For vertical current elements of vias and air bridges, attachment mode basis functions are employed to guarantee the continuity of the current at the junctions [2]. Applying the Galerkin's method and testing the sides of Eq. (7) results in a linear system of equations which in matrix notation is given by

$$\begin{bmatrix} \mathbf{Z}_{tt} & \mathbf{Z}_{tz} \\ \mathbf{Z}_{zt} & \mathbf{Z}_{zz} \end{bmatrix} \begin{bmatrix} \mathbf{I}_t \\ \mathbf{I}_z \end{bmatrix} = \begin{bmatrix} \mathbf{V}_t \\ \mathbf{V}_z \end{bmatrix} \quad (9)$$

In this equation the right hand side is the excitation vector defined by port voltages and the vector on the left is the unknown current coefficients. The moment impedance matrix \mathbf{Z} contains the interaction of the basis functions and is symmetric. A fast Fourier transform (FFT) algorithm is used in computing the elements of the moment matrix. This has resulted in a significant improvement in matrix fill time.

After solving Eq. (9) and obtaining the current distribution, S-parameter data is extracted by utilizing an accurate deembedding procedure which is detailed in [2]. In open environment analyses, the radiated power and far field data are computed through the use of equivalent magnetic currents on a fictitious surface above the structure [7]. Assuming that this fictitious surface is located at $z = h_0$, one can show that the far fields are related to the Fourier transform of the transverse components of the electric field by

$$E_\theta = \cos \phi \tilde{E}_x(k_x, k_y, h_0) + \sin \phi \tilde{E}_y(k_x, k_y, h_0) \quad (10)$$

$$E_\phi = -\cos \theta \times [\sin \phi \tilde{E}_x(k_x, k_y, h_0) - \cos \phi \tilde{E}_y(k_x, k_y, h_0)] \quad (11)$$

where $\tilde{\cdot}$ represents the two-dimensional Fourier transform.

An issue of prime importance in computing the moment matrix elements is the proper treatment of the poles of the spectral Green's function [6]. In the implementation of Microwave Explorer, these poles are extracted and accounted for through analytical integration in two-dimensional spectral space. The numerical results have remarkable accuracy and stability due to proper treatment of the Green's function poles.

III Simulation Results

In this section we will present simulated results for structures in packaged (MMIC) and open environments (antennas). These examples are intended to portray versatility and accuracy of Microwave Explorer. The first two circuits are analyzed using the packaged environment Green's function, i.e. inside a metallic enclosure.

Coplanar Waveguide Filter

The first circuit we shall consider is a coplanar waveguide (CPW) band reject filter as shown in Fig. 2. This filter was designed to have no transmission at 18 GHz and good transmission at 36 GHz. Air-bridges are used to equalize the potential of the two ground planes in order to eliminate the coupled slotline mode. At $f = 18$ GHz the stubs present short circuits, thereby allowing no transmission at this frequency. The stubs present open circuits at 36 GHz, thereby allowing good transmission.

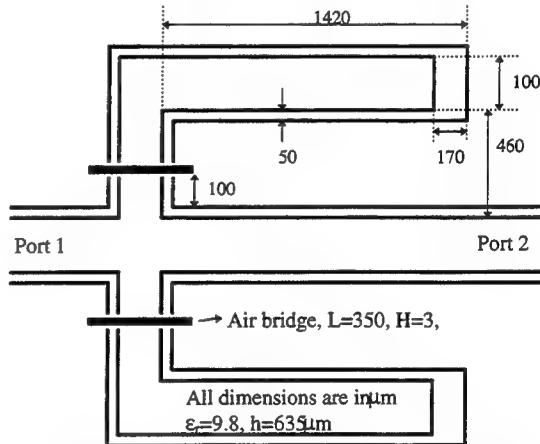


Fig. 2: The coplanar waveguide band reject filter.

Fig. 3 shows the comparison between the modeled and measured S_{11} of the CPW filter from 10-40 GHz. The results show an excellent agreement with the measured results [8]. This circuit validates the approach used to model coplanar waveguide circuits in a packaged environment. In addition, it also shows the ability of Microwave Explorer to deembed coplanar port discontinuities.

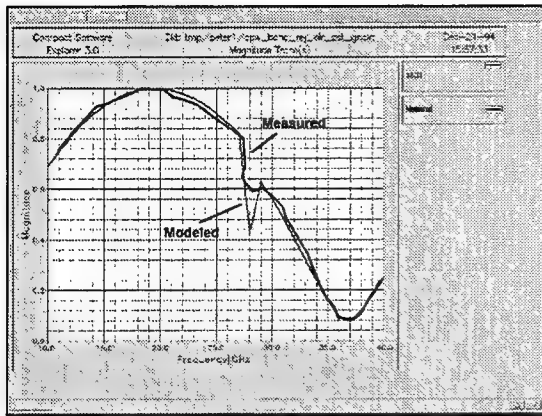


Fig. 3: Magnitude of S_{11} of the filter shown in Fig. 2.

Bandpass Filter

Figure 4 shows the layout of a bandpass filter, which is taken from the MIC Simulation Column [9]. The circuit is built on a GaAs substrate of thickness $125 \mu\text{m}$ and dielectric constant of 12.9. The dielectric loss tangent of the substrate is 0.0005. The metal has a thickness of $4 \mu\text{m}$ and conductivity of $4.9 \times 10^7 \text{ Sm}$. The circuit has via pads of dimension $175 \times 175 \mu\text{m}$ with the via holes extending to the ground plane. All the physical dimensions of the filter are shown in the figure. The circuit has two ports which are terminated with 50Ω loads.

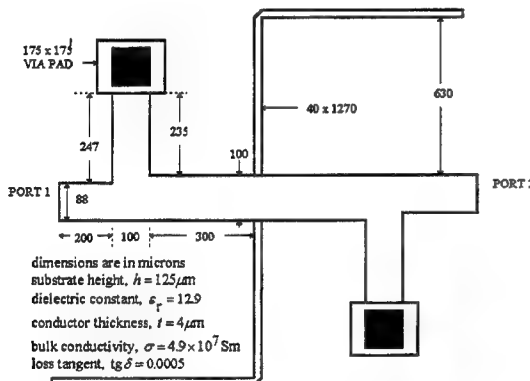


Fig. 4: The bandpass filter and its dimensions

The reflection coefficient and the transmission of the filter are plotted in Fig. 5 from 10 to 20 GHz. The response of the filter agrees well with the results of other electromagnetic simulators as reported in [10]. This circuit demonstrates the capability of Microwave Explorer to model the metal and dielectric losses accurately.

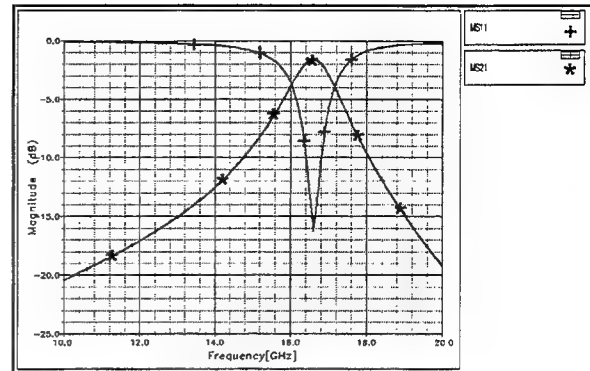


Fig. 5: Magnitude of S_{11} and S_{21} of filter shown in Fig. 4.

Patch Antenna

The rectangular microstrip patch antennas are among the most popular printed circuit antennas. In this example we consider an edge fed patch antenna whose dimensions are shown in Fig. 6. The substrate is a dielectric with $\epsilon_r = 2.213$ and thickness of 0.794mm. Fig. 7 shows the reflection coefficient (S_{11}) of this antenna between 5 and 20 GHz. It is observed that a good match is obtained at about 7.6 GHz due to the shorter edge being resonant. Also shown in Fig. 7 is the measured results as reported in [7]. The two results agree very well.

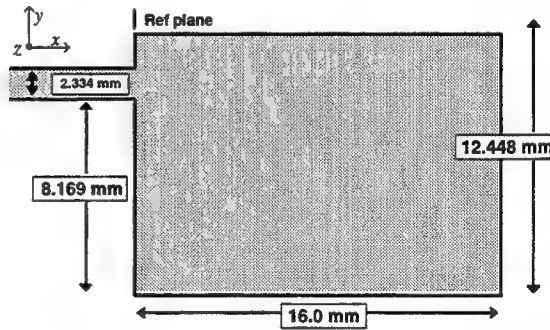


Fig. 6: Dimensions of edge-fed rectangular patch antenna

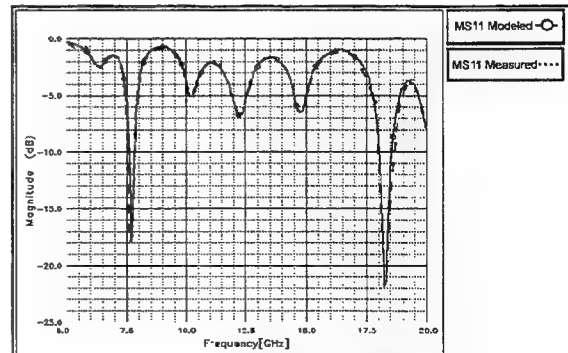


Fig. 7: Magnitude of the reflection coefficient (S_{11}) of the rectangular patch antenna of Figure 6.

The far field generated by this antenna is demonstrated in Figs. 8-a and 8-b. Note that the ripple in cross polarization in Fig. 8-a is due to the long feed line (115.6mm) used in the simulation. In fact Microwave Explorer does not need long feed lines to excite circuits. The accurate deembedding algorithm which is used in Microwave Explorer obviates the need for long feed lines. Marks (\times and $+$) in Fig. 8 represent the measured data obtained from Fig. 4 of [7]. The agreement is very good. Note that in [7] the elements of the moment matrix are evaluated through direct integration. Microwave Explorer uses FFT to obtain these interactions which leads to a superior speed performance.

Figs. 8-a, 8-b: Radiation pattern of the antenna of Fig. 6 at 7.6GHz on a dB scale. Marks (\times and $+$) represent the measured data [7]

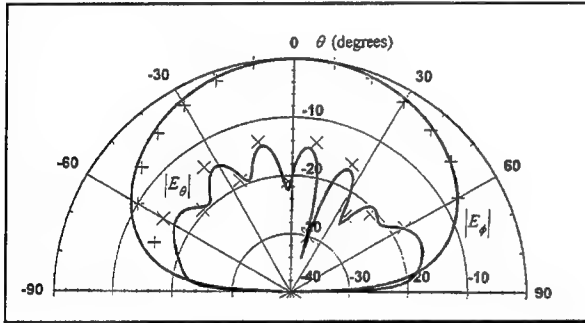


Figure 8-a. $\phi = 0^\circ$ cut

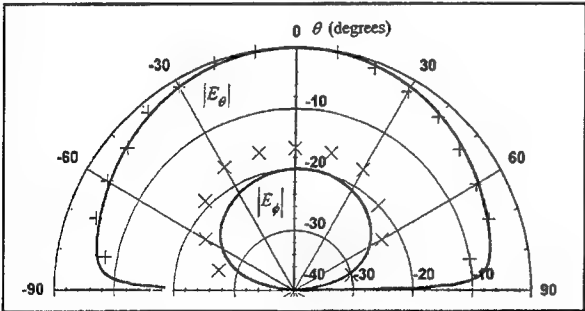


Figure 8-b. $\phi = 90^\circ$ cut

Four-Element Linear Array

The second example of open environment simulation is a four-element linear patch antenna array. It is made up of square patches all fed at their edges as shown in Fig. 9. The substrate which is backed by a ground plane has a thickness of 60 mils and is made of CuClad 250, with $\epsilon_r = 2.45 \pm 0.04$.

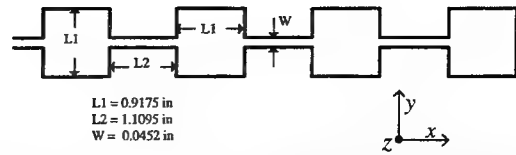


Figure 9. The four element linear patch antenna array

Antenna arrays are among problems that are considered very large and the computational cost of their simulation is usually very high. For this reason usually only one element of an array is analyzed and interactions between elements are either neglected or approximated for, e.g. [11]. In this example we analyze the entire circuit and therefore all the element interaction are automatically included in the solution.

The center frequency of the array is found to be at 3.915GHz as shown in Fig. 10. The computed far field data in E-plane ($\phi = 0^\circ$) at the frequency of resonance is shown in Fig. 11. Note that there is a large difference between the relative amplitudes of E_θ (solid line) and E_ϕ (broken line). During the simulation it was found that around the resonance frequency the radiation pattern was fairly insensitive to the changes in frequency. Microwave Explorer predicted a gain of almost 13dB for the array. The data presented in Figs. 10 and 11 agree very well with the measured and simulated results of Figs. 8 and 7 of [11].

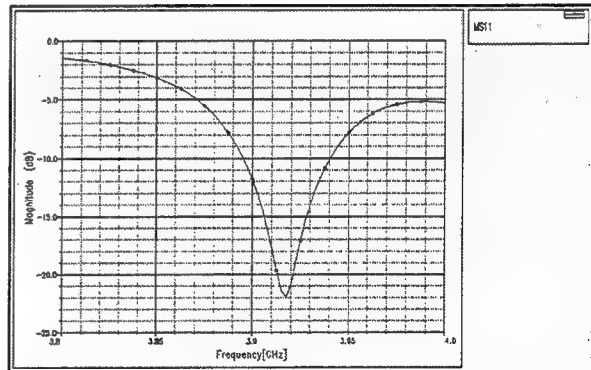


Fig. 10: Magnitude of the reflection coefficient (S_{11}) of the antenna array of Fig. 9.

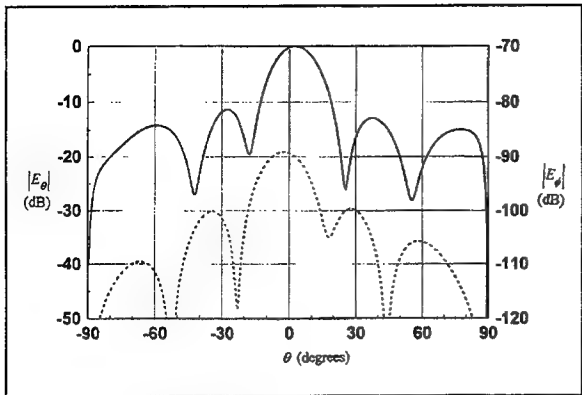


Fig. 11: Far field pattern in the E -plane ($\phi = 0^\circ$) of the antenna array of Fig. 9 at 3.915 GHz. Solid line represents the E_θ data and broken line the E_ϕ .

Two-Port Asymmetric Antenna

The structure for this two-layer problem is shown in Fig. 12. It consists of two orthogonal crossed dipoles which are electromagnetically coupled to two orthogonal microstrip lines. The length of the two dipoles are different and as a result a dual frequency operating mode is obtained. The feed lines are connected to 50 Ohm terminations.

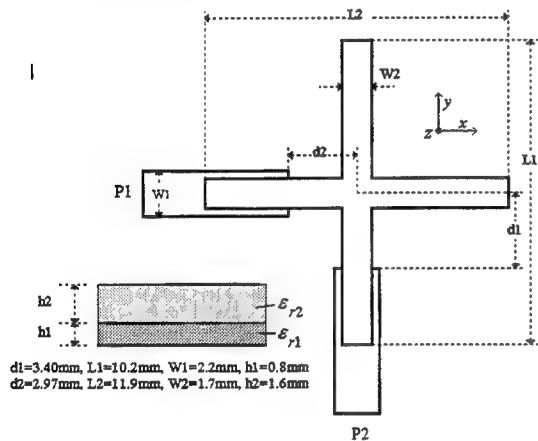


Figure 12. Dimensions of the 2-port asymmetric antenna

Fig. 13 shows the reflection coefficient of the ports (S_{11} and S_{22}) and the transmission between them (S_{12}) on a logarithmic scale. This data is in excellent agreement with the results shown in [12]. The resonant frequencies of the long dipole at 8.45 GHz and the short dipole at 9.55 GHz are within 0.5% of the values observed in [12]. As it is observed in the Figure, the incident power is largely radiated at the resonance frequencies of the dipoles and transmitted from one port to the other at 11.35 GHz.

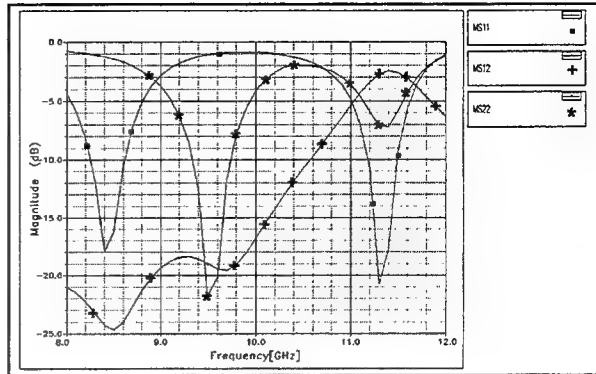
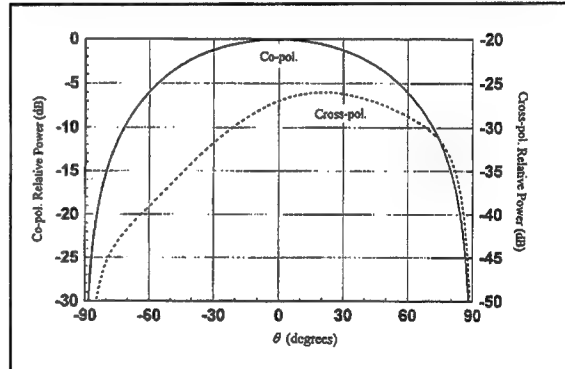


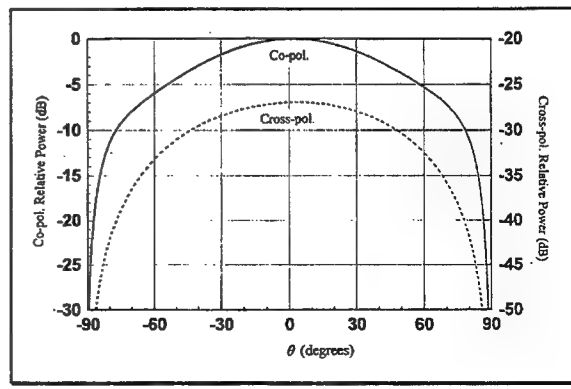
Fig. 13: Magnitude of the S-parameters of the antenna shown in Fig. 12.

The radiation pattern graphs for this structure at 8.45 GHz are presented in Figure 14. Here the first port is excited while the second one is terminated to a 50 Ohm load. Note that due to a good isolation between the ports at this frequency, the cross polarization level is low. This data also agrees favorably with the measured and calculated results in [12].

Fig. 14-a, 14-b: Radiation patterns at 8.45GHz for co-(solid line) and cross-polarization (broken line).



14-a) H -plane ($\phi = 90^\circ$)



14-b) E -plane ($\phi = 0^\circ$)

IV Conclusions

The article briefly addressed the underlying theory used in the development of Compact Software's full-wave EM simulator "Microwave Explorer." The use of FFT and other numerical techniques has resulted in a significant speed enhancement in the package. Simulated results for sample microwave and antenna structures were presented which demonstrate the versatility of the numerical techniques utilized in Microwave Explorer. The accuracy of the open structure analysis and the far field calculations, which have been recently added to the simulator, were verified against the measured or other available data.

Microwave Explorer belongs to a class of simulators which are referred to as 3-D planar. It is thus optimized to only handle structures which are planar in nature with homogenous dielectric layers.

References

- [1] T. Itoh, "Numerical Techniques for Microwave and Millimeter Wave Passive Structures," New York: Wiley, 1989.
- [2] A. Hill, J. Burke, and K. Kottapalli, "Three Dimensional Electromagnetic Analysis of Shielded Microstrip Circuits," International Journal of Microwave and Millimeter-Wave Computer-Aided Engineering, Vol. 2, No. 4, 1992, pp. 286-296.
- [3] T. Itoh, "Spectral Domain Imittance Approach for Dispersion Characteristics of Generalized Printed Transmission Lines," IEEE Transactions on Microwave Theory and Techniques, Vol. MTT-28, No. 7, July 1980, pp. 733-736.
- [4] S.G. Pan, and I. Wolff, "Scalarization of Dyadic Spectral Green's Functions and Network Formalism for Three-Dimensional Full-Wave Analysis of Planar Lines and Antennas," IEEE Transactions on Microwave Theory and Techniques, Vol. 42, No. 11, Nov. 1994, pp. 2118-2127.
- [5] R.W. Jackson, "Full-Wave, Finite Element Analysis of Irregular Microstrip Discontinuities," IEEE Transactions on Microwave Theory and Techniques, Vol. 37, No. 1, pp. 81-89.
- [6] F.J. Demuynck, G.A.E. Vanderbosch, and A.R. Van de Capelle, "Analytical Treatment of the Green's Function Singularities in a Stratified Dielectric Medium," Proceedings of the European Microwave Conference 1993, Madrid, Spain, September 1993, pp. 1000-1001.
- [7] S.C. Wu, N.G. Alexopoulos, and O. Fordham, "Feeding Structure Contribution to Radiation by Patch Antennas with Rectangular Boundaries," IEEE Transactions on Antennas and Propagation, Vol. 40, No. 10, October 1992, pp. 1245-1249.
- [8] Amjad. A. Omar, Y. Leonard Chow, "A solution of Coplanar Waveguide with Air-Bridges using Complex Images", IEEE Transactions on Microwave Theory and Techniques, Vol. 40, No. 11, Nov. 1992, pp. 2070-2077.
- [9] MIC Simulation Column, International Journal of Microwave and Millimeter-Wave Computer-Aided Engineering, Vol. 4, No. 2, April 1994, pp. 203-212.
- [10] MIC Simulation Column, International Journal of Microwave and Millimeter-Wave Computer-Aided Engineering, Vol. 4, No. 4, October 1994, pp. 411-431.
- [11] H.Y.D. Yang, C.H. Chen, J.A. Castaneda, and W.C. Wong, "Design of Microstrip Line-Fed Patch Arrays Including Mutual Coupling," International Journal of Microwave and Millimeter-Wave Computer-Aided Engineering, Vol. 4, No. 1, 1994, pp. 31-42.
- [12] R. Gillard, J.H. Corre, M. Drissi, and J. Citerne, "A General Treatment of Matched Terminations Using Integral Equation Modeling and Applications," IEEE Transactions on Microwave Theory and Techniques, Vol. 42, No. 12, Dec. 1994, pp. 2545-2553.

1995 INSTITUTIONAL MEMBERS

| | | |
|---|---|---|
| THE AEROSPACE CORPORATION PO Box 92957 Los Angeles, CA 90009-2957 | ANDREW CANADA INC. 606 Beach Street Whitby, ONT, CANADA L1N 5S2 | ANDREW CORPORATION 10500 W 153rd Street Orland Park, IL 60462 |
| ARC, INC 8201 Corporate Dr. Ste 3550 Landover, MD 20785 | ASELSAN INC. PO Box 101 Yenimahalle Ankara, TURKEY, 06172 | ATEA Raleigh Rd, Private Bag 12 Ascot Vale, VIC, AUSTRALIA 3032 |
| ATOMIC WEAPONS ESTAB UK Building E3, Awe Aldermaston Reading, BERKSHIRE, UK RG7 4PR | BNR London Rd. Harlow, ESSEX, UK CM17 9NA | BRITISH AEROSPACE Wharton Aerodrome Preston, LANC. UK PR4 1AX |
| BRITISH AEROSPACE FPC 267 PO Box 5 Filton, BRISTOL, UK BS12 7QW | BRITISH BROADCASTING CO. Kingswood Warren Teddington, SURREY, UK KT20 6NP | BRITISH LIBRARY Boston SPA Wetherby, W YORKS, UK LS23 7BQ |
| CAMBRIDGE CONSULTANTS LTD Milton Road/Science Park Cambridge, CAMBS, UK CB5 4DW | CHALMERS UNIV OF TECHNOLOGY Dept. of Microwave Technology Gothenburg, SWEDEN S 412 96 | CSC PROFESSIONAL SERVICES 8201 Corporate Dr. #350 Landover, MD 20785 |
| CSELT-RADIO Via Guglielmo Reiss Romoli 274 Turin, ITALY 10148 | CSIRO, CENTER FOR ADV TECH PO Box 883 Kenmore, QLD, AUSTRALIA 4069 | CULHAM LAB UK Atomic Energy Auth. Abingdon, OXFORD, UK OX14 3D8 |
| D L R OBERPAFFENHOFEN Zentralbibliothek Wessling, OBB, GERMANY 8031 | D S T O SALISBURY LIBRARY Box 1500 Salisbury, SA, AUSTRALIA 5108 | DEFENCE TECH & PROCUREMENT Nemp Lab - AC Zentrum Spiez, SWITZERLAND CH 3700 |
| DEFENSE RESEARCH ESTAB. 3701 Carling Ave. Ottawa, ON, CANADA K1A 0Z2 | DYNETICS, INCORPORATED PO Drawer B Huntsville, AL 35814-5050 | ERICSSON RADAR ELEC/ANT SYS. Bergfotsgatan 2 Molndal, SWEDEN S-43184 |
| FANFIELD LTD. Braxted Park Witham, ESSEX, UK CM8 3XB | FELDBERG LIBRARY Dartmouth College Hanover, NH 03755 | FGAN/FHP Neuenahrer Strasse 20 Wachtberg GERMANY 53343 |
| FOKKER AIRCRAFT B.V. PO Box 7600 Schiphol, NETHERLANDS 1117 ZJ | GEC MARCONI RESEARCH CENTER W. Hanningfield Road Gt. Baddow, Chelmsford, UK | GRINAKER AVTRONICS PO Box 8492 Hennopsmeir, S. AFRICA 0046 |
| HARRIS CORPORATION 1680 University Avenue Rochester, NY 14610-9983 | HKUST LIBRARY Clear Water Bay Road Kowloon, HONG KONG | HOKKAIDO DAIGAKU Nishi 8, Kita 13 Sapporo, JAPAN 060 |
| HUGHES RESEARCH LIBRARY 3011 Malibu Canyon Road Malibu, CA 90255-4797 | HUNTING ENGINEERING LTD Redding Wood, Ampthill, Bedford, UK MK45 2HD | IABG Einsteinstrasse 20 Ottobrunn, GERMANY D-85521 |
| IMAGINEERING LIMITED 95 Barber Greene Rd, Suite 112 Toronto, ON, CANADA | IMPERIAL COLLEGE Exhibition Road London, UK SW7 2BX | IPS RADIO & SPACE LIBRARY PO Box 5606 W. Chatswood, AUSTRALIA 2057 |
| KATHREIN-WERKE KG Postbox 100 444 Rosenheim 2, GERMANY D-8200 | KERSHNER, WRIGHT & HAGAMAN 5730 Gen. Washington Dr. Alexandria, VA 22312 | LINDA HALL LIBRARY 5109 Cherry Street Kansas City, MO 64110 |
| MATRA DEFENSE 37 Av. Louis Breguet BP1 Velizy, Cedex, FRANCE 78146 | MISSISSIPPI STATE UNIV LIBRARY PO Box 5408 Mississippi State, MS 39762 | MITRE CORPORATION LIBRARY 202 Burlington Road Bedford, MA 01730 |

1995 INSTITUTIONAL MEMBERS (Continued)

| | | |
|---|---|---|
| MONASH UNIVERSITY 900 Dandenong Road, Caulfield East Melbourne, VIC, AUSTRALIA 3145 | MOTOROLA INCORPORATED 1301 E Algonquin Road Schamburg, IL 60196 | MPB TECHNOLOGIES INC. 151 Hymus Blvd. Pointe-Claire, CANADA H9R 1E9 |
| NIKSAR 34/35 Gilbey Road Mt. Waverly, VIC, AUSTRALIA 3149 | PARAGON TECHNOLOGY, INC. 200 Innovation Blvd. Suite 240 State College, PA 16803 | PENNSYLVANIA STATE UNIV. Pattee Library University Park, PA 16802 |
| QUEEN MARY & WESTFLD COLLEGE Mile End Road London, UK E1 4NS | RADIO FREQUENCY SYSTEMS 12 Waddikee Road Lonsdale, SA, AUSTRALIA 5160 | RADIO FREQUENCY SYSTEMS 36 Garden Street Kilsyth, Vic, AUSTRALIA 3137 |
| RAND AFRIKAANS UNIV/ENERGY LAB PO Box 524 Aucklandpark Johannesburg, S. AFRICA 2006 | RESEARCH INSTITUTE OF IND. SCI. HANYANG UNIV/17 Haengdang-Dong Sungdong-ku, Seoul, S, KOREA 133-791 | ROCKWELL/COLLINS AVIONICS 350 Collins Road, NE Cedar Rapids, IA 52498 |
| SAAB-SCANIA AB Saab Military Aircraft Linkoping, SWEDEN S-58188 | SERCOS SERVICES Cheeseman's Lane Hambrook, W. SUSSEX, UK | SOUTHWEST RES. INSTITUTE PO Drawer 28510 San Antonio, TX 78228-0510 |
| SPEARS ASSOCIATES INC. 249 Vanderbilt Avenue Norwood, MA 02062-5033 | STG NATIONAL LUCHT-EM Ruimtevaart Lab. A Fokkerweg 2 Amsterdam, NETHERLANDS 1059 | SYMBIONICS NETWORK LTD. St. John's Innovation Pk. Cowle Rd. Cambridge, UK CB4 4WS |
| SYRACUSE RESEARCH CORP. Merrill Lane Syracuse, NY 13210-4080 | TASC LIBRARY 55 Walkers Brook Drive Reading, MA 01887 | TECHNICAL RESEARCH CENTRE Vit/Info Tech/PO Box 1202 Espoo, FINLAND 02044 |
| TECHNION PO Box 830701 Birmingham, AL 35283 | TECHNISCHE UNIV DELFT Elektrotech 200 Bibl/Mekelweg 4 Delft, HOLLAND, NETHERLANDS 2628 CD | TELEBRAS - CPQD Caixa Postal 1579 Predio 32 Campinas, SP, BRASIL 13088-061 |
| TELECOM AUSTRALIA Private Bag 37/770 Blackburn Road Clayton, VIC, AUSTRALIA 3168 | TELENOR MOBILE PO Box 6746 St. Olaus Plass Oslo, NORWAY N-0130 | UNIV. OF CENTRAL FLORIDA LIB. PO Box 162440 Orlando, FL 32816-2440 |
| UNIV OF MISSOURI-ROLLA Library Periodicals Rolla, MO 65401 | UNIVERSITY OF SURREY Centre for Satellite Research Guildford, SURREY, UK GU2 5XH | UNIV. AUTONOMA DE CHIHUAHUA Ciudad Universitaria Chihuahua-Chih, MEXICO 31170 |
| UNIVERSITAT DER BUNDESWEHR Werner Heisenberg Weg 39 Neubiberg, GERMANY W-8014 | US COAST GUARD ACADEMY 15 Mohegan Avenue New London, CT 06320-4195 | VISTA RESEARCH INC. 100 View St, #202, Box 998 Mountain View, CA 94042 |
| WATKINS-JOHNSON CO. LIBRARY 700 Quince Orchard Road Gaithersburg, MD | YORK ELECTRONICS CENTRE University of York Heslington, YORK, UK YO1 5DD | |

ACES COPYRIGHT FORM

This form is intended for original, previously unpublished manuscripts submitted to ACES periodicals and conference publications. The signed form, appropriately completed, MUST ACCOMPANY any paper in order to be published by ACES. PLEASE READ REVERSE SIDE OF THIS FORM FOR FURTHER DETAILS.

TITLE OF PAPER:

RETURN FORM TO:

Dr. Richard W. Adler
Naval Postgraduate School
Code EC/AB
Monterey, CA 93943

AUTHORS(S)

PUBLICATION TITLE/DATE:

PART A - COPYRIGHT TRANSFER FORM

(NOTE: Company or other forms may not be substituted for this form. U.S. Government employees whose work is not subject to copyright may so certify by signing Part B below. Authors whose work is subject to Crown Copyright may sign Part C overleaf).

The undersigned, desiring to publish the above paper in a publication of ACES, hereby transfer their copyrights in the above paper to The Applied Computational Electromagnetics Society (ACES). The undersigned hereby represents and warrants that the paper is original and that he/she is the author of the paper or otherwise has the power and authority to make and execute this assignment.

Returned Rights: In return for these rights, ACES hereby grants to the above authors, and the employers for whom the work was performed, royalty-free permission to:

1. Retain all proprietary rights other than copyright, such as patent rights.
2. Reuse all or portions of the above paper in other works.
3. Reproduce, or have reproduced, the above paper for the author's personal use or for internal company use provided that (a) the source and ACES copyright are indicated, (b) the copies are not used in a way that implies ACES endorsement of a product or service of an employer, and (c) the copies per se are not offered for sale.
4. Make limited distribution of all or portions of the above paper prior to publication.
5. In the case of work performed under U.S. Government contract, ACES grants the U.S. Government royalty-free permission to reproduce all or portions of the above paper, and to authorize others to do so, for U.S. Government purposes only.

ACES Obligations: In exercising its rights under copyright, ACES will make all reasonable efforts to act in the interests of the authors and employers as well as in its own interest. In particular, ACES REQUIRES that:

1. The consent of the first-named author be sought as a condition in granting re-publication permission to others.
2. The consent of the undersigned employer be obtained as a condition in granting permission to others to reuse all or portions of the paper for promotion or marketing purposes.

In the event the above paper is not accepted and published by ACES or is withdrawn by the author(s) before acceptance by ACES, this agreement becomes null and void.

AUTHORIZED SIGNATURE

TITLE (IF NOT AUTHOR)

EMPLOYER FOR WHOM WORK WAS PERFORMED

DATE FORM SIGNED

PART B - U.S. GOVERNMENT EMPLOYEE CERTIFICATION

(NOTE: If your work was performed under Government contract but you are not a Government employee, sign transfer form above and see item 5 under Returned Rights).

This certifies that all authors of the above paper are employees of the U.S. Government and performed this work as part of their employment and that the paper is therefore not subject to U.S. copyright protection.

AUTHORIZED SIGNATURE

TITLE (IF NOT AUTHOR)

NAME OF GOVERNMENT ORGANIZATION

DATE FORM SIGNED

PART C - CROWN COPYRIGHT

(Note: ACES recognizes and will honor Crown Copyright as it does U.S. Copyright. It is understood that, in asserting Crown Copyright, ACES in no way diminishes its rights as publisher. Sign only if *ALL* authors are subject to Crown Copyright.

This certifies that all authors of the above Paper are subject to Crown Copyright. (Appropriate documentation and instructions regarding form of Crown Copyright notice may be attached).

AUTHORIZED SIGNATURE

TITLE OF SIGHNEE

NAME OF GOVERNMENT BRANCH

DATE FORM SIGNED

Information to Authors

ACES POLICY

ACES distributes its technical publications throughout the world, and it may be necessary to translate and abstract its publications, and articles contained therein, for inclusion in various compendiums and similar publications, etc. When an article is submitted for publication by ACES, acceptance of the article implies that ACES has the rights to do all of the things it normally does with such an article.

In connection with its publishing activities, it is the policy of ACES to own the copyrights in its technical publications, and to the contributions contained therein, in order to protect the interests of ACES, its authors and their employers, and at the same time to facilitate the appropriate re-use of this material by others.

The new United States copyright law requires that the transfer of copyrights in each contribution from the author to ACES be confirmed in writing. It is therefore necessary that you execute either Part A-Copyright Transfer Form or Part B-U.S. Government Employee Certification or Part C-Crown Copyright on this sheet and return it to the Managing Editor (or person who supplied this sheet) as promptly as possible.

CLEARANCE OF PAPERS

ACES must of necessity assume that materials presented at its meetings or submitted to its publications is properly available for general dissemination to the audiences these activities are organized to serve. It is the responsibility of the authors, not ACES, to determine whether disclosure of their material requires the prior consent of other parties and if so, to obtain it. Furthermore, ACES must assume that, if an author uses within his/her article previously published and/or copyrighted material that permission has been obtained for such use and that any required credit lines, copyright notices, etc. are duly noted.

AUTHOR/COMPANY RIGHTS

If you are employed and you prepared your paper as a part of your job, the rights to your paper initially rest with your employer. In that case, when you sign the copyright form, we assume you are authorized to do so by your employer and that your employer has consented to all of the terms and conditions of this form. If not, it should be signed by someone so authorized.

NOTE RE RETURNED RIGHTS: Just as ACES now requires a signed copyright transfer form in order to do "business as usual", it is the intent of this form to return rights to the author and employer so that they too may do "business as usual". If further clarification is required, please contact: The Managing Editor, R.W. Adler, Naval Postgraduate School, Code EC/AB, Monterey, CA, 93943, USA (408)656-2352.

Please note that, although authors are permitted to re-use all or portions of their ACES copyrighted material in other works, this does not include granting third party requests for reprinting, republishing, or other types of re-use.

JOINT AUTHORSHIP

For jointly authored papers, only one signature is required, but we assume all authors have been advised and have consented to the terms of this form.

U.S. GOVERNMENT EMPLOYEES

Authors who are U.S. Government employees are not required to sign the Copyright Transfer Form (Part A), but any co-authors outside the Government are.

Part B of the form is to be used instead of Part A only if all authors are U.S. Government employees and prepared the paper as part of their job.

NOTE RE GOVERNMENT CONTRACT WORK: Authors whose work was performed under a U.S. Government contract but who are not Government employees are required to sign Part A-Copyright Transfer Form. However, item 5 of the form returns reproduction rights to the U.S. Government when required, even though ACES copyright policy is in effect with respect to the reuse of material by the general public.

For information regarding ACES or to become a member in the Applied Computational Electromagnetics Society, contact Dr. Richard W. Adler, ECE Department, Code EC/AB, Naval Postgraduate School, 833 Dyer Rd, Rm. 437, Monterey, CA. 93943-5121, telephone (408) 646-1111, Fax: (408) 649-0300. E-mail: rwa@mcmill.com. You can subscribe to the Journal and become a member of ACES by completing and returning the form below.

ACES MEMBERSHIP FORM

please print

LAST NAME

FIRST NAME

MIDDLE INITIAL

COMPANY/ORGANIZATION/UNIVERSITY

DEPARTMENT/MAIL STATION

PLEASE LIST THE ADDRESS YOU WANT USED FOR PUBLICATIONS

MAILING ADDRESS

CITY

PROVINCE/STATE

COUNTRY

ZIP/POSTAL CODE

TELEPHONE

FAX

AMATEUR RADIO CALL SIGN

E-MAIL ADDRESS

E-MAIL ADDRESS CAN BE INCLUDED IN ACES DATABASE

YES

NO

PERMISSION IS GRANTED TO HAVE MY NAME PLACED ON MAILING LISTS WHICH MAY BE SOLD

YES

NO

CURRENT SUBSCRIPTION PRICES

| AREA | INDIVIDUAL SURFACE MAIL | INDIVIDUAL AIRMAIL | ORGANIZATIONAL (AIRMAIL ONLY) |
|--|----------------------------|-----------------------|----------------------------------|
| U.S. & CANADA | () \$ 65 | () \$ 65 | () \$115 |
| MEXICO, CENTRAL & SOUTH AMERICA | () \$ 68 | () \$ 70 | () \$115 |
| EUROPE, FORMER USSR TURKEY, SCANDINAVIA | () \$ 68 | () \$ 78 | () \$115 |
| ASIA, AFRICA, MIDDLE EAST & PACIFIC RIM | () \$ 68 | () \$ 85 | () \$115 |

FULL-TIME STUDENT RATE IS \$25 FOR ALL COUNTRIES

Method of payment: A bank check for the total amount is enclosed.⁽¹⁾ **PAYABLE TO "ACES"**
 Traveler's checks for the total amount are enclosed.⁽²⁾
Card Exp. date: International Money Order is enclosed.⁽³⁾
Mo. ____ Yr. ____ Charge to: MasterCard Visa. Discover Amex.⁽⁴⁾

Card No. _____ than name above, print card holder name _____

SIGNATURE REQUIRED

Non-USA participants may remit via (1) **Bank Checks**, if (a) drawn on a U.S. Bank, (b) have bank address, (c) contain series of (9) digit mandatory routing numbers; (2) **Traveler's Checks** (in U.S. \$\$); (3) **International Money Order** drawn in U.S. funds, payable in U.S.; (4) **Credit Cards**: Visa, Master Card, Discover Card, Amex.

October 1995

Total Remittance (U.S. Dollars Only) \$_____

ADVERTISING RATES

| | FEE | PRINTED SIZE |
|-----------|--------|--------------------------------|
| Full page | \$200. | 7.5" x 10.0" |
| 1/2 page | \$100. | 7.5" x 4.7" or 3.5" x 10.0" |
| 1/4 page | \$ 50 | 3.5" x 4.7" |

All ads must be camera ready copy.

Ad deadlines are same as Newsletter copy deadlines.

Place ads with Ray Perez, Newsletter Editor, Martin Marietta Astronautics,
MS 58700, PO Box 179, Denver, CO 80201, USA. The editor reserves the right to
reject ads.

ACES NEWSLETTER AND JOURNAL COPY INFORMATION

| <u>Issue</u> | <u>Copy Deadline</u> |
|--------------|----------------------|
| March | January 13 |
| July | May 25 |
| November | September 25 |

APPLIED COMPUTATIONAL ELECTROMAGNETICS SOCIETY JOURNAL

INFORMATION FOR AUTHORS

PUBLICATION CRITERIA

Each paper is required to manifest some relation to applied computational electromagnetics. Papers may address general issues in applied computational electromagnetics, or they may focus on specific applications, techniques, codes, or computational issues. While the following list is not exhaustive, each paper will generally relate to at least one of these areas:

- 1. Code validation.** This is done using internal checks or experimental, analytical or other computational data. Measured data of potential utility to code validation efforts will also be considered for publication.
- 2. Code performance analysis.** This usually involves identification of numerical accuracy or other limitations, solution convergence, numerical and physical modeling error, and parameter tradeoffs. However, it is also permissible to address issues such as ease-of-use, set-up time, run time, special outputs, or other special features.
- 3. Computational studies of basic physics.** This involves using a code, algorithm, or computational technique to simulate reality in such a way that better or new physical insight or understanding is achieved.
- 4. New computational techniques,** or new applications for existing computational techniques or codes.
- 5. "Tricks of the trade"** in selecting and applying codes and techniques.
- 6. New codes, algorithms, code enhancement, and code fixes.** This category is self-explanatory but includes significant changes to existing codes, such as applicability extensions, algorithm optimization, problem correction, limitation removal, or other performance improvement. **Note: Code (or algorithm) capability descriptions are not acceptable, unless they contain sufficient technical material to justify consideration.**
- 7. Code input/output issues.** This normally involves innovations in input (such as input geometry standardization, automatic mesh generation, or computer-aided design) or in output (whether it be tabular, graphical, statistical, Fourier-transformed, or otherwise signal-processed). Material dealing with input/output database management, output interpretation, or other input/output issues will also be considered for publication.
- 8. Computer hardware issues.** This is the category for analysis of hardware capabilities and limitations in meeting

various types of electromagnetics computational requirements. Vector and parallel computational techniques and implementation are of particular interest.

Applications of interest include, but are not limited to, antennas (and their electromagnetic environments), networks, static fields, radar cross section, shielding, radiation hazards, biological effects, electromagnetic pulse (EMP), electromagnetic interference (EMI), electromagnetic compatibility (EMC), power transmission, charge transport, dielectric and magnetic materials, microwave components, MMIC technology, remote sensing and geophysics, communications systems, fiber optics, plasmas, particle accelerators, generators and motors, electromagnetic wave propagation, non-destructive evaluation, eddy currents, and inverse scattering.

Techniques of interest include frequency-domain and time-domain techniques, integral equation and differential equation techniques, diffraction theories, physical optics, moment methods, finite differences and finite element techniques, modal expansions, perturbation methods, and hybrid methods. This list is not exhaustive.

A unique feature of the Journal is the publication of unsuccessful efforts in applied computational electromagnetics. Publication of such material provides a means to discuss problem areas in electromagnetic modeling. Material representing an unsuccessful application or negative results in computational electromagnetics will be considered for publication only if a reasonable expectation of success (and a reasonable effort) are reflected. Moreover, such material must represent a problem area of potential interest to the ACES membership.

Where possible and appropriate, authors are required to provide statements of quantitative accuracy for measured and/or computed data. This issue is discussed in "Accuracy & Publication: Requiring quantitative accuracy statements to accompany data", by E.K. Miller, *ACES Newsletter*, Vol. 9, No. 3, pp. 23-29, 1994, ISBN 1056-9170.

EDITORIAL REVIEW

In order to ensure an appropriate level of quality control, papers are refereed. They are reviewed both for technical correctness and for adherence to the listed guidelines regarding information content. Authors should submit the initial manuscript in draft form so that any suggested changes can be made before the photo-ready copy is prepared for publication.

STYLE FOR CAMERA-READY COPY

The ACES Journal is flexible, within reason, in regard to style. However, certain requirements are in effect:

1. The paper title should NOT be placed on a separate page. The title, author(s), abstract, and (space permitting) beginning of the paper itself should all be on the first page. The title, author(s), and author affiliations should be centered (center-justified) on the first page.
2. An abstract is REQUIRED. The abstract should state the computer codes, computational techniques, and applications discussed in the paper (as applicable) and should otherwise be usable by technical abstracting and indexing services.
3. Either British English or American English spellings may be used, provided that each word is spelled consistently throughout the paper.
4. Any commonly-accepted format for referencing is permitted, provided that internal consistency of format is maintained. As a guideline for authors who have no other preference, we recommend that references be given by author(s) name and year in the body of the paper (with alphabetical listing of all references at the end of the paper). Titles of Journals, monographs, and similar publications should be in boldface or italic font or should be underlined. Titles of papers or articles should be in quotation marks.
5. Internal consistency shall also be maintained for other elements of style, such as equation numbering. As a guideline for authors who have no other preference, we suggest that equation numbers be placed in parentheses at the right column margin.
6. The intent and meaning of all text must be clear. For authors who are NOT masters of the English language, the ACES Editorial Staff will provide assistance with grammar (subject to clarity of intent and meaning).
7. Unused space should be minimized. Sections and subsections should not normally begin on a new page.

MATERIAL, SUBMITTAL FORMAT AND PROCEDURE

The preferred format for submission and subsequent review, is 12 point font or 12 cpi, double line spacing and single column per page. Four copies of all submissions should be sent to the Editor-in-Chief. Each submission must be accompanied by a covering letter. The letter should include the name, address, and telephone and/or fax number and/or e-mail address of at least one of the authors.

Only camera-ready original copies are accepted for publication. The term "camera-ready" means that the material is neat, legible, and reproducible. The preferred font style is Times Roman 10 point (or equivalent) such as that used in this text. A double column format similar to that used here is preferred. No author's work will be turned down once it has been accepted because of an inability to meet the requirements concerning fonts and format. Full details are sent to the author(s) with the letter of acceptance.

There is NO requirement for India ink or for special paper; any plain white paper may be used. However, faded lines on figures and white streaks along fold lines should be avoided. Original figures - even paste-ups - are preferred over "nth-generation" photocopies. These original figures will be returned if you so request.

While ACES reserves the right to re-type any submitted material, this is not generally done.

PUBLICATION CHARGES

ACES members are allowed 12 pages per paper without charge; non-members are allowed 8 pages per paper without charge. Mandatory page charges of \$75 a page apply to all pages in excess of 12 for members or 8 for non-members. Voluntary page charges are requested for the free (12 or 8) pages, but are NOT mandatory or required for publication. A priority courtesy guideline, which favors members, applies to paper backlogs. Full details are available from the Editor-in-Chief.

COPYRIGHTS AND RELEASES

Each primary author must sign a copyright form and obtain a release from his/her organization vesting the copyright with ACES. Forms will be provided by ACES. Both the author and his/her organization are allowed to use the copyrighted material freely for their own private purposes.

Permission is granted to quote short passages and reproduce figures and tables from an ACES Journal issue provided the source is cited. Copies of ACES Journal articles may be made in accordance with usage permitted by Sections 107 or 108 of the U.S. Copyright Law. This consent does not extend to other kinds of copying, such as for general distribution, for advertising or promotional purposes, for creating new collective works, or for resale. The reproduction of multiple copies and the use of articles or extracts for commercial purposes require the consent of the author and specific permission from ACES. Institutional members are allowed to copy any ACES Journal issue for their internal distribution only.